Dissertation

SUBMITTED TO THE

Combined Faculties of the Natural Sciences and Mathematics
of the Ruperto-Carola-University of Heidelberg, Germany

FOR THE DEGREE OF

Doctor of Natural Sciences

Put forward by

Suo Tang (唐琐)

Born in: Lianyungang, Jiangsu/ People's Republic of China

(出生地:中华人民共和国江苏省连云港市)

Oral examination: 04.07.2018

Plasma High Harmonic Generation and Single Attosecond Pulse Emission from Ultraintense Laser Pulses

Referees: Hon. Prof. Dr. Christoph H. Keitel
Prof. Dr. Jörg Jäckel

Zusammenfassung

Die Arbeit widmet sich der analytischen und numerischen Untersuchung der Oberwellenerzeugung höherer Ordnung und der Emission einzelner superintensiver Attosekundenpulse durch ultrarelativistische Laser-Plasma-Wechselwirkung. Im ultrarelativistischen Regime induziert der Strahlungsdruck des Lasers eine Plasma-Ionenbewegung durch den sogenannten Lochbohreffekt, was zu einer Frequenzverbreiterung der harmonischen Spektren führt. Diese Verbreiterung, analytisch analysiert und durch "particle-in-cell"-Simulationen validiert, erzeugt ein quasi-kontinuierliches Frequenzspektrum, eine Voraussetzung für die Erzeugung eines einzelnen intensiven Attosekundenpulses. Basierend auf den Ergebnissen und physikalischen Überlegungen werden Parameterkarten präsentiert, die die optimalen Regionen zur Erzeugung eines einzelnen intensiven Attosekundenpulses und kohärenter XUV-Strahlung hervorheben. Darüber hinaus wird ein robustes Plasma-Gating entwickelt, um einen super-intensiven phasenstabilisierten Attosekundenpuls zu erzeugen. Der Lochbohreffekt begrenzt die effizienteste Hochfrequenzemission in einem Laserzyklus, wodurch es möglich ist, einen einzelnen Attosekundenpuls zu isolieren. Der erzeugte Puls ist charakterisiert durch eine stabilisierte spektrale Phase $\psi(\omega) \approx \pm\pi/2$ und ein ultrabreites exponentielles Spektrum bis in den keV-Bereich, das durch ROM-Skalierung und CSE-Skalierung begrenzt ist. Die noch nie da gewesene Intensität unterstreicht das Potential isolierter Attosekundenpulse für die Durchführung von "Attosecond-Pump-Attosecond-Probe"-Experimenten.

Abstract

The thesis is devoted to the analytical and numerical studies of high-order harmonic generation and super-intense single attosecond pulse emission via ultra-relativistic laser-plasma interaction. In the ultra-relativistic regime, the laser radiation pressure induces plasma ion motion through the so called hole-boring effect, resulting in frequency widening of the harmonic spectra. This widening, analyzed analytically and validated by particle-in-cell simulations, produces a quasi-continuous frequency spectrum, a prerequisite for generating an intense single attosecond pulse. Based on the results and physical considerations, parameter maps highlighting the optimum regions for generating a single intense attosecond pulse and coherent XUV radiation are presented. Moreover, a robust plasma gating is developed to generate a super-intense phase-stabilized single attosecond pulse. The hole-boring effect limits the most efficient high-frequency emission in one laser cycle making it possible to isolate a single attosecond pulse. The generated pulse is characterized by a stabilized spectral phase $\psi(\omega) \approx \pm\pi/2$ and an ultra-broad exponential spectrum up to keV region bounded by ROM scaling and CSE scaling. The unprecedented intensity highlights the potential of the isolated attosecond pulse for performing attosecond-pump attosecond-probe experiments.

Within the framework of this thesis, the following article was published in refereed journal:

- ***Plasma High-order-harmonic Generation from Ultraintense Laser Pulses*** [1]
  Suo Tang, Naveen Kumar, and Christoph H. Keitel,
  Phys. Rev. E **95**, 051201(R) (2017).

Within the framework of this thesis, the following article was submitted for publication in refereed journal:

- ***Super-intense Single Attosecond Pulse Generation by Plasma Gating*** [2]
  Suo Tang, Naveen Kumar,
  arXiv:1803.02121 (2018).

Articles in preparation:

- ***Analytical Model for Pulse Emission from Plasma Surface Electron Layer*** [3]
  Suo Tang, Naveen Kumar

- ***Collisional Effect on Plasma High-order Harmonic Generation*** [4]
  Suo Tang

Contents

Chapter 1

Introduction

1.1 Laser development

Since the invention of the first laser in 1960 by Maiman [5], lasers have become an indispensable tool for studies of physical processes in various fields ranging from atomic and molecular physics to plasma and nuclear physics, even to high-energy astrophysics. The fast development in laser techniques has brought modern physics into an era, in which the physical processes with ultra-high energies in GeV level and ultra-short time scale about attosecond (10^{-18} s) became accessible [6]. The next-generation laser systems are predicted to extend the frontier of modern physics towards a new area with even more extreme conditions: TeV energy level and zeptosecond (10^{-21} s) timescale. The schematic diagram of the development of the laser intensity is illustrated in Fig. 1.1 [7].

The first significant improvement of the laser intensity took place in the 1960s with the development of Q-switching technique [8] and mode-locking technique [9]. The typical intensity of the laser pulse was improved rapidly in the first decade from gigawatts per square centimeter (10^9 W/cm^2) to hundreds of terawatts per square centimeter (10^{14} W/cm^2), and meanwhile, the typical duration was compressed from nanosecond (10^{-9} s) to picosecond (10^{-12} s) scale. As the strength of the laser electric field became comparable to the Coulomb field in atoms, the application of the laser to control the atomic transition and modulate the chemical bonds in molecules became feasible.

After a rather long stagnation, the second improvement of the laser intensity came in 1980s because of the invention of the chirped pulse amplification technique [10]. The laser power was taken into the terawatts (10^{12} W) regime and could be focused to intensities above 10^{20} W/cm^2. The associated laser duration was also compressed from the picosecond to the femtosecond (10^{-15} s) in the meantime. The laser field amplitude was orders of magnitude larger than the atomic Coulomb field and became strong enough to accelerate the electrons to high relativistic energies within one single laser period. If one shoots such a strong laser to a target, the exposed surface atoms could be ionized instantly, which opened the door to a new area-laser plasma interaction.

The next generation of the optical laser system in the ten petawatt ($\sim$ 10 PW) regime is under consideration [11, 12] and is expected to deliver the energy of hundreds of joules ($\sim$ 100 J) within ten femtoseconds ($\sim$ 10 fs). By focusing this laser into the diffraction-limit volume (about 1 μm^3), the laser intensity can enter the unprecedented regime of 10^{24} W/cm^2. Within one laser period, the electrons can be accelerated to ultra-relativistic energies in the GeV level and even ions can become relativistic. Such an intense laser field provides the possibility to investigate high-energy astrophysics in the lab and study the physics under extreme conditions.

It is predicted that the improvement of the laser intensity is restricted by the so called Schwinger limit [19] yielding the critical electric field $E_s = 1.32\times10^{18}$ V/m and magnetic field $B_s = 4.4\times10^9$ T corresponding to the optical laser intensity $I \sim 10^{29}$ W/cm^2. When this limit is closed, the electron-positron pairs could be created spontaneously from

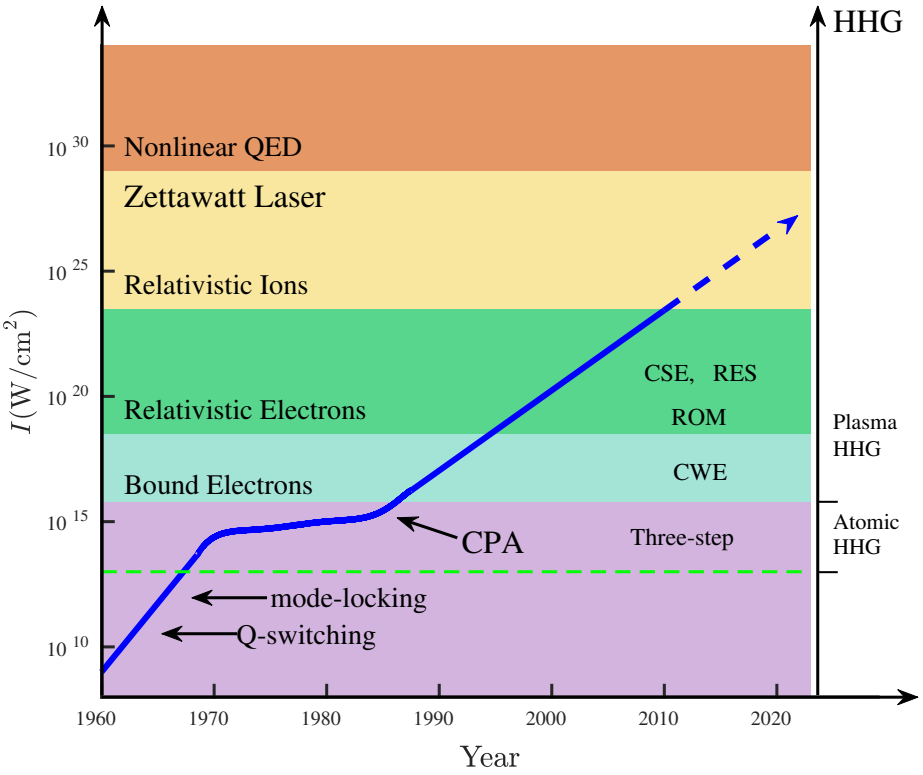

Figure 1.1: Schematic diagram of the evolution of the laser intensity taken from Ref. [7]. Different models for high-order harmonic generation in atomic physics (Three-step model [13, 14]) and plasma physics (CWE [15], ROM [16], CSE [17], RES [18]) are appended with the development of the laser intensity.

the vacuum and subsequently accelerated to ultra-relativistic energies triggering QED cascades [20]. In this case, the laser energy would be absorbed by the self-generated electron-positron plasma [21]. The estimation for the probability of the QED cascade initiated by the vacuum pair creation indicates that the limitation on the attainable intensity of the optical laser is 10^{26} W/cm^2 [22, 23].

To further improve the attainable intensity, lasers with very short wavelength $\lambda \ll 1\mu$m are considered in order to decrease the laser diffraction-limit. The electron-positron pairs created from the vacuum would be quickly expelled out of the laser focal volume by the extremely strong laser ponderomotive force and the probability of the initialization of the QED cascade can be effectively suppressed [24]. As recently proposed [25], coherent focusing of the high harmonics from the plasma surface paves a new way to achieve the extreme intensity. Numerical calculation in Ref. [25] manifests that the Schwinger limit can be reached by focusing the high-order harmonics from a concave plasma surface interacting with a strong femtosecond laser pulse with the attainable intensity $I \sim 10^{23}$ W/cm^2.

1.2 Laser-plasma interaction

The investigation of laser-matter interaction is one of the most promising fields in modern physics. Its applications range from the basic plasma phenomena [26] (such as plasma wave generation, plasma instability excitation and plasma energy transportation), to

the fundamental physical problems (such as vacuum nonlinearity [27], photon-particle interaction [28] and plasma radiation [29]), even to multiples of very important applications (such as particle acceleration [30–32], fast ignition fusion [33, 34], or high-order harmonic generation [35]).

A laser with an intensity of $I > 10^{16}$ W/cm^2 can rapidly ionize the matter, such as solid, liquid and gas, and transform the matter to the fourth state so called "plasma" which maintains atoms ionized but charge neutrality for the whole matter. The ionized electrons are subsequently caught in the strong laser field and accelerated to energies much larger than the atomic bounding energy. The fully or partially ionized ions can also be accelerated in the laser field, but due to the much smaller charge-to-mass ratio, the response of the ion acceleration is much slower than the response of the electrons. The electromagnetic field induced by the current of the charged particles feeds back into the interaction system and complements the incident fields to affect the motion of the particles. The physics of laser-plasma interaction aims to study this interaction system self-consistently.

A heuristic benchmark of the laser intensity is the normalized laser electric field a_0 ($a_0 = eE_l/(m_e c\omega_l)$ where e and m_e denote the charge and rest mass of the electron, respectively, E_l and ω_l are the electric field and frequency of the laser, respectively, and c is the light speed in vacuum). This normalized field a_0 has the very clear physical meaning that the typical energy absorbed by an electron from the laser field in one laser period in units of the electron rest energy $m_e c^2$. If $a_0 > 1$ (corresponding to $I\lambda_l^2 > 1.37 \times 10^{18}$ μm^2 W/cm^2), the laser intensity goes into the relativistic region as the electron relativistic effects become important in the laser-plasma interaction. If $a_0 < 1$, the relativistic effects can be ignored in the interaction physics.

One of the most important parameters in the laser-plasma interaction is the electron plasma frequency $\omega_{pe} = (e^2 n_{pe}/\epsilon_0 m_e)^{1/2}$, where n_{pe} is the electron number density of the plasma, and ϵ_0 is the vacuum dielectric constant. If the plasma frequency ω_{pe} is smaller than the laser frequency ω_l, the laser wave can propagate in the plasma. Otherwise, the laser field would be shielded out by the plasma electrons because of their rapid response to the laser field. The laser penetration is limited in the plasma skin layer c/ω_{pe} [36]. Hence, the condition for laser propagation in plasma can be used to define the plasma critical density $n_c = m_e \epsilon_0 \omega_l^2/e^2$ [26], which denotes that the plasma frequency is equal to the laser frequency $\omega_{pe} = \omega_l$.

When the laser intensity reaches the relativistic region $a_0 > 1$, the characteristic energy of the electron motion in the interaction becomes relativistic, $E_c = \gamma_0 m_e c^2 \approx (1 + a_0^2/2)^{1/2} m_e c^2$, and the effective electron mass, $\gamma_0 m_e$, increases. With this larger effective mass, the response of the electrons to the laser field becomes slower. Thus, the laser propagation in the plasma would be modified, and the self-induced transparency effect [36] should be considered. Hence, the plasma critical density has to be redefined to include the relativistic effect as $n_c^r = \gamma_0 m_e \epsilon_0 \omega_l^2/e^2$. If the plasma is overdense, $n_{pe} > n_c^r$, the laser field can not propagate in the plasma, but if the plasma is underdense, $n_{pe} < n_c^r$, the laser propagation in plasma is possible even if the plasma density is much than the critical density n_c.

Correspondingly, for plasma ions, the typical ion plasma frequency can also be given $\omega_{pi} = ((Ze)^2 n_{pi}/\epsilon_0 m_i)^{1/2}$, where n_{pi} is the ion number density, Z and m_i denote the charge number and rest mass of the ion. If one considers a neutral plasma with $Zn_{pi} = n_{pe}$, the ion-plasma frequency $\omega_{pi} = \omega_{pe}\sqrt{Zm_e/m_i}$ is orders of magnitude smaller than the electron-plasma frequency. This means that the response of the ions is much slower than the response of the electrons. For physical processes with the time scale of electron

response $\sim 1/\omega_{pe}$, the ions can be treated as a static, positively charged background which only provides an electrostatic field for the electron motion. The other effects from ions on the electron dynamics may be included by considering the collisions effect. If the duration of the interaction is comparable to the response time of the ions $\sim 1/\omega_{pi}$, the ion acoustic wave can be excited. In such case, the plasma dynamics would be governed by the interference among the low-frequency ion wave, the high-frequency electron wave and the electromagnetic wave.

In the experiments for ultra-short ($\sim$ 20 fs) and ultra-intense ($a_0 \gg 1$) laser- solid plasma ($n_{pe} \sim 100 n_c$) interactions, the duration of the interaction is on the time scale of the laser duration which is, in general, a multiple of the laser period $2\pi/\omega_l$. This interaction duration is much longer than the response time of electrons but shorter than or similar to the response time of ions. In this situation, the excitation of the ion acoustic wave is less important than the electron wave, but the collective motion of the ions due to the radiation pressure acceleration or the hole-boring effect [31, 37] becomes crucial because the laser ponderomotive force is extremely strong.

The physics of laser-plasma interaction is characterized with rich nonlinear effects which closely relate to the different channels for energy transfer, such as particle acceleration [30, 31], high frequency conversion [35, 38], and plasma wave excitation. All of these channels are associated with each other. For example, the stimulated Raman scattering [26] involves the phenomena of high frequency conversion and plasma wave excitation. The plasma wakefield formation interconnects the particle acceleration and the phenomenon of wavebreaking [36]. One of the main goals of the laser-plasma interaction physics is to control the dominance of the different energy transfer channels by tailoring the interaction with different set-up conditions.

In this thesis, I focus on the plasma high frequency conversion. In the laser-plasma interaction, there are various physical mechanisms responsible for the conversion, such as resonance absorption [26, 39], parametric instabilities [40], and high-order harmonic generation (HHG) [35]. HHG is one of the most promising effects with a high conversion efficiency and high order of the maximal conversion frequency. In HHG mechanism, the plasma modulates the incident laser wave nonlinearly and couples the high frequency components to the laser transmission [41, 42] and/or to the reflection [16]. As this plasma modulation happens normally in every (or half) period of the laser field, the harmonic peaks are equally spaced with one (or two) laser frequency in the frequency space. Because of the interference with the plasma wave, the typical plasma frequency may also be encoded in the generated harmonic spectrum [43–45].

1.3 High-order harmonics generation

The subject of high-order harmonic generation has been one of the hottest topics in the scientific community for decades. The motivations driving such long-time interests into this subject are fundamental. One of the primary motivations is the great potential of producing a light source with extreme optical properties, such as ultra-short pulse duration in attosecond or even zeptosecond regime [46, 47], intense coherent radiation in the extreme-ultraviolet region, and monochromatic light source in the soft x-ray region. Another very important motivation is the promising application of harmonics to diagnose the related nonlinear processes, in which the harmonic signal can provide the straightforward information and a deeper physical insight.

1.3.1 Atomic high-order harmonic generation

In Fig. 1.1, HHG from different interaction systems are pointed out along the evolution of the laser intensity. As shown, if the laser intensity reaches the region $I > 10^{13}$ W/cm^2, the atomic HHG from gaseous materials becomes achievable [48–50]. One of the most conspicuous characters of the atomic HHG is the evidence of a long plateau in the harmonic spectrum followed by a rapid drop at a cut-off frequency [46]. As the harmonic photon beam can be emitted in every half of the laser period, only odd-order harmonics can be found in the spectra of the atomic HHG.

In experiments [48, 50], picosecond or femtosecond laser pulses were focused onto the rare gas jets of helium, argon or xenon atoms and generated high-order harmonics via the nonlinear process of atom ionization and recombination. This process is normally described by the classical three-step model [13, 14]. In the strong electric field of the laser pulse, the bounded electrons firstly tunnel-ionize from the gas atoms. Subsequently, these free electrons are accelerated in the laser field to high kinetic energies. When the laser field changes its direction, these electrons are driven back to the parent ions. Finally, some of the high energy electrons recombine with the parent ions and release the obtained kinetic energy as high energetic harmonic photons. The various field-prescribed electron trajectories result in the different energies of the harmonic photons because of the different acceleration energies.

In the so-called three-step model, the third step for the recombination of electrons and ions essentially imposes one of the most fundamental restrictions on the application of the atomic HHG. In order to avoid the strong ionization, the electron kinetic energy cannot be too large to recombine with ions, the practical laser intensity has to be limited and kept below $I \approx 10^{16}$ W/cm^2. This would directly lead to the saturation of the high harmonic intensity. Another fundamental drawback for the atomic HHG is the poor performance of harmonic phase-matching [51]. Different orders of the harmonics are emitted at different times corresponding to the different electron trajectories. The consequence of this poor synchronization is the fact that the duration of the attosecond pulse synthesized by the harmonics [52] is much larger than the Fourier transformation limit of the harmonic spectrum [53].

If the incident laser intensity increases beyond the limit, $I > 10^{16}$ W/cm^2, the mechanism of the atomic HHG would break down, and an alternative mechanism − plasma HHG [35] − takes the place as shown in Fig. 1.1. With a well formed plasma target, there is, in principle, no upper limitation on the applicable laser intensity, and thus the saturation of the harmonic intensity does not exist in the plasma HHG.

1.3.2 Plasma high-order harmonic generation

In general, different physical mechanisms are responsible for plasma HHG. The underlying physical processes are extensively studied with different models, such as coherent wake emission (CWE) [15], relativistic oscillating mirror (ROM) [16], coherent synchrotron emission (CSE) [17], and relativistic electron spring (RES) [18]. These models are characterized by different properties [17, 54–56]: spectrum scaling, pulse divergence, inherent phase, and their onset depends on the plasma density of the target, laser intensity, incident angle and the plasma pre-gradient [35, 57–59]. The physical processes behind these models are associated with each other and may happen simultaneously in the same interaction. The dominance of each model depends on the laser intensity, plasma density and interaction geometry.

CWE [15] is caused by the plasma oscillation in the wake of the bunched Brunel

electrons [60]. In the interaction process, the surface plasma electrons are firstly dragged by the strong laser field out of the plasma into the vacuum, and then, when the laser field changes the sign, the electrons reverse their moving direction and are accelerated back to the plasma. These electrons bunched together penetrate into the plasma pre-gradient and excite the plasma oscillation in the wake field of the electron bunch. In this model, the oblique incidence of a laser with p-polarization[1] is required in order to have the field component perpendicular to the plasma surface, and the finite plasma pre-gradient in front of the bulk plasma is also essential for larger plasma oscillations [55, 61, 62]. The emission of the harmonics in CWE model is limited to the local plasma frequency ω_{pe}, and dominant in the non-relativistic region [63], $a_0 < 1$, as shown in Fig. 1.1. We want to point out that CWE model is different from the resonance absorption [26, 39], in which the plasma oscillation is excited directly by the laser field.

ROM [16] (also shown in Fig. 1.1) is predominant in the relativistic region [63], $a_0 > 1$. During the interaction, the surface of the plasma electrons, driven by the strong laser ponderomotive force, oscillates with a large velocity and reflects the incident laser field as a mirror. The plasma surface oscillation nonlinearly modulates the incident field and couples the harmonics to the reflection of the laser pulse. In ROM model, the frequency of the generated harmonics can be much higher than the plasma frequency. There is no prerequisite for the angle of the laser incidence and the plasma gradient, while for higher efficiency, the oblique incidence of the laser with p-polarization is preferred to irradiate the plasma with an appropriate plasma gradient [55, 59, 64]. The first theoretical calculation for ROM model [65] gave the harmonic intensity spectrum as a power-law scaling, $I(\omega) \propto \omega^{-2.5}$, rolling off at the Doppler up-shift frequency $4\gamma^2\omega_l$, where ω is the harmonic frequency and γ is the maximal relativistic factor of the surface "mirror". In BGP theory [54], under the assumption that the electric field becomes zero at the so-called apparent reflection point (ARP), *i.e.* $E^i(ct - x_{ARP}(t)) + E^r(ct + x_{ARP}(t)) = 0$, the intensity spectrum of the reflected wave is improved and analytically calculated as $I(\omega) \propto \omega^{-8/3}$ up to a roll-off frequency $\omega_r \propto \gamma^3\omega_l$, where $x_{ARP}(t)$ is the position of the ARP. Although the prediction of this spectral scaling is experimentally confirmed [66, 67], this theory is not universal. The validity of this theory depends strongly on the interaction parameters. According to the assumption, the reflected field is as strong as the incident field with a simple phase modulation. However, in some cases the amplitude of the reflected field could be much larger than the one of the incident field, leading to proposals of new models [17, 18, 68, 69].

CSE [17] has the distinct feature that the intensity of the reflection is much larger than the incident intensity, which cannot be obtained by a simple phase modulation of the incident laser. In contrast to CWE and ROM, the attosecond pulse contained in the reflection can be observed directly without any frequency filter. With the stationary phase approximation [70], the typical spectral scaling of CSE model is given by $I(\omega) \propto \omega^{-4/3}$ which is much flatter than the spectral scaling in BGP theory and manifests the higher efficiency for high-order harmonic emission. From numerical analyses, CSE tends to happen in ultra-relativistic region, $a_0 \gg 1$, with p-polarized oblique incidence. During the interaction, an ultra-dense nano-bunched electron layer is compressed at the plasma surface by the laser ponderomotive force, and then emits an extremely strong attosecond pulse. The occurrence of CSE depends strongly on the parameters of the interaction, such as plasma pre-gradient, laser intensity, incident angle and even laser carrier envelop phase (CEP). Actually, the high amplitude of the emission implies that there has to be an energy storage and release process during the interaction because of the energy

[1] The definitions for p- and s-polarization are given in Sec. 2.3.2.

conservation. This energy conversion process was firstly, to our knowledge, described explicitly in RES model [18]. These two models are quite similar. Both of them consider the emissions from the nano-bunched electron layer at the plasma surface, but from two different points of view, and show the harmonic spectral scaling in different regions. The detailed comparison between these two models will be presented in Sec. 3.4.

Within the aim of attosecond pulse emission, the performance of phase matching for harmonics from the different models is crucial. In CWE model, the harmonics with different order are emitted at different times because the oscillations of different plasma densities are located at the different positions in the plasma pre-gradient [56, 62, 71–73]. This leads to poor performance of the harmonic phase-matching and thus results in longer attosecond pulse duration. However, harmonics from ROM model are emitted synchronously by the plasma surface "mirror", thus giving better phase-matching performance [56]. Moreover, the emissions from the nano-bunched electron layer guarantees the excellent performance of the phase-matching in CSE and RES model.

The experimental investigations of plasma HHG started more than two decades ago. In the first experiment [74], a femtosecond laser with a focused intensity $I \sim 10^{17}$ W/cm^2 was used and the 15th order of harmonic was generated. Immediately, with the improvement the laser intensity to $I \sim 10^{19}$ W/cm^2, the harmonics up to 75th order was observed [75] in the interaction of a picosecond laser with a solid target. About ten year ago, the implementation of the laser with intensity, $I \sim 10^{20}$ W/cm^2, facilitated the generation of the keV harmonic photons [66, 67].

In order to improve the harmonic flux and photon energy, a laser with ultra-relativistic intensity $I > 10^{21}$ W/cm^2 is proposed to drive the interaction with a solid plasma target. In this ultra-relativistic regime, the assumption and approximation in previous literatures [16–18] may not be valid any more. For example, ion motion becomes essential because of HB effect [37]. The laser pressure pushes the plasma target surface inwards creating a double-layer structure. The electron layer in this structure oscillates around the ion layer emitting high-harmonics, but the structure itself moves slowly inside the target [1]. Additionally, the radiation reaction (RR) effects [76] also become important in the ultra-relativistic laser-solid interaction by affecting the electron dynamics and repartitioning the laser energy among electrons, ions and radiations in the plasma [77].

1.4 Thesis outline and key achievements

In this thesis, plasma HHG and single attosecond pulse emission via ultra-relativistic laser-plasma interaction are studied. The two main topics are covered in the following four chapters.

Chapter 2 presents the theoretical background for the whole thesis. We first introduce the relativistic plasma fluid equations and plasma current radiation, and then briefly summarize the basic viewpoints about plasma HHG. After this, we review the hole-boring effect and discuss the correction from hot-electron generation.

Chapter 3 develops an analytical model for pulse emission from a well-defined electron layer [3]. In this model, an analytical description for attosecond pulse is given, to our knowledge, for the first time. We validate the assumptions for our analytical model via particle-in-cell (PIC) simulations at the beginning, and then derive the expression, spectral and phase properties of the emitted pulse. Based on these derivations, the analytical description for attosecond pulse emission is given. Afterward, we discuss in detail the energy conversion process underpinning the pulse emission and provide a comparison with CSE and RES models at the end.

Chapter 4 explores the parameter maps which highlight the optimum regions for generating a single intense attosecond pulse and coherent extreme ultraviolet (XUV) radiations [1]. We start with a wide range of parametric studies to demonstrate the necessity of including the effects of ion motion, electron-ion collisions and the radiation reaction force. Further, we analyze analytically the widening of the harmonic spectra and validate it by PIC simulations. Based on the results and physical considerations, the parameter maps are presented.

Chapter 5 proposes a new scheme for an isolated ultra-intense phase-stabilized attosecond pulse generation from a robust plasma self-generated gate [2]. We start with a brief discussion about the motivations and introduce the basic method for attosecond pulse generation from plasma high harmonics. After this, we propose the scheme of "plasma gating" by means of PIC simulations and then analytically verify with our theoretical model. Moreover, an extensive discussion about the phase properties of the generated attosecond pulse is given.

Chapter 6 summarizes the main results presented in the thesis and gives a brief outlook for the future investigations.

In addition, an appendix is attached describing the mathematical techniques used in this thesis in a greater detail.

Chapter 2

Theoretical Background

In this chapter, we briefly introduce the theoretical background for the whole thesis. For the completeness, we start from the well-known relativistic Vlasov equation and Maxwell's equations to derive the plasma fluid equations in Sec. 2.1, and then, the coherent radiation from the plasma current is given in Sec. 2.2. On account of the these derivations, we give the harmonic generation from plasma current and the corresponding selection rule in Sec. 2.3. In ultra-intense laser-plasma interaction, the hole-boring effect becomes very important. In Sec. 2.4, we give the theoretical description of the hole-boring velocity, show the typical double-layer structure, and also discuss the velocity correction from the hot-electron generation. All the contents in this chapter are based on Kruer's book [26], Lichters's paper [16], Brügge's thesis [70], Levy's paper [78], and our papers [1, 2].

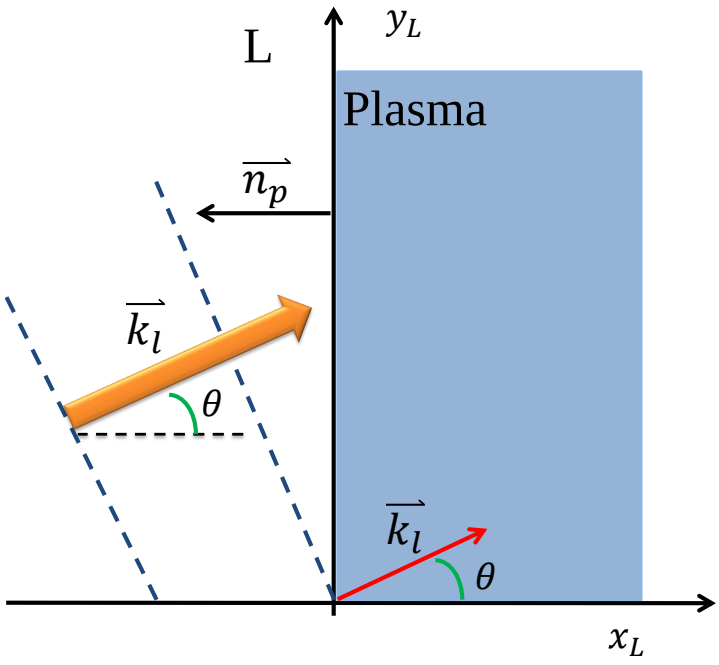

Figure 2.1: Schematic diagram of the laser-plasma interacting geometry.

Before we start the theoretical derivation, we first introduce the geometry of the laser-plasma interaction for all the discussions and simulations in this thesis. As shown in Fig. 2.1, a laser from the left side with the wave vector $\mathbf{k}_l$ irradiates the plasma target at the right side with the incident angle θ. The plasma target is too thick for the laser pulse to propagate through, thus we study the harmonics in the reflection. The incident plane

is defined by the vectors $\mathbf{k}_l$ and $\mathbf{n}_p$ as the $x-y$ plane, and the $z-$axis is perpendicular to the incident plane, where $\mathbf{n}_p$ is the normal direction of the plasma surface. Fig. 2.1 is the geometry in the frame of lab reference. In practical discussions and simulations, we transform this oblique incidence $\theta \neq 0$ in the lab reference to be a normal incidence $\theta = 0$ case in a boosted frame of reference by employing a simple Lorentz transformation [79], see Appendix A.4. In this thesis, we call the boosted frame of reference as the simulation reference. If normal incident ($\theta = 0$) is employed, the simulation reference is identical to the lab reference.

2.1 Relativistic Vlasov equation

In this thesis, we consider the fully ionized plasma without including any particle creation and/or annihilation processes. The distribution function $f(t, \mathbf{r}, \mathbf{p})$ of the different particle species obeys naturally the continuity equation in the phase space $(\mathbf{r}, \mathbf{p})$[1]:

$$\frac{\partial f}{\partial t} + \nabla_r \cdot \left(\frac{\mathbf{p}}{m\gamma} f \right) + \nabla_p \cdot \left(\frac{d\mathbf{p}}{dt} f \right) = 0 \,, \tag{2.1}$$

where $\mathbf{r}$ and $\mathbf{p}$ are the spatial and momentum coordinates for the plasma phase space. $\gamma = \sqrt{1 + \mathbf{p}^2/m^2c^2}$ is the Lorentz factor, m is the mass of the plasma particle. Since $\mathbf{r}$ and $\mathbf{p}$ are the independent variables, we can modify Eq. 2.1 and obtain

$$\frac{\partial f}{\partial t} + \frac{\mathbf{p}}{m\gamma} \cdot \nabla_r f + \frac{d\mathbf{p}}{dt} \cdot \nabla_p f = -f \left(\nabla_p \cdot \frac{d\mathbf{p}}{dt} \right) , \tag{2.2a}$$

or

$$\frac{d}{dt} f(t, \mathbf{r}, \mathbf{p}) = -f \left(\nabla_p \cdot \frac{d\mathbf{p}}{dt} \right) . \tag{2.2b}$$

The right term $-f(\nabla_p \cdot \frac{d\mathbf{p}}{dt})$ represents the source of the temporal derivative of the distribution function $f(t, \mathbf{r}, \mathbf{p})$, and is the consequence of the force divergence which may come from collision effect, radiation reaction force and so on. For convenience and clarity, we only consider the divergence-free force $\nabla_p \cdot \frac{d\mathbf{p}}{dt} = 0$ here and include the effects of the source term later. We get the source-free Vlasov equation [26]

$$\frac{\partial f}{\partial t} + \frac{\mathbf{p}}{m\gamma} \cdot \nabla_r f + q \left(\mathbf{E} + \frac{\mathbf{p}}{m\gamma} \times \mathbf{B} \right) \cdot \nabla_p f = 0 \,, \tag{2.3}$$

where the Lorentz equation $\frac{d\mathbf{p}}{dt} = q(\mathbf{E} + \frac{\mathbf{p}}{m\gamma} \times \mathbf{B})$ is included[2], and q is the charge of the particle species. The physical meaning of this equation is that the distribution function is a constant along the dynamic trajectory, *i.e.* $df(t, \mathbf{r}, \mathbf{p})/dt = 0$ [26].

2.1.1 Moment equations

Below we will follow the derivations in Kruer's book [26] for the non-relativistic Vlasov moment equations to get the relativistic version. Firstly, we introduce the expressions for the particle number density $n(t, \mathbf{r})$, the momentum current $n(t, \mathbf{r})\boldsymbol{\mathcal{P}}(t, \mathbf{r})$, and the

[1] Here, we give the discussion for each charge species, and do not distinguish the electrons and ions

[2] It is easy to verify that Lorentz force is divergence free

current of the number density $\mathbf{J}(t,\mathbf{r}) = n(t,\mathbf{r})\mathbf{u}(t,\mathbf{r})$:

$$n(t,\mathbf{r}) = \int f(t,\mathbf{r},\mathbf{p})d\mathbf{p}\,, \tag{2.4a}$$

$$n(t,\mathbf{r})\boldsymbol{\mathcal{P}}(t,\mathbf{r}) = \int \mathbf{p} f(t,\mathbf{r},\mathbf{p})d\mathbf{p}\,, \tag{2.4b}$$

$$n(t,\mathbf{r})\mathbf{u}(t,\mathbf{r}) = \int \frac{\mathbf{p}}{m\gamma} f(t,\mathbf{r},\mathbf{p})d\mathbf{p}\,, \tag{2.4c}$$

where $\mathbf{u}(t,\mathbf{r})$, $\boldsymbol{\mathcal{P}}(t,\mathbf{r})$ are the mean velocity and momentum of the plasma fluid. We want to stress that the relation, $\boldsymbol{\mathcal{P}} = m\mathbf{u}(1-\mathbf{u}^2)^{-1/2}$, is not correct for the general relativistic situations, but it is a good approximation for the cold relativistic plasma fluid dynamics and also the non-relativistic cases.

By integrating Eq. (2.3) over the momentum space, the first moment equation of the source-free Vlasov equation: conservation equation [26] can be obtained

$$\frac{\partial n}{\partial t} + \nabla_r \mathbf{J} = 0\,. \tag{2.5}$$

The second moment equation can be obtained via the integral:

$$\int \mathbf{p}\left[\frac{\partial f}{\partial t} + \frac{\mathbf{p}}{m\gamma}\cdot\nabla_r f + q\left(\mathbf{E} + \frac{\mathbf{p}}{m\gamma}\times\mathbf{B}\right)\cdot\nabla_p f\right] d\mathbf{p} = 0. \tag{2.6}$$

The first term gives

$$\int \mathbf{p}\frac{\partial f}{\partial t}d\mathbf{p} = \frac{\partial}{\partial t}(n\boldsymbol{\mathcal{P}}). \tag{2.7}$$

The second term can be calculated with a simple tensor algorithm as:

$$\begin{aligned}\int \mathbf{p}\frac{\mathbf{p}}{m\gamma}\cdot\nabla_r f d\mathbf{p} &= \int \mathbf{p}\mathbf{v}\cdot\nabla_r f d\mathbf{p} = \nabla_r\cdot\int \mathbf{v}\mathbf{p} f d\mathbf{p}\\ &= \nabla_r\cdot\int(\mathbf{v}-\mathbf{u})(\mathbf{p}-\boldsymbol{\mathcal{P}})f d\mathbf{p} + \nabla_r\cdot(n\mathbf{u}\boldsymbol{\mathcal{P}})\\ &= \nabla_r\cdot\tilde{\tilde{P}} + \nabla_r\cdot(n\mathbf{u}\boldsymbol{\mathcal{P}})\,,\end{aligned} \tag{2.8}$$

where $\mathbf{v} = \frac{\mathbf{p}}{m\gamma}$ and $\tilde{\tilde{P}} = \int(\mathbf{v}-\mathbf{u})(\mathbf{p}-\boldsymbol{\mathcal{P}})f d\mathbf{p}$ is the plasma thermal pressure tensor and is determined by the plasma temperature (T).

The third term can be evaluated as:

$$\begin{aligned}q\int \mathbf{p}\left(\mathbf{E} + \frac{\mathbf{p}}{m\gamma}\times\mathbf{B}\right)\cdot\nabla_p f d\mathbf{p} =& q\int \mathbf{p}\nabla_p\cdot\left[\left(\mathbf{E} + \frac{\mathbf{p}}{m\gamma}\times\mathbf{B}\right) f\right] d\mathbf{p}\\ =& q\int \nabla_p\cdot\left[\left(\mathbf{E} + \frac{\mathbf{p}}{m\gamma}\times\mathbf{B}\right)\mathbf{p} f\right] d\mathbf{p}\\ &- q\int\left(\mathbf{E} + \frac{\mathbf{p}}{m\gamma}\times\mathbf{B}\right) f d\mathbf{p}\\ =& -qn(\mathbf{E} + \mathbf{u}\times\mathbf{B})\,,\end{aligned} \tag{2.9}$$

here, we consider the boundary condition of the distribution function, *i.e.* $f(t,\mathbf{r},\mathbf{p}) = 0$ if $|\mathbf{p}| \to +\infty$.

With above derivations, we can know that the second moment equation is actually

the motion equation of the plasma fluid [26]:

$$\frac{\partial}{\partial t}(n\boldsymbol{\mathcal{P}}) + \nabla_r \cdot (n\mathbf{u}\boldsymbol{\mathcal{P}}) = qn(\mathbf{E} + \mathbf{u} \times \mathbf{B}) - \nabla_r \cdot \tilde{\tilde{P}}\,, \tag{2.10}$$

and with the conservation equation (Eq. 2.5), the motion equation can be simplified as:

$$\frac{\partial \boldsymbol{\mathcal{P}}}{\partial t} + \mathbf{u} \cdot \nabla_r \boldsymbol{\mathcal{P}} = q(\mathbf{E} + \mathbf{u} \times \mathbf{B}) - \frac{1}{n}\nabla_r \cdot \tilde{\tilde{P}}\,. \tag{2.11}$$

In the above derivation, we consider the dynamics of the source-free plasma. If the plasma is very dense ($n \gg n_c$) and has a low temperature (T), the collision effect would be very important and can contribute to the source term in Eq. (2.2). A detailed consideration of the collision effect is out of the scope of this thesis. Here, we just give a simple consideration and show the general result. As we know, collisions cannot change the number of the particles, thus the conservation equation (Eq. 2.5) is unchanged. However, the collision effect can act as a friction to effectively damp the motion of the plasma fluid, so we can modify the motion equation (Eq. 2.11) to phenomenologically include the collisional damping as:

$$\frac{\partial \boldsymbol{\mathcal{P}}}{\partial t} + \mathbf{u} \cdot \nabla_r \boldsymbol{\mathcal{P}} = q(\mathbf{E} + \mathbf{u} \times \mathbf{B}) - \frac{1}{n}\nabla_r \cdot \tilde{\tilde{P}} - \nu_c \boldsymbol{\mathcal{P}}\,, \tag{2.12}$$

where $\nu_c \propto nT^{-3/2}$ represents the collision frequency for the momentum damping [26, 29].

Until now, we consider the full-dimensional (3D) system which is not convenient to apply in the practical situation. In the case where the laser transverse width is much larger than the laser wavelength, the interaction system can be well approximated to be a one dimensional (1D) system, wherein the transverse spatial dependence of all the variables can be neglected. This geometry is capable to address both normal and oblique incidence cases in the simulation reference with a suitable Lorentz transformation (See Appendix A.4). As shown in Fig 2.1, we choose the direction x to be the propagating direction of the incident laser pulse, and for high-order harmonic generation, a linearly polarized laser is employed. Hence, we can simplify Eq. (2.12) as below:

$$\frac{\partial \mathcal{P}_x}{\partial t} + u_x \frac{\partial \mathcal{P}_x}{\partial x} = q(E_x + u_y B_z - u_z B_y) - \frac{1}{n}\frac{\partial}{\partial x}\tilde{\tilde{P}}_{xx} - \nu_c \mathcal{P}_x\,, \tag{2.13a}$$

$$\frac{\partial \mathcal{P}_y}{\partial t} + u_x \frac{\partial \mathcal{P}_y}{\partial x} = q(E_y - u_x B_z) - \frac{1}{n}\frac{\partial}{\partial x}\tilde{\tilde{P}}_{xy} - \nu_c \mathcal{P}_y\,, \tag{2.13b}$$

$$\frac{\partial \mathcal{P}_z}{\partial t} + u_x \frac{\partial \mathcal{P}_z}{\partial x} = q(E_z + u_x B_y) - \frac{1}{n}\frac{\partial}{\partial x}\tilde{\tilde{P}}_{xz} - \nu_c \mathcal{P}_z\,, \tag{2.13c}$$

with

$$\tilde{\tilde{P}}_{xx} = \int (v_x - u_x)(p_x - \mathcal{P}_x) f d\mathbf{p}\,,$$
$$\tilde{\tilde{P}}_{xy} = \int (v_x - u_x)(p_y - \mathcal{P}_y) f d\mathbf{p}\,,$$
$$\tilde{\tilde{P}}_{xz} = \int (v_x - u_x)(p_z - \mathcal{P}_z) f d\mathbf{p}\,,$$

where E_x is the plasma electrostatic field, and no static magnetic field $B_x = 0$ in x direction can be generated by plasma current.

2.2 Radiation from plasma current

Now, we proceed the general derivations for the coherent radiation from the plasma current which provides theoretical framework for the plasma high-order harmonic generation.

Starting from the Maxwell's equation:

$$\nabla_r \times \mathbf{B} = \mu_0 \mathbf{J} + \frac{1}{c^2}\frac{\partial \mathbf{E}}{\partial t}\,, \tag{2.15}$$

with $\mathbf{B} = \nabla_r \times \mathbf{A}$, $\mathbf{E} = -\nabla_r \psi - \partial \mathbf{A}_\perp / \partial t$ and the Coulomb gauge $\nabla_r \cdot \mathbf{A} = 0$, we can obtain the wave equation for the electromagnetic vector potential:

$$\left(\frac{1}{c^2}\frac{\partial^2}{\partial t^2} - \nabla_r^2\right)\mathbf{A}_\perp = \mu_0 \mathbf{J}_\perp\,, \tag{2.16}$$

where μ_0 is the vacuum permeability, $\mathbf{A}_\perp$ and $\mathbf{J}_\perp$ are the vector potential and plasma current in the perpendicular direction to the laser propagation. In 1D geometry, it can be simplified as:

$$\left(\frac{1}{c^2}\frac{\partial^2}{\partial t^2} - \frac{\partial^2}{\partial x^2}\right)\mathbf{A}_\perp = \mu_0 \mathbf{J}_\perp\,. \tag{2.17}$$

This is a classical wave equation, and can be solved with the help of a mature algebra−Green function $G(x,t;x^{'},t^{'})$.

By constructing a Green's function fulfilling the condition:

$$\left(\frac{1}{c^2}\frac{\partial^2}{\partial t^2} - \frac{\partial^2}{\partial x^2}\right) G(x,t;x^{'},t^{'}) = \delta(x-x^{'})\delta(t-t^{'})\,,$$

The wave equation of the vector potential can be solved as:

$$\mathbf{A}_\perp(x,t) = \mu_0 \int\int dt^{'} dx^{'} G(x,t;x^{'},t^{'})\mathbf{J}_\perp(x^{'},t^{'})\,. \tag{2.18}$$

In order to attain the specific expression of the Green function $G(x,t;x^{'},t^{'})$, the boundary condition of the vector potential $\mathbf{A}_\perp(x,t)$ has to be considered. In this thesis, we study the harmonics in the reflection from the plasma target. There is no laser pulse incident from the right side and all the leftward radiation is the reflection of the incident laser from the left side. The target plasma is thick and dense enough, so that no electromagnetic wave can propagate through. Hence, we can have the boundary condition: $|\mathbf{A}(t,x)| \to 0$ for $x \to +\infty$.

With this boundary condition, we can choose the Green function $G(x,t;x^{'},t^{'})$ as [70]:

$$G(x,t;x^{'},t^{'}) = \frac{c}{2}\left[\Theta\left(t-t^{'}+\frac{x-x^{'}}{c}\right) - \Theta\left(t-t^{'}+\frac{|x-x^{'}|}{c}\right)\right]\,, \tag{2.19}$$

where Θ is the Heaviside step function. There are different ways for the construction of Green functions, All of them will give the same result under the boundary condition. Here we just provide one possible way with clear physical meaning. Inserting this Green

function into Eq. (2.18), we can obtain the vector potential

$$\mathbf{A}_\perp(x,t) = \frac{\mu_0 c}{2}\int\int dt^{'}dx^{'}\left[\Theta\left(t-t^{'}+\frac{x-x^{'}}{c}\right)-\Theta\left(t-t^{'}+\frac{|x-x^{'}|}{c}\right)\right]\mathbf{J}_\perp(x^{'},t^{'}), \tag{2.20}$$

here we define $(x^{'},t^{'})$ as the space-time point in the plasma, and (x,t) as the space-time point for the field. To clearly show the physical meaning, we first calculate the electric field with $E_\perp = -\frac{\partial \mathbf{A}_\perp}{\partial t}$ and obtain:

$$\mathbf{E}_\perp(x,t) = \frac{\mu_0 c}{2}\int\int dt^{'}dx^{'}\left[\delta\left(t-t^{'}+\frac{|x-x^{'}|}{c}\right)-\delta\left(t-t^{'}+\frac{x-x^{'}}{c}\right)\right]\mathbf{J}_\perp(x^{'},t^{'}), \tag{2.21}$$

here the relation $\partial\Theta(x)/\partial x = \delta(x)$ is used. Assuming that during the interaction the plasma distributes from the leftmost location $x_l^{'}$ to the rightmost location $x_r^{'}$, *i.e.* $x^{'} \in (x_l^{'}, x_r^{'})$. If $x > x_r^{'}$, $\mathbf{E}_\perp(x,t) = 0$ in Eq. 2.21 because of the boundary condition. If $x < x_l^{'}$, the electric field can be divided into two parts:

$$\mathbf{E}_\perp^i(x,t) = \frac{\mu_0 c}{2}\int\int dt^{'}dx^{'}\delta\left(t-t^{'}-\frac{x-x^{'}}{c}\right)\mathbf{J}_\perp(x^{'},t^{'}), \tag{2.22a}$$

$$\mathbf{E}_\perp^r(x,t) = -\frac{\mu_0 c}{2}\int\int dt^{'}dx^{'}\delta\left(t-t^{'}+\frac{x-x^{'}}{c}\right)\mathbf{J}_\perp(x^{'},t^{'}), \tag{2.22b}$$

where $\mathbf{E}_\perp^i(x,t)$ denotes the incident laser field which drives the plasma current at $(x^{'},t^{'})$, and $\mathbf{E}_\perp^r(x,t)$ represents the reflected field coming from the superposition of the radiations from the plasma current at $(x^{'},t^{'})$. The δ functions in Eqs. (2.22) guarantee the retardation relations $ct - x = ct^{'} - x^{'}$ between the incident laser and the caused current and $ct + x = ct^{'} + x^{'}$ between the source current and the reflected wave. If we detect the field at the location x far enough from the plasma leftmost boundary, *i.e.* $x \ll x_l^{'}$, Eqs. (2.22) can be simplified as:

$$\mathbf{E}_\perp^i(x,t) = \frac{\mu_0 c}{2}\int_{-\infty}^{+\infty} dx^{'}\mathbf{J}_\perp\left(x^{'},t-\frac{x-x^{'}}{c}\right), \tag{2.23a}$$

$$\mathbf{E}_\perp^r(x,t) = -\frac{\mu_0 c}{2}\int_{-\infty}^{+\infty} dx^{'}\mathbf{J}_\perp\left(x^{'},t+\frac{x-x^{'}}{c}\right). \tag{2.23b}$$

Eq. (2.23b) describes the radiation from the collective current in the plasma target and can work as the starting point for the theory of the plasma high-order harmonic generation.

2.3 Harmonic generation

Plasma harmonic generation has been extensively discussed with different models as introduced in Sec 1.3.2 and from different points of view: incident field modulation in ROM model [16], and plasma current radiation inn CWE [15], CSE [17] and RES [18] models.

The first intuitive point of view from Eqs (2.23) is that the plasma surface, moving

as a "mirror" [54, 65, 80–82], modulates the incident wave and couples the harmonics to the reflected wave. To certify this point, an approximation that:

$$\mathbf{J}_\perp(x^{'},t^{'}) = \mathbf{J}_\perp(t^{'})\delta(x^{'} - x_{el}(t^{'})) \tag{2.24}$$

is used implying that the field modulation happens within an ultra-narrow interaction zone at the plasma surface. Inserting this approximation into Eqs (2.23), we can get

$$\mathbf{E}^i_\perp(x,t_i) = \left.\frac{\mu_0 c}{2}\frac{\mathbf{J}_\perp(t^{'})}{1-\beta_{el}(t^{'})}\right|_{ct^{'}-x_{el}(t^{'})=ct_i-x}, \tag{2.25a}$$

$$\mathbf{E}^r_\perp(x,t_r) = -\left.\frac{\mu_0 c}{2}\frac{\mathbf{J}_\perp(t^{'})}{1+\beta_{el}(t^{'})}\right|_{ct^{'}+x_{el}(t^{'})=ct_r+x}, \tag{2.25b}$$

where $x_{el}(t^{'})$ and$\beta_{el}(t^{'}) = dx_{el}(t^{'})/cdt^{'}$ are the location and velocity of the plasma "mirror", we specify the time t_i and t_r for the incident and reflected field. With the retardation relations in Eqs.(2.25), the reflected wave can be expressed as:

$$\mathbf{E}^r_\perp(x,t_r) = -\frac{1-\beta_{el}(t^{'})}{1+\beta_{el}(t^{'})}\ \mathbf{E}^i_\perp\left(x, t_r + 2\frac{x-x_{el}(t^{'})}{c}\right). \tag{2.26}$$

This is the so-called totally reflecting oscillating mirror model [70]. As we can clearly see, the reflected field is nothing but a modulation of the incident field: phase modulation and amplitude modulation.

Phase modulation: $-2x_{el}(t^{'})/c$ originates from the nonlinear motion of the plasma "mirror".

Amplitude modulation: $(1-\beta_{el}(t^{'}))/(1+\beta_{el}(t^{'}))$ can be regarded as the consequence of the Doppler effect from the plasma "mirror" motion.

This plasma "mirror" approximation is intuitive for understanding plasma harmonic generation, but can only works for long-wavelength harmonic emission with wavelength $\lambda_\omega \gg \Delta x$, where Δx is the thickness of the interaction zero.

The point of the plasma current radiation is that the abundant nonlinearities in the plasma current driven by the incident laser pulse is coupled to the reflected wave as harmonics. To verify this point, we trace the source of the harmonics in the reflected wave by transforming the reflected wave into the frequency space:

$$\widetilde{\mathbf{E}}^r_\perp(x,\omega) = \frac{1}{2\pi}\int_{-\infty}^{+\infty}\mathbf{E}^r_\perp(x,t)e^{i\omega t}dt\,,$$

and inserting Eq. (2.23b) into above equation, we can obtain

$$\begin{aligned}
\widetilde{\mathbf{E}}^r_\perp(x,\omega) &= -\frac{\mu_0 c}{4\pi}\int_{-\infty}^{+\infty}dt e^{i\omega t}\int_{-\infty}^{+\infty}dx^{'}\mathbf{J}_\perp\left(x^{'},t+\frac{x-x^{'}}{c}\right)\\
&= -\frac{\mu_0 c}{4\pi}\int_{-\infty}^{+\infty}dx^{'}\int_{-\infty}^{+\infty}dt^{'}e^{i\omega(t^{'}-\frac{x-x^{'}}{c})}\mathbf{J}_\perp(x^{'},t^{'})\\
&= -\frac{\mu_0 c}{4\pi}e^{-i\frac{\omega x}{c}}\int_{-\infty}^{+\infty}dx^{'}\int_{-\infty}^{+\infty}dt^{'}e^{i\omega(t^{'}+\frac{x^{'}}{c})}\mathbf{J}_\perp(x^{'},t^{'})
\end{aligned}$$

$$= -\mu_0 c\pi e^{-i\omega\frac{x}{c}} \widetilde{\widetilde{\mathbf{J}}}_\perp \left(-\frac{\omega}{c}, \omega\right) , \tag{2.27}$$

where the 2D Fourier transformation of the current $\mathbf{J}_\perp(x^{'}, t^{'})$ is used as

$$\widetilde{\widetilde{\mathbf{J}}}_\perp(k,\omega) = \frac{1}{4\pi^2}\int_{-\infty}^{+\infty} dx^{'} \int_{-\infty}^{+\infty} dt^{'} e^{i\omega t^{'}} e^{-kx^{'}} \mathbf{J}_\perp(x^{'}, t^{'}) .$$

From Eq. (2.27), we can clearly see that the harmonics contained in the reflected wave come from the different frequency components in the plasma current propagating to the left side. There is only a linear phase shift ($-i\omega x/c$) between the electromagnetic harmonics and plasma current harmonics. This phase shift stems from the retardation relation and can be compensated by a time shift in Eq. (2.27). The harmonic intensity spectrum can also be obtained

$$I(\omega) = \left|\widetilde{\mathbf{E}}_\perp^r(x,\omega)\right|^2 = \mu_0^2 c^2 \pi^2 \left|\widetilde{\widetilde{\mathbf{J}}}_\perp(-\frac{\omega}{c},\omega)\right|^2 . \tag{2.28}$$

As we see, the harmonic spectrum is nothing, but a spectrum of the plasma current.

2.3.1 Cold fluid approximation

To calculate harmonic spectrum, we have to know the analytical expression of the transverse current. In practical case, this can only be done by means of kinetic simulations with particle-in-cell (PIC) code [83, 84] or the Vlasov code [85, 86]. Here, we resort to the so-called relativistic cold fluid approximation, and give the analytical expression of the transverse current which is adequate to understand some general properties of the plasma harmonics.

In the cold fluid approximation, $\mathbf{u}$ and $\boldsymbol{\mathcal{P}}$ are the velocity and momentum of the cold fluid and fulfill the relation:

$$\boldsymbol{\mathcal{P}} = \gamma m \mathbf{u}, \qquad \gamma = \frac{1}{\sqrt{1-\mathbf{u}^2}}.$$

The transverse current can be given as

$$\mathbf{J}_\perp = -en_e\mathbf{u}_{e\perp} + Zen_i\mathbf{u}_0 . \tag{2.29}$$

Here we consider all the quantities in the simulation frame (See Appendix A.4) wherein the laser is normally incident and the plasma has the density, $n_0/\cos(\theta)$, and the initial velocity, $\mathbf{u}_0 = -c\sin(\theta)\hat{\mathbf{y}}$, θ is the incidence angle of the laser pulse and n_0 is the initial electron plasma density in lab reference. n_e is the distorted electron density, and we neglect the ion density perturbation, $Zen_i \equiv en_0/\cos(\theta)$, Z is the ion charge number. To calculate the velocity of the electron fluid, we make use of Eqs. (2.13b) and (2.13c)

$$\frac{\partial \boldsymbol{\mathcal{P}}_\perp}{\partial t} + u_x\frac{\partial \boldsymbol{\mathcal{P}}_\perp}{\partial x} = -e(\mathbf{E}_\perp + u_x \times \mathbf{B}_\perp) , \tag{2.30}$$

here we neglect the collisional damping and take the thermal pressure to be zero as a cold fluid. With $\mathbf{B}_\perp = \nabla_r \times \mathbf{A}_\perp$, $\mathbf{E}_\perp = -\partial\mathbf{A}_\perp/\partial t$ and $\frac{d}{dt} = \frac{\partial}{\partial t} + u_x\frac{\partial}{\partial x}$, we arrive the

conservation of canonical momentum for the fluid:

$$\frac{d}{dt}(\boldsymbol{\mathcal{P}}_\perp - e\mathbf{A}_\perp) = 0\,. \tag{2.31}$$

Hence we can have

$$\boldsymbol{\mathcal{P}}_{e\perp} - e\mathbf{A}_\perp = \text{const} = \boldsymbol{\mathcal{P}}^0_{e\perp} = -m_e c\tan(\theta)\hat{\mathbf{y}}, \tag{2.32}$$

and obtain

$$\boldsymbol{\mathcal{P}}_{e\perp} = e\mathbf{A}_\perp - m_e c\tan(\theta)\hat{\mathbf{y}}. \tag{2.33}$$

Inserting Eq. (2.33) into Eq. (2.29), we gain the expression of the current

$$\begin{aligned}\mathbf{J}_\perp &= -en_e\frac{\boldsymbol{\mathcal{P}}_{e\perp}}{m_e\gamma_e} + e\frac{n_0}{\cos(\theta)}\mathbf{u}_0 \\ &= -\frac{e^2}{m_e}\frac{n_e}{\gamma_e}\mathbf{A}_\perp + ec\tan(\theta)\left[\frac{n_e}{\gamma_e} - n_0\right]\hat{\mathbf{y}}\,,\end{aligned} \tag{2.34}$$

with

$$\gamma_e = \sqrt{\frac{1 + (\frac{e\mathbf{A}_\perp}{m_e c} - \tan(\theta)\hat{\mathbf{y}})^2}{1-\beta_{ex}^2}}\,, \tag{2.35}$$

where $\beta_{ex} = u_{ex}/c$ is the longitudinal velocity of the electron fluid. As we can see, there are two terms contributing to the current $\mathbf{J}_\perp$ [63]. The first term, proportional to $\mathbf{A}_\perp$, is driven by the total field. The second term, proportional to $\tan(\theta)$, originates from the oblique incidence with $\theta \neq 0$. Both terms include the contributions from the distortion of the electron density, n_e, and the acceleration, γ_e, of the electron fluid because of n_e/γ_e. In the first term, the total radiation field, $\mathbf{A}_\perp$, is coupled with the current leading to different parity[3] from the second term, *i.e.* if odd-order harmonics is radiated from the first term, the harmonics from the second term have to be even order, and vice versa.

To solve the temporal evolution of the transverse current, we have to know the dynamic evolution of the electron density distortion, n_e, and the electron fluid acceleration, γ_e. Using also the cold fluid approximation to Eqs. (2.13a), we can obtain

$$\frac{\partial \mathcal{P}_{ex}}{\partial t} + u_{ex}\frac{\partial \mathcal{P}_{ex}}{\partial x} = \frac{d\mathcal{P}_{ex}}{dt} = -e(E_x + \mathbf{u}_{e\perp}\times\mathbf{B}_\perp)\,.$$

Combining with Eq. (2.30) and making use of the relations $\gamma^2 m^2 c^4 = c^2\boldsymbol{\mathcal{P}}^2 + m^2c^4$, and $\mathbf{E}_\perp = -\partial\mathbf{A}_\perp/\partial t$, we arrive at

$$\begin{aligned}\frac{d\gamma_e}{dt} &= \frac{-e}{m_e^2c^2\gamma_e}(\mathcal{P}_{ex}E_x + \boldsymbol{\mathcal{P}}_{e\perp}\cdot\mathbf{E}_\perp) \\ &= \frac{-e}{m_e c}\left(\beta_{ex}E_x - \frac{e}{2m_e c\gamma_e}\frac{\partial}{\partial t}\mathbf{A}_\perp^2 + \frac{\tan(\theta)}{\gamma_e}\frac{\partial}{\partial t}\mathbf{A}_\perp\cdot\hat{\mathbf{y}}\right)\,.\end{aligned} \tag{2.36}$$

[3]Parity corresponds to the odd or even order of the harmonics

With the density conservation equation (2.5):

$$\frac{\partial n}{\partial t} + \nabla_r \mathbf{J} = 0 \Rightarrow \frac{\partial n_e}{\partial t} + c\frac{\partial n_e \beta_{ex}}{\partial x} = 0, \tag{2.37}$$

Poisson equation:

$$\nabla_r \mathbf{E} = \frac{-en_e + en_0 \cos^{-1}(\theta)}{\epsilon_0} \Rightarrow \frac{\partial E_x}{\partial x} = \frac{-en_e + en_0 \cos^{-1}(\theta)}{\epsilon_0}, \tag{2.38}$$

where ϵ_0 is vacuum permittivity, and Eq. (2.17):

$$\left(\frac{1}{c^2}\frac{\partial^2}{\partial t^2} - \frac{\partial^2}{\partial x^2}\right)\mathbf{A}_\perp = \mu_0\left[-\frac{e^2}{m_e}\frac{n_e}{\gamma_e}\mathbf{A}_\perp + ec\tan(\theta)\left(\frac{n_e}{\gamma_e} - n_0\right)\hat{\mathbf{y}}\right], \tag{2.39}$$

we can, in principle, solve the temporal evolution of the transverse current $\mathbf{J}_\perp$ and obtain the radiation $\mathbf{A}_\perp$ from the current. Here we do not solve this set of equations (2.35−2.39), but try to extract some information from the equations to give general facts about the plasma harmonics.

2.3.2 Selection rules

From the above fluid derivations, we can deduce the general "selection rules" of the plasma harmonics.

Before we start the deduction, we first give two definitions:

p-polarization: the electric field $\mathbf{E}_l$ of the incident laser is in the incident plane, and the magnetic field $\mathbf{B}_l$ is perpendicular to the incident plane, see Fig. 2.1.

s-polarization: the magnetic field $\mathbf{B}_l$ of the incident laser is in the incident plane, and the electric field $\mathbf{E}_l$ is perpendicular to the incident plane, see Fig. 2.1.

For normal incidence ($\theta = 0$): p-polarization and s-polarization are the same, we have

$$\mathbf{J}_\perp = -\frac{e^2}{m_e}\frac{n_e}{\gamma_e}\mathbf{A}_\perp\,. \tag{2.40}$$

From Eq. (2.36), we know that γ_e and $\beta_{ex}E_x$ relate to the square of the field $\mathbf{A}_\perp^2$, and from Eqs. (2.37, 2.38), we can infer n_e also contains only even order of $\mathbf{A}_\perp$ due to $\beta_{ex}E_x \to \beta_{ex}n_e \to n_e$. Hence, $\mathbf{J}_\perp$ is the function of the odd order of $\mathbf{A}_\perp$. If $\mathbf{A}_\perp \sim e^{i\omega_l t}$, only odd-order harmonics can be emitted from the transverse current, as we see in Fig. 2.2(a).

For oblique incidence with s-polarization: $\mathbf{A}_\perp = A_z\hat{\mathbf{z}}$, we obtain

$$\begin{aligned} J_y &= ec\tan(\theta)\left(\frac{n_e}{\gamma_e} - n_0\right)\,. \\ J_z &= -\frac{e^2}{m_e}\frac{n_e}{\gamma_e}A_z\,. \end{aligned} \tag{2.41}$$

Because $\mathbf{A}_\perp \cdot \hat{\mathbf{y}} = 0$ in Eq. (2.36), the same arguments can be used as those for normal incidence: n_e and γ_e are the function of A_z^2. Thus as we can see, J_y only contains the even order of A_z radiating the even-order harmonics with p-polarization, and J_z only

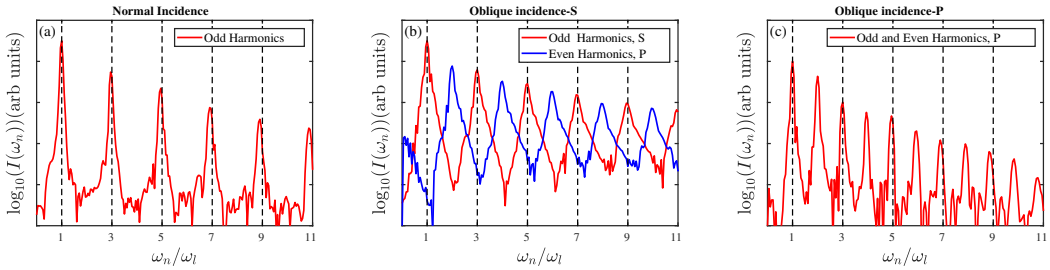

Figure 2.2: PIC simulations for HHG. (a) Harmonic spectrum for normal incidence. Only odd-order of harmonics are generated. (b) Harmonic spectrum for oblique incidence with s-polarization. Both odd and even order of harmonics are generated, but with different polarization. (c) Harmonic spectrum for oblique incidence with p-polarization. Both odd and even order of harmonics are generated with same polarization. The normalized laser electric field is $a_0 = eE_l/(m_e c\omega_l) = 40$ and the plasma target has the density $n_0 = 200n_c$. For (a), 1D simulation is used. For (b) and (c), 2D simulations are employed with incident angle $\theta = \pi/4$.

incident laser	Odd harmonics	Even harmonics
normal (linear)	same as incident	
oblique (s)	s	p
oblique (p)	p	p

Table 2.1: Selection rules for polarization (s-polarized, p-polarized) of harmonics depending on the polarization of the incident laser for normal and oblique incidence [16, 70].

contains the odd order of A_z contributing to the odd-order harmonics with s-polarization. The harmonics with p- and s-polarizations are clearly shown with the different parity in Fig. 2.2(b).

For oblique incidence with p-polarization: $\mathbf{A}_\perp = A_y\hat{\mathbf{y}}$, we get

$$J_y = -\frac{e^2}{m_e}\frac{n_e}{\gamma_e}A_y + ec\tan(\theta)\left(\frac{n_e}{\gamma_e} - n_0\right). \tag{2.42}$$

From Eq. (2.36), we can see that γ_e and $\beta_{ex}E_x$ are driven by both odd and even order of the field A_y. Hence the current J_y can contribute to both odd and even order of harmonics with p-polarization as shown in Fig. 2.2(c).

The selection rules deduced above are summarized in Table 2.1. In practice, these selection rules can be violated due to the high-dimensional effects and the nonlinear plasma effects, such as tight focused laser, hole-boring effect, plasma waves and wavebreaking effect etc.

2.4 Hole-boring effect

In the ultra-relativistic laser-plasma interaction, the hole-boring effect becomes essential as the super-strong laser ponderomotive force provides efficient ion acceleration [31, 32]. This acceleration can change the laser energy partition among ions, electrons and radiations. In the process of acceleration, ions can be strongly compressed at the plasma surface. This will affect the dynamics of the electron layer and the plasma surface current. All of these can influence the plasma high-order harmonic generation.

The hole-boring effect can be understood with a quasistationary laser piston model [37,

87], where the electrons are pushed forward by the laser ponderomotive pressure and the ions follow behind. In the hole-boring process, a double-layer structure is built up as show in Fig. 2.3.

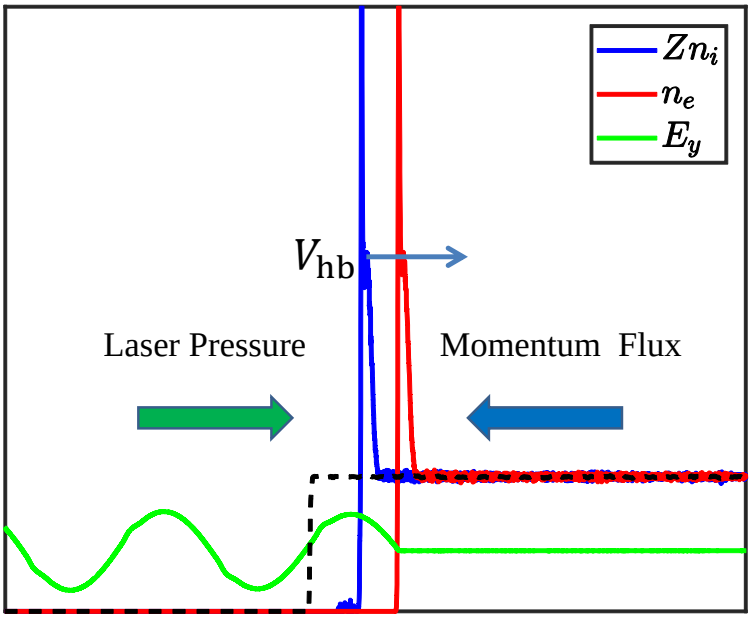

Figure 2.3: Schematic diagram for the double-layer structure of the laser piston model. Electron density (red line) and ion density (blue line) are strongly compressed at the surfaces. In the piston reference of frame, the laser pressure (green arrow) from the left side gets balance with the momentum flux (blue arrow) from the right side. The laser electric field (green line) and the initial profile of the plasma density (black dashed line) are also shown.

In the reference frame of the stationary piston moving with the velocity, $v_{hb} = c\beta_{hb}$, relative to the lab reference for normal incidence ($\theta = 0$), the laser intensity is given with a Doppler factor as

$$I_l^{'} = I_l \frac{1-\beta_{hb}}{1+\beta_{hb}} \,. \tag{2.43}$$

The unperturbed plasma coming from the right side with velocity $-v_{hb}$ interacts with the laser pulse at the laser-plasma interface, and is reflected elastically to the right side with velocity v_{hb}. At the interface of interaction, the laser momentum flux $2I_l^{'}/c$ gets balanced with the plasma momentum flux $2(n_e^{'} v_{hb} m_e \gamma_{hb} v_{hb} + n_i^{'} v_{hb} m_i \gamma_{hb} v_{hb})$:

$$\frac{2I_l^{'}}{c} = 2(n_e^{'} v_{hb} m_e \gamma_{hb} v_{hb} + n_i^{'} v_{hb} m_i \gamma_{hb} v_{hb}) \,, \tag{2.44}$$

where $\gamma_{hb} = (1-\beta_{hb}^2)^{-1/2}$, $n_e^{'} = n_0 \gamma_{hb}$ and $n_i^{'} = n_0 \gamma_{hb}/Z$ are the density of electrons and ions in the piston reference, Z is the ion charge number. Substituting all the variables in piston reference ($'$) with the variables in lab reference, we now arrive at

$$\frac{I_l}{n_0 m_e c^3 (1+\frac{m_i}{Z m_e})} = \frac{\beta_{hb}^2}{(1-\beta_{hb})^2} \,. \tag{2.45}$$

By introducing the new parameter

$$B = \sqrt{\frac{I_l}{n_0 m_e c^3 (1 + \frac{m_i}{Z m_e})}}, \tag{2.46}$$

we can obtain the velocity of the stationary piston

$$\beta_{hb} = \frac{B}{1+B}. \tag{2.47}$$

With the piston velocity, we can study the reflection coefficient (R) of the laser energy, which is crucial for the harmonics generation in the reflection. Via a simple Lorentz transformation, the reflected laser intensity in the lab reference can be obtained from the reflected laser intensity $I_l^{'}$ in piston reference:

$$I_l^r = I_l^{'} \frac{1-\beta_{hb}}{1+\beta_{hb}} = I_l \left(\frac{1-\beta_{hb}}{1+\beta_{hb}}\right)^2. \tag{2.48}$$

Considering the power incident to the plasma surface $I_l(1-\beta_{hb})$ and reflected from the plasma surface $I_l^r(1+\beta_{hb})$, the energy reflection coefficient is gained:

$$R = \frac{I_l^r(1+\beta_{hb})}{I_l(1-\beta_{hb})} = \frac{1-\beta_{hb}}{1+\beta_{hb}}. \tag{2.49}$$

As we can see, the energy reflection becomes less if the hole-boring velocity becomes larger, which would lead to weaker harmonic flux.

Until now, all the above derivations are given for normal incidence ($\theta = 0$). In order to generalize the expressions for oblique incidence, we can repeat the same derivations, but substitute the variables with the correspondences in the simulation reference via the Lorentz transformation (See Appendix A.3), *i.e.* $n_0 \to n_0/\cos(\theta)$, $I_l \to I_l \cos^2(\theta)$. The rest mass of the electron and ion should be replaced with the effective mass: $m_e \to m_e/\cos(\theta)$, $m_i \to m_i/\cos(\theta)$ because of the transverse momentum. Hence, we can have the same expressions for the piston velocity (β_{hb}) and the reflection coefficient (R) in the simulation reference, but with the new parameter:

$$B = \sqrt{\frac{I_l \cos^4(\theta)}{n_0 m_e c^3 (1 + \frac{m_i}{Z m_e})}}. \tag{2.50}$$

Here, we ignore the plasma heating effect [88–90] which absorbs the laser energy and warms the plasma particles in the interaction zone. The plasma heating effect could change the momentum balance for Eq. (2.44) and further change the energy reflection (R). We will show that the correction from hot-electron generation on the hole-boring velocity becomes considerable with low plasma densities, and this discussion will be included later in Sec. 2.4.2.

2.4.1 Double layer structure

We can clearly see the double-layer structure in Fig. 2.3. The charge separation between the electron layer and the ion layer is supported by the laser ponderomotive force $f_{pond} \sim \nabla E_l^2$. For circularly polarized lasers, the ponderomotive force is constant resulting in the constant charge separation. However, a linear polarized laser is employed

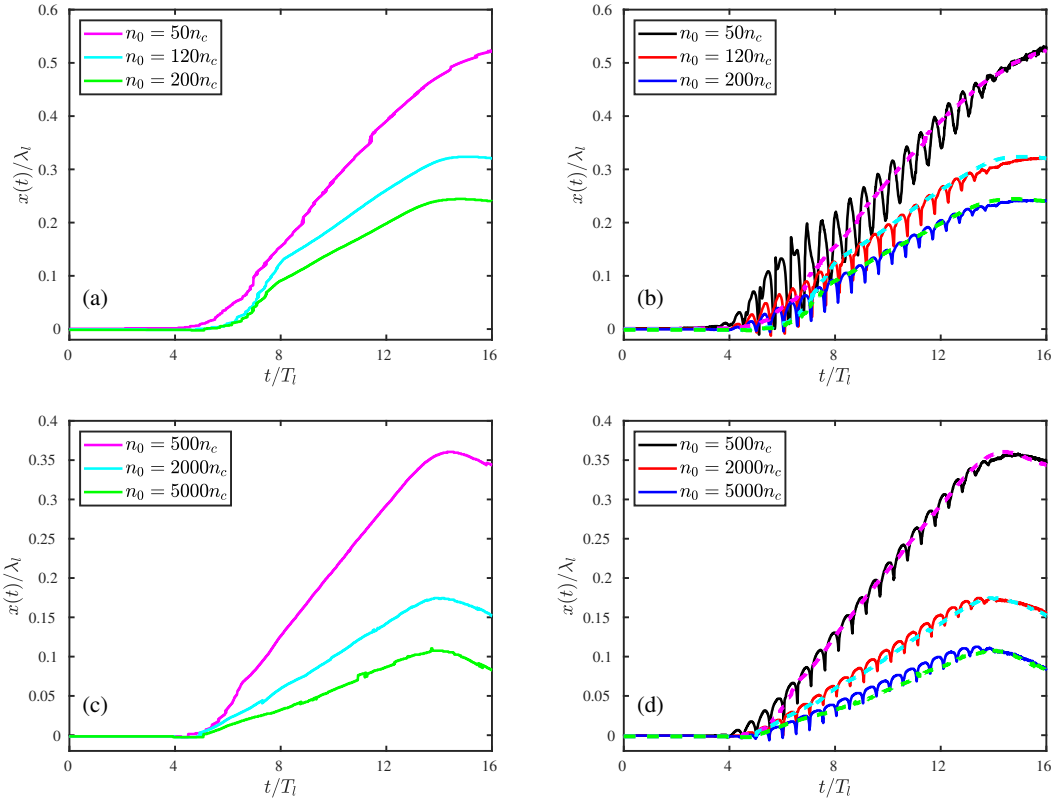

Figure 2.4: 1D PIC simulations of the temporal evolution of the double-layer structure for normal incidence ($\theta = 0$) case. (a), (c) Evolution of the ion layer surface. (b), (d) Evolution of the electron layer surface. The corresponding ion layer evolutions are attached with the dashed lines. The laser has the temporal profile $a(t) = a_0(\tanh((t-T_s)/W) - \tanh((t-T_e)/W))/2$, where $W = T_l = \lambda_l/c$, $T_s = 4T_l$, $T_e = 14T_l$, $a_0 = eE_l/(m_e c\omega_l) = 40$ for (a) and (b), $a_0 = 100$ for (c) and (d). The gold ($Z = 79$, $A = 197$) plasma is used with the constant density profile. We label the time $t = 0$ when the laser arrives the plasma surface at $x = 0$. The electron and ion surface are defined at the location with $n_e = Zn_i = a_0 n_c$

for plasma harmonic generation, the oscillatory ponderomotive force leads to the oscillation of the charge separation. In one laser cycle, when the laser electric field rises, the ponderomotive force pushing the electron layer forward gives a large charge separation, and then the laser electric field drops, the strong charge-separation (electrostatic) field accelerates the electron layer back crossing the ion layer to emit a pulse. The process can repeat in one (or half of) laser cycle to give a pulse train in time domain or a harmonic spectrum in frequency domain.

In Fig.2.4, we can clearly see the oscillation of the double-layer structure. The electron layer oscillates around the ion layer with the frequency $2\omega_l$ because of the oscillatory component in the laser ponderomotive force, where ω_l is the laser frequency. The ion layer has a roughly constant motion inside the target, and can not response to the oscillation of the laser ponderomotive force because the ion plasma frequency is much smaller.

According to Fig.2.4 (a) and (c), we can numerically calculate the hole-boring velocity $\beta = dx/cdt$ and compare with the theoretical calculations from Eq. (2.47). As shown in Table 2.2, we can clearly see that the simulation results match very well the theoretical results except that the simulation results are slightly smaller. This comes from the

$a_0 = 40$, $I_l = 800$, $\theta = 0$			
	Piston model	Simulation	Correction
$n_0 = 50$	$\beta_{hb} = 0.057$	$\beta_{hb} = 0.055$	$\beta_{hb} = 0.046$
$n_0 = 120$	$\beta_{hb} = 0.037$	$\beta_{hb} = 0.035$	$\beta_{hb} = 0.034$
$n_0 = 200$	$\beta_{hb} = 0.029$	$\beta_{hb} = 0.027$	$\beta_{hb} = 0.027$

$a_0 = 100$, $I_l = 5000$, $\theta = 0$			
	Piston model	Simulation	Correction
$n_0 = 500$	$\beta_{hb} = 0.045$	$\beta_{hb} = 0.042$	$\beta_{hb} = 0.043$
$n_0 = 2000$	$\beta_{hb} = 0.023$	$\beta_{hb} = 0.022$	$\beta_{hb} = 0.022$
$n_0 = 5000$	$\beta_{hb} = 0.015$	$\beta_{hb} = 0.013$	$\beta_{hb} = 0.014$

Table 2.2: Comparison between the theoretical calculations and simulation results of the hole-boring velocity. Eq. (2.47) and the corresponding parameters in Fig. 2.4 are used for theoretical calculations. The evolution of the ion surfaces in Fig. 2.4 (a) and (c) are used to calculate the hole-boring velocity. The corrections from the hot-electron generation are also included.

correction of hot-electron generation as we will discuss in the next section.

2.4.2 Correction from hot electron generation

The partitioning of the laser energy and momentum into the piston-punching particles (ions and electrons) and the hot electrons has been studied for decades [78, 91–94]. It is proved to be very complicate topic. It may depends on laser intensity, plasma density, interaction geometry etc. To date, no general theoretical framework has been built based on the first principles or matches the experiments in an extensive parameter range. Here, we take advantage of the theoretical model from Levy' paper [78] and the practical parameters used for plasma harmonic generation to calculate the hole-boring velocity with the account of correction from hot-electron generation.

In the simulation reference, the incident energy flux onto the plasma surface reads $(1-\beta_{hb})I_l\cos^2(\theta)$, which can bring the momentum flux, $(1-\beta_{hb})I_l\cos^2(\theta)/c$, to the plasma. The reflected energy flux from the plasma surface can be expressed as $R(1-\beta_{hb})I_l\cos^2(\theta)$ which can take the momentum flux, $-R(1-\beta_{hb})I_l\cos^2(\theta)/c$, from the plasma, where R is the reflection coefficient as discussed in Eq. (2.49). The plasma absorbed energy and momentum are partitioned for hot-electron generation and the acceleration of the piston-punching particles. We can assume that the hot electrons have the averaged energy, $\gamma_h m_e c^2$, and forward velocity, $v_h \approx c$. The velocity of the piston-punching particles can be calculated from the hole-boring velocity, v_{hb}, by a Lorentz transformation since they are elastically reflected in the piston reference:

$$v_{pp} = \frac{2\beta_{hb}c}{1+\beta_{hb}^2}, \qquad \gamma_{pp} = \frac{1+\beta_{hb}^2}{1-\beta_{hb}^2}\,.$$

For hot electrons, we can have the relations: $\gamma_h \gg \gamma_{pp}$ and $\gamma_h \gg \cos^{-1}(\theta)$. Hence, we can have the energy conservation:

$$\begin{aligned}(1-\beta_{hb})(1-R)I_l\cos^2(\theta) = \quad & (\gamma_h - 1)m_e c^2 n_h v_h \\ & + (\gamma_{pp}-1)\left(m_e + \frac{m_i}{Z}\right)c^2 n_0 v_{hb}\cos^{-2}(\theta)\,, \end{aligned} \tag{2.51}$$

and the momentum conservation:

$$(1-\beta_{hb})(1+R)\frac{I_l}{c}\cos^2(\theta) = \gamma_h m_e v_h n_h v_h + \gamma_{pp}\left(m_e+\frac{m_i}{Z}\right)v_{pp}n_0 v_{hb}\cos^{-2}(\theta)\,, \tag{2.52}$$

here we already consider the particle effective mass, $m_{i,e}/\cos(\theta)$, and plasma density, $n_0/\cos(theta)$, in the simulation reference. After simple calculations, we can simplify the conservation equations as:

$$(1-\beta_{hb})(1-R) = \frac{(\gamma_h-1)m_e c^3 n_h}{I_l\cos^2(\theta)} + \frac{2\beta_{hb}^2}{1-\beta_{hb}^2}\frac{\beta_{hb}}{B^2}\,, \tag{2.53a}$$

$$(1-\beta_{hb})(1+R) = \frac{\gamma_h m_e c^3 n_h}{I_l\cos^2(\theta)} + \frac{2\beta_{hb}^2}{1-\beta_{hb}^2}\frac{1}{B^2}\,, \tag{2.53b}$$

where B is the parameter define in Eq. (2.50). To calculate the hole-boring velocity v_{hb}, we sum Eq. (2.53a) and Eq. (2.53b), and gain that

$$2(1-\beta_{hb}) = 4X + \frac{2\beta_{hb}^2}{1-\beta_{hb}}\frac{1}{B^2}\,, \tag{2.54}$$

where

$$X = \frac{(2\gamma_h-1)m_e c^3 n_h}{4I_l\cos^2(\theta)} \approx \frac{\gamma_h m_e c^3 n_h}{2I_l\cos^2(\theta)} \tag{2.55}$$

denotes the rate of energy absorbed by the hot electrons. For plasma harmonic generation, an over-dense plasma, $n_0 \gg n_c$, is always employed. In this situation, hot electron generation is limited because the laser pulse can not penetrate deeply into the plasma. The hot electrons can only be excited in the plasma skin depth $d_s \sim \lambda_l(n_c/n_0)^{1/2} \ll \lambda_l$ by the plasma surface field $E_s \sim E_l(n_c/n_0)^{1/2} \ll E_l$, where $n_c = \epsilon_0 m_e\omega_l^2/e^2$ is the plasma critical density, λ_l and E_l are the laser wavelength and electric field. Thus we can have the assumption that

$$XB^2 = \frac{(2\gamma_h-1)m_e n_h}{4(m_e n_0 + m_i n_0/Z)}\cos^2(\theta) \ll 1\,, \tag{2.56}$$

which represents that the mass density of the hot electrons in the interaction region is much less than the total plasma mass density, and the relativistic factor γ_h can not play a significant role to change the ratio.

With the assumption $XB^2 \ll 1$ and keeping the first order of approximation, we can arrive at the hole-boring velocity with the correction from hot electron generation,

$$\beta_{hb} = \frac{B}{1+B}(1-X)\,, \tag{2.57}$$

To analytically calculate the correction term X, we have to first calculate the average energy γ_h and density n_h of the hot electrons. Since the precisely calculation is not possible, we just show the simple estimation of γ_h from the plasma surface field E_s and then summarize the hot electron density from previous results [93, 95–97].

As we know, the plasma surface electric field is estimated in ref. [16] for p-polarization

as

$$E_s \approx 2E_0\sqrt{\frac{n_c}{n_0}}\frac{1}{\cos(\theta)}, \tag{2.58}$$

and thus the average hot electron energy can be calculated:

$$\gamma_h \approx \frac{1}{2}\left\langle\left(\frac{eE_s}{m_e c\omega_l}\right)^2\right\rangle = \frac{2I_l/I_r}{n_0\cos^2(\theta)/n_c}\,, \tag{2.59}$$

where $I_r = \epsilon_0 c(m_e c\omega_l/e)^2 = m_e c^3 n_c$ corresponds to the normalized electric field, $a = 1$, and the average gives a factor, $1/2$, for a linearly polarized laser. From the previous literature [93, 95–97] and our simulation results, we can estimate the hot electron density as:

$$n_h \approx \frac{n_{rc}}{3}\,, \tag{2.60}$$

where n_{rc} represents the relativistic critical density:

$$\begin{aligned} n_{rc} &= n_c\cos^2\theta\sqrt{1+<p^2/(m_e c)^2>} \\ &\approx n_c\cos^2\theta\sqrt{1+\left\langle\left(\frac{eE_l}{m_e c\omega_l}\right)^2\right\rangle} \\ &= n_c\cos^2\theta\sqrt{1+I/I_r} \\ &\approx n_c\cos^2\theta\sqrt{I/I_r}\,. \end{aligned} \tag{2.61}$$

Inserting Eqs. (2.59)-(2.61) into Eqs. (2.55), we can obtain the correction from hot electron generation as:

$$X_h \approx \frac{\sqrt{I/I_r}}{3n_0\cos^2(\theta)/n_c}\,. \tag{2.62}$$

To check the correction of the hot-electron generation, we calculate the hole-boring velocity with Eqs. (2.57) and (2.62) for the parameters in Fig. 2.4 and show the results in Table 2.2. As we can clearly see, with hot electron correction, the theoretical results match better with the simulation results, except the one for case ($a_0 = 40$, $n_0 = 50n_c$). In this case, the hot electron correction is overestimated, this may because the plasma surface is strongly compressed, which would reduce the laser penetration and thus the hot-electron excitation.

Chapter 3

Pulse emission from plasma surface electron layer

In this chapter, we develop a theoretical model for pulse emission from a well-defined plasma surface electron layer in the ultra-relativistic laser-plasma interaction. In Sec. 3.1, we first introduce the theoretical model and derive the spectral and phase properties of the emitted pulse. The influence of the finite extension of the electron layer is also considered. Based on these derivations, we calculate the analytical expression of the attosecond pulse by filtering out low-frequency components in Sec. 3.2. Moreover, in Sec. 3.3, we discuss the energy conversion process underpinning the pulse emssion. At the end, we present the comparison between our model and the previous CSE and RES models in Sec. 3.4. The discussions about CSE and RES models are from Brügge's paper [17] and Gonoskov's paper [18], respectively. All the other contents in this chapter relate to our papers [1–3].

Hereafter, unless specifically stated, dimensionless quantities are used: $n_e = n_e/n_c$, $t = \omega_l t$, $x = k_l x$, $\beta = v/c$, $\omega_n = \omega_n/\omega_l$, $I = I/I_r$, $J = J/(ecn_c)$, $E = eE/(m_e c\omega_l)$, $B = eB/(m_e\omega_l)$, where the plasma critical density $n_c = \omega_l^2\epsilon_0 m_e/e^2 = 1.742 \times 10^{21}\mathrm{cm}^{-3}$ and the relativistic laser intensity $I_r = c\epsilon_0(m_e c\omega_l/e)^2 = 4.276 \times 10^{18}\,\mathrm{W/cm}^2$ for the laser wavelength $\lambda_l = 0.8\mu$m. In this system of units, we can have $T_l = \lambda_l = 2\pi$, $c = e = \omega_l = 1$.

3.1 Pulse emission

As we can see in Fig. 2.3, the plasma electrons are extremely compressed in the interaction zone of ultra-relativistic laser and plasma, leading to a well-defined electron layer with nanometer thickness [68] at the plasma surface. This electron layer is crucial for the laser-plasma interaction dynamics and dominates the plasma radiation.

3.1.1 Theoretical model

From previous literatures [17, 98] and our simulation results in Fig. 3.1, we know that the pulse is mainly emitted from the compressed electron layer at the plasma front surface and happens at the node where the longitudinal velocity of the electron layer gets its maximum and the transverse current changes its sign. Hence before our derivation, we first discuss the assumptions:

I The emission of the pulse is determined by an ultra-thin electron layer at the plasma surface as shown in Fig. 3.1 (b). The electron layer has the kinetic trajectory as $x'_{el}(t')$ and possesses the areal density $n_{el}(t')$. The spatial distribution $f(x' - x'_{el}(t'))$ of the electron layer can be approximated to $\delta(x' - x'_{el}(t'))$ for coherent emission if the emission wavelength λ_ω is much larger than the thickness Δx of the electron

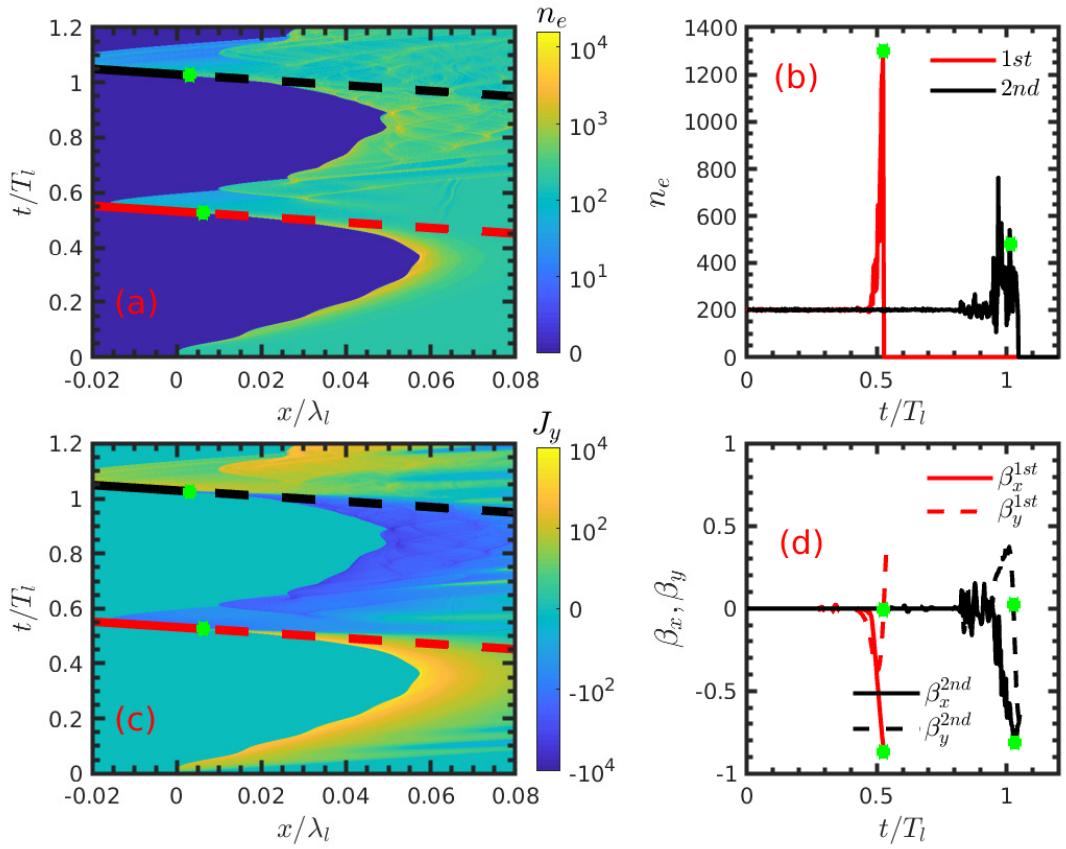

Figure 3.1: 1D PIC simulation of the pulse emission process. (a) Contour of the evolution of the electron density (n_e) at the plasma front surface overlaid with the retardation paths of the emitted pulse centers (red and black lines). Along the paths, we can trace the origins (green stars) of the two pulses. The solid-line part represents the pulse propagation in vacuum. The dashed-line part denotes the formation of the pulse ($E_y(x,t) \propto \int J_y(x', x+t-x')dx'$) in the plasma. (b) Electron density (n_e) along the retardation paths. One can see that the pulses are mainly emitted from the compressed electron layers, respectively. (c) Contour of the evolution of the electron current density (J_y) at the plasma surface with also the retardation paths. As shown, the pulse are emitted at the node when the transversed electron current changes sign. (d) Velocities ($\beta_x = -J_x/(en_ec)$, $\beta_y = -J_y/(en_ec)$) of the electron current along the retardation paths. At the emission points (green stars), the electron layers have the maximal longitudinal velocity β_x and the transverse velocity $\beta_y \approx 0$ change the sign. The red lines (solid and dashed) are for the 1st pulse, and the black lines (solid and dashed) are for the 2nd pulse. Normal incident geometry ($\theta = 0$) is employed. The laser has a step-like profile with a constant amplitude $a(t) = 40$,and the plasma (Carbon) has no pre-gradient with the constant density $n_0 = 200n_c$. Collision effect is not included and ions are fixed. The laser arrive the plasma surface at ($t = 0$, $x = 0$).

layer, *i.e.* $\lambda_\omega \gg \Delta x$. Thus, we can have the surface plasma current as

$$J_y(x^{'}, t^{'}) \approx -n_{el}(t^{'})\beta_y(t^{'})\delta(x^{'} - x^{'}_{el}(t^{'}))\,, \tag{3.1}$$

where $\beta_y(t^{'})$ is the transverse velocity of the electron layer, and $(x^{'}, t^{'})$ is the retarded spatio-temporal point of plasma current. From Ref. [68], the electron layer thickness is of the order of nanometer, *i.e.* $\Delta x \sim 1$nm, which can guarantee the coherence of the hundreds-order of harmonics for the incident laser with wavelength $\lambda_l = 0.8\mu$m.

II At the emission instant, the electron layer transverse current changes its sign, *i.e.* $\beta_y(t^{'}) \approx 0$, as one can see in Fig. 3.1 (c) and (d). Simultaneously, the longitudinal velocity approaches the speed of light, *i.e.* $\beta_x \approx -1$. This is because in the ultra-relativistic laser-plasma interaction, one can have the approximation $\beta_x^2 + \beta_y^2 \approx 1$ for the electrons in the interaction zone. For pulse emissions, the electron layer is backward accelerated efficiently in the plasma electrostatic field to the speed of light, *i.e.* $\beta_x \approx -1$ leading to $\beta_y \approx 0$. We want to stress that the condition $\beta_x \approx -1$ is very important for the approximations below and can simplify the formulae (see Eqs. (3.9), (3.10)), but will not change the form of the pulse expression and the spectral expression (see Eqs. (3.8), (3.17)). The odd-function form of the pulse expression is the consequence of the transverse current changing its sign at the emission instant as shown in Fig. 3.1 (c).

To gain the radiation from the surface electron layer, we can start from Eq. (2.23b) and replace the notation '$\perp$' with 'y' since we consider the case with p-polarization in the simulation reference (See Appendix. A.4). Thus we can have

$$E_y^r(x,t) = -\frac{1}{2}\int_{-\infty}^{+\infty} dx^{'} J_y\left(x^{'}, t^{'}\right)\,, \tag{3.2}$$

where (x,t) is the spatio-temporal point of the field detector and $(x^{'}, t^{'})$ is the retarded spatio-temporal point of plasma current. The retardation relation $t^{'} + x^{'} = t + x$ is satisfied.

Inserting Eq.(3.1) into Eq.(3.2), we obtain

$$\begin{aligned} E_y^r(x,t) &= \frac{1}{2}\int_{-\infty}^{+\infty} dx^{'} n_{el}(t^{'})\beta_y(t^{'})\delta[x^{'} - x^{'}_{el}(t^{'})] \\ &= \frac{1}{2}\int_{-\infty}^{+\infty} d\mathcal{X}\frac{n_{el}(t^{'})\beta_y(t^{'})}{1+\beta_x(t^{'})}\delta(\mathcal{X}) \\ &= \frac{1}{2}\left.\frac{n_{el}(t^{'})\beta_y(t^{'})}{1+\beta_x(t^{'})}\right|_{\mathcal{X}=0} \\ &= \frac{n_{el}(t^{'})(1-\beta_x(t^{'}))}{2}\left.\frac{\beta_y(t^{'})}{1-\beta_x^2(t^{'})}\right|_{\mathcal{X}=0}\,, \end{aligned} \tag{3.3}$$

here we replace the variable of the δ-function with $\mathcal{X} = x^{'} - x^{'}_{el}(t^{'})$. Because of the retardation relation $t^{'} + x^{'} = t + x \Rightarrow dt^{'} = -dx^{'}$, we can have $d\mathcal{X} = dx^{'} - \beta_x(t^{'})dt^{'} = (1 + \beta_x(t^{'}))dx^{'} = |1 + \beta_x(t^{'})|dx^{'}$, signifying that $\mathcal{X}$ is a monotonic function of $x^{'}$. Therefore, we can substitute the integral variable with $dx^{'} = d\mathcal{X}/(1 + \beta_x(t^{'}))$, where $\beta_x(t^{'})$ is the longitudinal velocity of the electron layer with the modulus $|\beta_x(t^{'})| < 1$ and $t^{'}(\mathcal{X})$ is a

function of $\mathcal{X}$. The condition, $\mathcal{X}=0 \Rightarrow x^{'}=x^{'}_{el}(t^{'})$, gives a new retardation relation:

$$t+x=t^{'}+x^{'}_{el}(t^{'})\,. \tag{3.4}$$

Making use of the general relation $\gamma \equiv (1-\beta_x^2-\beta_y^2)^{-1/2}$, we can have

$$\frac{1}{1-\beta_x^2}=\frac{\gamma^2}{1+(\gamma\beta_y)^2}\,.$$

Inserting this into Eq.(3.3), we can arrive at

$$E_y^r(x,t)=\frac{n_{el}(t^{'})(1-\beta_x(t^{'}))\gamma_{el}(t^{'})}{4}\frac{2p_y(t^{'})}{1+p_y^2(t^{'})}\bigg|_{t+x=t^{'}+x^{'}_{el}(t^{'})}\,, \tag{3.5}$$

where $\gamma_{el}(t^{'})$ and $p_y(t^{'})=\gamma_{el}(t^{'})\beta_y(t^{'})$ are the Lorentz factor and transverse momentum of the electron layer respectively.

Base on the condition (II), we know that the transverse momentum $p_y=\gamma\beta_y$ passes through its zero node during the pulse emission, and since the pulse emission happens on the attosecond time scale, the transverse momentum of the electron layer in the pulse emission process can be approximated in the first order:

$$p_y=\Delta t^{'}\,\frac{dp_y}{dt^{'}}\bigg|_{t^{'}=t_0^{'}}=\frac{\Delta t}{(1+\beta_x(t_0^{'}))}\,\frac{dp_y}{dt^{'}}\bigg|_{t^{'}=t_0^{'}}\,, \tag{3.6}$$

where $\Delta t^{'}$ is the short time duration around the node where $p_y(t_0^{'})=0$, and we make use of Eq. (3.4) and gain the relation:

$$\Delta t=\Delta t^{'}(1+\beta_x(t_0^{'}))\,, \tag{3.7}$$

Δt denotes the time duration around t_0 which fulfills the retardation relation $x+t_0=t_0^{'}+x^{'}_{el}(t_0^{'})$. Hereafter, we label $t_0=0$ for convenience, thus we can replace Δt with t.

Inserting Eq. (3.6) back into Eq. (3.5), we can gain the real-time dependent pulse expression:

$$E_y^r(x,t)=\hat{E}_y^r A_m\frac{2\omega_d t}{1+(\omega_d t)^2}\,, \tag{3.8}$$

where we introduce two crucial parameters:

$$A_m(t^{'})=\frac{n_{el}\gamma(1-\beta_x)}{4}\bigg|_{t+x=t^{'}+x^{'}_{el}(t^{'})}\approx\frac{n_{el}\gamma}{2}\bigg|_{t+x=t^{'}+x^{'}_{el}(t^{'})}\,, \tag{3.9}$$

which represents the pulse amplitude, and

$$\omega_d=\frac{1}{(1+\beta_x(t_0^{'}))}\left|\frac{dp_y}{dt^{'}}\bigg|_{t^{'}=t_0^{'}}\right|\approx 2\gamma^2\left|\frac{dp_y}{dt^{'}}\bigg|_{t^{'}=t_0^{'}}\right|\,, \tag{3.10}$$

which scales the time duration of the pulse, *i.e.* $T_d\sim 1/\omega_d$, and we also introduce $\hat{E}_y^r=\mathrm{sign}\left(\frac{dp_y}{dt^{'}}\right)$ denoting the sign of the reflected electric field. $\beta_x\approx -1$ is used for the approximations in Eqs. 3.9 and 3.10.

As one can see, the pulse amplitude $A_m(t^{'})$ is retarded-time dependent. With the first order approximation, we can transform it to be real-time dependent:

$$\begin{aligned} A_m(t^{'}) &= A_m(t_0^{'}) + \Delta t^{'} \left.\frac{dA_m}{dt^{'}}\right|_{t^{'}=t_0^{'}} \\ &= A_m(t_0^{'}) + \frac{t}{1+\beta_x(t_0^{'})} \left.\frac{dA_m}{dt^{'}}\right|_{t^{'}=t_0^{'}} . \end{aligned}$$

Thus, for simplicity, we can have

$$A_m(t) = A_m^0 + A_m^1 t\,, \tag{3.11}$$

where $A_m^0 = A_m(t_0^{'})$ is the constant pulse amplitude, and $A_m^1 = \left.\frac{dA_m}{dt^{'}}\right|_{t^{'}=t_0^{'}} /(1+\beta_x(t_0^{'}))$ denotes the first order of the temporal derivative of the pulse amplitude. As we can see, the straightforward consequence of this temporal variation of the amplitude is the pulse asymmetry and we will also see that this temporal variation induces a constant phase shift in the pulse spectral phase.

Furthermore, the temporal derivative of the transverse momentum can also be calculated as

$$\begin{aligned} \left.\frac{dp_y}{dt^{'}}\right|_{t^{'}=t_0^{'}} &= -(E_y - \beta_x B_z)|_{t^{'}=t_0^{'}} \\ &= -(E_y^i - \beta_x B_z^i) - (E_y^r - \beta_x B_z^r)\Big|_{t^{'}=t_0^{'}} \\ &\approx -(1-\beta_x(t_0^{'}))E_y^i(t_0^{'}) \\ &\approx -\hat{E}_y^i 2|E_y^i(t_0^{'})|\,, \end{aligned} \tag{3.12}$$

here $\hat{E}_y^i$ is the sign of the incident electric field at the emission instant $t_0^{'}$, and we consider the reflected pulse propagating in $-x$ direction with $E_y^r = -B_z^r$. Inserting Eq. (3.12) into Eq. (3.10), we can have

$$\omega_d \approx 4\gamma^2(t_0^{'}) \left|E_y^i(t_0^{'})\right| , \tag{3.13}$$

With this calculation, we also relate the sign of the reflected field to the sign of the incident field at the emission instant, *i.e.* $\hat{E}_y^r = -\hat{E}_y^i$.

As we can see, the pulse amplitude A_m depends on the product of the areal density n_{el} and relativistic factor γ of the electron layer, and ω_d is determined by the transverse acceleration $|dp_y/dt^{'}|$ of the electron layer at the emission instant and also the relativistic factor γ. Thus, in order to generate a more intense pulse with the shorter duration, we may employ a stronger incident laser pulse to interact with a denser plasma target. The extremely strong laser ponderomotive force can compress more electrons into the layer for stronger coherent emission. The more intense laser electric field leads to larger temporal derivative of the transverse momentum, which would effectively shorten the pulse duration. Moreover, the stronger laser ponderomotive force can result in larger charge separation field (See Sec. 3.3) which will lead to more efficient acceleration of the electron layer, also giving large amplitude and shorter duration of pulse.

The above derivations are based on the dynamic properties of the electron layer and do not take advantage of any specific effects, such as hole-boring effect, collision damping, temperature effect, or radiation reaction force etc. Hence, all of these effects can be

taken into account for the pulse emission (A_m, ω_d) by considering their influence on the kinetic parameters (n_{el},γ, $|dp_y/dt^{'}|$) of the electron layer.

For example, collision effect damps the backward motion of the electron layer and thus decreases the relativistic factor γ, which would lead to smaller pulse amplitude A_m and longer pulse duration $1/\omega_d$. The forward hole-boring motion would result in the expansion of the backward moving electron layer, which would decrease the pulse amplitude A_m by reducing the number of electrons for the coherent emission.

3.1.2 Spectral and phase properties

The spectral and phase properties are crucial for the application of the emitted pulse in experiments. A pulse with an ultra-broad spectrum is always needed for high-energy excitation processes in X-ray region [99] and a stabilized phase is very important for coherent control experiments [100, 101].

From Eq. (3.8), the pulse spectrum can be calculated via a simple Fourier transformation:

$$\begin{aligned}\widetilde{E}_y^r(\omega) &= \frac{1}{2\pi}\int_{-\infty}^{\infty} E_y^r(t)e^{i\omega t}dt \\ &= \frac{\hat{E}_y^r}{2\pi}\int_{-\infty}^{\infty} A_m(t)\frac{2\omega_d t}{1+(\omega_d t)^2}e^{i\omega t}dt \\ &= \frac{\hat{E}_y^r}{2\pi\omega_d}\int_{-\infty}^{\infty}\left(A_m^0+\frac{A_m^1}{\omega_d}\mathcal{X}\right)\frac{2\mathcal{X}}{1+\mathcal{X}^2}e^{i\frac{\omega}{\omega_d}\mathcal{X}}d\mathcal{X}\,,\end{aligned}$$

where the variable of integral is replaced with $\mathcal{X} = \omega_d t \Rightarrow dt = d\mathcal{X}/\omega_d$. The above integral can be calculated with the Residue Theorem as[1]

$$\widetilde{E}_y^r(\omega) = \frac{\hat{E}_y^r}{2\pi\omega_d}\int_{-\infty}^{\infty}\left(A_m^0+\frac{A_m^1}{\omega_d}\mathcal{X}\right)\left(\frac{1}{\mathcal{X}+i}+\frac{1}{\mathcal{X}-i}\right)e^{i\frac{\omega}{\omega_d}\mathcal{X}}d\mathcal{X}\,.$$

For $\omega > 0$,

$$\begin{aligned}\widetilde{E}_y^r(\omega) &= \frac{\hat{E}_y^r}{2\pi\omega_d}\int_{-\infty}^{\infty}\left(A_m^0+\frac{A_m^1}{\omega_d}\mathcal{X}\right)\frac{1}{\mathcal{X}-i}e^{i\frac{\omega}{\omega_d}\mathcal{X}}d\mathcal{X} \\ &= \frac{\hat{E}_y^r}{2\pi\omega_d}2\pi i\left(A_m^0+\frac{A_m^1}{\omega_d}i\right)e^{-\frac{\omega}{\omega_d}} \\ &= \frac{\hat{E}_y^r}{\omega_d}\left(A_m^0+\frac{A_m^1}{\omega_d}i\right)e^{-\frac{\omega}{\omega_d}}e^{i\frac{\pi}{2}} \\ &= \hat{E}_y^r\frac{\bar{A}_m}{\omega_d}e^{-\frac{\omega}{\omega_d}}e^{i(\frac{\pi}{2}+\psi_{A_m})}\,.\end{aligned} \tag{3.14}$$

For $\omega < 0$,

$$\widetilde{E}_y^r(\omega) = \frac{\hat{E}_y^r}{2\pi\omega_d}\int_{-\infty}^{\infty}\left(A_m^0+\frac{A_m^1}{\omega_d}\mathcal{X}\right)\frac{1}{\mathcal{X}+i}e^{i\frac{\omega}{\omega_d}\mathcal{X}}d\mathcal{X}$$

[1] For $\omega = 0$, $\widetilde{E}_y^r(\omega) = 0$ since the emitted pulse is an odd function of t without considering the temporal variation of A_m.

$$
\begin{aligned}
&= \frac{\hat{E}_y^r}{2\pi\omega_d}(-2\pi i)\left(A_m^0 - \frac{A_m^1}{\omega_d}i\right)e^{\frac{\omega}{\omega_d}} \\
&= \frac{\hat{E}_y^r}{\omega_d}\left(A_m^0 - \frac{A_m^1}{\omega_d}i\right)e^{\frac{\omega}{\omega_d}}e^{-i\frac{\pi}{2}} \\
&= \hat{E}_y^r\frac{\bar{A}_m}{\omega_d}e^{\frac{\omega}{\omega_d}}e^{-i(\frac{\pi}{2}+\psi_{A_m})}\,,
\end{aligned} \tag{3.15}
$$

where

$$\bar{A}_m = \sqrt{(A_m^0)^2 + (A_m^1/\omega_d)^2}\,, \tag{3.16a}$$

$$\cos(\psi_{A_m}) = \frac{A_m^0\omega_d}{\sqrt{(A_m^0\omega_d)^2 + (A_m^1)^2}}\,, \tag{3.16b}$$

$$\sin(\psi_{A_m}) = \frac{A_m^1}{\sqrt{(A_m^0\omega_d)^2 + (A_m^1)^2}}\,. \tag{3.16c}$$

With the above derivations, we can gain the pulse spectrum:

$$I(\omega) = |\widetilde{E}_y^r(\omega)|^2 = \frac{\bar{A}_m^2}{\omega_d^2}\exp\left(-\frac{2|\omega|}{\omega_d}\right). \tag{3.17}$$

As we see, the emitted pulse has an exponential spectrum with the spectral decay $2/\omega_d$. In the ultra-relativistic regime, the spectral decay $2/\omega_d \propto \gamma^{-2}|dp_y/dt^{'}|^{-1}$ would be very slow since the relativistic factor γ and the transverse acceleration $|dp_y/dt^{'}|$ would be very large in this regime, which results in the pulse possessing an ultra-broad spectrum. From another point of view, if the spectrum can be extended to ultrahigh frequency region, the spectrum can be used to diagnose tiny changes in the related physical processes as the high-frequency components are very sensitive to these changes even if their influences are negligible in low-frequency region.

This exponential spectrum is similar to the result in Ref. [18] for RES model. This is because in Ref. [18] the emission is from an ideal moving electron layer without considering the formation of the electron layer. Ref. [17] for CSE model also makes use of the assumptions as we do, but gives a power-law spectrum which is quite different from our result. A detailed comparison between these models will be presented in Sec. 3.4.

Now we start to discuss the pulse spectral phase $\psi(\omega)$ with the definition[2]:

$$\widetilde{E}_y^r(\omega) = \left|\widetilde{E}_y^r(\omega)\right| e^{-i\psi(\omega)}\,. \tag{3.18}$$

From the above derivations, we can have,

$$\psi(\omega) = \pm\frac{\pi}{2} + \psi_{A_m}\,, \qquad \text{for} \quad \omega > 0\,, \tag{3.19a}$$

$$\psi(\omega) = \pm\frac{\pi}{2} - \psi_{A_m}\,, \qquad \text{for} \quad \omega < 0\,. \tag{3.19b}$$

As we see, the pulse spectral phase is a constant and comprises of two parts:

1. $\pm\frac{\pi}{2}$: This particular phase is the consequence of the transverse current changing its sign at the emission instant when the transverse momentum passes through the

[2]The sign of $\psi(\omega)$ is chosen to be same with the linear term ωt in $E(t) = \int_{-\infty}^{\infty}|E(\omega)|e^{-i[\omega t+\psi(\omega)]}dt$.

zero node $p_y = 0$. This phase mainly regulates the pulse structure and results in a minimum at the pulse center, contrary to a synchrotron-like pulse [98]. From Eqs. (3.14) and (3.15), we know that the sign ($\pm$) of the spectral phase depends on the sign of the reflected electric field $\hat{E}_y^r$ which is determined by the sign of the incident electric field, $\hat{E}_y^r = -\hat{E}_y^i$. We wish to stress that this locked phase does not depend on the carrier-envelope-phase (CEP) of the incident laser[3], but on the dynamics of the well-defined electron layer during the emission. This is very important for the application of attosecond pulse because this stabilized phase is not only crucial for the attosecond pulse duration, but also for the temporal resolution of the attosecond pump-probe experiments [100, 102].

2. ψ_{A_m}: This term comes from the temporal variation of the pulse amplitude A_m during the emission. Because the duration ($\propto 1/\omega_d$) of pulse emission is extremely short on the attosecond time scale, the value of the temporal variation A_m^1/ω_d is relatively smaller than the constant value A_m^0, *i.e.* $A_m^1/\omega_d \ll A_m^0$. Therefore we can approximately gain

$$\psi_{A_m} \sim A_m^1/(A_m^0\omega_d)\,. \tag{3.20}$$

This phase slightly depends on the laser CEP. Because the temporal variation of the pulse amplitude $A_m(t)$ relates to the processes of layer compression (n_{el}) and acceleration (γ), both of the processes can be changed in the interaction driven by the laser with difference CEP. However the dependence should be slight since the phase ψ_{A_m} itself is very small.

We want to stress that this spectral phase denotes the *time-independent* phase of the different frequency components in a single emitted pulse (See Appendix A.2), it is different from, but related to the harmonic phase [51, 56, 103] which is the consequence of the interference among all the pulses in the whole reflection (See Appendix A.3).

3.1.3 Finite distribution of the electron layer

If the wavelength λ_ω of the emission is close to or smaller than the thickness of the layer $\lambda_\omega \lesssim \Delta x$, the δ-function approximation of the electron layer distribution can not work. The pulse spectrum and spectral phase would be modulated at least in the high-frequency region.

We now derive the spectrum directly from Eq. (3.2) with the finite extension of the current density [17]

$$J_y(t^{'}, x^{'}) = -n_{el}(t^{'})\beta_y(t^{'})f(x^{'} - x_{el}'(t^{'}))\,.$$

Thus we can have

$$\begin{aligned}\widetilde{E}_y^r(x,\omega) &= \frac{1}{2\pi}\int_{-\infty}^{\infty} E_y^r(x,t)e^{i\omega t}dt \\ &= \frac{-1}{4\pi}\int_{-\infty}^{\infty} dt e^{i\omega t}\int_{-\infty}^{\infty} dx^{'} J_y(x^{'},t^{'})\Big|_{x+t=x'+t'} \\ &= \frac{1}{4\pi}\int_{-\infty}^{\infty} dt e^{i\omega t}\int_{-\infty}^{\infty} dx^{'} n_{el}(t^{'})\beta_y(t^{'})f(x^{'} - x_{el}'(t^{'}))\Big|_{x+t=x'+t'}\,. \end{aligned} \tag{3.21}$$

[3]The laser has to be long and strong enough to compress the target and form an electron layer at the plasma surface for the pulse emission

By replacing the finite spatial distribution $f(x^{'}-x^{'}_{el}(t^{'}))$ with its Fourier expansion:

$$f(x^{'})=\int_{-\infty}^{\infty}\widetilde{F}(k)e^{ikx^{'}}dk\,,$$

and substituting the integral variable $x^{'}$ with $t^{'}$, *i.e.* $x^{'}=x+t-t^{'}$ and $dx^{'}=-dt^{'}$, we have

$$\begin{aligned}\widetilde{E}_y^r(x,\omega)&=\frac{1}{4\pi}\int_{-\infty}^{\infty}dte^{i\omega t}\int_{-\infty}^{\infty}dt^{'}n_{el}(t^{'})\beta_y(t^{'})\int_{-\infty}^{\infty}\widetilde{F}(k)e^{ik[x+t-t^{'}-x^{'}_{el}(t^{'})]}dk\\&=\frac{1}{4\pi}\int_{-\infty}^{\infty}dt^{'}n_{el}(t^{'})\beta_y(t^{'})\int_{-\infty}^{\infty}dk\widetilde{F}(k)e^{ikx}e^{-ik[t^{'}+x^{'}_{el}(t^{'})]}\int_{-\infty}^{\infty}dte^{i(\omega+k)t}\\&=\frac{1}{2}\int_{-\infty}^{\infty}dt^{'}n_{el}(t^{'})\beta_y(t^{'})\int_{-\infty}^{\infty}dk\widetilde{F}(k)e^{ikx}e^{-ik[t^{'}+x^{'}_{el}(t^{'})]}\delta(\omega+k)\\&=\frac{1}{2}e^{-i\omega x}\widetilde{F}(-\omega)\int_{-\infty}^{\infty}n_{el}(t^{'})\beta_y(t^{'})e^{i\omega[t^{'}+x^{'}_{el}(t^{'})]}dt^{'}\,,\end{aligned}\tag{3.22}$$

As we did in Sec. 3.1.1, the integral can be evaluated by doing substitution $dt^{'}=d\mathcal{X}/(1+\beta_x(t^{'}))$ with $\mathcal{X}=t^{'}+x^{'}_{el}(t^{'})$, thus we can have

$$\begin{aligned}\widetilde{E}_y^r(x,\omega)&=\frac{1}{2}e^{-i\omega x}\widetilde{F}(-\omega)\int_{-\infty}^{\infty}\frac{n_{el}(t^{'})\beta_y(t^{'})}{1+\beta_x(t^{'})}e^{i\omega\mathcal{X}}d\mathcal{X}\Big|_{\mathcal{X}=t'+x^{'}_{el}(t^{'})}\\&=e^{-i\omega x}\widetilde{F}(-\omega)\int_{-\infty}^{\infty}A_m(t^{'})\frac{2p_y(t^{'})}{1+p_y^2(t^{'})}e^{i\omega\mathcal{X}}d\mathcal{X}\Big|_{\mathcal{X}=t'+x^{'}_{el}(t^{'})}\\&\approx e^{-i\omega x}\widetilde{F}(-\omega)\hat{E}_y^r\int_{-\infty}^{\infty}A_m(\mathcal{X}-\mathcal{X}_0)\frac{2\omega_d(\mathcal{X}-\mathcal{X}_0)}{1+\omega_d^2(\mathcal{X}-\mathcal{X}_0)^2}e^{i\omega\mathcal{X}}d\mathcal{X}\Big|_{\mathcal{X}_0=t_0'+x^{'}_{el}(t_0')}\\&=e^{i\omega[t_0'+x^{'}_{el}(t_0')-x]}\widetilde{F}(-\omega)\hat{E}_y^r\int_{-\infty}^{\infty}A_m(\mathcal{X})\frac{2\omega_d\mathcal{X}}{1+\omega_d^2\mathcal{X}^2}e^{i\omega\mathcal{X}}d\mathcal{X}\,.\end{aligned}\tag{3.23}$$

Here we consider the main contribution around the emission instant when $\beta_y(t_0^{'})=0$, $\beta_x(t_0^{'})\approx-1$. This is in line with the stationary phase approximation in Refs. [17, 54, 65, 70]. During the emission, the phase term $\exp(i\omega\mathcal{X})$ is close to be a constant because of $d\mathcal{X}=dt^{'}(1+\beta_x(t^{'})\approx0$, which mainly contributes to the integral. However, at the non-stationary phase point, the phase term results in the rapid oscillation in the integral, especially for high frequency components, thus their contributions cancel each other and can be neglected [104].

After the same calculations in Eqs. (3.14) and (3.15), we obtain

$$\widetilde{E}_y^r(x,\omega)=\hat{E}_y^re^{-i\omega x}2\pi\left|\widetilde{F}(\omega)\right|\frac{\bar{A}_m}{\omega_d}e^{-\frac{|\omega|}{\omega_d}}e^{-i\psi_f(\omega)}\begin{cases}e^{\ i(\frac{\pi}{2}+\psi_{A_m})}, & \omega>0,\\ e^{-i(\frac{\pi}{2}+\psi_{A_m})}, & \omega<0.\end{cases}\tag{3.24}$$

and

$$I(\omega)=|\widetilde{E}_y^r(x,\omega)|^2=4\pi^2\frac{|\bar{A}_m|^2}{\omega_d^2}|\tilde{F}(\omega)|^2e^{-2\frac{\omega}{\omega_d}}\,,\tag{3.25}$$

where $\widetilde{F}(-\omega)=\widetilde{F}^*(\omega)=|\widetilde{F}(\omega)|e^{-i\psi_f(\omega)}$ is used. From Eq. (3.24) and (3.25), we clearly see that the finite distribution of the electron layer can affect not only the pulse spectrum

with $|\tilde{F}(\omega)|^2$ but also the spectral phase with $\psi_f(\omega)$.

To gain deep insight into the influence of the finite distribution of electron layer, we can qualitatively express $\widetilde{F}(\omega)$ as

$$\begin{aligned}\widetilde{F}(\omega) &= \int_{-\infty}^{\infty} f(x)e^{-ikx}dx \\ &\approx \int_{-\Delta x/2}^{\Delta x/2} f(x)e^{-i2\pi\frac{x}{\lambda_\omega}}dx\,.\end{aligned}$$

If wavelength $\lambda_\omega \gg \Delta x$, the phase, $2\pi x/\lambda_\omega$, is close to be zero, we have

$$\widetilde{F}(\omega) \approx \int_{-\Delta x/2}^{\Delta x/2} f(x)dx = 1\,,$$

which means that for low-frequency emission ($\lambda_\omega \gg \Delta x$), the finite distribution of the electron layer can not affect the spectrum or the spectral phase.

If $\lambda_\omega \ll \Delta x$, the phase $2\pi x/\lambda_\omega$ would be significant and results in rapid oscillation in the integral, thus

$$\widetilde{F}(\omega) \approx \int_{-\Delta x/2}^{\Delta x/2} f(x)e^{-i2\pi\frac{x}{\lambda_\omega}}dx \ll 1$$

which means that for high-frequency emission ($\lambda_\omega \ll \Delta x$), the finite distribution of the electron layer could speed up the spectral decay. Qualitatively, $\psi_f(\omega) \sim 2\pi\Delta x/\lambda_\omega$, would also be very important for the high-frequency spectral phase.

As one may note, the term, $\exp[i\omega(t_0^{'}+x_{el}^{\prime}-x)]$, in Eq. (3.24) does not affect the pulse spectrum. It only contributes the phase with the first order of ω, thus can be canceled with a time shift.

In the above derivation, we neglect the time-dependence of the finite distribution, *i.e.* $f(x^{'}-x_{el}^{'}(t^{'}),t^{'}) \approx f(x^{'}-x_{el}^{'}(t^{'}))$. This is a reasonable approximation since the extremely short duration of the pulse emission limits the expansion of the electron layer. Moreover, we assume that different parts of the electron layer emit the pulse coherently. It may be not true in practice. Different parts of the electron layer may give the emission at different time. The time difference $\Delta t \propto \Delta x/c$ could result in a phase difference $\Delta\psi(\omega) \approx \omega\Delta x/c$ between the emissions, thus affecting the intensity of the pulse which actually is the superposition of all the emissions. This incoherence of the emission would be considerable if $\lambda_\omega \lesssim \Delta x$ and would induce significant phase fluctuation in the high-frequency emission [2].

3.2 Attosecond pulse generation

With above derivations, we know that the high-frequency emissions are bunched in a very short duration when the compressed electron layer has the largest backward velocity. In general, this duration is in attoseocnd time scale. Thus, filtering out the low-frequency components makes it possible to form an intense attosecond pulse with the high-frequency components.

In order to obtain an analytical expression for the attosecond pulse, we filter out the low-frequency components ($\omega < \omega_f$) in Eqs. (3.14) and (3.15), and then inversely

transform the high-frequency components back to the time domain:

$$\begin{aligned}
E_y^r(\omega_f,t) &= \int_{\omega_f}^{+\infty}\widetilde{E}_y^r(\omega)e^{-i\omega t}d\omega+\int_{-\infty}^{-\omega_f}\widetilde{E}_y^r(\omega)e^{-i\omega t}d\omega\\
&= \hat{E}_y^r\frac{\bar{A}_m}{\omega_d}\left[\int_{\omega_f}^{+\infty}e^{-\frac{\omega}{\omega_d}}e^{-i\left(\omega t-\frac{\pi}{2}-\psi_{A_m}\right)}d\omega+\int_{-\infty}^{-\omega_f}e^{\frac{\omega}{\omega_d}}e^{-i\left(\omega t+\frac{\pi}{2}+\psi_{A_m}\right)}d\omega\right]\\
&= \hat{E}_y^r\frac{\bar{A}_m}{\omega_d}\int_{\omega_f}^{+\infty}e^{-\frac{\omega}{\omega_d}}\left[e^{-i\left(\omega t-\frac{\pi}{2}-\psi_{A_m}\right)}+e^{i\left(\omega t-\frac{\pi}{2}-\psi_{A_m}\right)}\right]d\omega\\
&= \hat{E}_y^r\frac{2\bar{A}_m}{\omega_d}\int_{\omega_f}^{+\infty}e^{-\frac{\omega}{\omega_d}}\cos\left(\omega t-\pi/2-\psi_{A_m}\right)d\omega\\
&= \hat{E}_y^r\frac{2\bar{A}_m}{\omega_d}\cos(\psi_{A_m})\int_{\omega_f}^{+\infty}e^{-\frac{\omega}{\omega_d}}\sin\left(\omega t\right)d\omega\\
&\quad -\hat{E}_y^r\frac{2\bar{A}_m}{\omega_d}\sin(\psi_{A_m})\int_{\omega_f}^{+\infty}e^{-\frac{\omega}{\omega_d}}\cos\left(\omega t\right)d\omega\,.
\end{aligned}\tag{3.26}$$

Here, we define two integral constants as below:

$$\begin{aligned}
C_s(\omega_f,\omega_d) &= \int_{\omega_f}^{+\infty}e^{-\frac{\omega}{\omega_d}}\sin\left(\omega t\right)d\omega\,,\\
C_c(\omega_f,\omega_d) &= \int_{\omega_f}^{+\infty}e^{-\frac{\omega}{\omega_d}}\cos\left(\omega t\right)d\omega\,.
\end{aligned}$$

With simple calculation:

$$\begin{aligned}
\left[-\omega_d e^{-\frac{\omega}{\omega_d}}\sin(\omega t)\right]\Big|_{\omega_f}^{+\infty} &= \int_{\omega_f}^{+\infty}e^{-\frac{\omega}{\omega_d}}\sin\left(\omega t\right)d\omega-\omega_d t\int_{\omega_f}^{+\infty}e^{-\frac{\omega}{\omega_d}}\cos\left(\omega t\right)d\omega\,,\\
\left[-\omega_d e^{-\frac{\omega}{\omega_d}}\cos(\omega t)\right]\Big|_{\omega_f}^{+\infty} &= \int_{\omega_f}^{+\infty}e^{-\frac{\omega}{\omega_d}}\cos\left(\omega t\right)d\omega+\omega_d t\int_{\omega_f}^{+\infty}e^{-\frac{\omega}{\omega_d}}\sin\left(\omega t\right)d\omega\,,
\end{aligned}$$

we arrive at

$$\begin{aligned}
\omega_d e^{-\frac{\omega_f}{\omega_d}}\sin(\omega_f t) &= C_s(\omega_f,\omega_d)-\omega_d t C_c(\omega_f,\omega_d)\,,\\
\omega_d e^{-\frac{\omega_f}{\omega_d}}\cos(\omega_f t) &= C_c(\omega_f,\omega_d)+\omega_d t C_s(\omega_f,\omega_d)\,.
\end{aligned}$$

Now, we can gain the two integral constants:

$$\begin{aligned}
C_s(\omega_f,\omega_d) &= \frac{\omega_d}{1+\omega_d^2t^2}e^{-\frac{\omega_f}{\omega_d}}\left[\sin(\omega_f t)+\omega_d t\cos(\omega_f t)\right]\,,\\
C_c(\omega_f,\omega_d) &= \frac{\omega_d}{1+\omega_d^2t^2}e^{-\frac{\omega_f}{\omega_d}}\left[\cos(\omega_f t)-\omega_d t\sin(\omega_f t)\right]\,.
\end{aligned}$$

Inserting these two integral constants into Eq. (3.26), we can obtain an explicit expression for the attosecond pulse:

$$\begin{aligned}
E_y^r(\omega_f,t) &= \hat{E}_y^r\frac{2\bar{A}_m}{\omega_d}\left[\cos(\psi_{A_m})C_s(\omega_f,\omega_d)-\sin(\psi_{A_m})C_c(\omega_f,\omega_d)\right]\\
&= \hat{E}_y^r\frac{2\bar{A}_m}{1+(\omega_d t)^2}e^{-\frac{\omega_f}{\omega_d}}\left[\ \cos(\psi_{A_m})\sin(\omega_f t)+\omega_d t\cos(\psi_{A_m})\cos(\omega_f t)\right]
\end{aligned}$$

$$+ \hat{E}_y^r \frac{2\bar{A}_m}{1+(\omega_d t)^2} e^{-\frac{\omega_f}{\omega_d}} \left[-\sin(\psi_{A_m})\cos(\omega_f t) + \omega_d t \sin(\psi_{A_m})\sin(\omega_f t)\right]$$
$$= \hat{E}_y^r \frac{2\bar{A}_m}{1+(\omega_d t)^2} e^{-\frac{\omega_f}{\omega_d}} \left[\sin(\omega_f t - \psi_{A_m}) + \omega_d t \cos(\omega_f t - \psi_{A_m})\right] . \quad (3.27)$$

As we can see, the filtering frequency ω_f works as the carrier frequency for the attosecond pulse, and the constant phase ψ_{A_m} can be regarded as the CEP of the attosecond pulse. Since ψ_{A_m} depends slightly on the laser CEP, we may obtain an attosecond pulse with a well-stabilized CEP (See Sec. 5.3.1), which will be very important for attosecond pump-probe experiments [102].

With the definition of the temporal phase chirp $\varphi(t)$:

$$\cos(\varphi(t)) = \frac{\omega_d t}{\sqrt{1+(\omega_d t)^2}}, \quad \sin(\varphi(t)) = \frac{-1}{\sqrt{1+(\omega_d t)^2}} , \quad (3.28)$$

we can rewrite expression of the attosecond pulse in a compact form:

$$E_y^r(\omega_f, t) = \hat{E}_y^r \frac{2\bar{A}_m}{\sqrt{1+(\omega_d t)^2}} e^{-\frac{\omega_f}{\omega_d}} \left[-\sin(\varphi(t))\sin(\omega_f t - \psi_{A_m}) + \cos(\varphi(t))\cos(\omega_f t - \psi_{A_m})\right]$$
$$= \hat{E}_y^r \frac{2\bar{A}_m}{\sqrt{1+(\omega_d t)^2}} e^{-\frac{\omega_f}{\omega_d}} \cos\left[\omega_f t + \varphi(t) - \psi_{A_m}\right] \quad (3.29)$$

From Eq. (3.29), we can gain the amplitude of the attosecond pulse:

$$A_{atto} = 2\bar{A}_m e^{-\frac{\omega_f}{\omega_d}} \quad (3.30)$$

which depends not only on the amplitude $\bar{A}_m$ of the original pulse but also on the ratio of the filtering frequency ω_f to ω_d. As we can see, if ω_d becomes very large in ultra-relativistic regime, the attosecond pulse can carry a very high frequency, and at the same time, keep strong intensity. On the other hand, in order to improve the attosecond pulse intensity, we can employ an intense laser driver to increase the original pulse amplitude $\bar{A}_m$ and the parameter ω_d as we discussed in Sec. 3.1.1.

The temporal profile of the attosecond pulse is expressed as

$$f_{atto}(t) = \frac{1}{\sqrt{1+(\omega_d t)^2}} . \quad (3.31)$$

This attosecond pulse profile does not depend on the filtering frequency ω_f, but only on the dynamic parameter ω_d of the electron layer. The attosecond pulse duration can be scaled as the full width at half maximum of the profile ($f_{atto}^2(t)$) and is given as

$$T_d = \frac{2}{\omega_d} . \quad (3.32)$$

If we neglect the temporal variation of the pulse amplitude A_m since this variation is very small in the ultra-relativistic regime, we may simplify the attosecond pulse expression as [2]

$$E_y^r(\omega_f, t) = \hat{E}_y^r \frac{2A_m}{\sqrt{1+(\omega_d t)^2}} \exp\left(-\frac{\omega_f}{\omega_d}\right) \cos[\omega_f t + \varphi(t)] . \quad (3.33)$$

3.3 Energy conversion process

Based on the above discussion, we already know how a pulse is emitted from the plasma surface electron layer. In this section, we will present the discussion about how the laser energy is transferred to the emitted pulse. We first give an overview about the energy conversion process and then a simple analytical model is introduced. After that we consider the energy conversion process with ion motion, which distinct our investigation from the RES model [18].

As one can see in Fig. 3.2 (a), (b), the strong laser ponderomotive force compresses the plasma electrons inside the target to form a strong charge separation field E_x as shown in Fig. 3.2 (a). In this compression process, the reflection of the laser field is weak, and the laser energy is first largely converted to the plasma internal electrostatic potential U as shown in Fig. 3.2 (b). After that, the strong electrostatic field accelerates the compressed electron layer back to the incident laser field as discussed in Fig. 3.1 (d). In this acceleration process, the stored energy S_E in the plasma field is transferred to the kinetic energy of the electrons in the layer. Subsequently, these high energetic electrons interact with the incident laser field coherently to emit a strong attosecond pulse.

In Fig. 3.2 (c), (d), the same energy conversion process happens, but the amount of the energy storage becomes less with the increasing of the plasma density. To understand this, a simple analytical model is given below.

3.3.1 Theoretical model

One can assume that for the largest compression, the radiation pressure (P_l) of the laser pulse gets balanced with the electrostatic pressure (P_s) at the surface of the electron layer. Here for simplicity, the plasma skin depth is neglected, we take the electron layer surface as the interface of the laser-plasma interaction. Thus one can have

$$P_l + P_s = 0\,, \tag{3.34}$$

where P_l pushes the electron layer to the left side, and P_s pulls the layer to the right side. The electrostatic pressure (P_s) can be expressed as

$$P_s = \int_{x_0}^{+\infty} E_x dQ = \int_{x_0}^{+\infty} E_x \rho dx\,, \tag{3.35}$$

where x_0 is the location of the electron layer surface and Q, ρ are the charge and charge density at the right of x_0. With the 1D Poisson equation (2.38): $\partial E_x/\partial x = \rho$, the electrostatic pressure P_s can be calculated as

$$\begin{aligned} P_s = & \int_{x_0}^{+\infty} E_x \frac{\partial E_x}{\partial x} dx \\ = & \frac{1}{2}\int_{x_0}^{+\infty} \frac{\partial E_x^2}{\partial x} dx \\ = & -\frac{1}{2}E_x^2(x_0)\,, \end{aligned} \tag{3.36}$$

where the electric field E_x vanishes far inside the target. The laser radiation pressure is

$$P_l = \frac{2I_l(t)}{c} = 2a_0^2 \sin^2(\omega_l t + k_l x_0)\,, \tag{3.37}$$

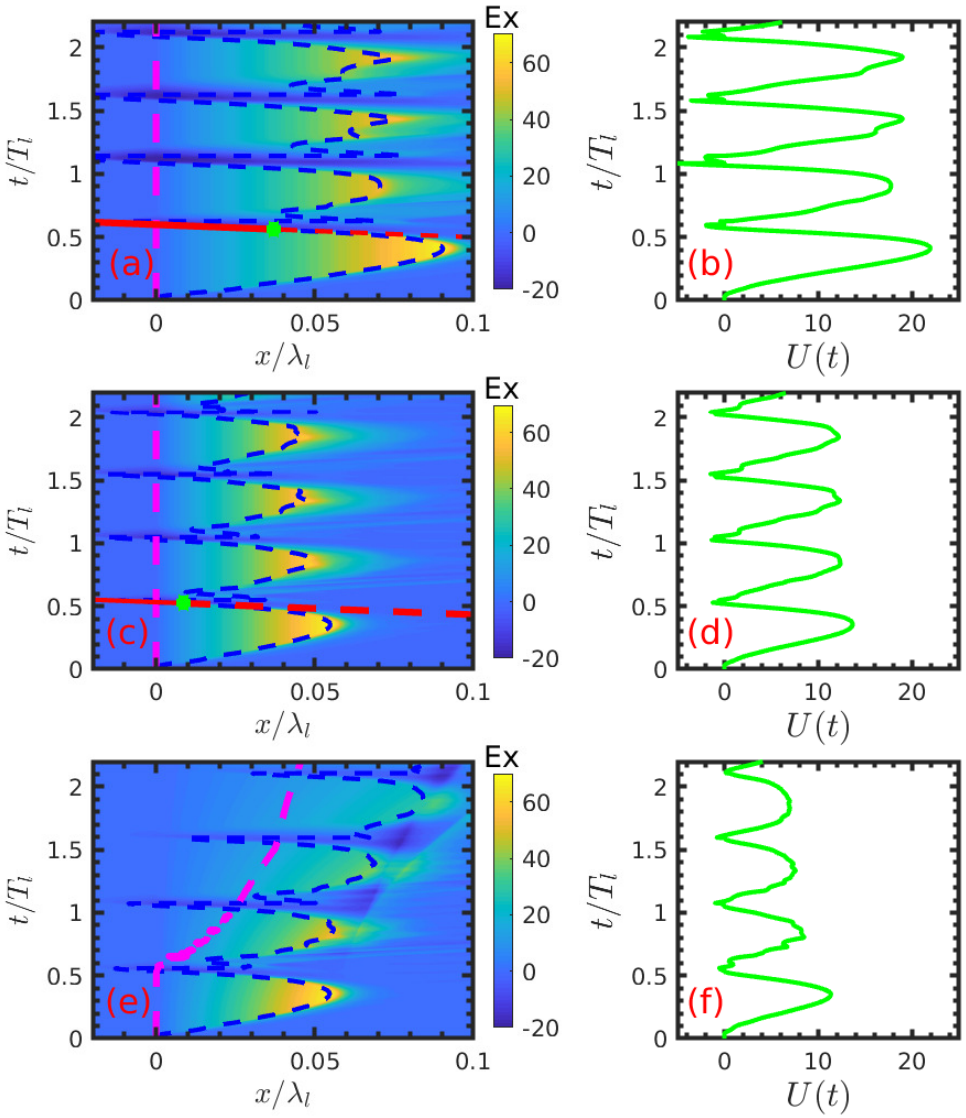

Figure 3.2: 1D PIC simulations for the pulse emission process. (a), (c), (e) Contour of the evolution of the electrostatic field (E_x) at the plasma front surface. The electron surface (blue dashed line) and ion surface (magenta dashed line) are also overlaid. (b), (d), (e) Temporal evolution of the electrostatic potential $U(t)$ at the plasma surface. $U(t) = \int E_x dx$ denotes the electrostatic potential of the charge separation field between the ion and electron surfaces. (a) and (b) are for the case with density $n_0 = 120n_c$ and fixed ions. (c) and (d) are for the case with density $n_0 = 200n_c$ and fixed ions. (e) and (f) are for the case with density $n_0 = 200n_c$ and mobile ions. In (a) and (c), we also plot the retardation paths (red dashed and solid lines) of the first pulse in each case. The physical interpretation of the retardation path can be found in Fig. 3.1. Collisional effect is included. Same other parameters are used as in Fig 3.1. The electron and ion surface are defined at the location with $n_e = Zn_i = a_0 n_c$

here the factor 2 comes from complete reflection. At the balance for the largest compression, we can have

$$P_l + P_s = 0 \Rightarrow 2a_0^2 = \frac{1}{2}E_x^2(x_0)\,, \tag{3.38}$$

and obtain the largest electrostatic field at the layer surface

$$E_x(x_0) = 2a_0\,. \tag{3.39}$$

At the left side of the electron layer surface, the charge separation field can also be calculated with the 1D Poisson equation

$$\frac{\partial E_x}{\partial x} = \rho \quad \Rightarrow \quad \frac{\partial E_x}{\partial x} = Zn_i \quad \Rightarrow \quad E_x(x) = n_0 x\,, \tag{3.40}$$

where we neglect the perturbation of the ion charge density $Zn_i = n_0$ and assume there are no electrons left behind the electron layer. At the surface, the boundary condition has to be satisfied:

$$E_x(x_0) = n_0 x_0 = 2a_0 \quad \Rightarrow \quad x_0 = \frac{2a_0}{n_0}\,. \tag{3.41}$$

Based on the above results, we can calculate the electrostatic potential of the charge separation field:

$$U = \int_0^{x_0} E_x(x)dx = \frac{n_0}{2}x_0^2 = \frac{2}{n_0}a_0^2\,. \tag{3.42}$$

On account of the laser intensity $I_l = a_0^2/2$ for linear polarization, we can also express the largest electrostatic potential as

$$U = 4\frac{I_l}{n_0}\,, \tag{3.43}$$

which directly relates to the single particle acceleration. With the parameters in Fig. 3.2, we can calculate: for $n_0 = 120n_c$, $U = 26.7m_ec^2$, and for $n_0 = 200n_c$, $U = 16m_ec^2$, qualitatively matching the simulation results in Fig. 3.2 (b), (d)and (f).

Moreover, the energy density of the electrostatic field can also be calculated:

$$\rho_{S_E} = \frac{1}{2}E_x^2 = \frac{1}{2}n_0^2x^2\,. \tag{3.44}$$

Integrating this energy density, we can gain the energy stored in the electrostatic field:

$$S_E = \int_0^{x_0} \rho_{S_E}dx = \int_0^{x_0} \frac{1}{2}n_0^2x^2dx = \frac{n_0^2}{6}x_0^3\,. \tag{3.45}$$

Inserting Eq. 3.41 into Eq. 3.45 and with a simple integral, the largest stored electrostatic energy can be expressed as:

$$S_E = \frac{4a_0^3}{3n_0} = \frac{8a_0}{3n_0}I_l\,. \tag{3.46}$$

For more straightforward physical meaning, we calculate the ratio of the energy storage

to the laser energy:

$$\frac{S_E}{S_l} = \frac{8a_0}{3\pi n_0}\,, \tag{3.47}$$

where $S_l = I_l T_l/2 = \pi I_l$ is the laser energy in half laser period. From the above results, we know that larger laser intensities and lower plasma densities can give more energy storage in the plasma field, and the ratio of the energy storage only depends on the ultra-relativistic similarity parameter, $s = n_0/a_0$ [105], which is in line with simulation results in Ref. [18] and clearly explain the simulation results: the ratio of the maximal energy storage to the laser energy is inversely proportional to the similarity parameter s in overdense plasma region.

In the above derivation, we consider the balance between the laser radiation pressure and plasma electrostatic pressure. This is a good approximation for cold and overdense plasma. For a warm or underdense plasma target, the energy storage would be overestimated. In such cases, this energy conversion process would be very complicated and could be affected by different effects such as plasma energy absorption, plasma heating and self-induced transparency. For example, if a relativistic under-dense plasma $n_0 < a_0$ is use, the laser can propagate in the plasma because of the effect of self-induced transparency (see Sec. 1.2). More laser energy would be absorbed by the plasma target and less would be reflected. Eq. 3.47 would significantly overestimate the energy storage. Moreover, in the pressure balance (see Eq. 3.34), the contribution from the plasma pressure, such as thermal pressure and surface expansion, are neglected, which may also reduce the energy storage.

3.3.2 Discussions

Based on the above derivations, we already know how the laser energy is stored in the plasma internal field. In this subsection, we show how the pulse emission is affected by the energy storage.

From Eqs. (3.43) and (3.46), we can know that the energy storage in the plasma charge separation field is proportional to the laser intensity, and inversely proportional to the plasma density. Keeping the same laser intensity and increasing the plasma density, the energy storage is reduced as shown in Fig. 3.2 (b), (d). The reduction of the stored energy results in a smaller relativistic factor γ because of less acceleration of the electron layer, which would weaken the emitted pulse amplitude A_m and more importantly reduce high-frequency emission with a more rapid spectral decay $1/\omega_d$. As we can see in Fig. 3.3, the pulses from the target with $n_0 = 120n_c$ are much stronger than those from the target with $n_0 = 200n_c$, and the pulse spectrum for $n_0 = 120n_c$ case decays much slower than that for $n_0 = 200n_c$ case implying higher efficiency for high-frequency emission.

In Fig. 3.2 (e), (f), we take the ion motion into account. As we can see, ion motion changes the energy conversion process significantly. With the evolution of the hole-boring effect, the charge charge separation field, E_x, becomes weaker and weaker, and electrostatic potential, U, becomes less and less. This is because the hole-boring effect decreases the laser radiation pressure via Doppler effect, and ions partially absorb the laser energy for acceleration.

With a weaker electrostatic field and less energy storage, the backward acceleration of the electron layer becomes slower, thus resulting in smaller pulse amplitude and faster spectral decay. As shown in Fig. 3.4, the amplitude of the emitted pulses becomes smaller and smaller, and the pulse spectrum decays faster and faster. We wish to stress

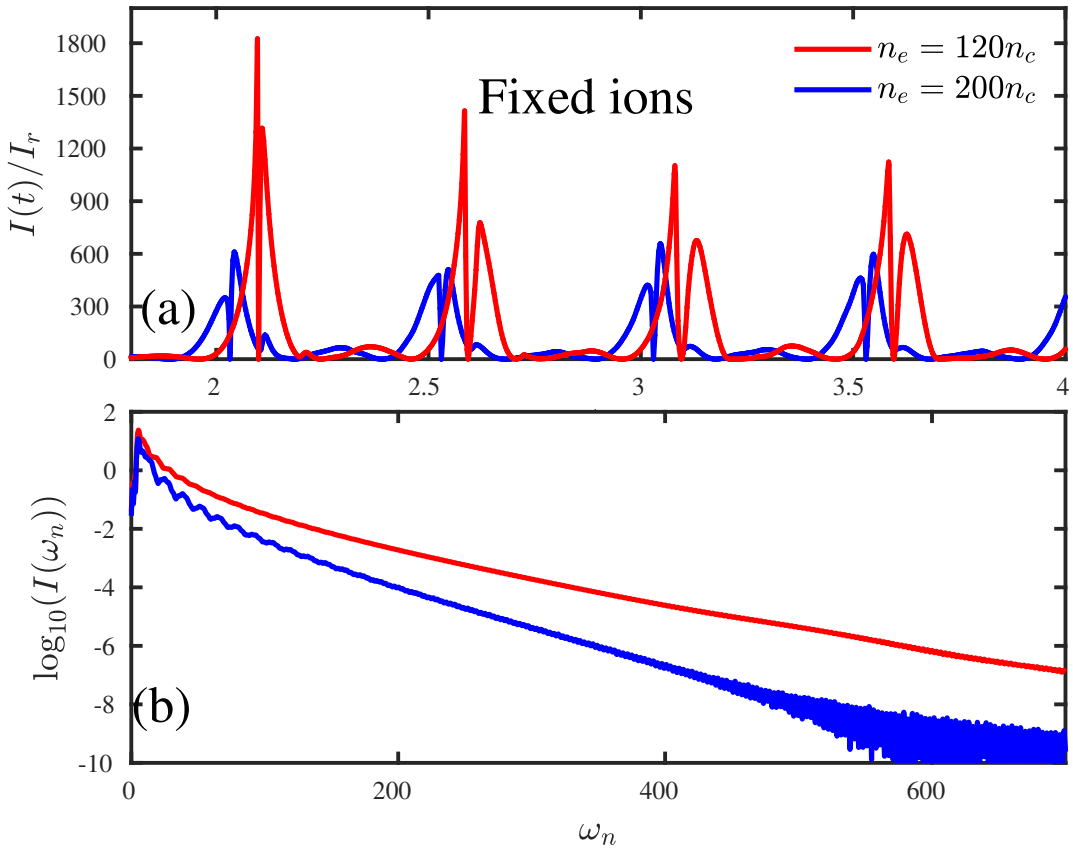

Figure 3.3: 1D PIC simulations for pulse emission corresponding to the fixed-ion cases in Fig. 3.2. (a) Pulse intensities for the case $n_0 = 120n_c$ (red line) and the case $n_0 = 200n_c$ (blue line). The low-frequency components ($\omega < 2\omega_l$) is filtered out. (b) Spectra of the 1st pulse in each case.

that the effect of ion motion on the energy conversion makes it possible to generate an isolated attosecond pulse (See Sec. 5.2) and highlights the main difference between our investigation and the RES model.

3.4 Comparison with CSE and RES

As we know from previous literatures, different models [15–18] have been built to interpret the plasma harmonic generation in different parameter regimes. In the ultra-relativistic regime ($a_0 \gg 1$), coherent synchrotron emission (CSE) [17] and relativistic electron spring (RES) [18] are associated with our model.

To make a clear comparison, we first briefly introduce the derivations in CES model. Starting from Eq. (3.22) with the replacement $J_y(t') = n_{el}(t')\beta_y(t')$ and canceling the phase shift term $e^{-i\omega x}$, we can have

$$\widetilde{E}_y^r(\omega) = \frac{1}{2}\widetilde{F}(-\omega)\int_{-\infty}^{\infty} J_y(t')e^{i\omega\left[t'+x'_{el}(t')\right]}dt' , \tag{3.48}$$

with the same preconditions that at the emission instant the layer current changes sign, and the backward velocity approaches to its maximum. Hence, we can have the Taylor

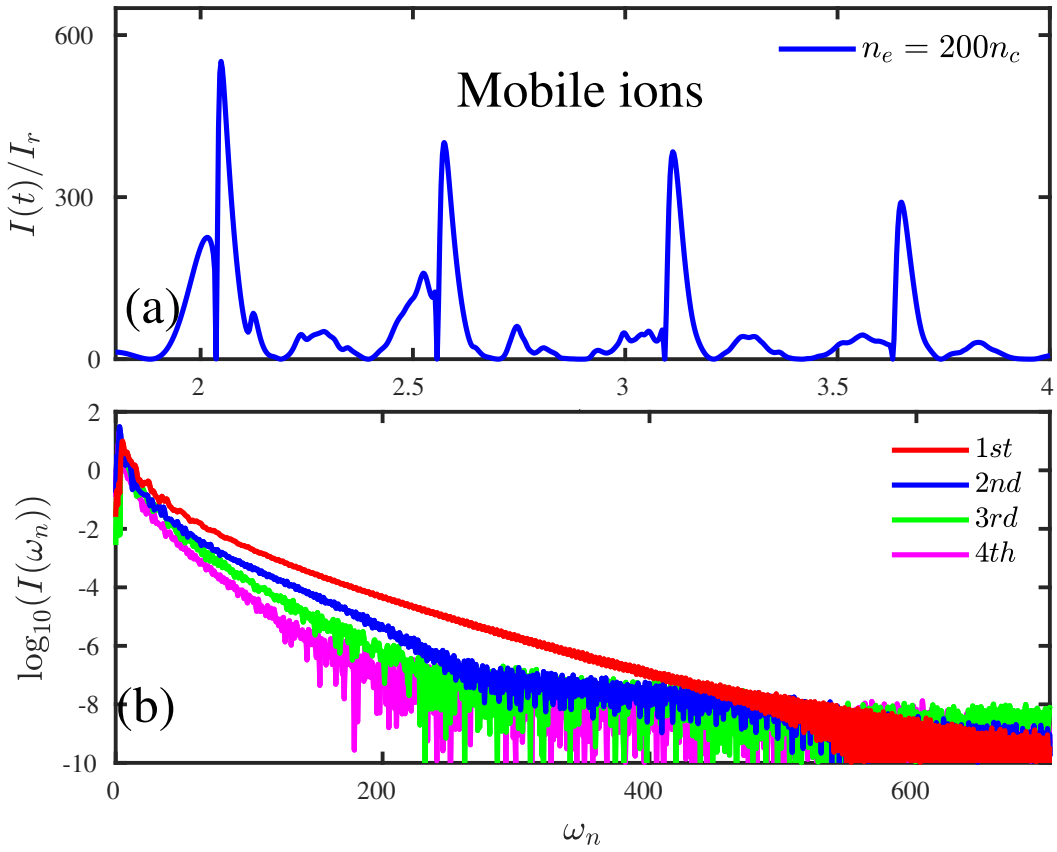

Figure 3.4: 1D PIC simulations for pulse emission corresponding to the mobile-ion cases in Fig. 3.2. (a) Pulse emitted in the case $n_0 = 200n_c$. The low-frequency components ($\omega < 2\omega_l$) is filtered out. (b) Spectra of the each pulses.

expansions for the transverse current, the longitudinal velocity, and the layer location:

$$J_y(t^{'}) = \alpha_0 t^{'}\,, \tag{3.49a}$$

$$\beta_x(t^{'}) = -v_0 + \alpha_1 t^{'2}\,, \tag{3.49b}$$

$$x^{'}_{el}(t^{'}) = -v_0 t^{'} + \alpha_1 t^{'3}/3\,. \tag{3.49c}$$

Here the pulse emission is labeled at ($t^{'}_0 = 0$, $x^{'}_0 = 0$). Below, we will cancel the superscript ‘′’ for convenience. Inserting Eq. (3.49) into Eq. (3.48), we obtain:

$$\begin{aligned}
\widetilde{E}^r_y(\omega) &= \frac{1}{2}\widetilde{F}(-\omega)\int_{-\infty}^{\infty}\alpha_0 t e^{i\omega\left[t - v_0 t + \alpha_1\frac{t^3}{3}\right]}dt \\
&= \frac{\alpha_0}{2}\widetilde{F}(-\omega)\int_{-\infty}^{\infty} t e^{i\omega\left[(1-v_0)t + \alpha_1\frac{t^3}{3}\right]}dt \\
&= \frac{\alpha_0}{2}\widetilde{F}(-\omega)(\omega\alpha_1)^{-\frac{2}{3}}\int_{-\infty}^{\infty}\mathcal{X} e^{i\left[\omega^{2/3}(1-v_0)\alpha_1^{-1/3}\mathcal{X} + \frac{\mathcal{X}^3}{3}\right]}d\mathcal{X}\,,
\end{aligned} \tag{3.50}$$

where we replace the integral variable: $\mathcal{X} = (\omega\alpha_1)^{1/3}t$.

With the well-known Airy function: $\mathrm{Ai}(x) \equiv \frac{1}{2\pi}\int_{-\infty}^{+\infty} \exp\left[i\left(x\mathcal{X} + \frac{\mathcal{X}^3}{3}\right)\right] d\mathcal{X}$, we have

$$\mathrm{Ai}^{'}(x) \equiv \frac{i}{2\pi}\int_{-\infty}^{+\infty} \mathcal{X} \exp\left[i\left(x\mathcal{X} + \frac{\mathcal{X}^3}{3}\right)\right] d\mathcal{X}\,.$$

By expressing the integral in Eq. (3.50) with Airy function, we can have:

$$\begin{aligned}\widetilde{E}_y^r(\omega) &= \frac{\alpha_0}{2}\widetilde{F}(-\omega)(\omega\alpha_1)^{-\frac{2}{3}}\mathrm{Ai}^{'}\left(\frac{\omega^{2/3}(1-v_0)}{\alpha_1^{1/3}}\right)\\ &= \frac{\alpha_0}{2}\widetilde{F}(-\omega)\alpha_1^{-\frac{2}{3}}\omega^{-\frac{2}{3}}\mathrm{Ai}^{'}\left(\frac{\omega^{2/3}}{\omega_{rs}^{2/3}}\right)\,,\end{aligned} \tag{3.51}$$

with the definition

$$\omega_{rs} = 2^{3/2}\alpha_1^{1/2}\gamma_0^3\,, \tag{3.52}$$

and the approximation $1 - v_0 = (1 - v_0^2)/(1 + v_0) \approx 1/(2\gamma_0^2)$. Now we can have the spectrum from CSE model:

$$I(\omega) = |\widetilde{E}_y^r(\omega)|^2 = \frac{\alpha_0^2}{4}|\widetilde{F}(\omega)|^2\alpha_1^{-\frac{4}{3}}\omega^{-\frac{4}{3}}\left[\mathrm{Ai}^{'}\left(\frac{\omega^{2/3}}{\omega_{rs}^{2/3}}\right)\right]^2\,. \tag{3.53}$$

As one can see, CSE spectrum seems quite different from our results in Eqs. (3.17) and (3.25). This difference may be because our derivation only depends on the condition: $\beta_y \approx 0$, but not on the specific form of β_x variation during the emission, even though we took $\beta_x \approx -1$ to simplify the expressions of ω_d and A_m in Eqs. (3.9), (3.10). However the expression of CSE model is determined by the variation of $\beta_x = -v_0 + \alpha_1 t^2$, in order to make use of Airy function.

Since both our theory and CSE model study the pulse emission in the ultra-relativistic regime with the conditions: $\beta_y \approx 0$ and $\beta_x \approx -1$, there must exist some similarities.

If $\omega \gg \omega_{rs}$, we can expand the spectrum (3.53) with the asymptotic expression of Airy function: $\mathrm{Ai}^{'}(x) \approx \frac{-1}{2\sqrt{\pi}}x^{\frac{1}{4}}e^{-\frac{2}{3}x^{3/2}}$ for $x \gg 1$, as

$$\begin{aligned}I(\omega) &\approx \frac{\alpha_0^2}{4}|\widetilde{F}(\omega)|^2\alpha_1^{-\frac{4}{3}}\omega^{-\frac{4}{3}}\frac{1}{4\pi}\left(\frac{\omega}{\omega_{rs}}\right)^{1/3}\exp\left(-\frac{4}{3}\frac{\omega}{\omega_{rs}}\right)\\ &\approx \frac{\alpha_0^2}{16\pi}|\widetilde{F}(\omega)|^2\alpha_1^{-\frac{4}{3}}\omega_{rs}^{-\frac{1}{3}}\omega^{-1}\exp\left(-\frac{4}{3}\frac{\omega}{\omega_{rs}}\right)\\ &\propto \exp\left(-\frac{4}{3}\frac{\omega}{\omega_{rs}}\right)\Big|_{\omega\gg\omega_{rs}}\end{aligned} \tag{3.54}$$

As one can see in high-frequency region ($\omega \gg \omega_{rs}$), CSE model also gives an exponential spectral decay which is the basic characteristic of our theory. The correction ω^{-1} is negligible in this region[4]. As shown in Fig. 3.5, the CSE spectrum matches very well with our spectrum in high-frequency region.

Moreover, with simple approximation, the decay parameter ω_{rs} can relate to our parameter ω_d as below:

[4] $\log_{10}(I(\omega)) \approx \mathrm{const} - \log_{10}(\omega) - \frac{4}{3}\frac{\omega}{\omega_{rs}}\log_{10}(e) \approx \mathrm{const} - \frac{4}{3}\frac{\omega}{\omega_{rs}}\log_{10}(e)$

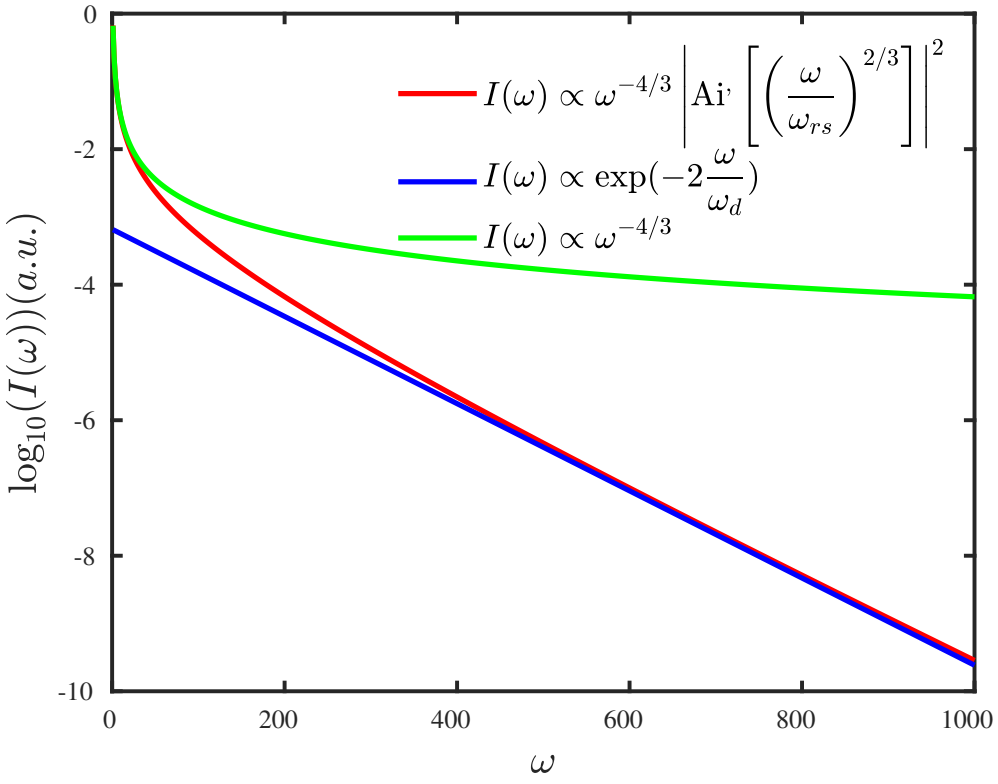

Figure 3.5: Comparison between the spectrum (Eq. 3.17) from our theory (blue line) and the spectrum (Eq. 3.53) from CSE model(red line). The power-law spectrum $I(\omega) \propto \omega^{-4/3}$ is also shown (green line). We set $\omega_{rs} = 100$, $\omega_d = 135$. The other parameters are chosen to make the spectra match in different regions.

With the general relation $\gamma_0^2 \equiv 1 + p_x^2 + p_y^2$, we have

$$\gamma_0 \frac{d\gamma_0}{dt} = p_x \frac{dp_x}{dt} + p_y \frac{dp_y}{dt} \approx p_y \frac{dp_y}{dt} \approx \left| \frac{dp_y}{dt} \right|^2 t \,, \tag{3.55}$$

here we utilize the approximation $p_y = \frac{dp_y}{dt} t$, and neglect the variation of p_x since at the emission instant, the electron layer comes out of or near the ion surface where $E_x \approx 0$, and the laser field drops off in the cycle leading to smaller ponderomotive force in the longitudinal direction. With this approximation, we can also have

$$\frac{dp_x}{dt} \approx 0 \quad \Rightarrow \quad \gamma_0 \frac{d\beta_x}{dt} + \beta_x \frac{d\gamma_0}{dt} \approx 0 \quad \Rightarrow \quad \frac{d\beta_x}{dt} \approx -\frac{\beta_x}{\gamma_0} \frac{d\gamma_0}{dt} \,. \tag{3.56}$$

Combining Eq. (3.55) and Eq. (3.56), the temporal derivative of β_x is expressed as:

$$\frac{d\beta_x}{dt} = -\frac{\beta_x}{\gamma_0^2} \left| \frac{dp_y}{dt} \right|^2 t \approx \frac{1}{\gamma_0^2} \left| \frac{dp_y}{dt} \right|^2 t \,. \tag{3.57}$$

With the approximation $\beta_x = -v_0 + \alpha_1 t^2$, we can have

$$\beta_x = -v_0 + \alpha_1 t^2 \Rightarrow \frac{d\beta_x}{dt} = 2\alpha_1 t \,. \tag{3.58}$$

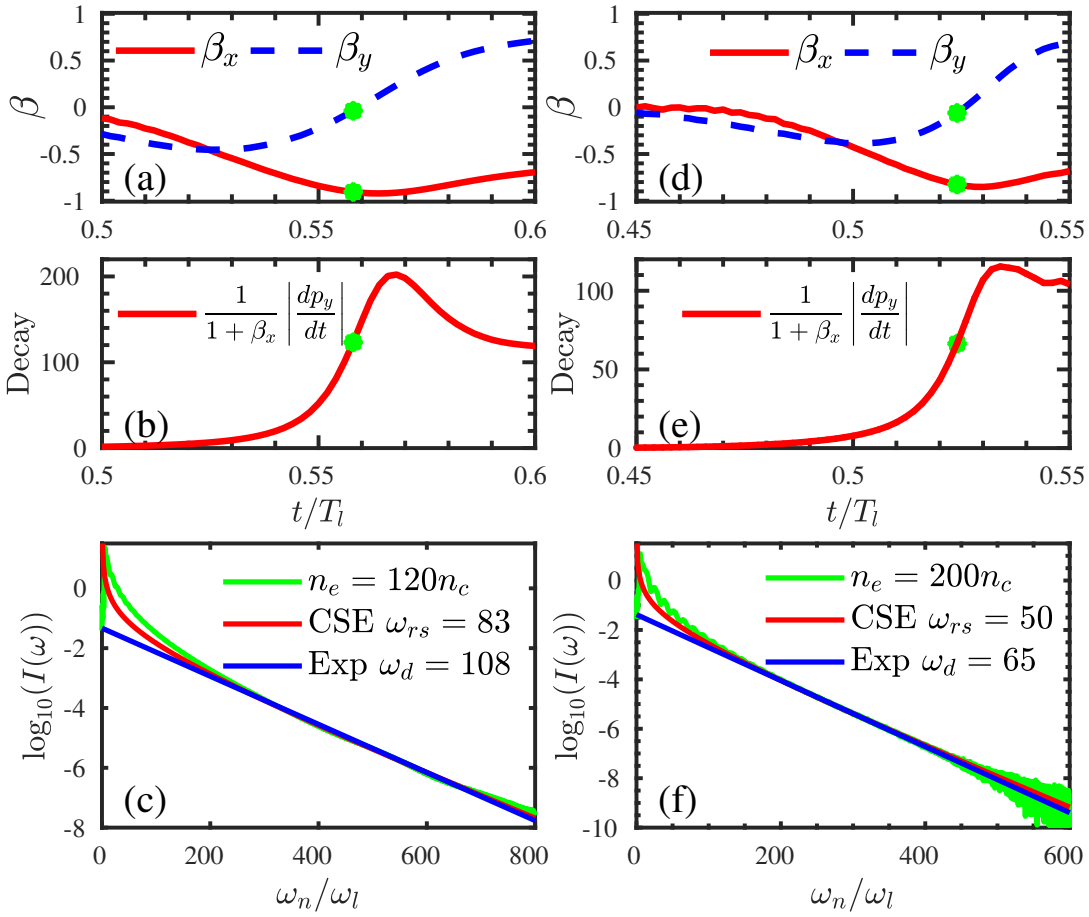

Figure 3.6: 1D PIC simulations for pulse emission. (a), (b) and (c) are for the fixed-ion case with $n_e = 120n_c$; (d), (e) and (f) are for the fixed-ion case with $n_e = 200n_c$ in Fig. 3.3. (a), (d) Velocities (β_x, β_y) of the electron current along the retardation paths of the first pulses in Fig. 3.3 (a) and (c) respectively. (b), (e) Decaying parameter calculation ($|dp/dt|/(1+\beta_x)$) along the retardation paths. (c), (f) Fitting of the pulse spectra in Fig. 3.3 (b) with CSE spectrum (Eq. 3.53) and our exponential spectrum (Eq. 3.17).

Comparing Eq. (3.57) and Eq. (3.58), the introduced parameter α_1 can be expressed approximately as:

$$\alpha_1 \approx \frac{1}{2\gamma_0^2}\left|\frac{dp_y}{dt}\right|^2 , \tag{3.59}$$

and inserting into the definition of ω_{rs} (Eq. 3.52), we can gain

$$\omega_{rs} \approx 2\gamma_0^2\left|\frac{dp_y}{dt}\right| \approx \omega_d . \tag{3.60}$$

Based on these calculations, we know that our theory and CSE model are similar in high-frequency region, both give an exponential spectra with the similar spectral decay as shown in Fig. 3.5. To further clarify this relation, we take use of the CSE spectrum (Eq. 3.53) and our exponential spectrum (Eq. 3.17) to fit the simulation results in Fig. 3.3 (b). As shown in Fig. 3.6 (c) and (f), the pulses clearly possess exponential spectra in

high-frequency region, and both CSE and our exponential spectra can fit the simulation results if proper decaying parameters (ω_{rs} and ω_d) are chosen.

However, we also note that the values of the decaying parameter for CES (ω_{rs}) and our model (ω_d) are quite different. In Fig. 3.6 (b) and (e), we numerically calculate the decaying parameter at the emission instant (green stars) based on Eq. 3.60:

$$D_{ecay} = \frac{1}{1+\beta_x}\left|\frac{dp}{dt}\right| \approx 2\gamma_0^2\left|\frac{dp_y}{dt}\right| . \tag{3.61}$$

and obtain that $D_{ecay} = 123.2$ in Fig. 3.6 (b) and $D_{ecay} = 66.4$ in Fig. 3.6 (e). Here, the emission instant (green stars) is defined at the point when $\beta_y = 0$ as shown in Fig. 3.6 (a) and (d)[5]. One can clearly see that the numerical calculations of the decaying parameter quantitatively confirm the spectral decay ω_d for our model, but only matche the CSE model qualitatively.

For low-frequency region, CSE model gives the famous power-law spectrum $I(\omega) \propto \omega^{-4/3}$ as also shown in Fig. 3.5. This may be the advantage of CSE model as this power-law spectrum has been observed in experiment[6] [106] and also in Fig. 3.6 (c) (f), CSE model has better performance in low-frequency region. Our theory cannot give this power-law spectrum in low-frequency region as we only consider the main radiation from the electron layer around the emission point where $\beta_y \approx 0$ and $\beta_x \approx -1$, the reflections during the electron layer formation and acceleration processes are ignored.

With the above comparison with CSE model, we can summarize that our theory has an advantage in high-frequency region as we can qualitatively predict the spectral decay, and a disadvantage in low-frequency region since we ignore the low-frequency radiations. Furthermore, our theory has a great advantage in giving the analytical expression for the attosecond pulse (see Eq. 3.29) and also predicting the phase property (see Eq. 3.19), all of these are missing in CSE model. In Chap. 5, we validate the expression of the attosecond pulse and phase property with the PIC simulations as shown in Figs. 5.2 and 5.3.

Our theory seems very close to the RES model [18], but with a big-step development. In RES model, the radiation is also given as

$$E_y^r = \frac{n_{el}}{2}\frac{\beta_y(t')}{1+\beta_x(t')} , \tag{3.62}$$

from an ideal moving charged layer with surface charge, n_{el}. This expression is same as our equation (3.3) and also implies an exponential spectrum. The "ideal moving charge layer" is a good approximation, but the information from the finite extension of the electron layer is completely ignored, which will have significant influence on the pulse spectral and phase properties in high-frequency region as we discussed in Sec.3.1.3. Furthermore, in their analytical calculations, the condition:

$$\beta_x^2 + \beta_y^2 = 1 , \tag{3.63}$$

is imposed in order to self-consistently evolve the layer motion equations. However, this condition (Eq. (3.63)) implies an infinity in the pulse radiation (Eq. (3.62)) at the

[5] In simulations, it is possible to have a small time shift between the point when $\beta_y = 0$ and the point when $|\beta_x|$ is maximal.

[6] In the experiment, the transmission harmonic spectrum is detected in the forward direction which is different from setup in our theory and CSE model, and the power-law spectrum extends to very high-frequency region.

emission instant when $\beta_x = -1$.

In RES model, the energy conversion process was explicitly discussed, to our knowledge, for the first time[7]. This energy conversion process is crucial for a strong attosecond pulse emission. However, in their discussion, ions are fixed. The energy converts from the incident laser to the emitted pulse via the electron layer compression and acceleration. In the ultra-relativistic regime, ion motion (hole-boring effect) becomes inevitable. Ion acceleration can effectively change the energy partitions in the energy conversion process and thus decrease the energy absorption for the layer acceleration and the pulse emission. As we can see in Fig. 3.4, ion motions can strongly affect the emitted pulse spectrum. This highlights the main difference between our discussion and the RES model.

3.5 Conclusions

In this chapter, we develop an analytical model for the pulse emission from a well-defined electron layer compressed by the strong laser ponderomotive force at the plasma surface.

We first validate the assumptions, via PIC simulations, that the pulse is emitted by a strongly compressed electron layer at the laser-plasma interface and the emission occurs at the node where the layer transverse current changes its sign $J_y \approx 0$, and its longitudinal velocity approaches the speed of light $\beta_x \approx -1$.

On account of these assumptions, we give the analytical expression for the emitted pulse, and derive the exponential spectrum and the constant spectral phase $\psi(\omega) = \pm\frac{\pi}{2} + \psi_{A_m}$ of the pulse. After this, we analytically analyze the influence of the finite extension of the electron layer on the pulse spectral and phase properties.

Based on these discussions, we know that high-frequency emissions are bunched on the attosecond time scale when the compressed electron layer has the largest backward velocity $\beta_x \approx -1$. By filtering out the low-frequency components ($\omega < \omega_f$) in the pulse, the analytical description for an attosecond pulse is derived.

Moreover, we discuss the energy conversion process behind the pulse emission in great details and give the numerical and analytical comparison with CSE and RES models at the end.

[7] This energy conversion process should also happen for CSE model, but they did not mention or discuss as detailed as RES model.

Chapter 4

Plasma high harmonic generation from ultraintense laser pulses

In this chapter, plasma high-order harmonic generation from an extremely intense short-pulse laser ($I_l > 10^{21}\mathrm{W/cm^2}$) is explored by including the effects of ion motion, electron-ion collisions, temperature effect and radiation reaction force in the plasma dynamics. In Sec. 4.1, we first introduce the motivation for our study and the simulation setup for the whole thesis. Then, in Sec. 4.2, we show the parametric study to highlight the necessity for the inclusion of the effects of ion motion, collisions, temperature and radiation reaction in this extremely intense regime. Next, in Sec. 4.3, we show that the super-strong laser ponderomotive force induces plasma ion motion through the hole-boring effect leading to frequency shifting and widening of the harmonic spectra which would result in the discrete harmonic peaks in low-frequency region but quasi-continuous spectrum in high-frequency region. We analyze analytically the widening of the harmonic spectra and validate it by particle-in-cell (PIC) simulations. Based on these results and physical considerations, parameter maps highlighting optimum regions for generating a single intense attosecond pulse and coherent extreme ultraviolet (XUV) radiation are presented in Sec. 4.4 for different plasma targets and incidence angles. In Sec. 4.5, a brief conclusion of the whole chapter is presented. Parts of the contents in this chapter have been published in our paper [1].

Same dimensionless quantities are used as in Chapter 3.

4.1 Motivation and simulation setup

A powerful and coherent source of radiation operating in the XUV region has multitudes of applications ranging from the novel field of attosecond physics [47] to probing the nonlinear effects in hot and warm dense matter [107, 108]. High-order harmonic generation (HHG) via the femtosecond relativistic laser-solid interaction is predicted to be one of the most suitable to extend the coherent radiation sources into the XUV region [35, 58, 59, 66, 109–113]. Although the HHG from the linearly polarized laser pulse interaction with gaseous targets has been experimentally demonstrated, the harmonic flux and conversion efficiency are saturated at nonrelativistic regimes [35], as shown in Fig. 1.1.

One of the underlying advantages of the solid HHG, in comparison to gaseous HHG, is to be able to use higher incident laser intensity, see Fig. 1.1. In order to improve the flux of the high-order harmonics or build a super-strong XUV source, we propose to employ an ultra-relativistic laser ($a_0 = eE_l/(m_e c\omega_l) \gg 1$, $I\lambda_l^2 \gg 1.37\times10^{18}$ $\mu\mathrm{m^2}$ $\mathrm{W/cm^2}$ e and m_e denote the charge and rest-mass of the electron respectively, E_l and ω_l are the electric field and frequency of the laser respectively, c is the light speed in vacuum.) to drive the solid HHG, since the laser systems with intensities $I \geq 10^{21}\mathrm{W/cm^2}$ are currently either available or on the horizon [6, 114].

In this ultra-relativistic regime, the plasma ion motion and radiation reaction (RR) force [27, 76] must instructively be taken into account. Ions cannot be taken as a positive charge background as in the previous HHG models [15–18]. The direct contribution from ion current to the plasma HHG is always negligible because of the low-frequency response, but the indirect influence is significant as ion motion effectively affects the electron dynamics and changes the energy conversion process. As we discussed in Sec. 2.4, the plasma ion motion originates from the hole-boring (HB) effect [37, 91, 115], in which the laser ponderomotive force pushes the plasma target surface inwards, creating a double-layer structure. The electron layer in this structure oscillates around the ion layer emitting high-harmonics but the structure itself has a slow motion inward the target, which can significantly change the energy conversion efficiency as discussed in Sec. 3.3 and thus the harmonic spectrum [1, 116]. The HB effect leads to strong compression of the plasma density at the laser-target interface as shown in Fig. 2.3, which necessitates the inclusion of electron-ion collisions in plasma dynamics. While the ion motion and collisions affect the electron layer dynamics, the plasma is effectively heated, thus necessitating the consideration of plasma temperature effect. Moreover, the radiation reaction force changes the laser energy partition among electrons, ions and radiation in the plasma [77, 117–122], thus can also change the harmonic spectrum.

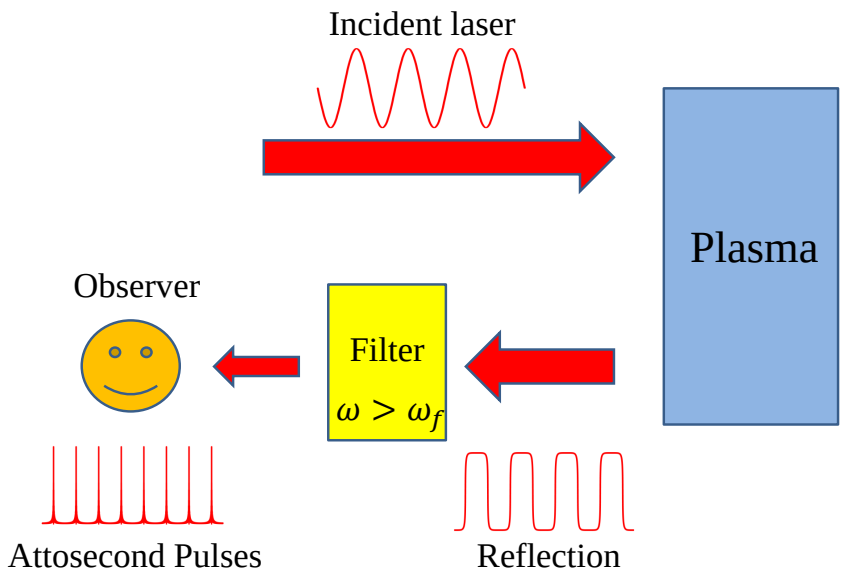

Figure 4.1: Schematic diagram of the simulations for HHG via laser-plasma interaction.

To setup the simulation, we irradiate a strong linearly polarized laser pulse onto an over-dense plasma as shown in Fig 4.1. The strong laser ponderomotive force can oscillate the plasma surface. This surface oscillation will effectively modulate the incident laser pulse, and couple abundant harmonics of the incident laser frequency into the reflection. In this chapter, we analyze the intensity spectrum of the harmonics contained in the reflection by Fourier transforming the reflection from the time domain to the frequency domain. If a suitable frequency filter is applied to cut off the low-frequency components or select the components in a particular frequency interval from the reflection, we can obtain a train of attosecond pulses or a single attosecond pulse. This will be the topic

for Chapter 5.

4.2 Parametric study

In this section, we present the parametric studies of plasma HHG in the ultra-relativistic regime ($I_l > 10^{21}\mathrm{W/cm}^2$) and highlight the necessity for the consideration of the hole-boring effect, collision damping, temperature effect and the radiation reaction effect in this regime for plasma harmonic generation.

4.2.1 Hole-boring effect

We first study the effect of hole-boring motion on the intensity spectrum of harmonics. The hole-boring effect [37] is the inevitable and straightforward consequence if we improve the intensity of the driving laser pulse. The extremely strong laser ponderomotive force can drive the ion motion in the first few laser cycles, which would effectively change the energy partitioning among electrons, ions and the reflection as we discussed in Sec. 3.3.

In Fig 4.2, we show the obtained harmonic intensity spectra in the cases with and without ion motion. As we can see, ion motion significantly reduces the harmonic intensity for the whole spectral region in (a). This is because the ion acceleration increases the laser energy absorption, thus decreasing the energy reflection coefficient R as discussed in Eq. (2.49). One can also see in (b) that ion motion results in the shifting of the harmonic frequency and broadening of the harmonic peak. In the mobile-ion case, the harmonic spectrum violates the well-known selection rules in Sec. 2.3.2 [16], and non-integer harmonics are generated, while in the fixed ion case, only integer harmonics are generated as described in the selection rules. This harmonic shifting originates from the Doppler effect arising due to the plasma surface motion, and the harmonic peak broadening is concomitant with the frequency shifting.

To gain deep insight into the action of the ion motion, we compare the cases with different target materials in Fig 4.3. As shown in Fig 4.3 (a), the plasma target with different material gives the indistinguishable harmonic spectrum for the fixed-ion case. This is expected because ions work in the fixed-ion case as a positive charge background which only provides the electrostatic field to oscillate the surface electron layer. In Fig 4.3 (b) for the mobile-ion case, the difference between the harmonic spectra from different plasma materials, albeit slight, is clearly distinguishable. As one can see, the target material with higher charge-to-mass ratio (Z/A) gives weaker harmonic intensity and larger harmonic frequency shifting, where A and Z are the mass and charge number of the ion, respectively. This is reasonable since the hole-boring velocity β_{hb} is larger if the material ion has higher charge-to-mass ratio. From Eqs. (2.46) and (2.47), we can know that

$$\beta_{hb} \propto B \propto \left(1 + \frac{m_i}{Zm_e}\right)^{-\frac{1}{2}} \propto \left(\frac{Z}{A}\frac{1}{1836.2}\right)^{\frac{1}{2}}, \tag{4.1}$$

where $B \ll 1$ and the relation $m_i = 1836.2Am_e$ are used. The larger hole-boring velocity results in larger harmonic frequency shifting and smaller energy reflection coefficient as proved by Eq. (2.49).

From another point of view, harmonic is the consequence of the interference between the different pulses in the reflection. Hole-boring effect reduces the pulse emission by repartitioning the laser energy in the energy conversion process as discussed in Sec. 3.3,

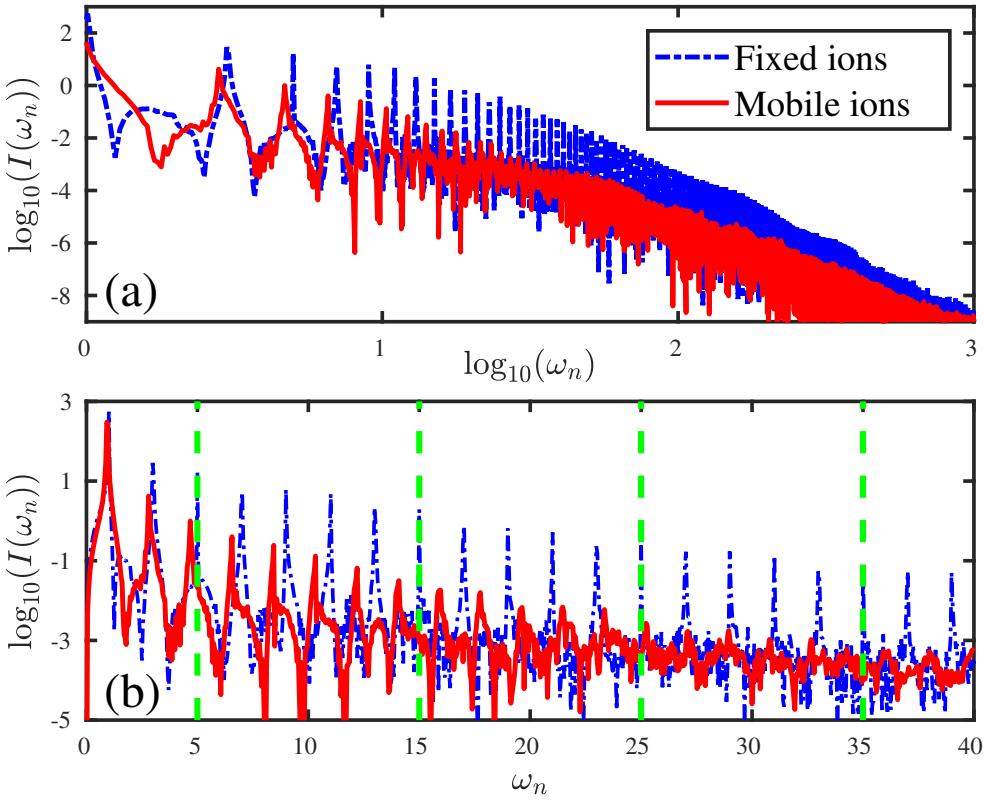

Figure 4.2: 1D PIC simulations of HHG for the cases with (red solid line) and without (blue dashed line) ion (Carbon) motion. Normal incident geometry ($\theta = 0$) is employed. In (a), we show the harmonic spectrum in a wide range of frequency with a logarithmic x-axis. In (b), we zoom in the spectrum in the low-frequency region with a linear x-axis. With ion motion, the harmonic intensity is significantly reduced, and the harmonic peaks clearly violate the selection rule while the harmonic peaks in the fixed ion case obey the selection rule. The green dashed lines correspond to integer harmonics from selection rules discussed in Sec. 2.3.2 [16]. The laser has a step-like profile with a constant amplitude $a(t) = 40$ for $0 < t < T_d = 18T_l$. The plasma has no pre-gradient with the constant density $n_0 = 200$. The interaction is collisionless with the initial temperature $T_e = 0$eV.

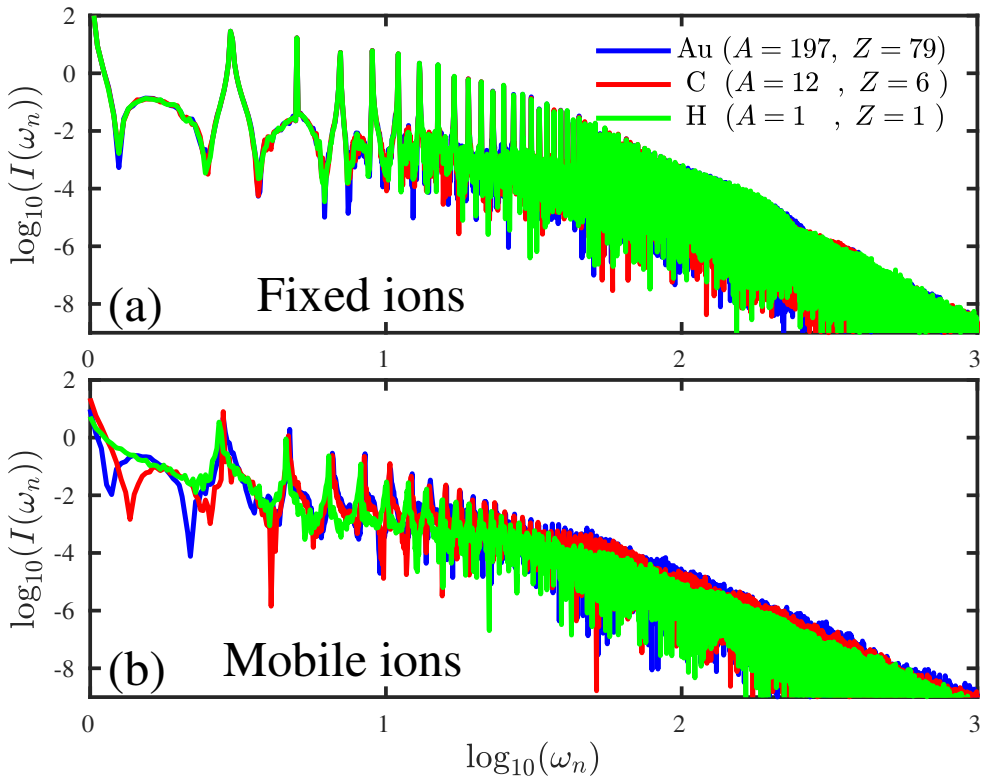

Figure 4.3: 1D PIC simulations of HHG for the cases with (a) and without (b) ion motion for different target material: Gold (Au, blue line), Carbon (C, red line), Hydrogen (H, green line). Normal incident geometry ($\theta = 0$) is employed. In the fixed-ion case (a), the targets with the different materials have the same harmonic spectra; While in the mobile-ion case (b), the harmonic intensity from the target with larger charge-to-mass ratio is smaller. A and Z are the mass and charge number of the ion in the target material, respectively. Same laser and plasma parameters are used as in Fig. 4.2.

thus decreasing the harmonic intensity.

4.2.2 Collision effect

In low-temperature ultra-dense plasma physics, the collisional effect plays a very important role in the transport theory, such as fast particles transfer in the fast-ignition for the laser fusion [123]. In high-temperature under-dense plasma physics, the collisional effect is mostly negligible as the collisional frequency ν_{ei} is much smaller than the typical plasma frequency ω_{pe} and the laser frequency ω_l. In the interaction of an ultra-relativistic laser with an ultra-dense plasma for plasma HHG, the necessity for the consideration of the collisional effect becomes more complicated and needs detailed discussion [4].

For the Coulomb binary scattering, the electron-ion collision frequency [29] is[1]

$$\nu_{ei} \approx \frac{Z^2 n_i e^4 \ln(\Lambda)}{2\pi\epsilon_0^2 m_e^{1/2} T_e^{3/2}}, \tag{4.2}$$

where $\ln(\Lambda) \approx 10 \sim 20$ is the Coulomb logarithm [124], T_e is the electron temperature, Z is the ion charge number, and n_i is the ion density. To show the importance of collisional

[1] In this subsection, the international system of units (SI) are used since the numerical calculation is need

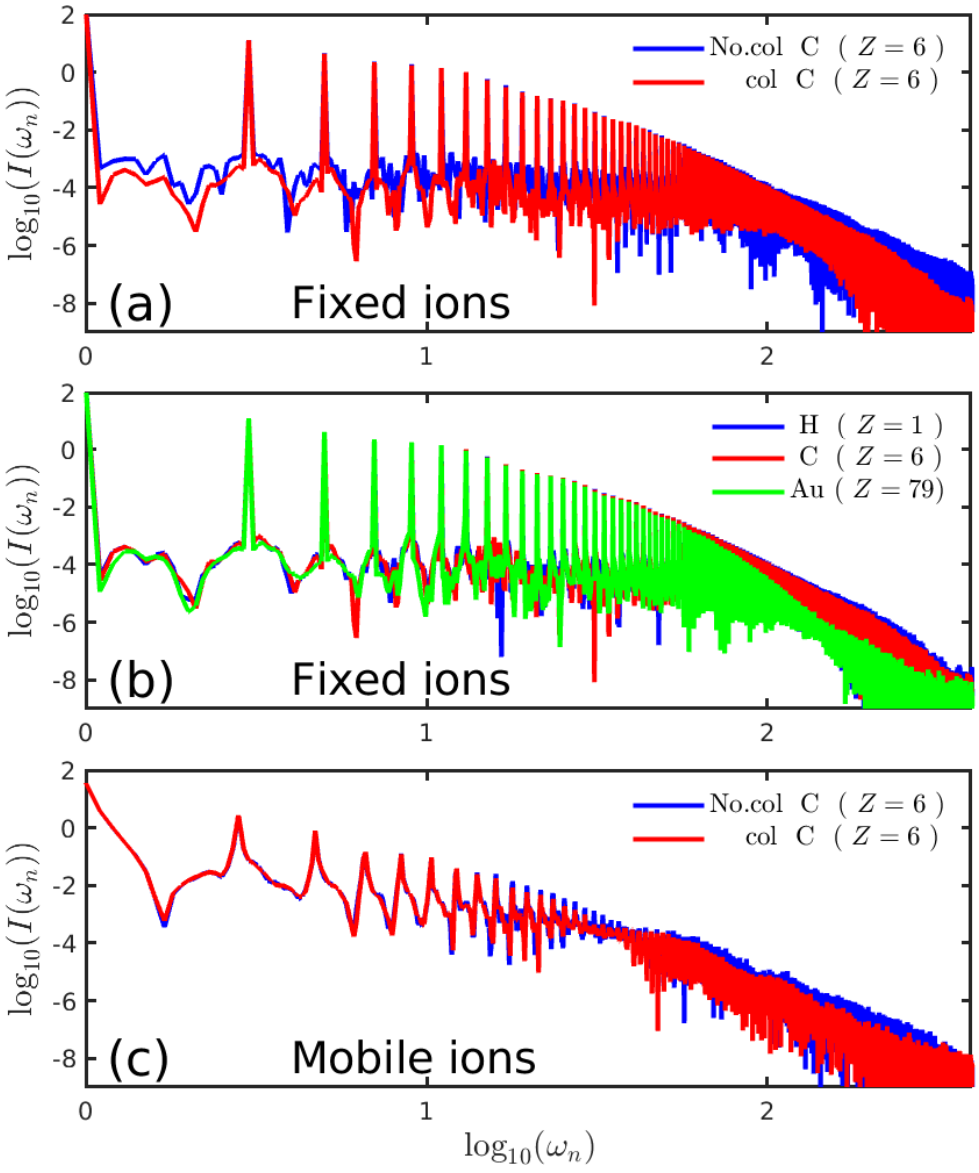

Figure 4.4: 1D PIC simulations of HHG for the collisional effect. (a) Comparison of the harmonic intensity spectrum in the cases with (red line) and without (blue) the collisional effect. The collisional effect reduces the higher-order harmonic emission. (b) Harmonic spectrum with collisional effect for different target material: Hydrogen (H, blue line), Carbon (C, blue line), Gold (Au, green line). The harmonics from the material with larger charge number have weaker intensity. In (a) and (b), ions are fixed. (c) Comparison of the harmonic spectrum in the cases with (red line) and without (blue) collisional effect. Ions are mobile. The collisional effect damps the higher-order harmonic emission. The plasma has the initial temperature $T_e = 500$eV. The same laser and plasma parameters are used as in Fig. 4.2.

effect, we calculate the ratio of the collision frequency to the plasma frequency ω_{pe} of the background electrons as

$$\begin{aligned}\frac{\nu_{ei}}{\omega_{pe}} &= \frac{Z^2 n_i e^4 \ln(\Lambda)}{2\pi\epsilon_0^2 m_e^{1/2} T_e^{3/2}} \left(\frac{\epsilon_0 m_e}{e^2 n_{pe}}\right)^{1/2} \\ &= \frac{4\pi^2 Z \ln(\Lambda)}{\lambda_l^3 n_c} \frac{Z n_i}{\sqrt{n_e n_c}} \frac{m_e^{3/2} c^3}{T_e^{3/2}}\,,\end{aligned} \tag{4.3}$$

where we make use of the plasma frequency $\omega_{pe} = \sqrt{e^2 n_{pe}/(\epsilon_0 m_e)}$, the plasma critical density $n_c = \omega_l^2 \epsilon_0 m_e / e^2$ and $\lambda_l = 2\pi c/\omega_l$. For the laser wavelength $\lambda_l = 0.8\mu m$, the corresponding plasma critical density is $n_c = 1.742 * 10^{21} cm^{-3}$. The carbon ($Z = 6$) plasma is used with initial conditions: $Z n_i^0 = n_e^0 = 100 n_c$, $T_e = 1keV$. The plasma frequency is obtained as $\omega_{pe} = 10\omega_l$. The Coulomb logarithm is taken as $\ln(\Lambda) = 15$. Therefore, the ratio gives rise to

$$\frac{\nu_{ei}}{\omega_{pe}} \approx 0.46\,. \tag{4.4}$$

Consequently, in the ultra-dense plasma with moderate temperature, the collisional effect has to be taken into account for plasma HHG as the collision frequency is even comparable to the plasma frequency.

However, after a long time interaction with the ultra-relativistic laser, the plasma electrons would be extremely heated to the temperature, $T_e \sim m_e c^2$ and simultaneously, the plasma ions would be dramatically compressed at the laser-target interface as shown in Fig. 2.3. In general, this compression could be orders of magnitude, and here we estimate as $n_i \sim 100 n_i^0$ [37, 125]. Thus the collision frequency is recalculated as

$$\nu_{ei} \sim 0.004\omega_{pe} = 0.04\omega_l. \tag{4.5}$$

For the laser with duration $T_l^d \sim 10T_l \sim 27$fs, the average binary collisions during the interaction can be estimated as:

$$\nu_{ei} T_l^d \approx 2.5 > 1\,, \tag{4.6}$$

which also highlights the necessity for the consideration of the collisional effect on plasma HHG in a long time ultra-relativistic laser-plasma interaction.

With the above simple estimation, we can know that in the process of plasma HHG, the collision effect which is neglected in the low-intensity regime [16, 126], is indeed non-negligible in the ultra-relativistic regime.

As shown in Fig. 4.4, we can clearly see the effect of collisions on plasma harmonic spectra. With the inclusion of collisions, the harmonic spectrum decays faster, leading to lower efficiency for high-order harmonic generation as shown in Fig. 4.4 (a). Since the collision frequency is proportional to the square of the ion charge number, *i.e.* $\nu_{ei} \propto Z^2$, plasma HHG from the target with larger charge number is more damped by the collisional effect as shown in Fig. 4.4 (b). If the ions are mobile, the collisional effect would be boosted with the dramatically compressed ion layer by the hole-boring effect. Comparing (a) and (c), the decrease of the intensity starts from about ten order of harmonics ($\omega_n > 10\omega_l$) for mobile-ion case, while for fixed-ion case, the decrease is from hundred order of harmonics ($\omega_n > 100\omega_l$).

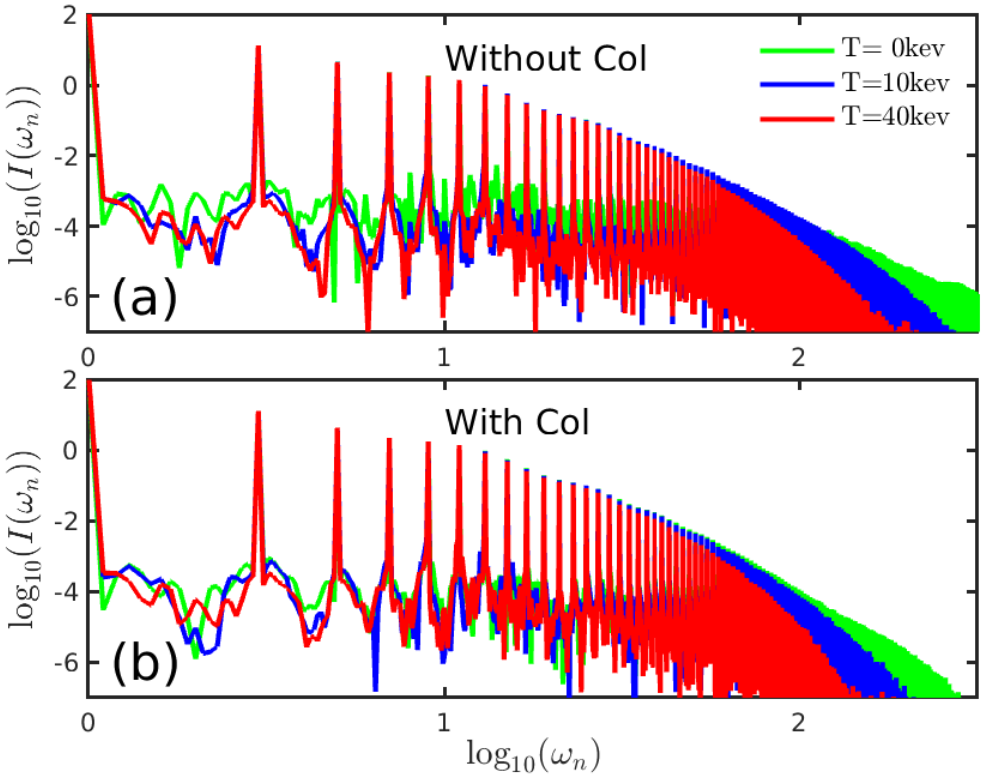

Figure 4.5: 1D PIC simulations of HHG for the temperature effect in the cases with (a) and without (b) collisional effect. The high-order harmonic intensity becomes weaker for both collisional and collisionless case if the plasma has higher initial temperature. Ions are fixed. The same laser and plasma parameters are used as in Fig. 4.2.

To understand these effects, we resort to Eq. (2.13). From that, we can see that the collisional effect acts as a friction which damps the motion of the plasma current, thus hindering the background acceleration of the electron layer in the energy conversion process. With a smaller relativistic factor γ, the emitted pulse would have a spectrum with faster decay, $1/\omega_d \propto \gamma^{-2}$ (see Eq. (3.10)).

As we also see, the influence on low-order harmonics from collisional effect is not significant, which may imply that the total energy of the reflection is not reduced evidently by the collisional effects.

4.2.3 Temperature effect

In practical experiments, plasmas are created on solid targets irradiated by strong laser pulses. In the ionization process, the plasma electrons are heated to high temperature from hundreds of electronvolts (eV) to thousands of electronvolts (keV). In the ultra-relativistic laser-plasma interaction, the plasma target could be extremely heated via vacuum heating [60] and $J \times B$ heating [127], especially in the oblique incidence with linear polarization. The strong oscillatory laser ponderomotive force drives the electron layer oscillation, which would push large numbers of hot electrons inward the target [128] and produce high-temperature plasma background. All of these bring the necessity for the consideration of temperature effect.

As shown in Fig. 4.5, we can clearly see the influence of the plasma temperature on the harmonic generation. The plasma target with higher initial temperature T_e can suppress

the generation of high-order harmonics for both collisional and collisionless case [129].

To interpret these results, we can make use of Eq. (2.13a):

$$\begin{aligned}\frac{\partial \mathcal{P}_x}{\partial t}+u_x\frac{\partial \mathcal{P}_x}{\partial x} &= q(E_x+u_yB_z-u_zB_y)-\frac{1}{n}\frac{\partial}{\partial x}\tilde{\tilde{P}}_{xx}-\nu_c\mathcal{P}_x\\ &= q(E_x+\frac{\mathcal{P}_y}{\gamma}\frac{\partial A_y}{\partial x}+\frac{\mathcal{P}_z}{\gamma}\frac{\partial A_z}{\partial x})-\frac{1}{n}\frac{\partial}{\partial x}\tilde{\tilde{P}}_{xx}-\nu_c\mathcal{P}_x\\ &= q(E_x-q\frac{A_y}{\gamma}\frac{\partial A_y}{\partial x}-q\frac{A_z}{\gamma}\frac{\partial A_z}{\partial x})-\frac{1}{n}\frac{\partial}{\partial x}\tilde{\tilde{P}}_{xx}-\nu_c\mathcal{P}_x\\ &= -E_x-\frac{1}{2\gamma}\frac{\partial A^2}{\partial x}-\frac{1}{n}\frac{\partial}{\partial x}(n_eT_e)-\nu_c\mathcal{P}_x\,, \end{aligned} \tag{4.7}$$

where the conservation of canonical momentum is used: $\mathcal{P}_{y,z}=A_{y,z}$, $q=-1$ for electron, and we take the plasma compression as an isothermal process: $\tilde{\tilde{P}}_{xx}=n_eT_e$. In the interface of interaction, the vector potential decays with x, $\partial A^2/\partial x<0$, and the density increases, $\partial n_e/\partial x<0$, thus for the largest compression, where $d\mathcal{P}_x/dt=0$ and $\mathcal{P}_x=0$, we can have

$$E_x=\frac{1}{2\gamma}\left|\frac{\partial A^2}{\partial x}\right|-\frac{1}{n}\frac{\partial}{\partial x}(n_eT_e)\,. \tag{4.8}$$

As we can see, the thermal pressure changes the pressure balance for the largest compression, $P_l+P_s+P_{T_e}=0$ (See Eq. (3.34)), which reduces the charge separation field E_x and the energy storage in the field, where P_{T_e} denotes the thermal pressure. Thus, the subsequent acceleration of the electron layer would also be decreased, leading to a smaller relativistic factor γ and resulting in a weaker pulse emission with a faster spectral decay , $1/\omega_d\propto\gamma^{-2}$ (see Eq. (3.10)).

Here, we just give a general discussion about the effect of the plasma initial temperature on plasma HHG. During the laser-plasma interaction, the plasma temperature is both temporally and spatially dependent, it is too complicated to give an explicit discussion about the effects of the changeable temperature on the real-time plasma HHG. Fortunately, these effects are included by PIC simulations self-consistently [83, 84]. For the discussion below, we setup the simulations with an initial temperature without further discussion about the variations of the temperature.

4.2.4 Radiation reaction effect

At higher laser intensity $I\gg 10^{22}$ W/cm^2, the electrons could be accelerated to ultra-relativistic energy $\gamma\gg 1$, which motivates the consideration of the radiation reaction (RR) force [27, 76]. From the previous literature [77], the RR force influences the electron motion and can repartition the laser energy among different particles: ions, electrons and photons. Consequently, it can influence the harmonic generation.

In our work, the classical radiation reaction force is considered with the Landau-Lifshitz prescription [76][2]:

$$\begin{aligned}\mathbf{F}_{LL}=&\frac{4\pi}{3}\frac{r_e}{\lambda_l}\gamma\left[(\frac{\partial}{\partial t}+\frac{\mathbf{p}}{\gamma}\cdot\nabla)\mathbf{E}+\frac{\mathbf{p}}{\gamma}\times(\frac{\partial}{\partial t}+\frac{\mathbf{p}}{\gamma}\cdot\nabla)\mathbf{B}\right]\\ &+\frac{4\pi}{3}\frac{r_e}{\lambda_l}\left[(\mathbf{E}+\frac{\mathbf{p}}{\gamma}\times\mathbf{B})\times\mathbf{B}+(\frac{\mathbf{p}}{\gamma}\cdot\mathbf{E})\mathbf{E}\right]\end{aligned}$$

[2]The RR force in the international system of units (SI) is shown in Appendix A.1

$$- \frac{4\pi}{3}\frac{r_e}{\lambda_l}\left[(\mathbf{E}+\frac{\mathbf{p}}{\gamma}\times\mathbf{B})^2-(\frac{\mathbf{p}}{\gamma}\cdot\mathbf{E})^2\right]\gamma\mathbf{p}\,, \tag{4.9}$$

where $r_e = 2.81794\times10^{-15}$m is the classical electron radius, and $\lambda_l = 0.8\mu$m is the laser wavelength.

As we can see, the last term in Eq. 4.9 is proportional to γ^2 opposite to the direction of the particle momentum, dominating the RR force [130]. For the ultra-relativistic electrons, $\gamma \gg 1$, the proceeding term in Eq. 4.9 is much smaller than the last term because of the missing of γ factor. The term containing the temporal and spatial derivatives is also negligible compared to the dominant term (proportional to γ^2). From a numerical point of view, the calculation of the temporal derivative depends on quantities ($\mathbf{E}$, $\mathbf{B}$) at the proceeding and succeeding time steps. This calculation would tremendously increase the computational complexity and also the numerical noise in the simulation. For simplicity, we ignore the terms related to the temporal and spatial derivatives in Eq. (4.9) and only consider the other terms in Eq. (4.10) as the reduced radiation reaction force in the particle motion equation:

$$\begin{aligned}\mathbf{F}^r_{LL} = &\frac{4\pi}{3}\frac{r_e}{\lambda_l}\left[(\mathbf{E}+\frac{\mathbf{p}}{\gamma}\times\mathbf{B})\times\mathbf{B}+(\frac{\mathbf{p}}{\gamma}\cdot\mathbf{E})\mathbf{E}\right]\\ &-\frac{4\pi}{3}\frac{r_e}{\lambda_l}\left[(\mathbf{E}+\frac{\mathbf{p}}{\gamma}\times\mathbf{B})^2-(\frac{\mathbf{p}}{\gamma}\cdot\mathbf{E})^2\right]\gamma\mathbf{p}.\end{aligned} \tag{4.10}$$

To show the importance of RR force in the ultra-relativistic regime, we try to compare the main term of the RR force to the electron Lorentz force, $F_{Lor} = -(\mathbf{E}+\frac{\mathbf{p}}{\gamma}\times\mathbf{B})$ as

$$\begin{aligned}\frac{F_{LL}}{F_{Lor}} &\approx \frac{4\pi}{3}\frac{r_e}{\lambda_l}\left|\mathbf{E}+\frac{\mathbf{p}}{\gamma}\times\mathbf{B}\right|\gamma^2\\ &\approx \frac{8\pi}{3}\frac{r_e}{\lambda_l}E\gamma^2\,.\end{aligned} \tag{4.11}$$

Here we consider a single electron moving opposite to a laser electric field. For a laser with normalized electric field $a_0 = 250$, the typical relativistic factor of an electron moving in this laser field can be estimated as $\gamma \approx a_0 = 250$. Inserting these into Eq. (4.11), we can have

$$\frac{F_{LL}}{F_{Lor}} \approx 0.46\,. \tag{4.12}$$

This ratio does highlight the importance of the RR force in the electron dynamics. We wish to stress that the above estimation is done for a single electron. In the practical ultra-relativistic laser-plasma interaction, the situation would be extremely complicated, the importance of the RR force should be demonstrated via PIC simulations. The numerical consideration of the RR force in EPOCH (PIC) [83] is discussed in detail in Appendix A.1

In Fig. 4.6, we show the comparison for plasma HHG between the cases with and without the RR force. As we can see, the RR force reduces the intensity of the reflected field, but the reduction becomes significant only after a long time interaction. This is easy to understand: at the beginning of the interaction, the plasma is very dense and the electrons are dramatically compressed, the laser penetration depth is much smaller than the laser wavelength, $d \ll \lambda_l$, and thus not enough high energetic electrons are excited. The reflection is same for the cases with and without the RR force. However,

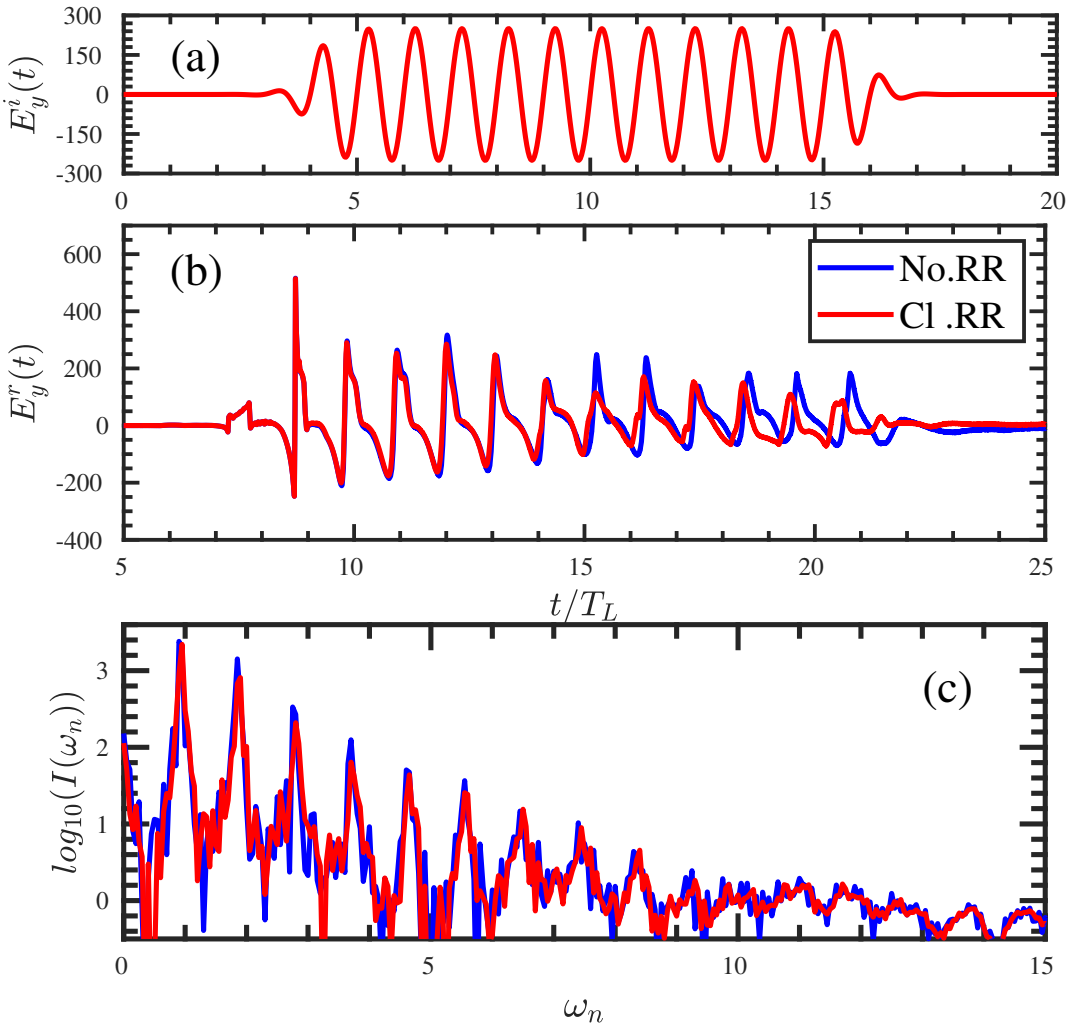

Figure 4.6: 1D PIC simulations of plasma HHG for the radiation reaction (RR) force. (a) Incident field. (b) Reflected field for the case with (red lines) and without (blue line) RR force. The RR force reduces the reflected field after a long time interaction. (c) Harmonic spectrum of the reflected field for the case with (red lines) and without (blue line) RR force. The RR force decreases the low-order harmonic intensity. The laser has the temporal profile: $a(t) = a_0(\tanh((t-T_s)/W) - \tanh((t-T_e)/W))/2$, where $a_0 = 250$, $W = 0.5T_l$. The laser pulse has maximum intensity from $T_s = 4T_l$ to $T_e = 16T_l$. Oblique incidence $\theta = \pi/4$ is used, and the plasma density is $n_0 = 1100n_c$.

because of the plasma $J \times B$ heating [127] from the oscillatory laser ponderomotive force, the electron layer would be expanded after a long time interaction, thus the laser field could penetrate deeper into the electron layer to excite more high-energy electrons [128]. Therefore, the RR force can act to quench these high-energy electrons, increasing the laser absorption and decreasing the reflection. The decrease of the reflected field results in the weaker low-order harmonics as shown in Fig. 4.6(c).

4.3 Harmonic peak broadening

With the above paranetric study, we can clearly see the necessity of including the effects of plasma ion motion, electron-ion collisions, initial plasma temperature and the RR force together in the ultra-relativistic laser-plasma interaction for plasma HHG. The Doppler shift of incident laser frequency, arising due to the HB effect (ion motion), in the rest frame of the target leads to non-integer harmonics being generated in a laboratory frame of reference (see Fig. 4.2). We show that this inevitable frequency shift leads to the widening of the harmonic peaks resulting in a large frequency bandwidth in the generated harmonic spectra.

4.3.1 Theoretical model

Essentially the physical mechanism behind the frequency broadening is the dynamic HB effect. During the initial stage of the interaction, the HB velocity is not constant. This causes variable frequency shifts and since the whole spectrum is a superposition of variable frequency shifts, it results in the broadening of the harmonic spectra.

To estimate the broadening, we proceed by recalling the peak frequency shift in the laboratory frame of reference [37, 116]. The frequency shift is the consequence of the Doppler effect from the hole-boring motion. In the hole-boring frame of reference, the incident laser frequency is

$$\omega_l^{'} = \omega_l \gamma_{hb}(1-\beta_{hb}) = \omega_l \left(\frac{1-\beta_{hb}}{1+\beta_{hb}}\right)^{1/2}, \tag{4.13}$$

where β_{hb} is the hole-boring velocity, $\gamma_{hb} = (1-\beta_{hb}^2)^{1/2}$ is the relativistic factor, and ω_l is the incident laser frequency in the laboratory frame of reference. The nth harmonic in the hole-boring frame of reference is $\omega_n^{'} = n\omega_l^{'}$. In the laboratory frame of reference, the nth harmonic frequency becomes

$$\begin{aligned} \omega_n &= \omega_n^{'}\gamma_{hb}(1-\beta_{hb}) \\ &= n\omega_l^{'}\left(\frac{1-\beta_{hb}}{1+\beta_{hb}}\right)^{1/2} \\ &= n\omega_l \frac{1-\beta_{hb}}{1+\beta_{hb}}. \end{aligned} \tag{4.14}$$

Therefore, we can gain the peak frequency shift of the nth harmonic in the laboratory frame of reference:

$$\delta\omega_n = n\omega_l - \omega_n^{'} = n\omega_l \frac{2\beta_{hb}}{1+\beta_{hb}}. \tag{4.15}$$

The HB velocity β_{hb} is defined as

$$\beta_{hb} = \frac{B}{1+B}(1 - X_h)\,, \tag{4.16}$$

with

$$B = \sqrt{\frac{I_l \cos^4(\theta)}{n_0(1 + m_i/Zm_e)}}, \qquad X_h \approx \frac{\sqrt{I_l}}{3n_0 \cos^2(\theta)}\,, \tag{4.17}$$

where I_l is the incident laser intensity, θ is the incidence angle, n_0 is the plasma initial density, and X_h denotes the rate of energy absorbed by the hot electrons [78, 94]. The detailed discussions about the hole-boring velocity β_{hb} and the correction X_h from hot-electron generation are given in Sec. 2.4.

We wish to emphasize that this peak frequency shift is indeed important for both lower and higher order harmonics. While the large HB velocity is bound to cause substantial frequency shifts, even the small HB velocity induces inevitably large frequency shifts in higher-order harmonics.

Since the HB effect is not a stationary effect, this frequency shift can lead to broadening of the harmonic peaks. Considering that the maximum frequency shift and the highest intensity of the harmonics occurs at the highest intensity of the laser pulse, one can scale the width (FWHM) of each harmonic peak quantitatively as half of the peak frequency shift:

$$\Delta\omega_n = \frac{\delta\omega_n}{2}. \tag{4.18}$$

4.3.2 Simulation results

Below, we validate the theoretical discussions with the extensive simulations performed with the EPOCH (PIC) code [83] .

Fig. 4.7 shows 1D PIC simulation results of HHG in which a linearly polarized laser pulse with wavelength $\lambda_l = 0.8\mu m$ is normally incident on a preionized Gold (Au, $A = 197$, $Z = 79$) plasma target. Fig. 4.7 (a) shows the frequency shift $\delta\omega_n$ and harmonic spectrum broadening $\Delta\omega_n$ with and without the ion motion for constant laser profile. As we can clearly see, the hole-boring effect arise the frequency shift of the harmonic peaks.

For the parameters in Fig. 4.7 (a): laser intensity $I_l = 800$, plasma initial density $n_0 = 200n_c$, one gets the analytical estimates as $\delta\omega_{25} = 1.30$, $\Delta\omega_{25} = 0.65$; In Fig. 4.7 (b), a laser pulse with temporal profile is used. The peak laser intensity $I_l = 800$ with average field $< a >= 20$ and $n_0 = 80$ gives the analytical estimates: $\delta\omega_{25} = 1.95$, $\Delta\omega_{25} = 0.97$; For the parameters in Fig. 4.7 (c), the analytical estimates for the density gradient $L = \lambda_l/32$ case (red dash-dotted line) are the same as in Fig. 4.7(a) which has a step-function density profile. The frequency shifts ($\delta\omega_n$) and broadening ($\Delta\omega_n$) for all the harmonic peaks in Fig. 4.7 have been summarized in Table. 4.1 with both the analytical estimates and simulation results. As one can see, the analytical estimates are confirmed by the PIC simulation results.

To further validate the analytical model, Fig. 4.8 shows 2D PIC simulation results of HHG on fully ionized gold (Au, $A/Z = 197/79$) and carbon (C, $A/Z = 12/6$) plasma targets with plasma density gradient. For the (a) gold and (b) carbon plasma targets, the analytical estimates yields the frequency bandwidth of the 21st harmonic as (a)

$a_0 = 40$, $I_l = 800$, $n_0 = 200n_c$ in Fig. 4.7(a)

	n	21	23	25	27	29
Analytical	$\delta\omega_n$	1.09	1.20	1.30	1.40	1.51
Simulation	$\delta\omega_n$	1.14	1.23	1.32	1.41	1.50
Analytical	$\Delta\omega_n$	0.55	0.60	0.65	0.70	0.76
Simulation	$\Delta\omega_n$	0.50	0.68	0.72	0.73	0.73

$< a_0 >= 20$, $I_l^{\max} = 800$, $n_0 = 80n_c$ in Fig. 4.7(b)

	n	21	23	25	27	29
Analytical	$\delta\omega_n$	1.64	1.79	1.95	2.11	2.26
Simulation	$\delta\omega_n$	1.64	1.73	1.86	2.05	2.23
Analytical	$\Delta\omega_n$	0.82	0.89	0.97	1.05	1.13
Simulation	$\Delta\omega_n$	0.77	0.82	0.77	0.95	1.13

$a_0 = 40$, $I_l = 800$, $n_0 = 200n_c$, $L = \lambda_l/32$ in Fig. 4.7(c)

	n	21	23	25	27	29	31	33	35
Analytical	$\delta\omega_n$	1.09	1.20	1.30	1.40	1.51	1.61	1.72	1.82
Simulation	$\delta\omega_n$	1.10	1.20	1.30	1.40	1.50	1.65	1.70	1.80
Analytical	$\Delta\omega_n$	0.55	0.60	0.65	0.70	0.76	0.80	0.86	0.91
Simulation	$\Delta\omega_n$	0.55	0.65	0.80	0.75	0.95	0.95	0.10	0.95

Table 4.1: Comparison between analytical calculations and simulation results of the frequency shift ($\delta\omega_n$) and harmonic spectrum broadening ($\Delta\omega_n$). Eqs. (4.15)-(4.18) and the corresponding parameters in Fig. 4.7 are used for analytical calculations. The simulation results are extracted from Fig. 4.7.

Au, $a_0 = 40$, $I_l = 800$, $\theta = 0$, $n_0 = 200n_c$ in Fig. 4.8(a)

	n	17	19	21	23	25
Analytical	$\delta\omega_n$	1.10	1.22	1.34	1.46	1.58
Simulation	$\delta\omega_n$	1.08	1.19	1.24	1.36	1.47
Analytical	$\Delta\omega_n$	0.55	0.61	0.67	0.73	0.79
Simulation	$\Delta\omega_n$	0.60	0.46	0.56	0.41	0.35

Au, $a_0 = 40$, $I_l = 800$, $\theta = \pi/4$, $n_0 = 200n_c$ in Fig. 4.8(a)

	n	16	17	18	19	20	21	22	23	24	25
Analytical	$\delta\omega_n$	0.31	0.33	0.35	0.37	0.39	0.41	0.43	0.45	0.47	0.49
Simulation	$\delta\omega_n$	0.30	0.35	0.30	0.30	0.40	0.35	0.35	0.40	0.45	0.40
Analytical	$\Delta\omega_n$	0.16	0.17	0.18	0.19	0.20	0.20	0.21	0.22	0.23	0.24
Simulation	$\Delta\omega_n$	0.20	0.15	0.20	0.25	0.25	0.15	0.15	0.20	0.20	0.25

C, $a_0 = 40$, $I_l = 800$, $\theta = 0$, $n_0 = 200n_c$ in Fig. 4.8(b)

	n	17	19	21	23	25
Analytical	$\delta\omega_n$	1.00	1.11	1.22	1.34	1.46
Simulation	$\delta\omega_n$	1.03	1.14	1.27	1.37	1.49
Analytical	$\Delta\omega_n$	0.50	0.56	0.61	0.67	0.73
Simulation	$\Delta\omega_n$	0.37	0.41	0.63	0.68	0.71

C, $a_0 = 40$, $I_l = 800$, $\theta = \pi/4$, $n_0 = 200n_c$ in Fig. 4.8(b)

	n	16	17	18	19	20	21	22	23	24	25
Analytical	$\delta\omega_n$	0.38	0.41	0.43	0.46	0.48	0.50	0.53	0.55	0.58	0.60
Simulation	$\delta\omega_n$	0.34	0.34	0.39	0.39	0.44	0.42	0.49	0.49	0.54	0.54
Analytical	$\Delta\omega_n$	0.19	0.20	0.22	0.23	0.24	0.25	0.26	0.27	0.29	0.30
Simulation	$\Delta\omega_n$	0.20	0.15	0.15	0.25	0.25	0.15	0.15	0.20	0.20	0.25

Table 4.2: Comparison between analytical calculations and simulation results of the frequency shift ($\delta\omega_n$) and harmonic spectrum broadening ($\Delta\omega_n$). Eqs. (4.15)-(4.18) and the corresponding parameters in Fig. 4.8 are used for analytical calculations. The simulation results are extracted from Fig. 4.8.

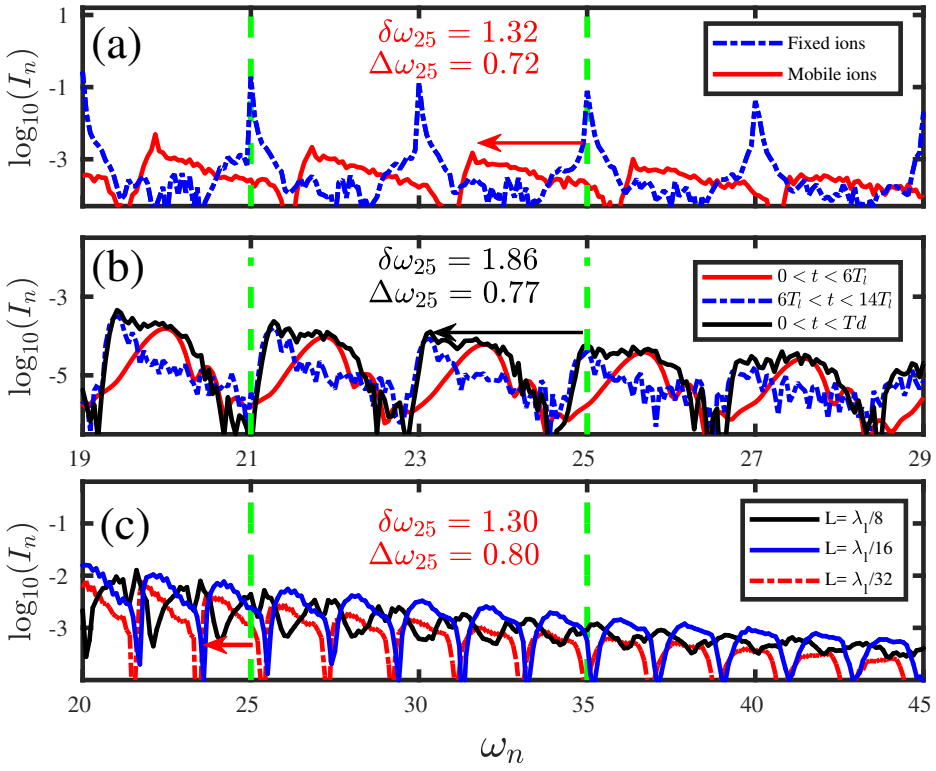

Figure 4.7: 1D PIC simulations of HHG for harmonic frequency shifts and peak broadening. The frequency shift (deviation from the green dashed lines) is clearly seen. (a) With and without ion motion at plasma density $n_0 = 200$ and with a constant laser amplitude $a(t) = a_0$ for $0 < t < T_d$. (b) With a laser pulse of temporal profile $a(t) = a_0 \sin^2(\pi t/T_d)$, where $T_d = 20T_l$, at plasma density $n_0 = 80$. (c) HHG with different plasma density gradients L. The maximal plasma density is $n_0 = 200$ with the same laser profile as in (a) except $T_d = 5T_l$. The Gold (Au, $A = 197$, $Z = 79$) plasma is used. The green dashed lines correspond to integer harmonics from selection rules defined in [16].

$\Delta\omega_{21} = 0.67\omega_l(\theta = 0)$, $\Delta\omega_{21} = 0.20\omega_l(\theta = 45°)$ and (b) $\Delta\omega_{21} = 0.61\omega_l(\theta = 0)$, $\Delta\omega_{21} = 0.25\omega_l(\theta = 45°)$ respectively and they match well with the corresponding PIC simulation results in Fig. 4.8. The analytical estimates and simulation results for all the other harmonics in Fig. 4.8 can be found in Table. 4.2. Here we only show harmonics up to order $n \leq 25$ since the peak frequency shift and widening are expected to be large for higher-order harmonics.

4.3.3 Discussions

With all the simulations in Figs. 4.7 and 4.8 and summarized dates in Tables. 4.1 and 4.2, we can validate our analytical calculations in Eqs. (4.15)-(4.18).

Fig. 4.9 summarizes the comparison between the simulation results (stars) and the analytical calculations (solid lines). As we can see in Fig. 4.9 (a), (b) and (c), the frequency shifts $\delta\omega_n$ in simulations (Fig. 4.7 and Fig. 4.8) match well with the analytical estimates for the parameters therein, and in Fig. 4.9 (d), the harmonic peak broadening $\Delta\omega_n$ matches qualitatively the relation, $\Delta\omega_n = \delta\omega_n/2$, (see Eq. (4.18)) with the frequency shift $\delta\omega_n$. The slight discrepancy between analytical estimates and PIC simulation results can be attributed to the rough estimation of the hot electron generation in the analytical model and the numerical noise in simulations. Therefore, the analytical

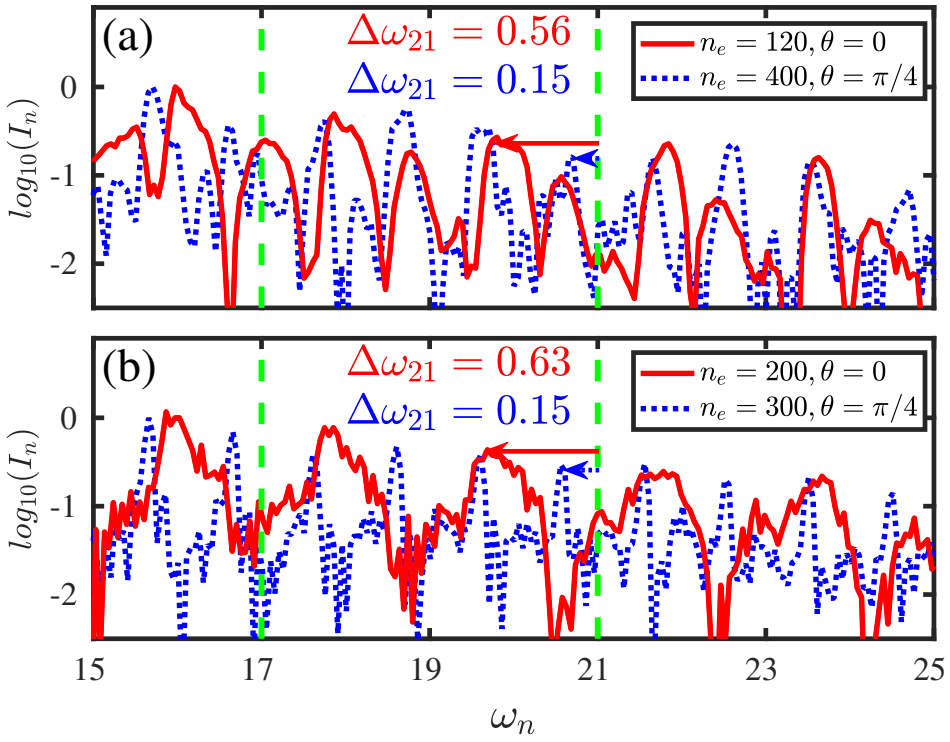

Figure 4.8: (2D PIC simulations with different targets and incident angles. The intensities are normalized to the intensity of the 17th harmonic for normal incidence and the 16th harmonic for oblique incidence. (a) Gold plasma with density gradient $L = \lambda_l/8$. (b) Carbon plasma with $L = \lambda_l/16$. The laser has the temporal profile $a(t) = a_0(\tanh((t - T_s)/W) - \tanh((t - T_e)/W))/2$ and the transverse profile $a(t, y) = a(t)\exp(-y^2/\sigma^2)$, where $a_0 = 40$, $W = T_l = \lambda_l/c$ and $\sigma = 4\lambda_l$. The laser pulse has maximum intensity from $T_s = 5T_l$ to $T_e = 13T_l$.

calculations in Eqs. (4.15)-(4.18) can be validated.

Apart from hole-boring-induced frequency broadening, two other effects are also responsible for broadening the harmonic spectrum: first, because of the laser temporal profile, see also in Ref. [111, 112], harmonics generated by different parts of the laser pulse can have different frequency shifts as shown by the solid red and dash-dotted blue lines in Fig. 4.7 (b), leading to the total frequency broadening, as shown by the solid black line in Fig. 4.7 (b). Second, harmonic spectra can also be broadened due to variable frequency shifts arising from the plasma density gradient *i.e.* $n_e = n_c \exp(x/L)/2$. Fig. 4.7 (c) depicts this broadening and one can clearly see that steep density gradient results into a narrower spectrum, while longer density gradient leads to widening of the harmonic spectrum. One may note that the ion-motion-induced broadening dominates over the last two mechanisms and it occurs in the first few cycles of the laser pulse and therefore can not be mitigated by resorting to few cycle laser pulses for HHG as shown by the red dotted line in Fig. 4.7 (b).

If the laser intensity reaches the regime $I \gg 10^{22}\mathrm{W/cm}^2$, the effect of the RR force [27, 76] is important as it repartitions the laser energy among different particles [77], and consequently influences harmonic generation. Fig. 4.10 (a) and (b) show the 2D PIC simulation results depicting the influence of the RR force on plasma HHG. One can see that the peak frequency shift and the frequency widening of the harmonics is smaller with the RR force effect. This difference, albeit smaller, is clearly noticeable (see inset of Fig. 4.10(a)). Essentially the RR force leads to redistribution of the laser energy among

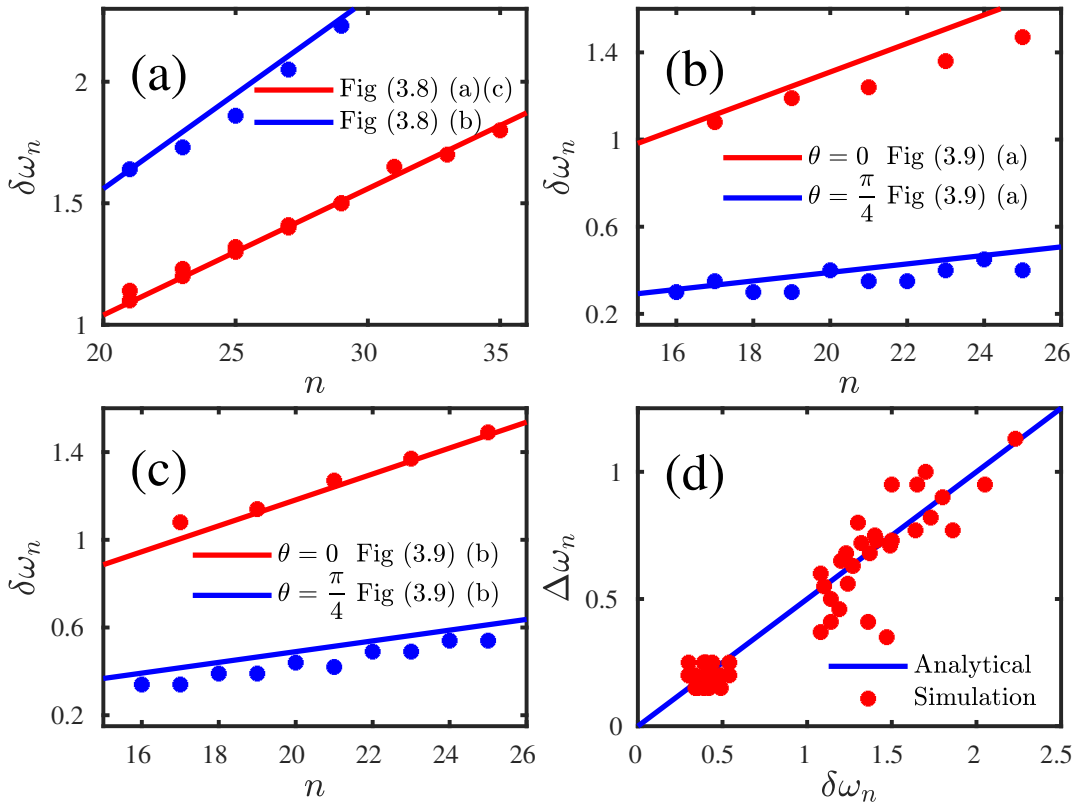

Figure 4.9: Analytical calculations (solid lines) and simulation dates (stars). The frequency shifts obtained from the simulations, (a) in Fig. 4.7, (b) in Fig. 4.8(a), (c) in Fig. 4.8(b), are compared with the analytical shifts calculated with Eq. 4.15 and the parameters in Figs. 4.7, 4.8, respectively. (d) Frequency shifts and harmonic peak broadening gained from the simulations in Figs. 4.7, 4.8. The solid line is the analytical relation $\Delta\omega_n = \delta\omega_n/2$ (see Eq. (4.18)). All the dates have been summarized in Tables. 4.1, 4.2.

different species of particles (electrons, ions and photons) which enhances the laser energy absorption and accordingly decreases the HB velocity [37, 77, 115] as shown in Fig. 4.10 (c). However, the intensity of the harmonics emitted is also reduced by the RR force in the oblique incidence case. The same interpretation can be used as in Sec. 4.2.4. Here, we give the more detailed understanding: HHG depends strongly on the backward motion of the electron layer towards the laser pulse. For the backward motion of the electrons, the RR force is stronger and it tends to slow down the electron layer movement as shown clearly in Fig. 4.10 (d). In the oblique incidence case, the backward motion can be accelerated by the E_x component of the laser field thereby enhancing the RR force compared to the normal incidence case. Consequently, the intensity of the generated harmonics can be slightly more reduced in the oblique incidence case. Hence, the RR effects can slightly reduce the harmonic intensity, but at the same time slightly improve the frequency broadening of the generated harmonic. The same analytical calculation for harmonic frequency shift and peak broadening can be used for the case in the RR force regime.

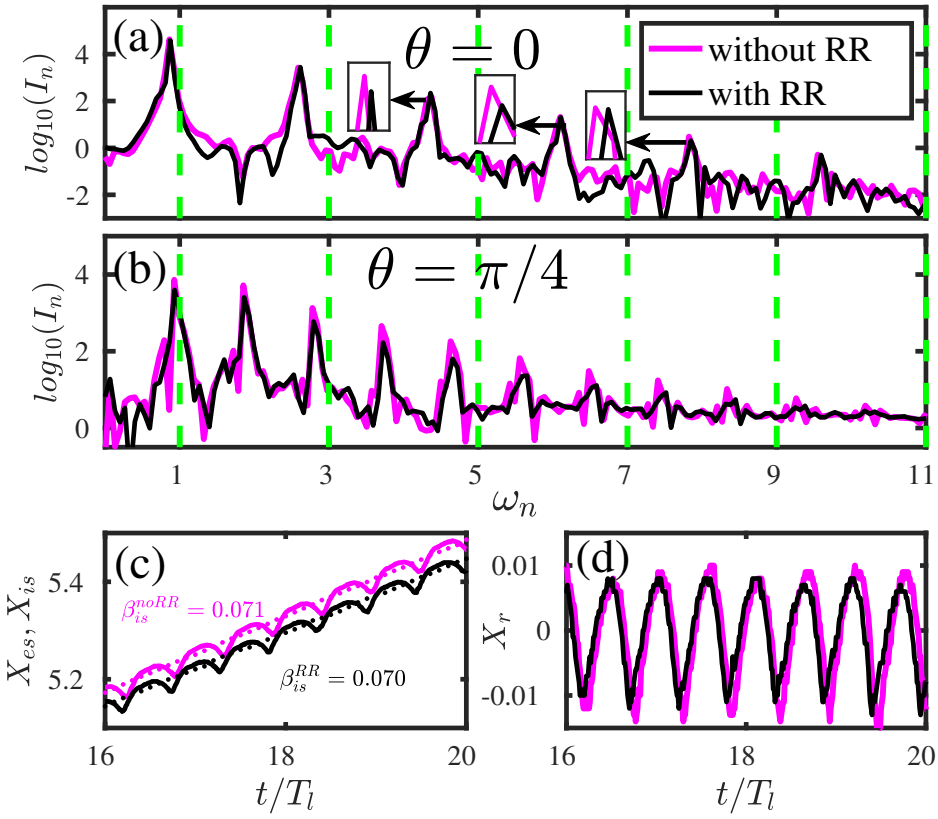

Figure 4.10: 2D PIC simulations of plasma HHG for the radiation reaction (RR) force. The black lines account for the RR force while the magenta lines do not. (a) Harmonic spectrum in normal incidence $\theta = 0$; (b) Harmonic spectrum in oblique incidence $\theta = \pi/4$. (c) Temporal position (y-axis) of the electron (X_{es}/λ_l, solid line) and ion (X_{is}/λ_l, dotted line) layers. The electron and ion layers are defined at the position with density $n_e = Zn_i = a_0 n_c$. (d) Relative position (y-axis) of the electron layer, $(X_{es} - X_{is})/\lambda_l$, with respect to the ion layer. (c), (d) are for simplified 1D normal incidence case for (a). The laser has a constant profile with $a_0 = 250$ for $0 < t < T_d = 20T_l$. The lasma density is $n_0 = 1100n_c$ without plasma gradient.

4.4 Parameter maps

We analyze and validate the widening of the harmonic spectra caused by the hole-boring-induced frequency shifts analytically as well as by PIC simulations. This widening can produce a quasi-continuous frequency spectrum which is the prerequisite for generating an intense isolated attosecond pulse [109, 110], though this frequency broadening can limit the temporal coherence of the high-frequency extreme ultraviolet (XUV) radiation. This juxtaposition can be exploited to create a parameter map (laser intensity vs plasma density) where different regions of the parameter map correspond to different applications, such as coherent XUV radiation and single attosecond pulse generations.

4.4.1 Frequency bound

The frequency bound is the line that separates the region for coherent XUV radiation and the region for a single attosecond pulse generation in a parameter map (laser intensity vs plasma density)

The line that separates the two regions corresponds to a case when the frequency

broadening equals the frequency separation between the adjacent harmonic peaks. This implies the maximal frequency widening of the nth harmonic

$$\Delta\omega_n^{\max} = d\ \omega_l\,, \tag{4.19}$$

where $d = 1, 2$ for oblique incidence (p-polarization) and normal incidence, respectively, on taking into account the selection rules for plasma HHG [16]. On using Eq. (4.18), one gets the maximal frequency shift

$$\delta\omega_n^{\max} = 2d\ \omega_l\,, \tag{4.20}$$

and making use of Eq. (4.15), one can connect the frequency shift to the hole-boring velocity β_{hb} which is the function of laser intensity I_l and plasma density n_0, and obtains the maximal hole-boring velocity:

$$\beta_{hb}^{\max} = \frac{d}{n-d}\,. \tag{4.21}$$

The hole-boring velocity has to be smaller than $\beta_{hb}^{\max}$ in case the frequency broadening of the nth harmonic $\Delta\omega_n > d\ \omega_l$. Replacing the hole-boring velocity with Eq. (4.16), one can have

$$B^{\max} = \frac{d}{n-2d}\left(1 - \frac{n-d}{n-2d}X_h\right)^{-1}\,, \tag{4.22}$$

and substituting the parameter B with Eq. (4.17), one can yield a bound on plasma density as

$$n_{e1}^{\min} = \frac{(n-2d)^2 I_l \cos^4(\theta)}{d^2\,(1 + m_i/Zm_e)}\left(1 - \frac{n-d}{n-2d}X_h\right)^2\,. \tag{4.23}$$

As we can see, $n_{e1}^{\min}$ depends on the hot electron generation X_h which is also a function of plasma density. Hence, Eq. (4.23) has to be solved numerically.

For plasma densities lower than Eq. (4.23), *i.e.* $n_0 < n_{e1}^{\min}$, the hole-boring velocity is large enough to make the harmonics with order higher than n overlap with each other, producing a quasi-continuous frequency spectrum, while at higher plasma densities, *i.e.* $n_0 > n_{e1}^{\min}$, the harmonics with order lower than n possess sharp harmonic peak, which can be spectrally filtered to produce a high-frequency radiation source with high temporal coherence. Here and below we do not taken into account RR force as it does not strongly affect the frequency shift of high-harmonics as shown in Fig. 4.10.

4.4.2 Intensity bounds

The intensity of the generated harmonics is also crucial for intense XUV and attosecond physics experiments. Fig. 4.7 (a) shows strong reduction in the harmonic intensity due to the ion motion. This reduction can be attributed to the change in the electron layer density and the amplitude of layer oscillation, arising significantly due to the HB effect and to a lesser extent by electron-ion collisions. Moreover, a very high plasma density does inhibit the formation and oscillation of the electron layer, and consequently suppresses the harmonic generation efficiency, which poses an upper limit on the plasma density for plasma HHG.

In ultra-dense plasma HHG, the energy conversion process (see Sec. 3.3) is very inef-

ficient [18], the local energy conservation is approximately satisfied, thus the Leontovich boundary condition can be used [54, 133]:

$$E^r(x(t^{'}),t^{'}) + E^i(x(t^{'}),t^{'}) = 0\,, \tag{4.24}$$

where $x(t^{'})$ is the location of the plasma surface at time $t^{'}$. With the retardation relation: $x + t = x(t^{'}) + t^{'}$, we can have the reflected field

$$E^r(x,t) = -E^i(x(t^{'}),t^{'}) = -E_0\cos(t^{'} - x(t^{'}))\,, \tag{4.25}$$

where the incident field is given as $E^i(x,t) = E_0\cos(t-x)$. The laser ponderomotive force

$$f_{\text{ponder}} \propto \cos^2(t^{'} - x(t^{'})) \propto 1 + \cos(2(t^{'} - x(t^{'}))) \tag{4.26}$$

drives the plasma surface oscillation harmonically, and gives an oscillation as:

$$x(t^{'}) = X_{\text{am}}\cos(2t^{'} + \phi)\,, \tag{4.27}$$

where X_{am} is the amplitude of the oscillation, ϕ is the relative phase between the driving field and the plasma surface oscillation, and the plasma surface is located at $x = 0$. With the very high plasma frequency $\omega_{pe} \gg \omega_l$, $\phi \approx 0$ is expected [16, 109]. Inserting Eq. (4.27) into the retardation relation and Eq. (4.25), we can have:

$$t^{'} = x + t - X_{\text{am}}\cos(2t^{'})\,, \tag{4.28a}$$

$$E^r(x,t) = -E_0\cos(t - 2x(t^{'}))\,. \tag{4.28b}$$

Numerically solving Eqs. (4.28), we can obtain the reflected field and the harmonic spectrum as we show in Fig. 4.11.

With this simple oscillating mirror model [3], we can know that the harmonic intensity $I(\omega_n)$ decays faster with a smaller oscillating amplitude X_{am}. In order to prevent the harmonic intensity from decaying faster than $I_n \propto \omega_n^{-8/3}$ [54], a minimal oscillating amplitude is imposed: $X_{\text{am}}^{\text{min}} \geq 0.05\lambda_l$.

The plasma oscillating amplitude X_{am} can be estimated by balancing the electrostatic force acting on the electron layer inside the plasma shin depth with the ponderomotive force of the laser, *i.e.*

$$\frac{n_0}{\cos(\theta)}X_{\text{am}} \approx a_{es}\left|\frac{\partial}{\partial x}a_{es}\right|\,, \tag{4.29}$$

where $E_x = X_{\text{am}}n_0/\cos(\theta)$ is electrostatic field, and $f_{\text{ponder}} \approx a_{es}\partial_x a_{es}$ denotes the laser ponderomotive force. a_{es} is the field inside the electron surface and can be expressed as $a_{es} = a_s\exp(-x/\lambda_s)$ [16] with the skin-depth $\lambda_s \propto n_0^{-1/2}$ and the electric field $a_s \approx 2a_0\cos^{-1}(\theta)/n_0^{1/2}$ at the electron surface [16]. In this ultra-dense case, we can neglect the plasma compression becomes of the small oscillation amplitude. With all of

[3] In principle, this simple oscillating mirror model can only work for ultra-dense plasmas, for which the oscillating amplitude is much smaller than the laser wavelength.

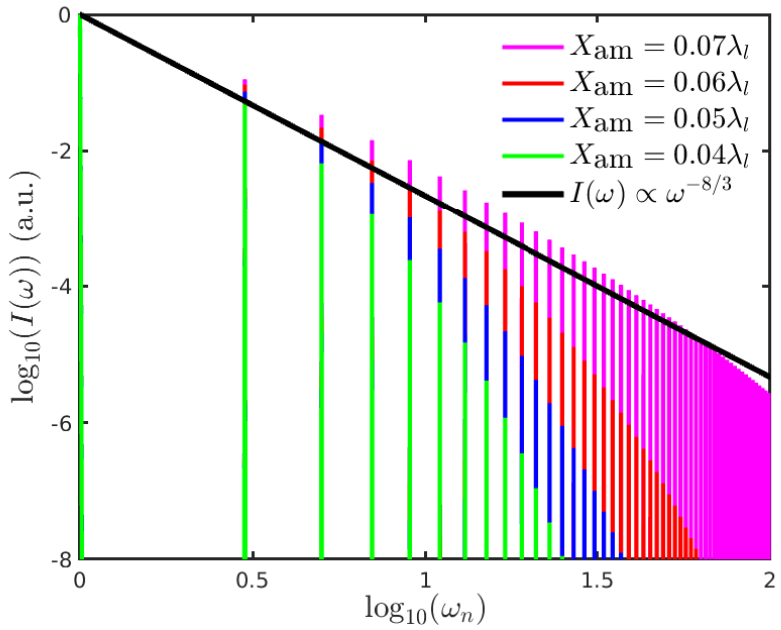

Figure 4.11: Harmonic spectra for different oscillating amplitude $X_{\rm am}$. The smaller amplitude shows less efficient harmonic generation. The black line represents the spectral scaling $I(\omega_n) \propto \omega_n^{-8/3}$ from Ref. [54].

these, we can have:

$$X_{\rm am} \approx \frac{8I_l}{\cos(\theta) n_0^{3/2}}\,, \tag{4.30}$$

showing that the oscillation amplitude vanishes at very high plasma density.

On equating the plasma oscillating amplitude $X_{\rm am}$ with the minimal amplitude $X_{\rm am}^{\rm min}$, one can place the upper limit on the plasma density for intense HHG. Consequently, with the given laser intensity I, the maximum density $n_e^{\rm max}$ of the target plasma can be cast as

$$n_e^{\rm max} = 8.656 I_l^{2/3} (\cos\theta)^{-2/3}\,. \tag{4.31}$$

In case of laser deep penetration leading to large laser absorption, a lowest limit on the plasma density for HHG is placed at the plasma relativistic critical density,

$$\begin{aligned} n_e^{\rm min} = n_{rc} &= \cos^2(\theta) < \gamma > \\ &\approx \cos^2(\theta)\sqrt{1+ < p^2 >} \\ &\approx \cos^2(\theta)\sqrt{1+I_l} \end{aligned} \tag{4.32}$$

For the plasma densities higher than Eq. (4.31) or lower than Eq. (4.32), the emitted harmonics are too weak to have any promising applications in both XUV or attosecond physics experiments.

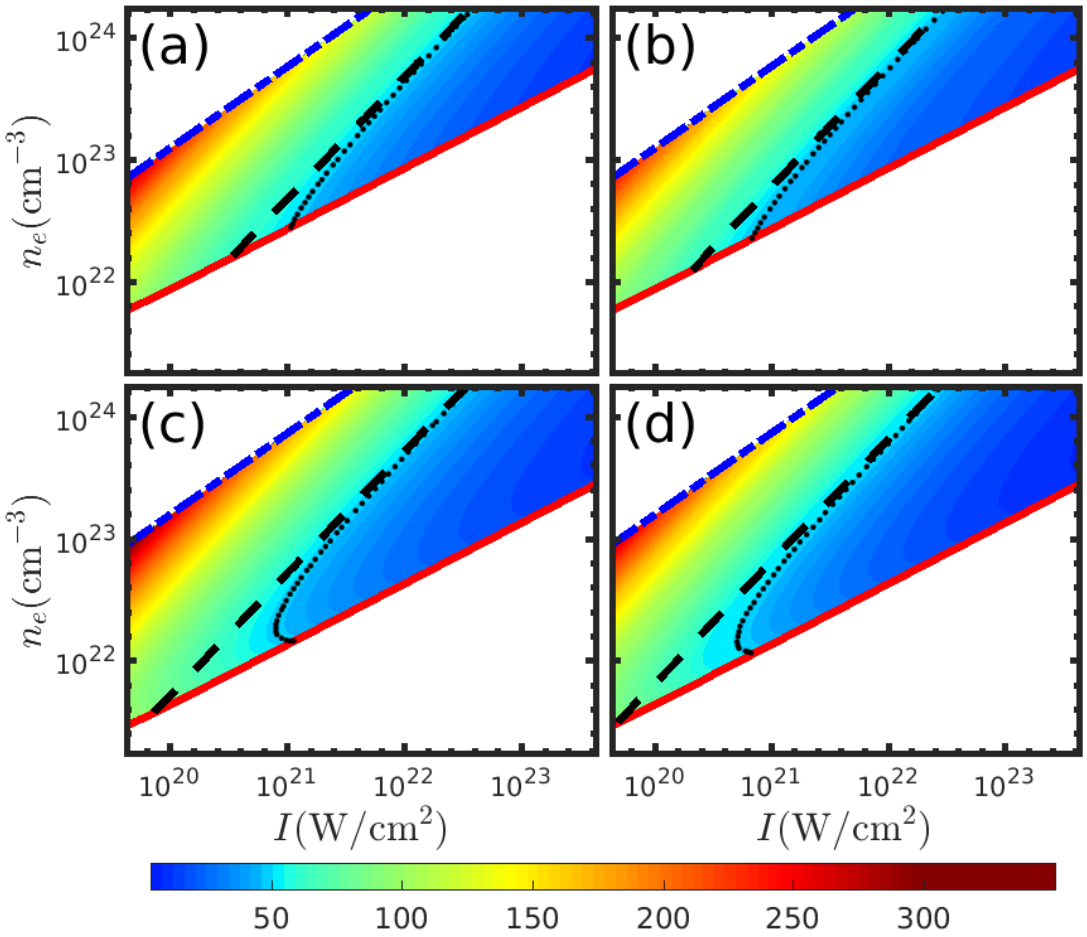

Figure 4.12: Parameter maps for optimum HHG for (a), (b) normal incidence and (c), (d) oblique incidence ($\theta = 45°$) with p-polarizations. (a), (c) are for gold plasma; (b), (d) are for carbon plasma. The color bar represents the harmonic numbers. The black line is plotted for the 50th harmonic in each case. See text for explanation.

4.4.3 Discussions

With the help of the bounds given by Eqs. (4.23), (4.31) and (4.32), one can construct a parameter map relating the plasma density with the laser intensity and demarcate the map into two regions corresponding to both the coherent XUV radiation and an intense single attosecond pulse generations.

Fig. 4.12 shows these parameter maps for normal ($\theta = 0$) and oblique ($\theta = \pi/4$) incidences of the laser pulse on gold (Au, $A = 197$, $Z = 79$) and carbon (C, $A = 12$, $Z = 6$) plasma targets. The lowest line (red) corresponds to Eq. (4.32) and sets a lower bound for HHG. The upper most line (blue dash-dotted) comes from Eq. (4.31) and it denotes the maximum density for intense plasma HHG. The region between these two lines shows the contours of plasma densities given by Eq. (4.23) with the color bar representing different harmonic orders. For instance, the middle dashed and dotted black lines have been plotted for the 50th harmonic corresponding to a photon of energy 77.5 eV in the XUV region of the electromagnetic spectrum. The dotted black line accounts for the hot-electron generation and it deviates from the dashed black line only at lower plasma densities where the generation of the hot electrons effectively reduces the hole-boring velocity. Thus, the region of the map below the topmost dashed-dotted blue

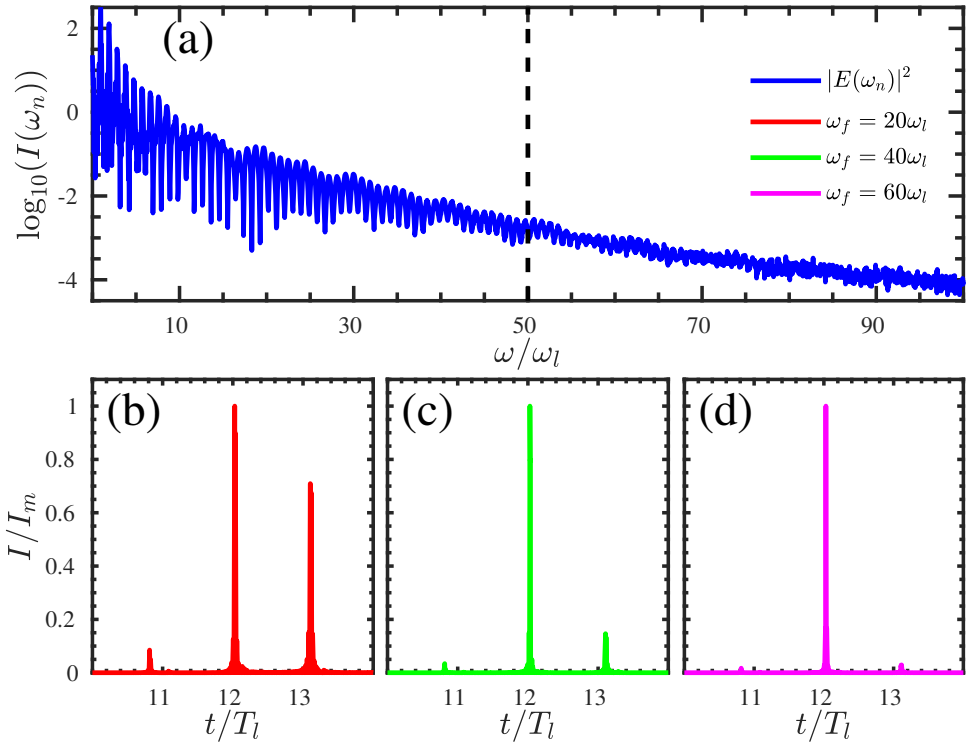

Figure 4.13: 1D PIC simulation of HHG. (a) Harmonic spectrum of the reflection. The black dashed line represents the harmonic order ($n = 50$) from where the harmonic spectrum becomes quasi-continuous. (b), (c), and (d) denote the normalized attosecond pulses obtained by applying spectral filters with different frequency (b) $\omega_f = 20\omega_l$, (c) $\omega_f = 40\omega_l$ and (d) $\omega_f = 60\omega_l$. The laser has the temporal profile $a(t) = a_0(\tanh((t - T_s)/W) - \tanh((t - T_e)/W))/2$, where $a_0 = 100$, $W = T_l/2 = \lambda_l/(2c)$, $T_s = 4T_l$, $T_e = 16T_l$, and irradiates the plasma ($n_0 = 500n_c$, $L = \lambda_l/8$) with incident angle $\theta = \pi/4$.

line, and above the intersection of the middle dotted black and lowermost red lines, is the region where the overlap between harmonics with order ($n \leq 50$) is not significant, and it is suitable for generating coherent XUV radiations in the water-window region with high temporal coherence. While the region of the map between the middle dotted black and lowermost red lines depicts a region where harmonics with order ($n > 50$) overlap significantly with each other, yielding quasi-continuous spectra suitable for single attosecond pulse generation.

To test this parameter map, we do the 1D simulation of HHG and show the obtained harmonic spectrum and attosecond pulses in Fig. 4.13. With the parameters herein and based on Eqs. (4.15)-(4.18), we can gain $\Delta\omega_{50} = \omega_l$. Therefore, the harmonics with order ($n < 50$) keep the well-defined shape harmonic peaks, while for harmonics with order ($n > 50$), the spectrum becomes quasi-continuous. This prediction matches well with the simulation result in Fig. 4.13 (a). On filtering out the low-order harmonics, one can obtain a train of attosecond pulses or a single attosecond pulse [109] as shown in Fig. 4.13 (b), (c) and (d). If the filtering frequency is in the coherent XUV region, *i.e.* $\omega_f < 50\omega_l$, a train of attosecond pulses is presented. However, if the filtering frequency is increased into the quasi-continuous region $\omega_f > 50\omega_l$, one can obtain an intense isolated attosecond pulse. The details of a single attosecond pulse generation is presented in Chapter. 5.

4.5 Conclusions

In this chapter, plasma high-order harmonic generation from an extremely intense short-pulse laser ($I_l > 10^{21}$ W/cm^2) is explored.

We first give a wide range parametric studies to highlight the necessity of including the effects of ion motion, electron-ion collisions, plasma temperature and the radiation reaction force in the dynamics of ultra-relativistic laser-plasma interaction for plasma high-order harmonic generation.

In the ultra-relativistic regime, the ion motion, induced by the HB effect, tends to strongly broaden the frequency bandwidth of the generated harmonics. We analyze analytically the broadening of the harmonic spectra and validate it by PIC simulations. The classical RR force does not strongly affect the frequency bandwidth but can lead to the slight reduction in the intensity of the harmonics.

Based on these considerations, we have scanned parameter maps (plasma density vs laser intensity) for different target materials at normal as well as oblique incidences of the laser pulse. These maps highlight the optimum regions for the generations of coherent XUV radiation in the water-window part of the electromagnetic spectrum as well as an intense single attosecond pulse.

Chapter 5

Super-intense single attosecond pulse generation

In this chapter, we propose a new scheme to generate an ultra-intense phase-stabilized isolated attosecond pulse from a robust plasma self-generated gate. In Sec. 5.1, we briefly give the motivation for our investigation of ultra-intense single attosecond pulse generation and introduce the basic method for generating attosecond pulses from plasma high-order harmonic generation. In Sec. 5.2, a robust plasma gating scheme to generate a single ultra-intense attosecond pulse is proposed and then verified with the theoretical model and particle-in-cell (PIC) simulations. It is manifested that the hole-boring effect mainly contributes to the plasma gate isolating the strongest pulse emission within one laser cycle. Moreover, we present a comprehensive discussion about the pulse phase properties in different frequency regions in Sec. 5.3. In Sec. 5.4, we shortly conclude all the discussions in this chapter.

Same dimensionless quantities are used as in Chapter 3.

5.1 Introduction

5.1.1 Motivation

Attosecond (10^{-18} s) metrology is an emerging area of research spanning a range of applications from atomic physics to biological sciences [134]. An attosecond pulse is regarded as a camera that can capture the hyperfast motion of electrons, making it an invaluable tool to study many fundamental physical processes in real-time (attosecond spectroscopy) [47]. Due to the small flux and low photon energy of the current attosecond pulse source, the application of attosecond spectroscopy is so far limited [47, 135]. The generation of an isolated, ultra-intense, phase stabilized attosecond pulse with ultra-broad spectrum can open the hitherto unexplored regime of attosecond spectroscopy [99, 136, 137], extending attosecond metrology to inner-shell processes in high-Z atoms and high-energy quantum electrodynamical processes [27, 28].

Isolated attosecond pulse generation can be accomplished via high-order harmonic generation (HHG) in the interaction of strong laser pulses with either gaseous or solid targets. The underlying physical mechanisms for both cases have been extensively studied. Although the generation of a single attosecond pulse has been experimentally demonstrated in gaseous HHG, the attosecond pulse intensity saturates at relativistic incident intensity $a_0 = eE_l/(m_e c\omega_l) = 1$ [35], where e and m_e denote the electron charge and mass, E_l and ω_l are the laser electric field and frequency, c is the light speed in vacuum. In contrast, attosecond pulses from solid HHG scale favorably at relativistic intensities. After filtering out the low-order harmonics, the solid HHG usually results in a train of attosecond pulses [109]. To isolate an attosecond pulse, several techniques [98, 109, 110, 138, 139], *e.g.* polarization and intensity gatings, attosecond

lighthouse effect and reflection from a tightly focused laser have been implemented. However, the implementation of these techniques for ultra-intense isolated attosecond pulse generation may not be practical due to severe constraints on the ultra-relativistic laser ($a_0 \gg 1$) and target parameters *e.g.* stable carrier-envelope-phase (CEP), few cycle duration, extremely thin target, ionization of optical device etc. Moreover, the spectral phase-stabilization of the isolated attosecond pulse, which is essential not only for the attosecond pulse duration [51] but also for the temporal resolution of attosecond pump-probe experiments [102], has not been illuminated in these techniques or in the previous solid HHG models [15, 16, 18, 54, 58, 66, 103, 111, 132, 140–143], *e.g.* relativistically oscillating mirror (ROM), coherent wake emission (CWE), coherent synchrotron emission (CSE) and relativistic electron spring (RES).

In this chapter, we propose a new scheme for isolated super-intense attosecond pulse generation via the ultra-relativistic laser-solid interaction and expound, for the first time, the pulse spectral phase stabilization. Based on the result in Sec. 4.3 that the hole-boring effect [37, 115] broadens the harmonic peaks leading to a quasi-continuous spectrum [1], we show that the hole-boring effect effectively limits the strongest pulse emission within one laser cycle, making it possible to isolate an attosecond pulse. We term this hole-boring induced pulse isolation as a "Plasma Gate". This scheme is indeed predominant in the ultra-relativistic regime and works for long laser pulses. The harmonics constituting the isolated pulse are phase-locked to $\psi(\omega) \approx \pm\pi/2$ due to the dynamics of the plasma surface electron layer. In this ultra-relativistic regime, the radiation reaction force becomes important and can be included by employing Landau-Lifshitz prescription [76].

5.1.2 Route to attosecond pulse generation

On one hand, the generation of very short pulses can be regarded as the consequence of the superposition of large numbers of properly phased monochromatic light waves. The interference among these coherent waves results in the spatial and temporal confinement of the wave energy−short pulse generation. Fourier synthesis manifests that the duration of the generated pulse is inversely proportional to the width of the spectrum of the wave components with comparable amplitudes. Based on this concept, the ultra-broad and relatively flat plasma harmonic spectra pave the way to attosecond pulse generation.

On the other hand, the emission of high-frequency components is bunched in the attoseconds duration in which relativistic factor γ of the plasma surface presents to be a very sharp spike [54, 109], while the low-frequency components could be emitted in the entire interacting duration. Therefore, to extract the attosecond pulses from plasma HHG, the low frequency components, in general, have to be filtered out of the reflection as we show in Fig. 4.1.

In experiments, the generation of attosecond pulses is accomplished via passing the reflected pulse through a suitable thin metal foil which filters out the low-frequency components in reflection [109]. In this chapter, we proceed in the same way as in experiments, but cut off the low-order harmonics numerically. Below we disintegrate this general process and explain step by step.

In Fig. 5.1 (a), we present the reflected field (red solid line) modulated from an incident field (blue dashed line) via interacting with a plasma target. From the reflected field, we can gain the harmonic spectrum shown in Fig. 5.1 (b) via Fourier transformation. To obtain the attosecond pulses, we filter out the low-order harmonics in the frequency domain and then inversely transform the high-frequency harmonics back to the temporal domain. For instance, in Fig. 5.1 (c), the filtering frequency is $\omega_f = 20\omega_l$, which means

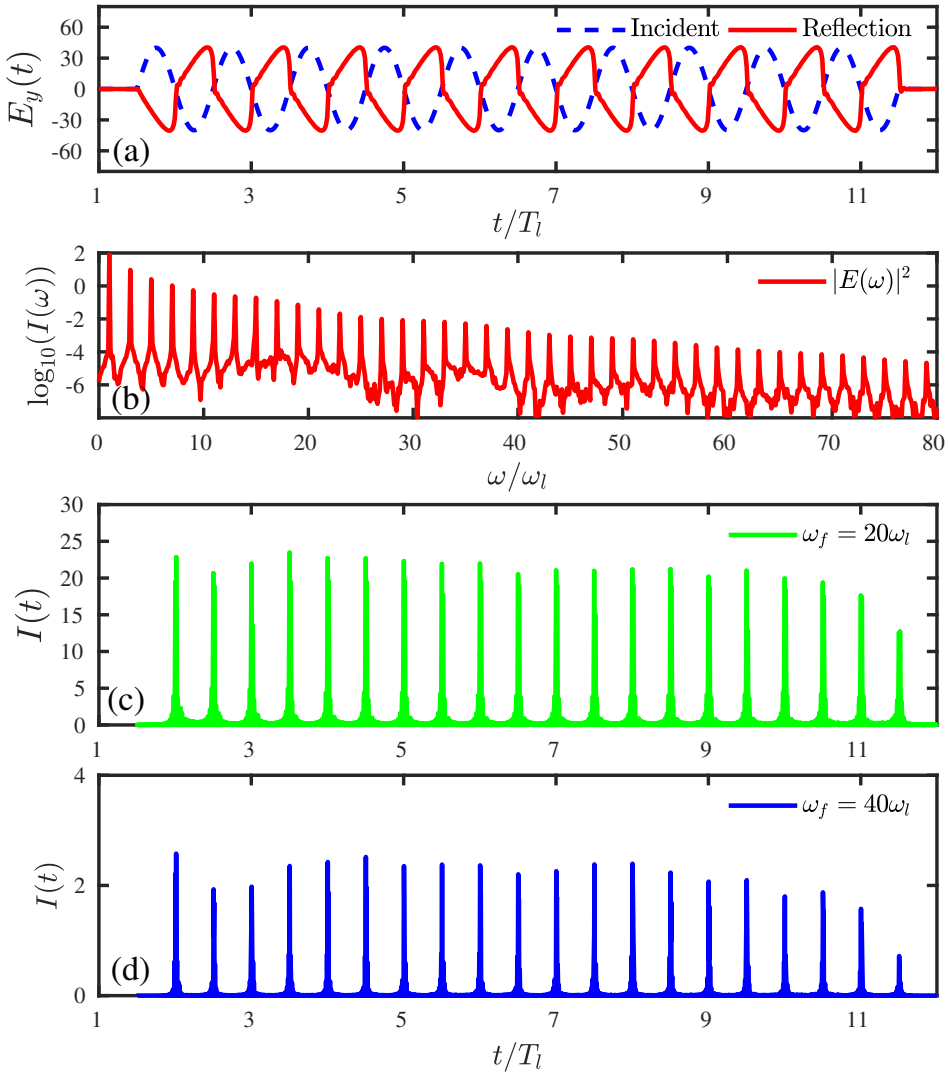

Figure 5.1: 1D PIC simulation of HHG for attosecond pulse generation. (a) Incident field (blue dashed line) and reflected field (red solid line). Reflected field is strongly modulated from the incident field. (b) Harmonic spectrum of the reflected field (c) Attosecond pulse train obtained with filtering frequency $\omega_f = 20$. (d) Attosecond pulse train obtained with filtering frequency $\omega_f = 40$. Ions are fixed, and collisions are included. The laser has a step-like profile with a constant amplitude $a(t) = 40$ for $0 < t < T_d = 10T_l$. The plasma has no pre-gradient with constant density $n_0 = 280$. Two pulses are emitted in one laser cycle in the normal incident geometry ($\theta = 0$).

that the harmonics with order $n \leq 20$ are cut-off, the harmonics with order $n > 20$ are transformed back and constitute a train of attosecond pulses. In the same way, if the filtering frequency is changed to be $\omega_f = 20\omega_l$, we can obtain the attosecond pulses with weaker intensity in Fig. 5.1 (d).

As shown in Fig. 5.1 (c) and (d), trains of attosecond pulses are presented. To generate a single attosecond pulse, different gating techniques are used in experiments [109, 110, 139, 144, 145]. In next section, we propose a new scheme−plasma gating−to isolate a super-intense attosecond pulse.

5.2 Single attosecond pulse generation

A quasi-continuous spectrum is the prerequisite for the generation of a single attosecond pulse. Based on the results in Sec. 4.3 and 4.4, hole-boring effect broadens the harmonic peaks leading to a quasi-continuous spectrum, which provide the possibility to build a new scheme to generate a single ultra-intense attosecond pulse. In this section, we show that the hole-boring effect effectively limits the most efficient high-frequency emission within one laser cycle, making it possible to isolate an attosecond pulse. We term this hole-boring induced pulse isolation as a "Plasma Gate". This scheme is indeed predominant in the ultra-relativistic regime and works for general situations.

5.2.1 Plasma gate

A 1D simulation result is shown in Fig. 5.2 to verify the action of the plasma gate for most-general situations *e.g.* plasma density gradient, oblique incidence, long laser pulse driver. For generality, we consider a fully ionized plasma with a pre-gradient, $n_e(x) = n_c/2 \exp(x/L)$ and a bulk plasma n_0 behind.

In Fig. 5.2, we show the obtained attosecond pulses by filtering out low-order harmonics ($\omega < \omega_f$) in the reflection from a solid plasma irradiated by a long duration laser pulse. One can clearly see the action of the plasma gate for pulse isolation as only three attosecond pulses are seen. Although the laser is still on, no strong attosecond pulse is emitted after the 3rd one in Fig. 5.2 (a).

Here the 1st pulse with weak intensity arises due to the reflection of the laser ramp from the plasma pre-gradient present at the target surface. The 2nd pulse with ultrahigh intensity $I_2 \approx 9.2 \times 10^{21}\mathrm{W/cm}^2$ is emitted in the first cycle of the peak laser interacting with the bulk of the plasma. During the interaction, a large part of the laser energy is first stored in the plasma electrostatic field due to the compression of the electrons into an ultra-dense nanometer layer. Without notable ion motion, the stored energy is then absorbed mainly by the electron layer accelerating backward to emit an ultra-intense attosecond pulse. This energy conversion process, described in detail in Sec. 3.3, is similar to the description for RES model [18] and guarantees the ultrahigh intensity of the emitted pulse which could be orders of magnitude stronger than the isolated attosecond pulses reported before [98, 109, 110, 138, 139]. The 3rd attosecond pulse is emitted in the next cycle with much weaker intensity. In this cycle, the energy conversion process is effectively impacted by the pronounced hole-boring effect. Ion motion decreases the energy partition for the electron layer acceleration in the energy conversion process as also discussed in Sec. 3.3, thus reduces the subsequent pulse emission.

We confirm this reduction in Fig. 5.3 (a). As shown, the 1st and 3rd pulses have much rapider intensity decay than the 2nd pulse, implying lower efficiency for high frequency emission. To gain deeper insight into this plasma gating, we also show the spectral phase

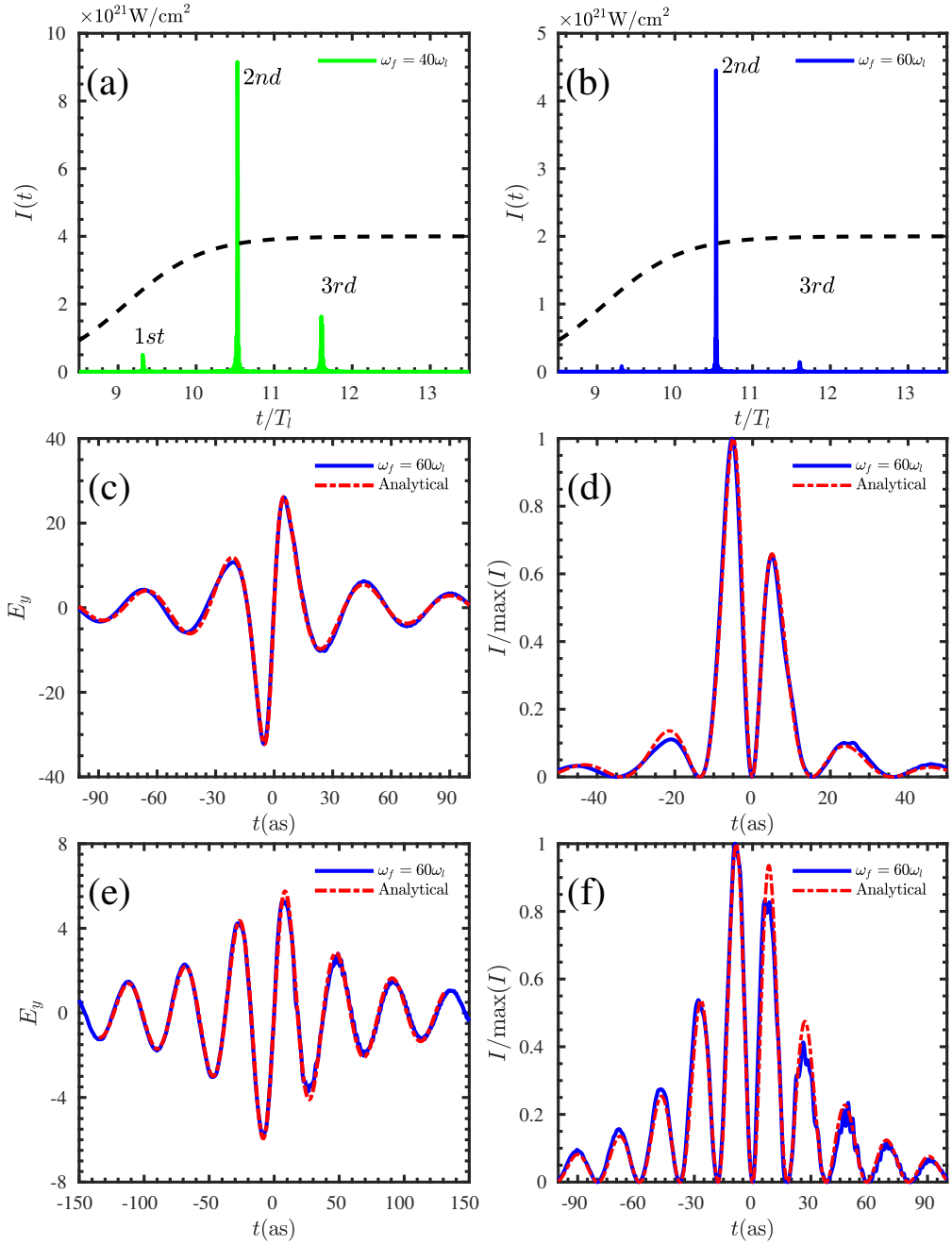

Figure 5.2: 1D PIC simulation of HHG for attosecond pulse generation. Attosecond pulses obtained by applying different filter frequency ω_f: (a) $\omega_f = 40\omega_l$, (b) $\omega_f = 60\omega_l$. The upper frequency of the filter is $2000\omega_l$. (c) Electric field E_y and (d) normalized intensity of the 2nd pulse compared with the analytical expressions. (e) Electric field E_y and (f) normalized intensity of the 3rd pulse compared with the analytical expressions. We label the pulse centers at time $t = 0$ and zoom in the time axis in unit of as for (c), (d), (e), (f). The laser, $a(t) = a_0(\tanh((t - T_s)/W) - \tanh((t - T_e)/W))/2$, radiates the plasma ($n_0 = 500n_c$, $L = \lambda_l/8$) with incident angle $\theta = \pi/4$, where $a_0 = 100$, $W = T_l = \lambda_l/c$, $T_s = 6T_l$, $T_e = 14T_l$, $\lambda_l = 0.8\mu m$. The laser profile (black dashed line) is shown in (a), (b) with a.u.. The field detector is located at $3\lambda_l$ from the plasma surface.

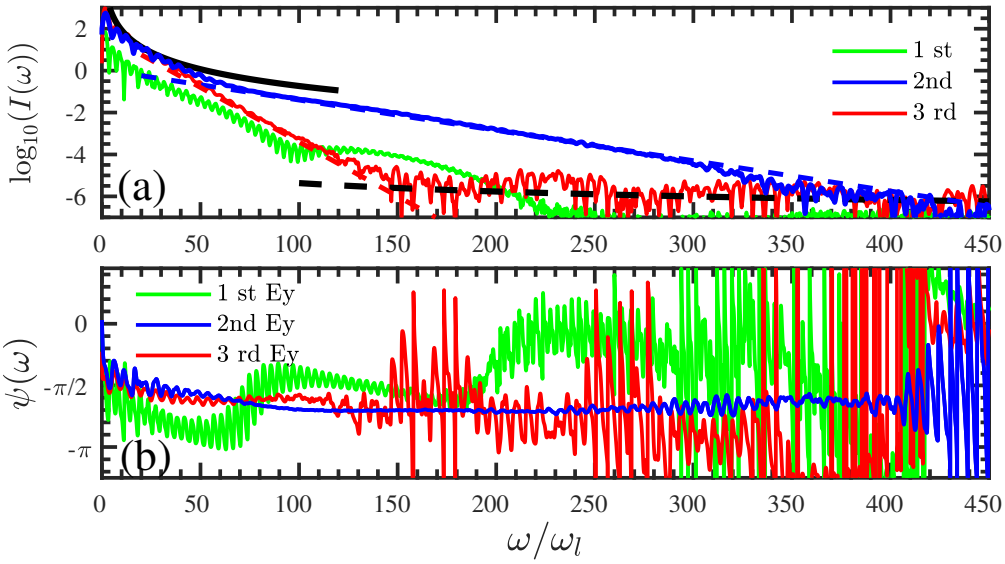

Figure 5.3: Intensity spectra (a) and spectral phase (b) for the pulses in Fig. 5.2. The spectral fittings of the 2nd pulse ($\log_{10}(I) = 0.1 - 0.0145\omega$, blue dashed line) and the 3rd pulse ($\log_{10}(I) = 1.9 - 0.052\omega$, red dashed line) are shown with the power-law spectral scalings ($I = 10^{4.6}\omega^{-8/3}$ [54], black solid, $I = 10^{-2.7}\omega^{-4/3}$ [17], black dashed) fitting the low-frequency and high-frequency regions in the spectra.

of the each pulse in Fig. 5.3 (b), and find that the high-frequency components in the 1st and 3rd pulses display larger phase fluctuation than that in the 2nd pulse, which could further reduce the pulse intensity and extend the duration.

In the following cycles, the pulse emission would have much faster spectral decay and more fluctuated phase. Thus, we can isolate the 2nd pulse with a suitable frequency filter and enhance the isolation with a larger filtering frequency ω_f, *e.g.* $I_2/I_3 = 6.10$ for $\omega_f = 40$ in (a), $I_2/I_3 = 31.13$ for $\omega_f = 60$ in (b). This is in line with our previous results, the cut-off-frequency in (b) corresponds to Eq. 4.23 in Sec. 4.4 for the parameters considered here.

From above discussion, we can say that the "plasma gate" acts to isolate the 2nd pulse by speeding up the spectral decay and degrading the spectral phase coherence of the other pulse, or we can also say that the "plasma gate" limits the most efficient high-frequency emission within one laser cycle, making it possible to isolate an attosecond pulse.

5.2.2 Theoretical model

To complement the simulation results and to depict the properties of the emitted pulse, we resort to the analytical model for the pulse emission from an electron layer described in Sec. 3.1.

We first scan the emission process for the 2nd and 3rd pulses in Fig. 5.4. As shown, the pulses are clearly emitted by the surface electron layer at the node (green stars in Fig. 5.4 (b),(c) for 2nd pulse, (e),(f) for 3rd pulse) where the layer transverse momentum $p_y = \gamma\beta_y(t')$ changes sign [98] and its backward velocity $\beta_x(t') \approx -1$ approaches the speed of light, which satisfies the conditions (I, II) for our pulse emission model in Sec. 3.1. Therefore, the same derivations can be given. For the coherent emission with

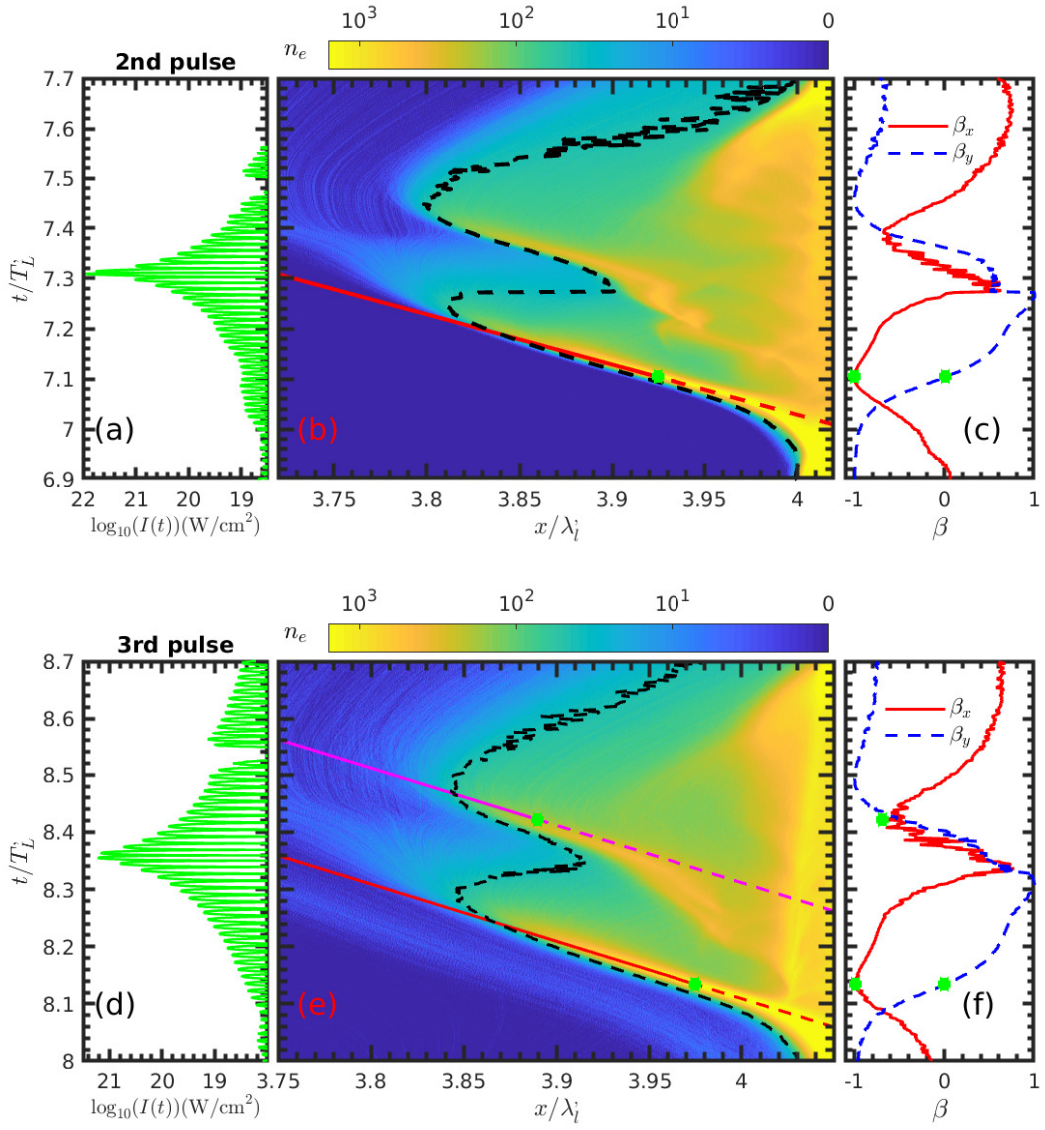

Figure 5.4: 1D PIC simulation for the 2nd and 3rd pulse emission processes in Fig. 5.2. (a) Temporal shape of the 2nd pulse in Fig. 5.2 (a) shifted along the retardation relation. (b) Evolution of the electron density n_e at the plasma surface around the instant of the emission (green star) of the 2nd pulse overlaid with the retardation path of the pulse center. Red dashed line denotes the retardation path before emission, and red solid line is after emission. The evolution of the electron surface ($n_e = a_0 n_c'$) is also shown (black dashed line). (c) Velocity (β_x, β_y) along the electron surface. In (d), (e), (f), we repeat all the plots in (a), (b), (c), but for 3rd pulse. In (c), we can obtain $\beta_x = -0.9988$ at the emission instant (green star) for the main pulse, and in (f) $\beta_x = -0.9877$ at the emission instant (green star) for the main pulse. The retardation relation is satisfied along the retardation paths. $\lambda_l' = \lambda_l/\cos(\theta)$, $T_l' = T_l/\cos(\theta)$, $n_c' = n_c\cos^2(\theta)$ are defined in the Lorentz boosted frame [79]

wavelength $\lambda_\omega \gg \Delta x$, we can make use of the pulse spectrum (Eq. (3.17))

$$I(\omega) = |\widetilde{E}_y^r(\omega)|^2 = \frac{\bar{A}_m^2}{\omega_d^2} \exp\left(-\frac{2|\omega|}{\omega_d}\right), \tag{5.1}$$

and the expression of the attosecond pulse (Eq. (3.29))

$$E_y^r(\omega_f, t) = \hat{E}_y^r \frac{2\bar{A}_m}{\sqrt{1+(\omega_d t)^2}} e^{-\frac{\omega_f}{\omega_d}} \cos\left[\omega_f t + \varphi(t) - \psi_{A_m}\right], \tag{5.2}$$

where all the variables are defined in Sec. 3.1. For convenience, we label the pulse center at $t = 0$. This formula is applicable for oblique incidence by treating in a Lorentz boosted frame [79] with

$$\bar{A}_m \approx A_m^0 \approx \frac{n_{el}\gamma}{2} \cos^{-2}(\theta). \tag{5.3}$$

As we can see from Eq. (5.1), the pulse possesses an exponential spectrum [18]. In Fig. 5.3 (a), we confirm this exponential spectrum with the linear-logarithm fitting

$$\log_{10}(I(\omega)) = 2\log_{10}\left(\frac{\bar{A}_m}{\omega_d}\right) - \frac{2\log_{10}(e)}{\omega_d}\omega. \tag{5.4}$$

The fitting slope of the pulse spectrum (blue dashed line for the 2nd pulse and red dashed line for the 3rd pulse) reveals the spectral decay:

$$-\frac{2\log_{10}(e)}{\omega_d} = -0.0145 \quad \Rightarrow \quad \frac{1}{\omega_d} = 0.017, \qquad \text{for 2nd Pulse}, \tag{5.5a}$$

$$-\frac{2\log_{10}(e)}{\omega_d} = -0.0052 \quad \Rightarrow \quad \frac{1}{\omega_d} = 0.060, \qquad \text{for 3rd Pulse}, \tag{5.5b}$$

and precisely gives the 2nd pulse duration $T_d = 2/\omega_d = 14.2$as which is much shorter than the duration of the 3rd pulse ($T_d = 50.8$as). The pulse duration is extremely shortened with the relativistic backward velocity and larger transverse acceleration. In Fig. 5.3 (a) we can also find that the exponential region is bounded by ROM scaling $I(\omega) \propto \omega^{-8/3}$ [54] in low-frequency region and CSE scaling $I(\omega) \propto \omega^{-4/3}$ [17] in high-frequency region.

The distinct feature of the pulse is the constant spectral phase, $\psi_0(\omega) = -\pi/2 + \psi_{A_m}$ (or $\pi/2 + \psi_{A_m}$ if E_y^i changes sign). This particular locked phase is the consequence of the transverse current changing its sign at the node where $p_y = 0$, and the temporal variation of $A_m(t)$ during the pulse emission. The phase $\pm\pi/2$ regulates the pulse structure and results in a minimum at the pulse center, contrary to a synchrotron-like pulse [98]. We stress that this particular locked phase does not depend on the laser carrier-envelope-phase (CEP) , but on the dynamics of the well-defined electron layer during the emission. The phase ψ_{A_m}, depending slightly on laser CEP (See Sec. 5.3.1), results in the slight asymmetry of the emitted pulse in Fig. 5.2 (d) and (f). In ultra-relativistic regime, $\psi_{A_m} \sim A_m^1/(A_m^0\omega_d)$ (See Eq. 3.20) would be very small because A_m^0 and ω_d would be extremely large. The detailed discussion about this constant phase can be found in Sec. 3.1.2.

In Fig. 5.3(b) we quantitatively confirm the constant spectral phase for 2nd and 3rd pulses in E_y, $\psi(\omega) \approx -\pi/2$ and in B_z, $\psi(\omega) \approx \pi/2$ as propagating in $-x$ direction (not

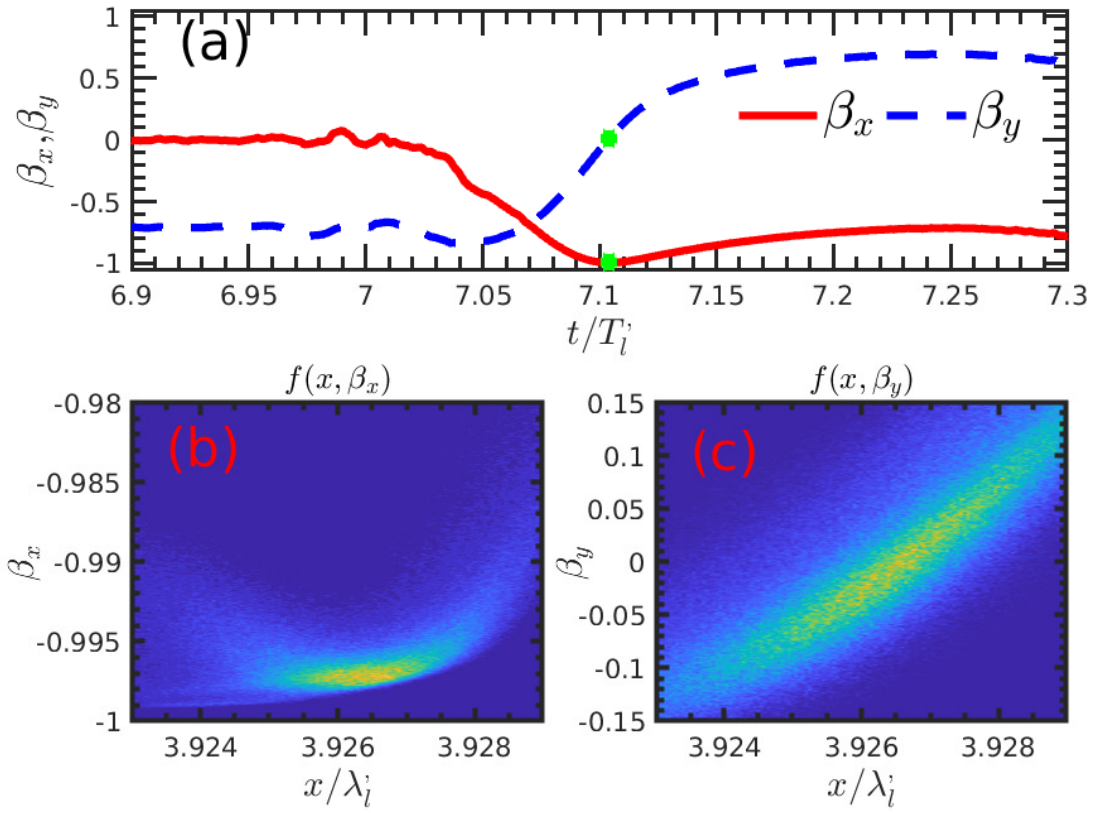

Figure 5.5: 1D PIC simulation for the 2nd pulse in Fig. 5.2. (a) Velocity (β_x, β_y) of the plasma current along the retardation path of 2nd pulse in Fig. 5.2. Phase -space distributions $f(x,\beta_x)$ (a) and $f(x,\beta_y)$ (b) of the electrons in the surface layer at instant of the emission (green stars). The distribution functions are normalized as: $f_{\max}(x,\beta_x)=1$, $f_{\max}(x,\beta_y))=1$. Same parameters as in FIg. 5.4

shown). The phase mismatch in lower frequency regions may come from the interference with the emissions from ROM/CWE. Combining with Eq. 3.19, we can obtain that:

$$\psi_{A_m} = -0.12\pi \quad \text{for 2nd Pulse}, \tag{5.6a}$$
$$\psi_{A_m} = -0.06\pi \quad \text{for 3rd Pulse}. \tag{5.6b}$$

In the ultrahigh frequency region, the phase fluctuation occurs. This phase fluctuation, $\psi_f(\omega) \sim 2\pi\Delta x/\lambda_\omega$, originates from the finite extension of the surface layer and may reflect the incoherence of the high frequency emission from different part of the layer if $\lambda_\omega \lesssim \Delta x$. We verify this by calculating the layer thickness Δx and observing the threshold of the phase fluctuation

$$\omega_f^{th} \approx \frac{2\pi c}{\Delta x} \tag{5.7}$$

in the simulations. As shown in Fig. 5.6, the thickness of the electron layer is about $\Delta x \approx 0.002\lambda_l'$, which corresponds to the phase fluctuation threshold $\omega_f^{th} \approx 400\omega_l$ for the 2nd pulse in Fig. 5.3 (b). The appearance of this fluctuated phase truncates the coherent spectra of the attosecond pulses in high-frequency region.

In order to further confirm our theoretical model, we try to reproduce the 2nd and

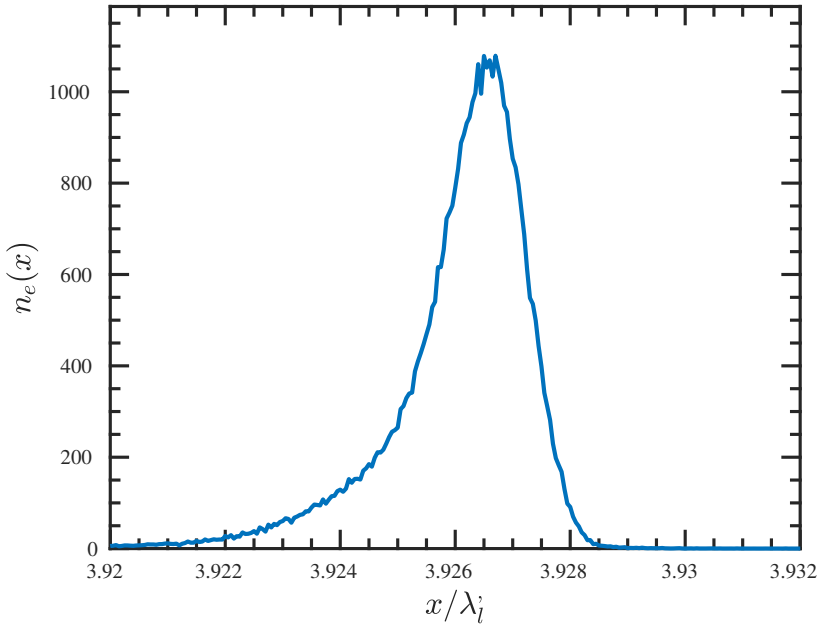

Figure 5.6: 1D PIC simulation for the 2nd pulse in Fig. 5.2. Density distribution $n_e(x)$ of the electron filling the conditions: $\beta_x < -0.995$ and $\beta_y < |0.025|$.

3rd attosecond pulses in Fig. 5.2 with parameters from Eqs. (5.5), (5.6) and choose

$$\bar{A}_m = \quad 52 \quad \text{for 2nd Pulse}\,, \tag{5.8a}$$

$$\bar{A}_m = 112 \quad \text{for 3rd Pulse}\,. \tag{5.8b}$$

Inserting into Eq. (5.2), the 2nd pulse can be precisely reproduced in Fig. 5.2 (c), (d) for $\omega_f = 60\omega_l$ and the 3rd pulse in Fig. 5.2 (e), (f) with slight difference. With such accurate agreements, we can completely confirm that the 2nd and 3rd pulses are emitted by the surface electron layer within our analytical model in Sec. 3.1.

In order to estimate the amplitude of the attosecond pulse A_m, we have to go to the deep insight of the electron layer at the emission instant. In Fig. 5.5 (a), we plot the velocity (β_x, β_y) of the plasma current along the retardation path of the 2nd pulse in Fig. 5.4 (b). The emission instant is labeled with the green stars, which further confirms the conditions for our pulse emission model in Sec. 3.1. At the emission instant, the phase-space distribution of the electrons in the layer are also plotted in Fig. 5.5 (b) $f(x, \beta_x)$ and (c) $f(x, \beta_y)$. As shown, the electrons in the surface layer have the backward velocity $\beta_x \approx -1$ and the transverse velocity $\beta_y \approx 0$, corresponding the Lorentz factor,

$$\gamma = \frac{1}{\sqrt{1-\beta_x^2-\beta_y^2}} \approx \frac{1}{\sqrt{1-\beta_x^2}} \approx 13\,. \tag{5.9}$$

Simultaneously, the electrons in the layer have a spread phase space, especially in $f(x, \beta_y)$. We assume the emitted pulse is synthesized by the radiation from the electrons with conditions: $v_x < 0.995$ and $|v_y| < 0.025$ in the phase space. In Figure.5.6, the density distribution $n_e(x) = \int f(x, \beta_x, \beta_y) d\beta_x d\beta_y$ of the electrons under the conditions

are presented. We integrate the electron density,

$$n_{el} = \int n_e(x)dx \approx 8.7\,. \tag{5.10}$$

Therefore, we can have the estimation for the amplitude of the 2nd pulse[1]:

$$\bar{A}_m \approx n_{el}\gamma/2 \approx 57\,. \tag{5.11}$$

which is very close to the value in Eq. (5.8) (a).

5.2.3 Robust plasma gating

This plasma gating mechanism is very robust and can work for the most general situation. In this section, we show the action of plasma gate with different laser ramping front, plasma gradient and laser CEP. The filtering frequency is fixed to be $\omega_f = 60\omega_l$ for all the cases here.

Fig. 5.7 (a), (b) show the action of plasma gate with different laser ramping front. As shown, the laser with a longer ramp results in a weaker attosecond pulse. This may be because the plasma target is warmed by the laser ramping field before the main pulse emitted. One can also see that the longer laser ramp reduces the action of plasma gate with a relatively larger attosecond pulse emission after the main one, but the ratio of the pulse intensities is still larger than one magnitude. For these cases, a single attosecond pulse can be isolated by plasma gating. If we keep increasing the laser ramping front, the action of plasma gate would be worse, more attosecond pulses would be emitted during the interaction of laser ramp with plasma.

In Fig. 5.7 (c) and (d), we show the action of plasma gate with different plasma gradient. As one can see, the isolated attosecond pulse has the largest intensity at $L = \lambda_l/8$. This can be understood in the following way: for a very long plasma gradient, the plasma wave and instabilities are excited in the interaction, which increases the laser energy absorption and perturbs the dynamics of the electron layer. Both could decrease the energy for pulse emission; For a steep gradient, the amplitude of the plasma surface oscillation is smaller which reduces the energy storage in the plasma charge separation field and thus results in less energy conversion for pulse emission (see Sec. 3.3). The largest pulse emission comes from a suitable plasma pre-gradient which balances the excitation of the plasma wave and the efficiency of the energy conversion to pulse emission. This result is in line with the result in Ref. [59] for plasma HHG. Moreover, for the long plasma gradient ($L = \lambda_l/6$), a strong subpulse is emitted which would lead to the large spectral and phase oscillations in the low-frequency region as discussed in Sec. 5.3.2, and weaken the plasma gating effect. For other shorter plasma gradients, plasma gating scheme works very well.

In Fig. 5.7 (e) (f), we show the action of plasma gate with different laser CEP. As shown, the laser CEP could also change the attosecond pulse intensity by modulating the laser-plasma interaction before the main pulse emission. However, the influence of laser CEP on the plasma gating scheme is slight, which would be very important for the ultra-intense laser-plasma experiments with unstable CEP, and could avoid the shot-to-shot

[1] Here, we normalize all the quantities in the simulation reference as shown in Figs. 5.4, 5.5, 5.6, thus the angle factor in Eq. (5.3) donot need to be included. This normalization cannot affect the value of the normalized electric field in lab reference, since it is Lorentz invariant see Appendix A.4. Moreover, the temporal variation of $A_m(t)$ is neglected which may result in the difference between the estimated value in Eq. 5.10 and the value in Eq. 5.8, see the definition of $\bar{A}_m$ in Eq. 3.16.

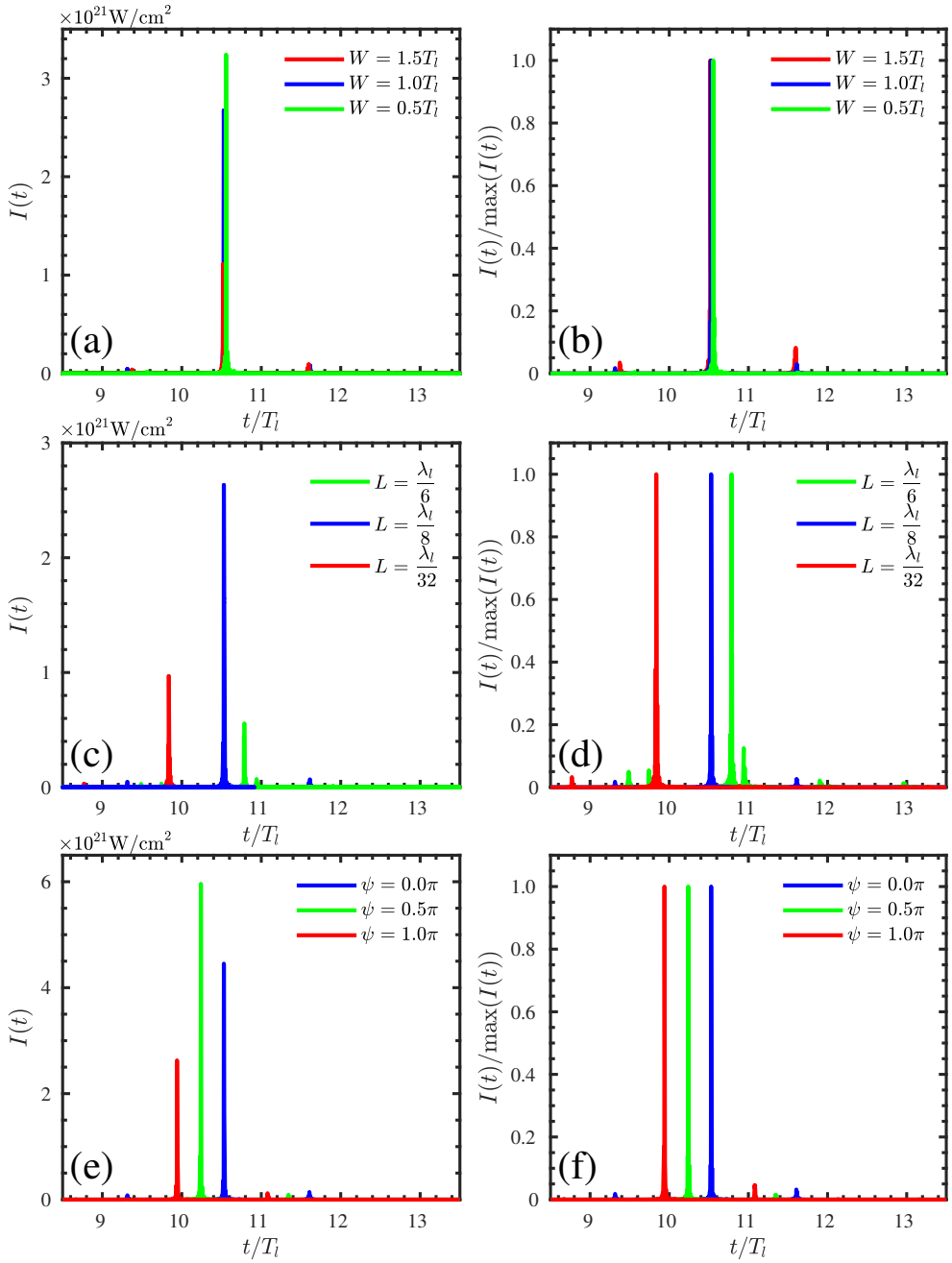

Figure 5.7: 1D PIC simulations of HHG for attosecond pulse generation with filtering frequency $\omega_f = 60\omega_l$. The laser $a(t) = a_0 \sin(\omega_l t + \phi)(\tanh((t-T_s)/W) - \tanh((t-T_e)/W))/2$, radiates the plasma ($n_e = n_c/2\exp(x/L)$) with incident angle $\theta = \pi/4$, where $a_0 = 100$, $T_s = 6T_l$, $T_e = 14T_l$, $\lambda_l = 0.8\mu m$, W is the laser ramping parameter, ϕ is laser CEP, and L is plasma gradient parameter, The field detector is located at $3\lambda_l$ from the plasma surface. (a) (b) Different laser ramping front W for gold plasma (Au, $Z = 79$, $A = 197$) with bulk density $n_0 = 500n_c$, $L = \lambda_l/8$, $\phi = 0.0$. (c) (d) Different plasma gradient L. for gold plasma (Au, $Z = 79$, $A = 197$) with bulk density $n_0 = 400n_c$, $W = 1.0T_l$, $\phi = 0.0$. (e) (f) Different laser CEP ϕ. for carbon plasma (Ca, $Z = 6$, $A = 12$) with bulk density $n_0 = 500n_c$, $W = 1.0T_l$, $L = \lambda_l/8$. (a) (b) (c) show the obtained attosecond pulses intensity in lab reference. (d) (e) (f) show the attosecond pulse with normalized intensity.

changes [146].

5.2.4 Discussion

With the simulation results and analytical calculations, we can obtain a comprehensive understanding of the plasma gating.

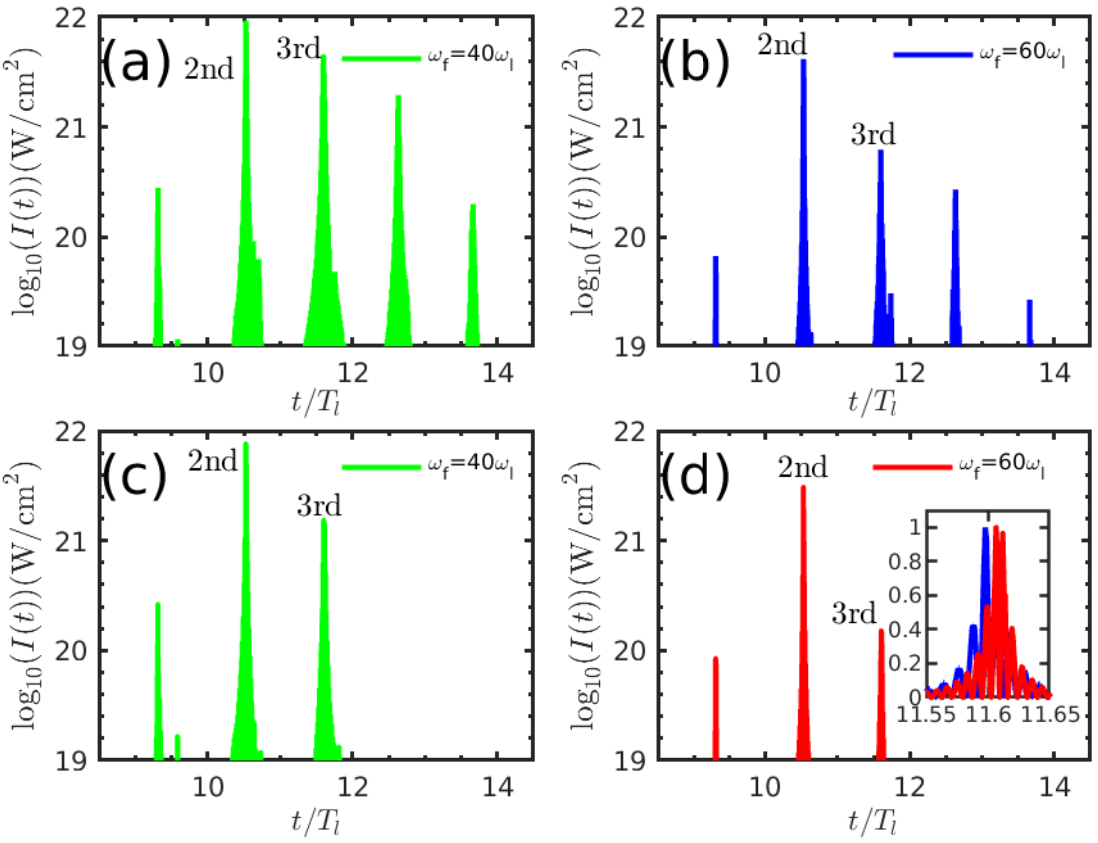

Figure 5.8: 1D PIC simulations for attosecond pulse generation with different filter frequencies ω_f: (a) (c) $\omega_f = 40\omega_l$, (b) (d) $\omega_f = 60\omega_l$. (a) (b) are for the case without ion motion, and in (c) (d), we repeat the results in Fig. 5.2 (a) (b) but with logarithm axis for mobile ion case. Same simulation parameters as in Fig. 5.2. we zoom in the time axis and compare the 3rd pulses in (b), (d) with normalized intensity in the inset of (d).

As discussed in Sec. 3.1, the pulse amplitude $\bar{A}_m \propto \gamma$ and spectral decay $1/\omega_d \propto \gamma^{-2}$ depend sensitively on γ which is determined by the backward acceleration of the electron layer due to the charge separation field (see Sec. 3.3). With hole-boring motion, the charge separation is mitigated because the Doppler effect decreases the laser pressure, and part of the energy in the electrostatic field is absorbed by mobile ions. The layer acceleration thus would be restricted by the hole-boring effect, leading to a smaller amplitude and faster decay of the 3rd pulse, for which the hole-boring velocity is pronounced. Moreover, the forward hole-boring motion inevitably spreads the structure of the backward-moving electron layer and thus reduces the phase fluctuation threshold ω_f^{th}, which shortens the coherent phase interval and further decreases the 3rd pulse amplitude. Essentially, the hole-boring effect isolates the 2nd pulse via suppressing the coherent emission for the 3rd pulse.

To demonstrate the isolating effect of the hole-boring motion, we present the attosec-

ond pulses from the case without ion motion in Fig. 5.8(a), (b) and compare with the results in (c), (d) for the case with ion motion. For fixed-ion case in Fig. 5.8 (a) and (b), one expects a train of attosecond pulses (only five are shown). Here the 1st pulse arises also due to the reflection of the laser pulse with the plasma pre-gradient present at the target surface while the other pulses are generated due to peak of the laser interacting with the main target and have decaying intensities. This decay in the intensity is not so pronounced and the intensities of the two adjacent pulses are not more than an order of magnitude different from each other, For example, $I_2/I_3 = 2.04$ for $\omega_f = 40$ in (a), $I_2/I_3 = 6.61$ for $\omega_f = 60$ in (b). Hence, it becomes difficult to isolate a single attosecond pulse from this train. However, one can clearly see "Plasma Gate" in action in Fig. 5.8 (c) and (d) where one takes the ion motion into account and the hole-boring effects are dominant. No strong attosecond pulse ($I < 10^{19}$ W/cm^2) is emitted after the 3rd one. One can notice that a higher-cut-off frequency in (d) ($\omega_f = 60$) yields an intense single attosecond pulse (the 2nd one) as it's intensity is more than an order of magnitude higher than the other pulses, *i.e.* $I_2/I_3 = 31.13$. Hence, this pulse can be easily isolated from the other two pulses.

Comparing the pulses in Fig. 5.8 (d) with the pulses in Fig. 5.8 (b) respectively, we can find that the 1st pulses (before 2nd one) are same since both come from the laser rising front interacting with the plasma pre-gradient; The 2nd pulses are also similar, except in Fig. 5.8 (d) the 2nd pulse is sightly weaker than that in Fig. 5.8 (b). This may be because the hole-boring motion starts during the 2nd pulse emission; The obvious difference appears for the 3rd emission. In the cycle, the hole-boring velocity is pronounced, ion motion reduces the energy storage in the energy conversion process (see Sec. 3.3)) and decreases the partitions of the stored energy for electron layer acceleration. To show the hole-boring motion, we zoom in the time axis and compare the 3rd pulses in Fig. 5.8 (b), (d) with normalized intensity in the inset of Fig. 5.8 (d). As we can see, there is an obvious time delay for the 3rd pulse in Fig. 5.8 (d) (red line), which clearly manifests the hole-boring motion during the pulse emission. We cannot observe this time delay between the 2nd pulses.

To understand how the hole-boring effect isolates the attosecond pulse, we compare the pulse spectra and the spectral phase in the cases with mobile and immobile ions, wherein a slow and almost pure hole-boring effect is in action. As shown in Fig. 5.9 (a), the decay of the pulse spectra becomes faster and faster for the mobile-ion case, while in Fig. 5.9 (b) for the immobile case, the pulse spectra sustain the same decay. This is in line with our discussion in Sec, 3.3: the hole-boring effect reduces the energy storage in the charge separation field and thus decreases the energy conversion to the high-frequency emissions. In Fig. 5.9 (c), the more phase fluctuation is induced in the emitted pulses with hole-boring effect than that in Fig. 5.9 (d) for immobile case. The hole-boring effect extends the spatial distribution of the electron layer, thus takes down the threshold ω_f^{th} of the incoherent emission.

Another effect also contributing to the pulse isolation is plasma heating. It expands the layer and decreases the number of electrons for coherent emission. In Fig. 5.9 (b), the subsequent pulses have the same spectral decay as the 1st one but weaker intensity. This is because the pulse emission process is roughly repeatable since ions are fixed, but the layer compression becomes less in longer time interaction. In Fig. 5.9 (d), the phase fluctuation threshold is also reduced by thermal expansion.

With oblique incidence and long plasma pre-gradient in Fig. 5.2, the plasma heating is more considerable with the re-injection of Brunel electrons [60] which could severely disperse the layer structure making larger phase fluctuations in the pulse, and hinder

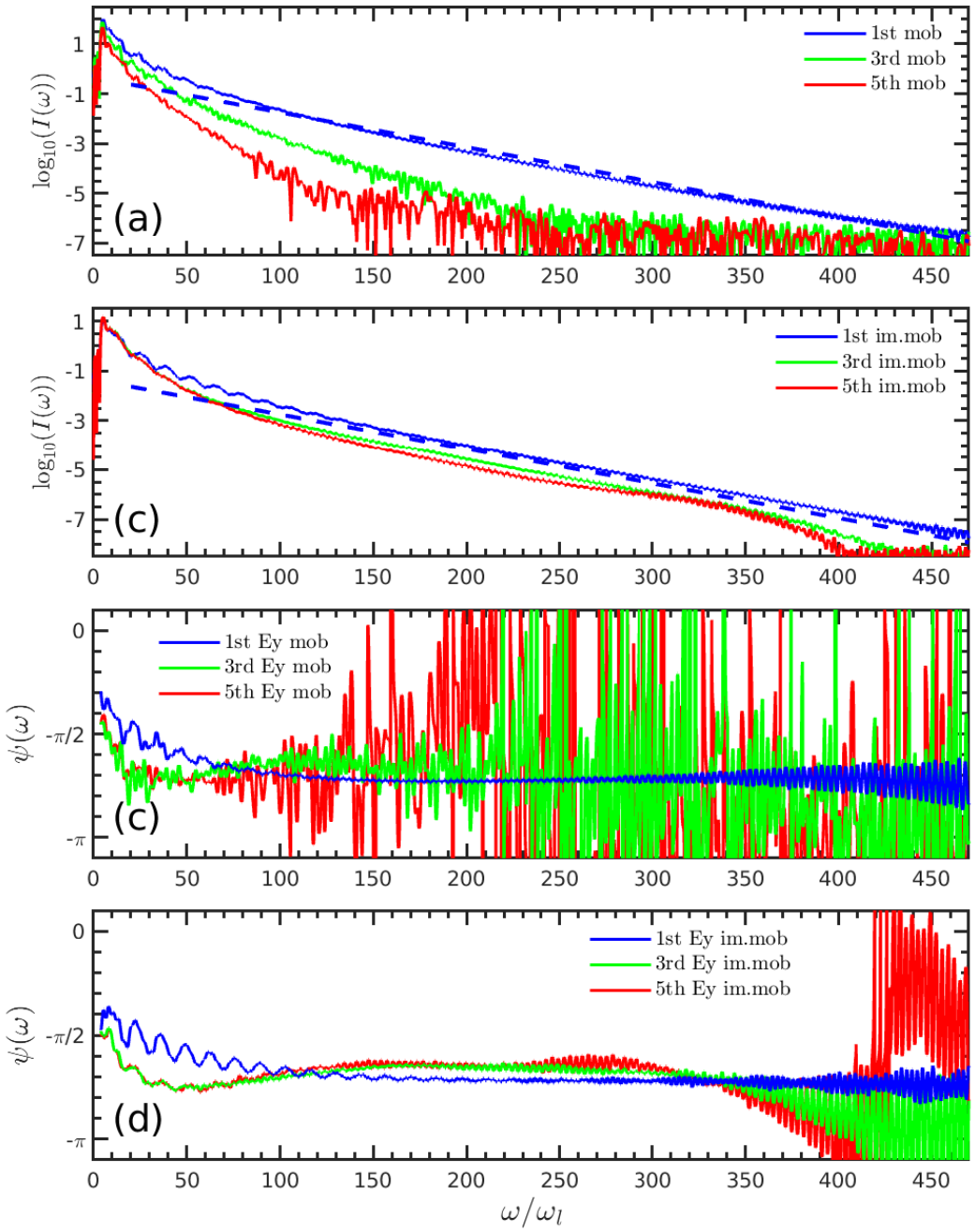

Figure 5.9: Intensity spectra (a) (b) and the corresponding spectral phase (c) (d). (a), (c) correspond to the case with mobile ions and (b), (d) immobile ions. The blue dashed lines are the spectral fitting for the 1st pulses in both cases. The laser, $a_0 = 40$ with step-like temporal profile, radiates normally on the plasma ($n_0 = 200n_c$, $L = 0$), and the laser duration is long enough to emit the 5th pulse.

the layer acceleration decreasing the pulse emission. Both of these can also induce a weaker isolating effect in the pulse train as shown in Fig. 5.8(a) and (b).

For the 1st pulse in Fig. 5.2, the plasma heating is also strong in the interaction of the laser ramp with plasma pre-gradient. A well-defined electron layer can't be formed because of the weak laser intensity in the ramp and thermal expansion, leading to weaker intensity in Fig. 5.3 (a) and large phase fluctuations in Fig. 5.3 (b).

Based on above discussions, we can know that the hole-boring effects mainly contribute to the plasma gating and isolates the 2nd pulse in Fig. 5.2 with the most efficient high-frequency emission and the widest coherent phase interval. The plasma heating effects could also assist the plasma gating via thermally expanding the electron layer for the subsequent pulse emissions.

5.3 Phase property

Phase property is one of the crucial aspects for single attosecond pulse generation. An isolated attosecond pulse with a constant spectral phase is essential for the temporal resolution of attosecond pump-probe experiments. The unstable spectral phase can extend the pulse duration and make it significantly larger than the Fourier transformation limit. However, the analysis of these unstable phase can provide the deep insight into the pulse emission process.

With the results in Fig. 5.2 (b), the spectral phase of the isolated pulse (2nd pulse) can, in principle, be divided into three regions with different properties:

1. $100\omega_l \lesssim \omega \lesssim 400\omega_l$: constant phase.
2. $\omega \lesssim 100\omega_l$: oscillating phase in low-frequency region.
3. $\omega \lesssim 400\omega_l$: fluctuated phase in high-frequency region.

Below, the phase properties in the three regions are discussed separately.

5.3.1 Constant spectral phase

As predicted in our theoretical model in Sec. 3.1.2 and validated with the simulation results in Fig. 5.3 and 5.9, the attosecond pulse has a constant spectral phase for a rather long frequency interval. This constant phase is determined by the dynamics of the well-defined electron layer during the emission, and slightly perturbed by the temporal variation of pulse amplitude $A_m(t)$. In ultra-intense ultra-short laser-plasma experiments, the laser CEP has a significant impact on the interaction physics [146, 147]. However, generation of an ultra-short and ultra-intense laser pulse with a stabilized CEP is difficult in experiments leading to shot-to-shot changes [146]. Here, we highlight the spectral phase stabilization from the unstable laser CEP.

In Fig. 5.10, we present the spectral phase in magnetic fields (a) and electric fields (b) of the attosecond pulses in Fig. 5.7 (e). As we can see, with the laser CEP scanning from $\phi = 0.0\pi$ to $\phi = 1.0\pi$, the constant spectral phase in the region ($100\omega_l \lesssim \omega \lesssim 300\omega_l$) has a rather small change within $\Delta\psi \approx 0.1\pi$. This implies that with an appropriate frequency filter $\omega_f \approx 100\omega_l$, the obtained attosecond pulse has a quasi-constant spectral phase extending to a bound ($\omega \sim 500$eV), which is very important for the applications of the attosecond pulse in experiments avoiding shot-to-shot changes [146].

During the pulse emission, the plasma transverse current changing its sign regulates the pulse structure to be a quasi odd function (see Eq. 3.8) which locks the pulse spectral

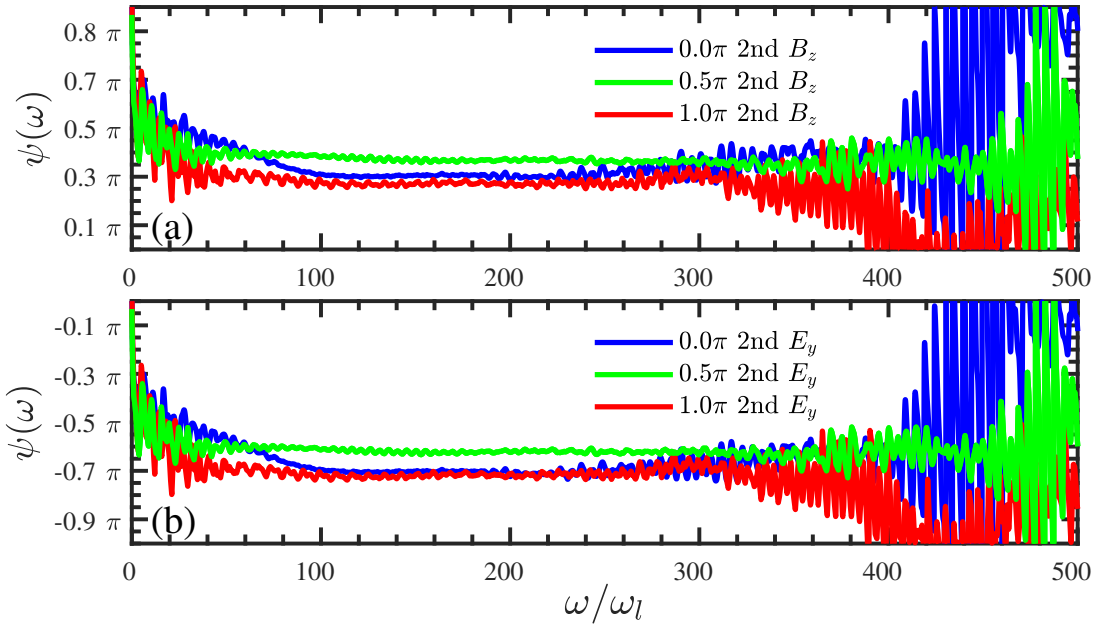

Figure 5.10: 1D PIC simulations of HHG for attosecond pulse spectral phase. The spectral phase of the attosecond pulses generated by the lasers with different laser CEP are shown in (a) magnetic field and (b) electric field corresponding to the attosecond pulses in Fig. 5.7 (e). As one can see, $\psi_B - \psi_E = \pi$ as propagating in $-x$ direction. The laser has the temporal profile $a(t) = a_0 \sin(\omega_l t + \phi)(\tanh((t-T_s)/W) - \tanh((t-T_e)/W))/2$, ψ is laser CEP.

phase to be $\pm\pi/2$. On the other hand, with the very larger backward velocity $\beta_x \approx -1$, the pulse duration, $T_d = 2/\omega_d$, is extremely shortened, limiting the temporal variation of $A_m(t)$ and also the constant phase shift $\psi_{A_m} \sim A_m^1/(A_m^0\omega_d)$ (See Eq. 3.20). Hence, the spectral phase of the isolated attosecond pulse approximates to be a constant, *i.e.* $\psi = \pm\pi/2 + \psi_{A_m} \approx \pm\pi/2$, in the ultra-intense laser-plasma interaction.

We can also see that even though the constant spectral phase is approximately independent on the laser CEP, the coherent spectral interval can be extended to higher-frequency region ($\omega_{th}^f \approx 450\omega_l \approx 700$ev) with a well controlled laser CEP ($\phi = \pi/2$), as the laser CEP has larger influence on phase fluctuations in high-frequency region and also phase oscillations in low-frequency region.

5.3.2 Phase oscillation in low-frequency region

In Figs. 5.3, 5.9 and 5.10, the spectral and phase oscillation in low-frequency region are clearly presented. This oscillation corresponds to a double-pulse structure in one emitted pulse.

In Fig. 5.11 (a), we zoom in the structure of the 2nd pulse in Fig. 5.2 (a) and find that it consists of a main pulse E_y^m and a sub-pulse E_y^s:

$$E_y(t) = E_y^m(t) + E_y^s(t - \Delta t) \tag{5.12}$$

where the amplitude of the main pulse is orders of magnitude larger than the amplitude of the sub-pulse, *i.e.* $E_y^m(t) \gg E_y^s(t)$, and $\Delta t \approx 0.18T_l$ is the time separation.

In Fig. 5.4 (b), we plot the contour of the evolution of the electron density and show that a secondary electron bunch [148] is formed behind the first electron layer. Here in

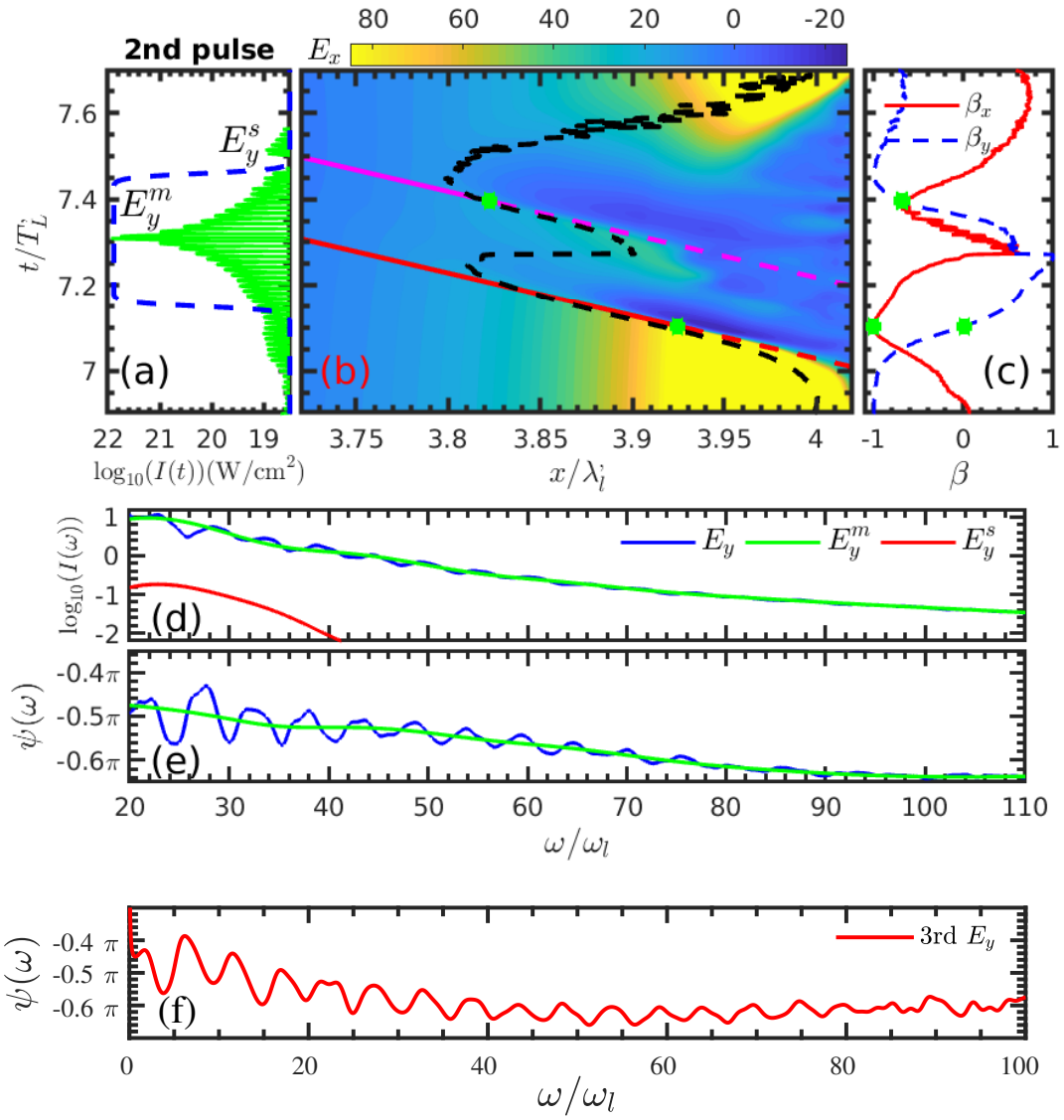

Figure 5.11: (a) Temporal shape of the 2nd pulse in Fig. 5.2 (a) shifted along the retardation relation. The temporal window (blue dashed line) is used to exclude the sub-pulse pulse (b) Evolution of the longitudinal electric field E_x at the plasma surface around the emission of the 2nd pulse overlaid with the retardation paths of the pulse centers (red and magenta lines). The evolution of the electron surface ($n_e = a_0 n_c'$) is also shown (black dashed line). (c) Velocity (β_x,β_y) along the electron surface. (d) Spectra of the main pulse (green line) and sub-pulse (red line). (e) Spectral phase of the main pulse (green line). The spectrum and spectral phase in Fig. 5.3 of the 2nd pulse in the low frequency region are repeated in (d) and (e) respectively. The spectral phase of the 3rd pulse in Fig. 5.3 is also zoomed in for (f). Same parameters as in Fig. 5.4.

Fig. 5.11 (b), we repeat the evolution of the electron surface (black dashed line) as in Fig. 5.4 (b) and overlay the retardation paths of the two pulses, which confirms that the sub-pulse is certainly emitted by the secondary electron bunch. In Fig. 5.11 (b), we also replace the density evolution in Fig. 5.4 (b) with the evolution of the longitudinal electric field E_x. As we can see, a positive electric field is generated when the first electron layer is moving away from the target [148]. The secondary electron bunch is clumped by this electric field E_x and accelerated to radiate the sub-pulse with a much slower backward velocity, since this electric field is much weaker than the accelerating field in front of the first electron layer. Therefore, the intensity of the high frequency emission in the sub-pulse is significantly lower than that in the main pulse as shown in Fig. 5.11 (d).

By artificially excluding the sub-pulse with the temporal window (blue dashed line in Fig. 5.11 (a)), one can see that in Fig. 5.11 (d) (e) the main pulse has no spectral and phase oscillations while the whole 2nd pulse which is a superimposition of the two pulses shows the oscillations.

To describe the oscillation analytically, we calculate spectral and phase oscillations in the whole pulse from the double pulse interference:

$$|E_y(\omega)|\, e^{i\psi(\omega)} = \left|E_y^m(\omega)\right| e^{i\psi_m(\omega)} + \left|E_y^s(\omega)\right| e^{i\psi_s(\omega)} e^{i\omega\Delta t} \tag{5.13}$$

where $|E_y^{m,s}(\omega)|$ denotes the modulus of the different frequency components and $\psi_{m,s}$ is the spectral phase of each pulse. We can obtain

$$\begin{aligned} |E_y(\omega)|^2 &= \left|E_y^m(\omega)\right|^2 + \left|E_y^s(\omega)\right|^2 + 2\left|E_y^m(\omega)\right|\left|E_y^s(\omega)\right|\cos(\vartheta) \\ &= \left|E_y^m(\omega)\right|^2 \left(1 + 2\frac{\left|E_y^s(\omega)\right|}{\left|E_y^m(\omega)\right|}\cos(\vartheta) + \frac{\left|E_y^s(\omega)\right|^2}{\left|E_y^m(\omega)\right|^2}\right), \end{aligned} \tag{5.14}$$

where

$$\vartheta(\omega) = \psi_s(\omega) - \psi_m(\omega) + \omega\Delta t\,. \tag{5.15}$$

Here we only keep the first order of approximation for $\left|E_y^s(\omega)\right| / \left|E_y^m(\omega)\right|$, since $E_y^m(t) \gg E_y^s(t)$, thus we can have:

$$I(\omega) = |E_y(\omega)|^2 \approx \left|E_y^m(\omega)\right|^2 \left(1 + 2\frac{\left|E_y^s(\omega)\right|}{\left|E_y^m(\omega)\right|}\cos(\vartheta)\right) \tag{5.16}$$

In order to calculate the phase oscillation, we also start from Eq. (5.13) and show the analytical calculation below:

$$\begin{aligned} e^{i\psi(\omega)} &= e^{i\psi_m(\omega)} \frac{\left|E_y^m(\omega)\right| + \left|E_y^s(\omega)\right| e^{i\vartheta}}{|E_y(\omega)|} \\ &= e^{i\psi_m(\omega)} \frac{\left|E_y^m(\omega)\right| + \left|E_y^s(\omega)\right|\cos(\vartheta) + i\left|E_y^s(\omega)\right|\sin(\vartheta)}{|E_y(\omega)|} \\ &= e^{i\psi_m(\omega)} \left[\cos(\phi_{ms}) + i\sin(\phi_{ms})\right] \end{aligned} \tag{5.17}$$

where we have the new quantity as:

$$\cos(\phi_{ms}) = \frac{\left|E_y^m(\omega)\right| + \left|E_y^s(\omega)\right|\cos(\vartheta)}{|E_y(\omega)|} \approx 1\,,$$
$$\sin(\phi_{ms}) = \frac{\left|E_y^s(\omega)\right|\sin(\vartheta)}{|E_y(\omega)|} \approx \frac{|E_y^s(\omega)|}{|E_y^m(\omega)|}\sin(\vartheta)\,.$$

The first order approximation has also be done for the calculation of ϕ_{ms}. Thus, we can reach the phase oscillation:

$$\psi(\omega) = \psi_m(\omega) + \phi_{ms} \approx \psi_m(\omega) + \frac{|E_y^s(\omega)|}{|E_y^m(\omega)|}\sin(\vartheta)\,. \tag{5.19}$$

From Eq. (5.15), we can know that the spectrum and phase oscillate qualitatively with the frequency

$$\omega_t = \frac{2\pi}{\Delta t} \approx 5.56\omega_l\,, \tag{5.20}$$

which matches very well with the simulation results in Fig. 5.11 (d), (e). Fig. 5.11 (f) shows the phase oscillation with frequency $\omega_t = 5.26\omega_l$ for 3rd pulse, which corresponds to the pulse separation $\Delta t \approx 0.19T_l$ as clearly shown in Fig. 5.4 (e).

From Eqs. (5.16) and (5.19), we can also see that the oscillating amplitude is proportional to $|E_y^s(\omega)|/|E_y^m(\omega)|$ which attenuates for higher frequency because of the less efficient high frequency emission from the secondary electron bunch.

We wish to stress that this oscillation is the consequence of the interference between the double pulses, which is essentially different from the plasma-wave modulation in harmonic emission spectrum of the total reflection [43–45]. In order to get an attosecond pulse with a constant phase, a high frequency filter is needed to overcome the phase oscillation.

5.3.3 Phase fluctuation in high-frequency region

In the high-frequency region, the phase fluctuation occurs. This phase fluctuation originates from the incoherent emissions ($\lambda_\omega \lesssim \Delta x$) from different part of the electron layer and results in the limit on the interval of the constant spectral phase for coherent emissions.

In order to extend the coherent emission interval to ultrahigh frequency region, an stronger laser pulse ($I \sim 10^{23}\,\mathrm{W/cm^2}$) with shorter ramp is used to compress the electron layer narrower. As shown in Fig. 5.12 (a), the phase fluctuation threshold ω_f^{th} is clearly improved, because the electron layer is further compressed $\Delta x \sim (n_e a_0)^{-1/3}$ [18] by the extremely strong laser. Here the 1st pulse is the strongest because no laser ramp exists. As we can see, the coherent emission interval is extended to the ultrahigh region with $\omega_f^{th} \approx 1000\omega_l \approx 1.5\mathrm{keV}$.

In this ultra-relativistic case, the radiation reaction (RR) force would also be important. As shown in Fig. 5.12 (a), RR force reduces the phase fluctuation in ultrahigh-frequency region. This may suggest the role of RR force in further compressing the electron layer. During the backward acceleration, RR force, $f_{RR} \propto (1 - v_x)^2|E_y^i|^2$ quenches the hot electrons expansion at the layer front and thus enforces the layer structure for pulse emission.

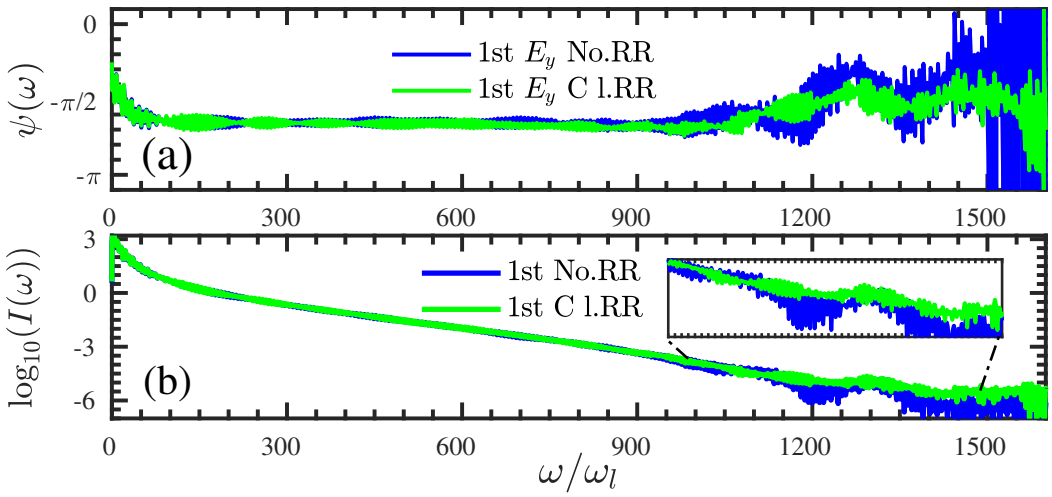

Figure 5.12: 1D PIC simulations of HHG for attosecond pulse spectral phase. Spectral phase (a) and intensity spectrum (b) for the cases with and without RR force. Same parameters in Fig. 5.2 except $a_0 = 250$, $W = 0T_l$, $n_e = 1000n_c$..

One can also see in Fig. 5.12 (b) the emitted pulse with RR force has the same spectral decay as the case without RR force but smaller spectral fluctuation in the region, $\omega > 1000\omega_l$. This may be because the layer collective motion can hardly be impeded by RR force as the laser field can not penetrate deeply into the ultra-dense electron layer. This is in line with the simulation result in Fig. 4.6 (b), wherein the RR force cannot affect the reflection in the first few laser cycle, but can reduce the reflection after a long time interaction when the plasma is effectively heated by the incident laser pulse.

The spectral fluctuation comes from the superposition of the incoherent emissions from the electron layer and the RR force smooths the fluctuation by further compressing the layer structure. With the same spectral decay and smaller phase fluctuation, a stronger attosecond pulse may be synthesized [2].

5.4 Conclusions

In this chapter, we propose a new scheme−plasma gating−for the generation of an isolated ultra-intense phase-stabilized attosecond pulse in the ultra-relativistic regime. The generated pulse with duration $T_d < 20$as is characterized by a stabilized spectral phase $\psi(\omega) \approx \pm\pi/2$ and an ultra-broad exponential spectrum up to keV region bounded by ROM scaling in low-frequency region and CSE scaling in high-frequency region. The unprecedented intensity stemming from an effective energy conversion highlights the potential of the isolated attosecond pulse for performing attosecond-pump attosecond-probe experiments [149, 150].

We first show the existence of the plasma gate by means of particle-in-cell simulations with the most general conditions and then highlight the robustness of this plasma gating scheme with a extensive parametric studies. The analytical model is employed to reproduce the emitted attosecond pulses and validated by the numerical calculations.

[2] In a large part of the simulation results, we can observe the enlargement of the attosecond pulse intensity with the RR force, but in other results, this enlargement is submerged in the numerical noise.

Based on the analytical model and simulation results, the formation of the plasma gating scheme is comprehensively understood: the hole-boring effect mainly contributes to the plasma gate by isolating the most efficient high-frequency emission within one laser cycle

Moreover, the phase properties of the isolated attosecond pulse are extensively discussed. The phase oscillation in low-frequency region stems from the double-pulse structure and attenuates at higher frequencies. The frequency of this oscillation is calculated analytically and validated with the simulation results. Above the region of oscillation, the pulse spectral phase is locked to be $\psi = \pm\pi/2 + \psi_{A_m} \approx \pm\pi/2$ by the dynamics of the surface electron layer. This constant spectral phase is approximately independent on the laser CEP and truncated in high-frequency region by the phase fluctuation, which originates from the incoherent emissions from the electron layer. This phase fluctuation is reduced by radiation reaction force in the ultra-relativistic regime.

Chapter 6

Summary and outlook

Summary

High-order harmonic generation and attosecond pulse emission are like the two sides of the same coin. On one hand in the frequency domain, harmonic spectra are the consequence of the interference among a train of attosecond pulses. On the other hand in the time domain, attosecond pulses come from the superposition of a larger group of harmonic waves.

In this thesis, we set out our investigation from both sides to study the plasma high harmonic generation via laser-plasma interaction in the ultra-relativistic regime, $a_0 \gg 1$. In this regime the inevitable hole-boring effect, induced by the extremely strong laser ponderomotive force, tends to strongly affect the spectra of harmonics and the intensities of attosecond pulses.

We first give an extensive introduction in Chapter 1 to the historical evolution of the laser intensity, basic properties for the physics of laser-plasma interaction, and high harmonic generation with gaseous and solid targets. In particular, we associate the different harmonic generation mechanisms in both gaseous and solid targets with the evolution of the laser intensity.

We then introduce the theoretical background for this thesis in Chapter 2. From the relativistic plasma fluid equation and plasma current radiation, we review the basic viewpoints of plasma high harmonic generation and give the general selection rules for plasma harmonics. Afterward, we discuss the typical piston model for the hole-boring effect and highlight the correction from hot-electron generation.

In Chapter 3, we develop a new analytical model for pulse emission from a well-defined electron layer compressed by the extremely strong laser ponderomotive force at the interface of the laser-plasma interaction. The pulse emission occurs at the node where the layer transverse momentum changes its sign and the backward velocity approaches its maximum. In this model, the exponential spectrum and the constant spectral phase of the emitted pulse are analytically derived and, more importantly, an analytical description for the attosecond pulse is given and validated via particle-in-cell simulations. The energy conversion process underpinning the pulse emission is also analytically analyzed and confirmed with simulation results. Moreover, detailed comparisons to the previous models are provided numerically and analytically.

After this, we carry on our study from the side of high harmonic generation in Chapter 4. In the ultra-relativistic regime, the hole-boring effect widens the harmonic peaks, leading to a quasi-continuous spectra in high-frequency region. We analytically analyze this widening and validate it by particle-in-cell simulations. Based on the simulation results and physical considerations, we constitute the parameter maps (plasma density vs laser intensity) highlighting the optimum regions for generating a single intense attosecond pulse and coherent radiation in the extreme ultraviolet region. These results are important for studies aimed at designing the next generation of short-wavelength

radiation sources by employing plasma high harmonics.

We proceed with our investigation in Chapter 5 from the side of attosecond pulse emission. A robust plasma gating scheme for a single attosecond pulse generation is proposed. Contrary to other schemes, this plasma gating scheme is robust for general situations and works in the ultra-relativistic regime. The hole-boring effect limits the most efficient high-frequency emission in one laser cycle, making it possible to isolate a single attosecond pulse. The isolated pulse has a constant spectral phase, $\psi \approx \pm\pi/2$. This particular locked phase does not depend on the carrier-envelop-phase (CEP) of the laser pulse, but on the dynamics of the well-defined electron layer during the emission when the layer transverse current changes its sign. This spectral phase regulates the pulse structure and results in a minimum at the pulse center, contrary to a synchrotron-like pulse. The unprecedented intensity $I \sim 10^{22}$ W/cm^2 of the isolated attosecond pulse stems from an effective energy conversion process. The isolated pulse is also characterized by an exponential spectrum bounded by ROM-scaling in low-frequency region and CSE-scaling in ultrahigh-frequency region. By improving the laser intensity, the spectrum of the isolated pulse can be coherently extended to keV region. A promising application of this ultra-intense, ultra-broadband attosecond pulse is to investigate the inner-shell electron dynamics in high-Z atoms with attosecond-pump attosecond-probe experiments. The stable phase can enable the experiments with sub-attosecond precision.

Moreover, due to the strongly compressed electron and ion layers at the plasma surface, collisional effects become non-negligible and can reduce the efficiency of high harmonic generation. Furthermore, in the ultra-relativistic laser-plasma interaction, the inclusion of the radiation reaction force is necessary. From our results, the classical radiation reaction force slightly reduces the intensity of the harmonics and smooths the phase fluctuation in high-frequency region.

Outlook

The results in this thesis present the first step, to our knowledge, toward plasma high harmonic generation and single attosecond pulse emission in the ultra-relativistic regime. It may induce further discussions on this topic.

From a numerical point of view, fully dimensional simulations with high resolution are needed. In this thesis, most of the simulations were done in one dimensional geometry for both normal and oblique incidence in order to obtain high enough resolution. For future studies, when the computational resource is further developed, fully dimensional effects on plasma high harmonic generation and single attosecond pulse emission should be investigated. For example, because of the transverse gradient of the laser intensity, the plasma surface could be strongly curved, affecting the dynamics of the surface electron layer and thus the high harmonic generation. The curved surface could also influence the propagation of the harmonic wave and the attosecond pulse, which relates directly to the experimental applications, since large surface curvature leads to focusing of the harmonic wave in the vicinity of the surface and divergence of the harmonic wave at the location far from the surface.

From a physical point of view, a general theory for plasma high harmonic generation is absent. As we introduced in Sec. 1.3.2, different models were proposed for plasma high harmonic generation, but give different spectral properties. The physical reason leading to these differences is not clear. A general theory, from first principle, is needed to cover all the models and point out the dominance of the different models in different parameter regimes. Furthermore, all the models are based on the point of plasma collective current,

which completely ignore the effects of single particle radiation. A theory considering the superposition of the radiation from single particles may reveal more information about the dynamics of harmonic generation and even about other plasma radiations.

Appendix A

Numerical Techniques

A.1 Particle-in-Cell code

In modern physics, computer numerical simulation is an indispensable tool as it bridges the theoretical physics and the experimental physics. Generally, simulation could uncover more details of physical processes, which can hardly be shown directly from experimental result, and is a convenient method to justify the validity of the approximations and assumptions in theoretical derivations.

The numerical description of plasma physics, in general, develops into two different pictures [151]: fluid description and kinetic description. In the fluid picture, the magnetohydrodynamic (MHD) equations [29], which provide the macroscopic information of the plasma and ignore the physical details at the microscopic level, are solved analytically and/or evolved numerically. In the kinetic picture, Vlasov-Fokker-Planck simulation [152–155] and particle-in-cell (PIC) simulation [84] have been developed independently and used to compute the temporal evolution of the plasma phase space $f(t, \mathbf{r}, \mathbf{p})$ self-consistently in an external and internal field,

$$\frac{\partial f}{\partial t} + \mathbf{v} \cdot \nabla_r f + \frac{d\mathbf{p}}{dt} \cdot \nabla_p f = \text{source term}, \tag{A.1}$$

where the source term may come from the collisional effect, radiation reaction force, pair production, ionization and so on. Vlasov-Fokker-Planck simulation solves directly the Vlasov equation A.1, while PIC code recovers the plasma phase space via simulating a collection of so-called pseudo-particles which move in an external field and/or internal field. Vlasov simulation has an advantage in resolving the physics processes which depend sensitively on the tail of the plasma phase space, and its application is technically restricted by the extreme requirement of the computer storage space. The tail of the plasma phase space is difficult to be represented by PIC simulation since the computational time consumption will be largely increased if enough number of pseudo-particles are simulated to accurately resolve the phase-space tail. However, for the physical processes which mainly depend on the bulk of the plasma phase space and/or require higher dimensional calculation, PIC simulation has the great advantages in saving the computational time and also guaranteeing the simulation resolution.

In this thesis, we study the plasma high-order harmonic generation which is determined by the plasma collective current. The single particle effect is imperceptible and can only be conspicuous for ultra-high order harmonics in the keV region. Therefore, we employ the widely used PIC code-EPOCH [83, 84] for all the simulations in this thesis.

The PIC simulation is proceeded as the basic algorithm cycle in Fig. A.1. At the beginning, the simulation is set up in the simulation box with an initial configuration for the laser field, particle distribution, spatial resolution and so on. During the running, the integral of the particle motion equations advances the particle position and momentum

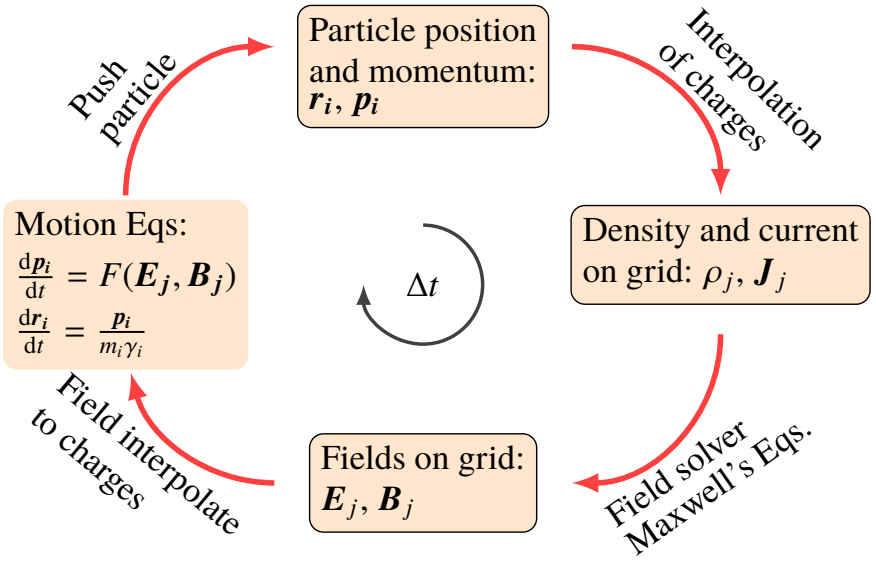

Figure A.1: The basic algorithm cycle of the PIC simulation in one time step Δt [151]. i is the number of the particles, and the grid cells are numbered as j.

$(\mathbf{r}_i, \mathbf{p}_i)$ in the electromagnetic field, which would refresh the charge and current density $(\rho_j, \mathbf{J}_j)$ on the grid. The electromagnetic fields $(\mathbf{E}_j, \mathbf{B}_j)$ are updated by solving the Maxwell's equations with $(\rho_j, \mathbf{J}_j)$ for the advance of particle position and momentum in next time step. After the advance of the particle momentum, the different physical processes, such as collision, photon emission, and pair creation, could be included to modify the particle momentum and influence the current on the grid.

In our work, the classical radiation reaction force is considered according to the Landau-Lifshitz prescription [76]:

$$\begin{aligned}\mathbf{F}_{LL} = &\frac{2}{3}\frac{e^2}{4\pi\varepsilon_0}\frac{e}{mc^3}\gamma\left[(\frac{\partial}{\partial t}+\frac{\mathbf{p}}{m\gamma}\cdot\nabla)\mathbf{E}+\frac{\mathbf{p}}{m\gamma}\times(\frac{\partial}{\partial t}+\frac{\mathbf{p}}{m\gamma}\cdot\nabla)\mathbf{B}\right]\\ &+\frac{2}{3}\frac{e^2}{4\pi\varepsilon_0}\frac{e^2}{m^2c^4}\left[(\mathbf{E}+\frac{\mathbf{p}}{m\gamma}\times\mathbf{B})\times c\mathbf{B}+(\frac{\mathbf{p}}{mc\gamma}\cdot\mathbf{E})\mathbf{E}\right]\\ &-\frac{2}{3}\frac{e^2}{4\pi\varepsilon_0}\frac{e^2}{m^2c^4}\left[(\mathbf{E}+\frac{\mathbf{p}}{m\gamma}\times\mathbf{B})^2-(\frac{\mathbf{p}}{mc\gamma}\cdot\mathbf{E})^2\right]\frac{\gamma\mathbf{p}}{mc}.\end{aligned} \tag{A.2}$$

As we can see, the last term in Eq.A.2 is proportional to γ^2 opposite to the direction of the particle momentum, dominating the radiation reaction force [130]. For ultra-relativistic electrons for which the radiation reaction force is important, the proceeding term in Eq.A.2 is much smaller than the last term because of the missing of γ factor. The term containing the temporal and spatial derivatives is also negligible compared to the dominant term (proportional to γ^2). The ratio between these two terms is approximated [130]:

$$\text{Ratio} \sim \frac{\frac{e}{mc^3}\gamma\frac{\partial E}{\partial t}}{\frac{e^2}{m^2c^4}E^2\gamma^2} \sim \frac{\frac{e}{mc^3}\gamma\omega E}{\frac{e^2}{m^2c^4}E^2\gamma^2} = \frac{1}{a_0\gamma} \ll 1 \tag{A.3}$$

where $a_0 = eE_l/(mc\omega_l)$ is the normalized laser electric field. From a numerical point of view, the calculation of the temporal derivative depends on quantities ($\mathbf{E}$, $\mathbf{B}$) at the proceeding and succeeding time steps. This calculation would tremendously increase the computational complexity and also the numerical noise in the simulation. For simplicity, we ignore the terms related to the temporal and spatial derivatives in Eq. (A.2) and only consider the other terms in Eq. (A.4) as the reduced radiation reaction force in the particle motion equation.

$$\begin{aligned}\mathbf{F}^r_{LL} =& \frac{2}{3}\frac{e^2}{4\pi\varepsilon_0}\frac{e^2}{m^2c^4}\left[(\mathbf{E}+\frac{\mathbf{p}}{m\gamma}\times\mathbf{B})\times c\mathbf{B}+(\frac{\mathbf{p}}{mc\gamma}\cdot\mathbf{E})\mathbf{E}\right]\\ &-\frac{2}{3}\frac{e^2}{4\pi\varepsilon_0}\frac{e^2}{m^2c^4}\left[(\mathbf{E}+\frac{\mathbf{p}}{m\gamma}\times\mathbf{B})^2-(\frac{\mathbf{p}}{mc\gamma}\cdot\mathbf{E})^2\right]\frac{\gamma\mathbf{p}}{mc}.\end{aligned} \tag{A.4}$$

In our simulations, the pseudo-particles follow the motion equation as below:

$$\frac{\mathrm{d}\mathbf{p}_i}{\mathrm{d}t} = q_i(\mathbf{E}_j+\frac{\mathbf{p}_i}{m_i\gamma_i}\times\mathbf{B}_j)+\mathbf{F}^r_{LL}(\mathbf{E}_j,\vec{B}_j) \tag{A.5a}$$

$$\frac{\mathrm{d}\mathbf{r}_i}{\mathrm{d}t} = \frac{\mathbf{p}_i}{m_i\gamma_i} \tag{A.5b}$$

A.2 Numerical calculation for phase

In this thesis, we study the spectral phase $\psi(\omega)$ of a single attosecond pulse, which depends only on the pulse emission dynamics. By studying this phase property, one can get deeper insight into the dynamics of the emission system on the attosecond time scale.

Before we present the numerical method for calculation, a clear definition for this pulse spectral phase has to be given. We assume that the attosecond pulse has the waveform $E_w(t)$, and its temporal center is located at t_0. Thus, the pulse electric field can be denoted as $E(t) = E_w(t-t_0)$. The physical meaning of the pulse center will be clarified later.

The pulse properties in time and frequency domain are connected with each other via a simple Fourier transformation:

$$\begin{aligned}\widetilde{E}(\omega) &= \frac{1}{2\pi}\int_{-\infty}^{\infty}E(t)e^{i\omega t}dt\\ &= \frac{1}{2\pi}\int_{-\infty}^{\infty}E_w(t-t_0)e^{i\omega t}dt\\ &= \frac{1}{2\pi}e^{i\omega t_0}\int_{-\infty}^{\infty}E_w(t)e^{i\omega t}dt\\ &= e^{i\omega t_0}\widetilde{E}_w(\omega)\,.\end{aligned} \tag{A.6}$$

Separating the modulus and phase of the frequency spectra, we can have[1]

$$|\widetilde{E}(\omega)|e^{-i\psi(\omega)} = e^{i\omega t_0}|\widetilde{E}_w(\omega)|e^{-i\psi_w(\omega)}\,. \tag{A.7}$$

[1]The sign of $\psi(\omega)$ is chosen to be same with the linear term ωt in $E(t) = \int_{-\infty}^{\infty}|E(\omega)|e^{-i[\omega t+\psi(\omega)]}dt$.

For modulus:

$$|\widetilde{E}(\omega)| = |\widetilde{E}_w(\omega)|\,. \tag{A.8}$$

The intensity spectrum $I(\omega) = |\widetilde{E}(\omega)|^2$ of the pulse is determined by the modulus $|\widetilde{E}_w(\omega)|$ of the waveform.

For phase:

$$\psi(\omega) = \psi_w(\omega) - \omega t_0\,. \tag{A.9}$$

The phase $\psi(\omega)$ of the different frequency component in the pulse electric field depends not only on the phase $\psi_w(\omega)$ from the waveform, but also on a time-shift phase ωt_0. We can polynomially expand $\psi_w(\omega)$ as below:

$$\psi_w(\omega) = \psi_0 + a_1\omega + a_2\omega^2 + a_3\omega^3 + \dots\,, \tag{A.10}$$

where ψ_0 is the absolute phase and plays a role similar to the carrier-envelop-phase. The higher-order terms (ω^n, $n \geq 2$) represent the group delay dispersion causing the pulse expansion and the pulse shape deformation [156]. One can also note the linear term $a_1\omega$, which does not affect the temporal pulse properties and only contributes a time-shift to the pulse.

Here, we define the pulse center at $t_0 = a_1$ to compensate the linear term resulting in a *time-independent* phase:

$$\psi(\omega) = a_0 + a_2\omega^2 + a_2\omega^3 + \dots\,, \tag{A.11}$$

which will not change during pulse propagation.

The *time-independent* phase of each frequency component in a single pulse is termed as *spectral phase* [156] (or atto-chirp [51, 56]). This spectral phase relates closely to the temporal properties of the attosecond pulse, such as duration, intensity and waveform, and is determined by the pulse emission dynamics [56, 71, 157].

The practical calculation of the pulse spectral phase is not convenient since one cannot know the temporal position of the pulse center. To calculate the pulse spectral phase, we start from the discrete Fourier transformation as below:

$$E(t_k) = \sum_{j=0}^{N-1} \widetilde{E}(\omega_j) e^{-i\omega_j t_k}\,, \tag{A.12}$$

where $t_k = t_0 + k\Delta t$, $\omega_j = \omega_0 j$, $T = nT_l = N\Delta t$ is the duration of the pulse, T_l and ω_l are the laser period and frequency, $\omega_0 = 2\pi/T = \omega_l/n$ and Δt are the frequency and temporal resolution, respectively. Rewriting $\widetilde{E}(\omega_j)$ with its modulus and spectral phase:

$$\widetilde{E}(\omega_j) = |\widetilde{E}(\omega_j)| e^{-i\psi(\omega_j)}\,, \tag{A.13}$$

and inserting this into Eq. (A.12), we can get:

$$E(t_k) = \sum_{j=0}^{N-1} |\widetilde{E}(\omega_j)| e^{-i\omega_j \Delta t k} e^{-i\Psi(\omega_j, t_0)}\,, \tag{A.14}$$

here $\Psi(\omega_j, t_0) = \omega_j t_0 + \psi(\omega_j)$ is the *time-dependent* phase which is the straightforward

result via the inverse Fourier transformation:

$$|\widetilde{E}(\omega_j)|e^{-i\Psi(\omega_j,t_0)} = \frac{1}{N}\sum_{k=0}^{N-1} E(t_k)e^{i\omega_j k\Delta t} = \widetilde{E}_r(\omega_j) + i\widetilde{E}_i(\omega_j)\,, \tag{A.15}$$

where we make use of

$$\begin{aligned}
|\widetilde{E}(\omega_j)| &= \sqrt{\widetilde{E}_r^2(\omega_j) + \widetilde{E}_i^2(\omega_j)},\\
\widetilde{E}_r(\omega_j) &= \frac{1}{N}\sum_{k=0}^{N-1} E(t_k)\cos(\omega_j k\Delta t),\\
\widetilde{E}_i(\omega_j) &= \frac{1}{N}\sum_{k=0}^{N-1} E(t_k)\sin(\omega_j k\Delta t).
\end{aligned} \tag{A.16}$$

From Eq. (A.15), we can calculate the *time-dependent* phase $\Psi(\omega_j, t_0)$:

$$\begin{aligned}
\cos[\Psi(\omega_j,t_0)] &= \frac{\widetilde{E}_r(\omega_j)}{|\widetilde{E}(\omega_j)|},\\
\sin[\Psi(\omega_j,t_0)] &= -\frac{\widetilde{E}_i(\omega_j)}{|\widetilde{E}(\omega_j)|}.
\end{aligned} \tag{A.17}$$

To guarantee $\Psi(\omega_j, t_0)$ in $(-\pi, \pi]$, we can do in this way:
if $\sin[\Psi(\omega_j,t_0)] \geqslant 0$

$$\Psi(\omega_j,t_0) = \arccos\left(\frac{\widetilde{E}_r(\omega_j)}{|\widetilde{E}(\omega_j)|}\right). \tag{A.18}$$

if $\sin[\Psi(\omega_j,t_0)] < 0$,

$$\Psi(\omega_j,t_0) = -\arccos\left(\frac{\widetilde{E}_r(\omega_j)}{|\widetilde{E}(\omega_j)|}\right). \tag{A.19}$$

From this calculation, we can get the *time-dependent* phase chirp $\Psi(\omega, t_0)$. To obtain the *time-independent* phase $\psi(\omega)$ from this *time-dependent* phase $\Psi(\omega, t_0)$, we have two different methods:

First one: find the point where $t_0 = 0$. If $t_0 \approx 0$, $\psi(\omega) \approx \Psi(\omega, t_0)$.

For general cases, this method may be impossible, because the field shape in the pulse is erratic. However for our case, this is convenient as the pulse has very simple structure and the pulse center is obvious. In the practical calculation, we select five points around the pulse center (two before the pulse center, two after the pulse center, and one at the pulse center), and then find the one with slope closest to 0.

Second one: delete the first-order term in Taylor expansion of the time-dependent phase $\Psi(\omega, t_0) = a_0 + a_1\omega + a_2\omega^2 + ...$

Using polynomial fitting to the *time-dependent* spectral phase, and deleting the coefficient for the first order term, we can in principle obtain the *time-independent* spectral phase $\psi(\omega_j)$.

We did not use this method for the phase calculation in the thesis, because if one calculates the time-dependent phase $\Psi(\omega, t_0)$ with t_0 far away from the pulse center, one will get a large jump in $\Psi(\omega, t_0)$ from π to $-\pi$ as ωt_0 increase rapidly for large ω.

A.3 Spectral phase and harmonic phase

Based on above discussions, we can calculate the spectral phase of a single attosecond pulse as we show in Sec 5.3. The property of spectral phase associates closely to the temporal property of the attosecond pulse, such as duration, intensity and waveform. From Fig. 5.1, we also know that the reflection consists of a train of attosecond pulses and its spectrum is the typical harmonic spectrum. Thus, a fundamental question has to be asked: how does the spectral phase of each pulse relate to the phase of individual harmonic contained in the reflection.

To clarify the relation between pulse spectral phase and harmonic phase, we can start from the equation:

$$E^r(t) = \sum_{k=1}^{N} A_k E_k(t - t_k)\,, \tag{A.20}$$

where the total reflection $E^r(t)$ includes a train of N attosecond pulses, A_k, $E_k(t)$ and t_k are the amplitude, temporal waveform and temporal center of the kth attosecond pulse in the train.

Via a simple Fourier transformation, we can have:

$$\begin{aligned}\widetilde{E}^r(\omega) &= \frac{1}{2\pi}\int_{-\infty}^{\infty} E^r(t)e^{i\omega t}dt \\ &= \sum_{k=1}^{N} A_k e^{i\omega t_k}\frac{1}{2\pi}\int_{-\infty}^{\infty} E_k(t-t_k)e^{i\omega(t-t_k)}dt \\ &= \sum_{k=1}^{N} A_k e^{i\omega t_k}\widetilde{E}_k(\omega)\,,\end{aligned} \tag{A.21}$$

where $\widetilde{E}^r(\omega) = \left|\widetilde{E}^r(\omega)\right| e^{-i\psi^r(\omega)}$ represents the spectral modulus $\left|\widetilde{E}^r(\omega)\right|$ and phase $\psi^r(\omega)$ of the harmonics contained in the reflection, and $\widetilde{E}_k(\omega) = \left|\widetilde{E}_k(\omega)\right| e^{-i\psi_k(\omega)}$ denotes the spectrum of kth attosecond pulse with modulus $\left|\widetilde{E}_k(\omega)\right|$ and spectral phase $\psi_k(\omega)$. With Eq. A.21, we can connect the harmonic quantities to the quantities of each pulse:

$$[I^r(\omega)]^{\frac{1}{2}} e^{-i\psi^r(\omega)} = \sum_{k=1}^{N} A_k I_k^{\frac{1}{2}}(\omega)e^{-i\psi_k(\omega)}e^{i\omega t_k}\,, \tag{A.22}$$

where intensity spectra $I^r(\omega) = \left|\widetilde{E}^r(\omega)\right|^2$ and $I_k(\omega) = \left|\widetilde{E}_k(\omega)\right|^2$ are used. As one can clearly see, harmonic spectrum $I^r(\omega)$ and phase $\psi^r(\omega)$ come from the superposition of the pulse spectra and phase in frequency domain.

To clearly illustrate the relations, we consider the ideal case where the attosecond pulses have the same amplitude and waveform, *i.e.* $A_k \equiv A_0$, $E_k(t) \equiv E_0(t)$, leading to $\widetilde{E}_k(\omega) \equiv \widetilde{E}_0(\omega)$ and $\psi_k(\omega) \equiv \psi_0(\omega)$. Thus Eq. A.22 can be simplified as

$$[I^r(\omega)]^{\frac{1}{2}} e^{-i\psi^r(\omega)} = A_0 I_0^{\frac{1}{2}}(\omega)e^{-i\psi_0(\omega)}\sum_{k=1}^{N} e^{i\omega t_k}\,, \tag{A.23}$$

where $I_0(\omega) = \left|\widetilde{E}_0(\omega)\right|^2$.

For a perfect periodic case: the attosecond pulses in the train are equally separated in time, *i.e.* $t_k = (k-1)\Delta t$, thus we can have:

$$[I^r(\omega)]^{\frac{1}{2}} e^{-i\psi^r(\omega)} = A_0 I_k^{\frac{1}{2}}(\omega) e^{-i\psi_0(\omega)} \begin{cases} \frac{e^{iN\omega\Delta t}-1}{e^{(i\omega\Delta t)}-1} & ,\omega\Delta t \neq 2\pi\,, \\ N & ,\omega\Delta t = 2\pi\,, \end{cases} \tag{A.24}$$

where the time origin is chosen at the center of the 1st pulse. If the pulse train is very long $N \gg 1$, we can have $N \gg (e^{iN\omega\Delta t}-1)/(e^{i\omega\Delta t}-1)$ for $\omega\Delta t \neq 2\pi$. Hence, a well-peaked harmonic spectrum can be obtained:

$$I^r(\omega_n) = N^2 A_0^2 I_k(\omega_n)\,, \tag{A.25}$$

$$\psi^r(\omega_n) = \psi_0(\omega_n)\,, \tag{A.26}$$

where $\omega_n = n2\pi/\Delta t$ and n is an integer. In this situation, harmonic phase is identical to pulse spectral phase.

For an aperiodic case: the attosecond pulses in the train are separated in time as $t_k = (k-1)\Delta t + \tau_k$, τ_k is the deviation from perfect periodicity, thus we can have:

$$[I^r(\omega)]^{\frac{1}{2}} e^{-i\psi^r(\omega)} = A_0 I_0^{\frac{1}{2}}(\omega) e^{-i\psi_0(\omega)} \sum_{k=1}^{N} e^{i\omega\tau_k} e^{i\omega(k-1)\Delta t}\,, \tag{A.27}$$

and also consider the nth harmonic with frequency $\omega_n = n2\pi/\Delta t$:

$$[I^r(\omega_n)]^{\frac{1}{2}} e^{-i\psi^r(\omega_n)} = A_0 I_0^{\frac{1}{2}}(\omega_n) e^{-i\psi_0(\omega_n)} \sum_{k=1}^{N} e^{in2\pi\frac{\tau_k}{\Delta t}}\,, \tag{A.28}$$

As one can see, the harmonic phase $\psi^r(\omega_n)$ depends not only on the pulse spectral phase $\psi_0(\omega_n)$, but also on the deviation of the periodicity. The contribution of the spectral phase is an intrinsic property of the emission dynamics, while the contribution of aperiodicity relies on the order of the harmonic.

However, for practical situations, especially for plasma harmonic generation in the ultra-relativistic regime, attosecond pulse generated in different laser cycle has different amplitude and waveform, leading to a very complicated harmonic phase which is quite different from the pulse spectral phase.

A.4 Lorentz transformation for oblique incidence

In laser-plasma experiments, the interaction geometry is always high-dimensional, but it is sometimes convenient to consider the involved physical processes in a one-dimensional (1D) system, *i.e.* the spatial dependence perpendicular to the laser propagation is neglected. This approximation is reasonable if the laser wavelength is much smaller than the transverse width of the laser pulse. For theoretical analysis, 1D geometry sometimes can provide a simplified but more straightforward and comprehensive insight into the physical process. For numerical simulations, the resolution for a 1D system is orders of magnitude higher than that for a high-dimensional system. In the case of normal incidence ($\theta = 0$), this 1D approximation is obvious. In the case of oblique incidence ($\theta \neq 0$), Bourdier in Ref. [79] provides an effective method for this 1D approximation via a proper Lorentz transformation.

For laser oblique incidence, we make a Lorentz transformation from the lab reference

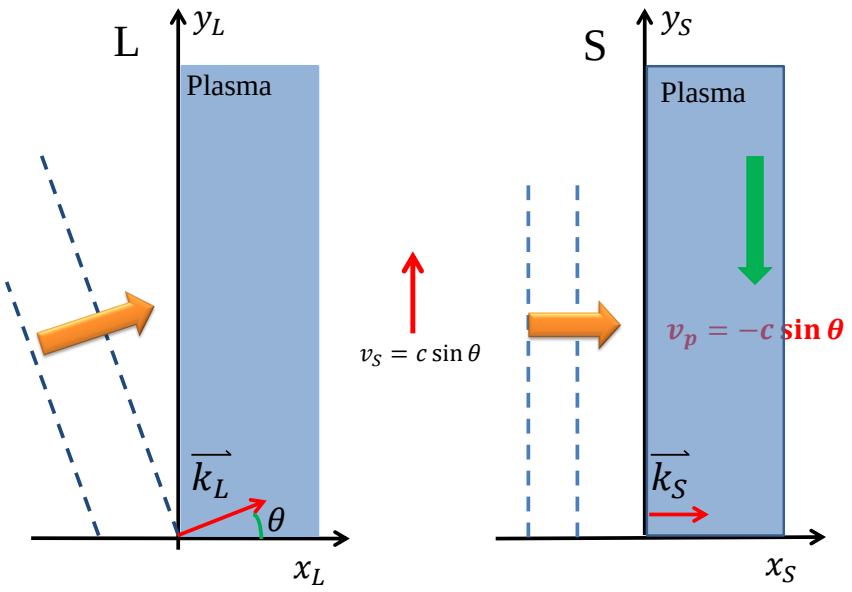

Figure A.2: Lorentz transformation from a lab frame of reference to the simulation boosted frame of reference along the y axis [79]. "L" denotes the lab reference and "S" represents the simulation reference.

(L-reference) to the simulation boosted reference (S-reference) in which the laser is normally incident onto the plasma, as shown in Fig. A.2. This boosted frame is achieved with a velocity $v_S = c\sin(\theta)$ in the y-axis direction parallel to the plasma surface, where θ is the laser incident angle in lab frame. In S-reference, the unperturbed plasma has the density $n_{0S} = n_{0L}/\cos(\theta)$ with an initial velocity $v_p = -c\sin(\theta)$ in $-y$ direction.

Transforming from L-reference to S-reference, 4-dimensional vectors have to be transformed with the Lorentz matrix:

$$\begin{pmatrix} \gamma & 0 & -\gamma\beta & 0 \\ 0 & 1 & 0 & 0 \\ -\gamma\beta & 0 & \gamma & 0 \\ 0 & 0 & 0 & 1 \end{pmatrix} \tag{A.29}$$

where

$$\beta = v_S/c = \sin(\theta), \qquad \gamma = (1-\beta^2)^{-1/2} = \cos^{-1}(\theta)\,. \tag{A.30}$$

Hence, we can obtain the laser frequency ω_S and wave vector $\mathbf{k}_S$ in S-reference from the laser frequency and wave vector

$$\omega_L = \omega_l\,, \tag{A.31a}$$
$$\mathbf{k}_L = k_l(\cos(\theta), \sin(\theta), 0)\,, \tag{A.31b}$$

in L-reference via a Lorentz transformation:

$$\omega_S = \gamma(\omega_L - \beta c k_L^y) = \omega_l\cos(\theta)\,, \tag{A.32a}$$

$$k_S^x = k_L^x = k_l \cos(\theta)\,, \tag{A.32b}$$
$$k_S^y = \gamma(k_L^y - \beta\frac{\omega_L}{c}) = 0\,, \tag{A.32c}$$
$$k_S^z = k_L^z = 0\,, \tag{A.32d}$$

where ω_l is the laser frequency and k_l is the modulus of the laser wave vector in L-reference, $\omega_l = ck_l$. As we can see, the laser in S-reference propagates in x direction with

$$\omega_S = ck_S = \omega_l \cos(\theta)\,, \tag{A.33a}$$
$$\mathbf{k}_S = k_l \cos(\theta)(1,0,0)\,. \tag{A.33b}$$

The transformation of the electromagnetic fields between S- and L-reference are:
For p-polarization[2]:

$$\mathbf{E}_L = E_l(-\sin(\theta), \cos(\theta), 0)\,, \tag{A.34a}$$
$$\mathbf{B}_L = B_l(0,0,1)\,, \tag{A.34b}$$

where E_l and B_l is the amplitude of the laser field in the L-reference. Via Lorentz transformation:

$$E_S^x = \gamma(E_L^x + \beta c B_L^z) = 0\,, \tag{A.35a}$$
$$E_S^y = E_L^y = E_l \cos(\theta)\,, \tag{A.35b}$$
$$B_S^z = \gamma(B_L^z + \beta E_L^x/c) = B_l \cos(\theta)\,, \tag{A.35c}$$

we can have the electromagnetic fields in S-reference:

$$\mathbf{E}_S = E_l \cos(\theta)(0,1,0)\,, \tag{A.36a}$$
$$\mathbf{B}_S = B_l \cos(\theta)(0,0,1)\,. \tag{A.36b}$$

For s-polarization:

$$\mathbf{E}_L = E_l(0,0,1)\,, \tag{A.37a}$$
$$\mathbf{B}_L = B_l(\sin(\theta), -\cos(\theta), 0)\,, \tag{A.37b}$$

in the L-reference. Via Lorentz transformation:

$$E_S^z = \gamma(E_L^z - \beta c B_L^x) = E_l \cos(\theta)\,, \tag{A.38a}$$
$$B_S^x = \gamma(B_L^x - \beta E_L^z/c) = 0\,, \tag{A.38b}$$
$$B_S^y = B_L^y = -B_l \cos(\theta)\,, \tag{A.38c}$$

we can have the electromagnetic fields in S-reference:

$$\mathbf{E}_S = E_l \cos(\theta)(0,0,1)\,, \tag{A.39a}$$
$$\mathbf{B}_S = B_l \cos(\theta)(0,-1,0)\,. \tag{A.39b}$$

One may note that the normalized laser electric field $a = eE_l/(mc\omega_l)$ is Lorentz

[2]The definitions of p- and s- polarization are given in Sec. 2.3.2

invariant:

$$a_L = \frac{eE_L}{m_e c\omega_L} = \frac{eE_S}{m_e c\omega_S} = a_S\,, \tag{A.40}$$

which is very important for our calculation. With this Lorentz invariant, we can do all the calculations in S-reference conveniently and then equate the normalized electromagnetic field in L-reference.

Transforming the nth harmonic in S-reference:

$$\omega_{nS} = \quad n\omega_S = \quad n\omega_l \cos(\theta)\,, \tag{A.41a}$$
$$\mathbf{k}_{nS} = -n\mathbf{k}_S = -nk_l \cos(\theta)(1,0,0)\,, \tag{A.41b}$$

back to L-reference as

$$\omega_{nL} = \gamma(\omega_{nS} + \beta c k^y_{nS}) = \omega_{nS}/\cos(\theta) = n\omega_l\,, \tag{A.42a}$$
$$k^x_{nL} = k^x_{nS} = -nk_l \cos(\theta)\,, \tag{A.42b}$$
$$k^y_{nL} = \gamma(k^y_{nS} + \beta\frac{\omega_{nS}}{c}) = \gamma\beta\frac{\omega_{nS}}{c} = nk_l \sin(\theta)\,, \tag{A.42c}$$
$$k^z_{nL} = k^z_{nS} = 0\,, \tag{A.42d}$$

we can have

$$\omega_{nL} = n\omega_l\,, \tag{A.43a}$$
$$\mathbf{k}_{nL} = nk_l(-\cos(\theta), \sin(\theta), 0)\,. \tag{A.43b}$$

Thus the order (n) of the harmonic is also Lorentz invariant.

Bibliography

[1] S. Tang, N. Kumar, and C. H. Keitel, "Plasma high-order-harmonic generation from ultraintense laser pulses," Phys. Rev. E **95**, 051201 (2017).

[2] S. Tang and N. Kumar, "Super-intense Single Attosecond Pulse Generation by Plasma Gating," arXiv preprint arXiv:1803.02121 (2018).

[3] S. Tang and N. Kumar, "Analytical Model for Pulse Emission from Plasma Surface Electron Layer," In preparation (2018).

[4] S. Tang, "Collisional Effect on Plasma High-order Harmonic Generation," In preparation (2018).

[5] T. H. Maiman, "Stimulated optical radiation in ruby," nature **187**, 493 (1960).

[6] "The Extreme Light Infrastructure Project," .

[7] T. Tajima and G. Mourou, "Zettawatt-exawatt lasers and their applications in ultrastrong-field physics," Phys. Rev. ST Accel. Beams **5**, 031301 (2002).

[8] F. J. McClung and R. W. Hellwarth, "Giant Optical Pulsations from Ruby," Appl. Opt. **1**, 103 (1962).

[9] W. E. Lamb, "Theory of an Optical Maser," Phys. Rev. **134**, A1429 (1964).

[10] G. A. Mourou, T. Tajima, and S. V. Bulanov, "Optics in the relativistic regime," Rev. Mod. Phys. **78**, 309 (2006).

[11] G. Mourou, S. Mironov, E. Khazanov, and A. Sergeev, "Single cycle thin film compressor opening the door to Zeptosecond-Exawatt physics," The European Physical Journal Special Topics **223**, 1181 (2014).

[12] "The vulcan 10 petawatt project," .

[13] K. J. Schafer, B. Yang, L. F. DiMauro, and K. C. Kulander, "Above threshold ionization beyond the high harmonic cutoff," Phys. Rev. Lett. **70**, 1599 (1993).

[14] P. B. Corkum, "Plasma perspective on strong field multiphoton ionization," Phys. Rev. Lett. **71**, 1994 (1993).

[15] F. Quéré, C. Thaury, P. Monot, *et al.*, "Coherent Wake Emission of High-Order Harmonics from Overdense Plasmas," Phys. Rev. Lett. **96**, 125004 (2006).

[16] R. Lichters, J. Meyer-ter Vehn, and A. Pukhov, "Short-pulse laser harmonics from oscillating plasma surfaces driven at relativistic intensity," Physics of Plasmas **3**, 3425 (1996).

[17] D. an der Brügge and A. Pukhov, "Enhanced relativistic harmonics by electron nanobunching," Physics of Plasmas **17**, 033110 (2010).

[18] A. A. Gonoskov, A. V. Korzhimanov, A. V. Kim, M. Marklund, and A. M. Sergeev, "Ultrarelativistic nanoplasmonics as a route towards extreme-intensity attosecond pulses," Phys. Rev. E **84**, 046403 (2011).

[19] J. Schwinger, "On Gauge Invariance and Vacuum Polarization," Phys. Rev. **82**, 664 (1951).

[20] S. Tang, M. A. Bake, H.-Y. Wang, and B.-S. Xie, "QED cascade induced by a high-energy γ photon in a strong laser field," Phys. Rev. A **89**, 022105 (2014).

[21] E. N. Nerush, I. Y. Kostyukov, A. M. Fedotov, N. B. Narozhny, N. V. Elkina, and H. Ruhl, "Laser Field Absorption in Self-Generated Electron-Positron Pair Plasma," Phys. Rev. Lett. **106**, 035001 (2011).

[22] A. M. Fedotov, N. B. Narozhny, G. Mourou, and G. Korn, "Limitations on the Attainable Intensity of High Power Lasers," Phys. Rev. Lett. **105**, 080402 (2010).

[23] S. S. Bulanov, T. Z. Esirkepov, A. G. R. Thomas, J. K. Koga, and S. V. Bulanov, "Schwinger Limit Attainability with Extreme Power Lasers," Phys. Rev. Lett. **105**, 220407 (2010).

[24] M. Tamburini, A. Di Piazza, and C. H. Keitel, "Laser-pulse-shape control of seeded QED cascades," Scientific Reports **7**, 5694 (2017).

[25] S. Gordienko, A. Pukhov, O. Shorokhov, and T. Baeva, "Coherent Focusing of High Harmonics: A New Way Towards the Extreme Intensities," Phys. Rev. Lett. **94**, 103903 (2005).

[26] W. Kruer, *The Physics Of Laser Plasma Interactions (Frontiers in Physics)* (Westview Press, 2003).

[27] A. Di Piazza, C. Müller, K. Z. Hatsagortsyan, and C. H. Keitel, "Extremely high-intensity laser interactions with fundamental quantum systems," Rev. Mod. Phys. **84**, 1177 (2012).

[28] M. Marklund and P. K. Shukla, "Nonlinear collective effects in photon-photon and photon-plasma interactions," Rev. Mod. Phys. **78**, 591 (2006).

[29] T. J. M. Boyd and J. J. Sanderson, *The physics of plasmas* (Cambridge University Press, 2003).

[30] E. Esarey, C. B. Schroeder, and W. P. Leemans, "Physics of laser-driven plasma-based electron accelerators," Rev. Mod. Phys. **81**, 1229 (2009).

[31] A. Macchi, M. Borghesi, and M. Passoni, "Ion acceleration by superintense laser-plasma interaction," Rev. Mod. Phys. **85**, 751 (2013).

[32] Y. Shi, B. Shen, L. Zhang, X. Zhang, W. Wang, and Z. Xu, "Light Fan Driven by a Relativistic Laser Pulse," Phys. Rev. Lett. **112**, 235001 (2014).

[33] M. Tabak, J. Hammer, M. E. Glinsky, W. L. Kruer, S. C. Wilks, J. Woodworth, E. M. Campbell, M. D. Perry, and R. J. Mason, "Ignition and high gain with ultrapowerful lasers," Physics of Plasmas **1**, 1626 (1994).

[34] R. Kodama, P. A. Norreys, K. Mima, A. E. Dangor, R. G. Evans, H. Fujita, Y. Kitagawa, K. Krushelnick, T. Miyakoshi, N. Miyanaga, T. Norimatsu, S. J. Rose, T. Shozaki, K. Shigemori, A. Sunahara, M. Tampo, K. A. Tanaka, Y. Toyama, T. Yamanaka, and M. Zepf, "Fast heating of ultrahigh-density plasma as a step towards laser fusion ignition," Nature **412**, 798 EP (2001).

[35] U. Teubner and P. Gibbon, "High-order harmonics from laser-irradiated plasma surfaces," Rev. Mod. Phys. **81**, 445 (2009).

[36] P. Gibbon, *Short pulse laser interactions with matter* (World Scientific Publishing Company, 2004).

[37] T. Schlegel, N. Naumova, V. T. Tikhonchuk, C. Labaune, I. V. Sokolov, and G. Mourou, "Relativistic laser piston model: Ponderomotive ion acceleration in dense plasmas using ultraintense laser pulses," Physics of Plasmas **16**, 083103 (2009).

[38] S. Corde, K. Ta Phuoc, G. Lambert, R. Fitour, V. Malka, A. Rousse, A. Beck, and E. Lefebvre, "Femtosecond x rays from laser-plasma accelerators," Rev. Mod. Phys. **85**, 1 (2013).

[39] V. Ginzburg, "The propagation of electromagnetic waves in plasmas," .

[40] J. Bobin, "High intensity laser plasma interaction," Physics Reports **122**, 173 (1985).

[41] H. George, F. Quéré, C. Thaury, G. Bonnaud, and P. Martin, "Mechanisms of forward laser harmonic emission from thin overdense plasmas," New Journal of Physics **11**, 113028 (2009).

[42] B. Dromey, S. Cousens, S. Rykovanov, M. Yeung, D. Jung, D. C. Gautier, T. Dzelzainis, D. Kiefer, S. Palaniyppan, R. Shah, J. Schreiber, J. C. Fernandez, C. L. S. Lewis, M. Zepf, and B. M. Hegelich, "Coherent synchrotron emission in transmission from ultrathin relativistic laser plasmas," New Journal of Physics **15**, 015025 (2013).

[43] T. J. M. Boyd and R. Ondarza-Rovira, "Plasma Line Emission from Short Pulse Laser Interactions with Dense Plasmas," Phys. Rev. Lett. **85**, 1440 (2000).

[44] I. Watts, M. Zepf, E. L. Clark, M. Tatarakis, K. Krushelnick, A. E. Dangor, R. M. Allott, R. J. Clarke, D. Neely, and P. A. Norreys, "Dynamics of the Critical Surface in High-Intensity Laser-Solid Interactions: Modulation of the XUV Harmonic Spectra," Phys. Rev. Lett. **88**, 155001 (2002).

[45] T. J. M. Boyd and R. Ondarza-Rovira, "Plasma Modulation of Harmonic Emission Spectra from Laser-Plasma Interactions," Phys. Rev. Lett. **98**, 105001 (2007).

[46] P. Agostini and L. F. DiMauro, "The physics of attosecond light pulses," Reports on Progress in Physics **67**, 813 (2004).

[47] F. Krausz and M. Ivanov, "Attosecond physics," Rev. Mod. Phys. **81**, 163 (2009).

[48] M. Ferray, A. L'Huillier, X. F. Li, L. A. Lompre, G. Mainfray, and C. Manus, "Multiple-harmonic conversion of 1064 nm radiation in rare gases," Journal of Physics B: Atomic, Molecular and Optical Physics **21**, L31 (1988).

[49] K. C. Kulander and B. W. Shore, "Calculations of Multiple-Harmonic Conversion of 1064-nm Radiation in Xe," Phys. Rev. Lett. **62**, 524 (1989).

[50] A. L'Huillier and P. Balcou, "High-order harmonic generation in rare gases with a 1-ps 1053-nm laser," Phys. Rev. Lett. **70**, 774 (1993).

[51] K. Varjú, Y. Mairesse, B. Carré, M. B. Gaarde, P. Johnsson, S. Kazamias, R. López-Martens, J. Mauritsson, K. J. Schafer, P. Balcou, A. L'huillier, and P. Saliéres, "Frequency chirp of harmonic and attosecond pulses," Journal of Modern Optics **52**, 379 (2005).

[52] G. Farkas and C. Tóth, "Proposal for attosecond light pulse generation using laser induced multiple-harmonic conversion processes in rare gases," Physics Letters A **168**, 447 (1992).

[53] Y. Mairesse, A. de Bohan, L. J. Frasinski, H. Merdji, L. C. Dinu, P. Monchicourt, P. Breger, M. Kovačev, R. Taïeb, B. Carré, H. G. Muller, P. Agostini, and P. Salières, "Attosecond Synchronization of High-Harmonic Soft X-rays," Science **302**, 1540 (2003), http://science.sciencemag.org/content/302/5650/1540.full.pdf .

[54] T. Baeva, S. Gordienko, and A. Pukhov, "Theory of high-order harmonic generation in relativistic laser interaction with overdense plasma," Phys. Rev. E **74**, 046404 (2006).

[55] S. Kahaly, S. Monchocé, H. Vincenti, T. Dzelzainis, B. Dromey, M. Zepf, P. Martin, and F. Quéré, "Direct Observation of Density-Gradient Effects in Harmonic Generation from Plasma Mirrors," Phys. Rev. Lett. **110**, 175001 (2013).

[56] F. Quéré, C. Thaury, J.-P. Geindre, G. Bonnaud, P. Monot, and P. Martin, "Phase Properties of Laser High-Order Harmonics Generated on Plasma Mirrors," Phys. Rev. Lett. **100**, 095004 (2008).

[57] C. Thaury, F. Quere, J. P. Geindre, A. Levy, T. Ceccotti, P. Monot, M. Bougeard, F. Reau, P. d/'Oliveira, P. Audebert, R. Marjoribanks, and P. Martin, "Plasma mirrors for ultrahigh-intensity optics," Nat Phys **3**, 424 (2007).

[58] C. Rödel, D. an der Brügge, J. Bierbach, M. Yeung, T. Hahn, B. Dromey, S. Herzer, S. Fuchs, A. G. Pour, E. Eckner, M. Behmke, M. Cerchez, O. Jäckel, D. Hemmers, T. Toncian, M. C. Kaluza, A. Belyanin, G. Pretzler, O. Willi, A. Pukhov, M. Zepf, and G. G. Paulus, "Harmonic Generation from Relativistic Plasma Surfaces in Ultrasteep Plasma Density Gradients," Phys. Rev. Lett. **109**, 125002 (2012).

[59] F. Dollar, P. Cummings, V. Chvykov, L. Willingale, M. Vargas, V. Yanovsky, C. Zulick, A. Maksimchuk, A. G. R. Thomas, and K. Krushelnick, "Scaling High-Order Harmonic Generation from Laser-Solid Interactions to Ultrahigh Intensity," Phys. Rev. Lett. **110**, 175002 (2013).

[60] F. Brunel, "Not-so-resonant, resonant absorption," Phys. Rev. Lett. **59**, 52 (1987).

[61] M. Zepf, G. D. Tsakiris, G. Pretzler, I. Watts, D. M. Chambers, P. A. Norreys, U. Andiel, A. E. Dangor, K. Eidmann, C. Gahn, A. Machacek, J. S. Wark, and K. Witte, "Role of the plasma scale length in the harmonic generation from solid targets," Phys. Rev. E **58**, R5253 (1998).

[62] F. Quéré, C. Thaury, H. George, J. Geindre, E. Lefebvre, G. Bonnaud, S. Hüller, P. Monot, and P. Martin, "Basic mechanisms of laser high-order harmonic generation from plasma mirrors," Journal of Modern Optics **55**, 2711 (2008), https://doi.org/10.1080/09500340802187381 .

[63] C. Thaury and F. Quéré, "High-order harmonic and attosecond pulse generation on plasma mirrors: basic mechanisms," Journal of Physics B: Atomic, Molecular and Optical Physics **43**, 213001 (2010).

[64] A. Tarasevitch, K. Lobov, C. Wünsche, and D. von der Linde, "Transition to the Relativistic Regime in High Order Harmonic Generation," Phys. Rev. Lett. **98**, 103902 (2007).

[65] S. Gordienko, A. Pukhov, O. Shorokhov, and T. Baeva, "Relativistic Doppler Effect: Universal Spectra and Zeptosecond Pulses," Phys. Rev. Lett. **93**, 115002 (2004).

[66] B. Dromey, M. Zepf, A. Gopal, K. Lancaster, M. S. Wei, K. Krushelnick, M. Tatarakis, N. Vakakis, S. Moustaizis, R. Kodama, M. Tampo, C. Stoeckl, R. Clarke, H. Habara, D. Neely, S. Karsch, and P. Norreys, "High harmonic generation in the relativistic limit," Nat Phys **2**, 456 (2006).

[67] B. Dromey, S. Kar, C. Bellei, D. C. Carroll, R. J. Clarke, J. S. Green, S. Kneip, K. Markey, S. R. Nagel, P. T. Simpson, L. Willingale, P. McKenna, D. Neely, Z. Najmudin, K. Krushelnick, P. A. Norreys, and M. Zepf, "Bright Multi-keV Harmonic Generation from Relativistically Oscillating Plasma Surfaces," Phys. Rev. Lett. **99**, 085001 (2007).

[68] M. Cherednychek and A. Pukhov, "Analytical approach to high harmonics spectrum in the nanobunching regime," Physics of Plasmas **23**, 103301 (2016).

[69] A. Gonoskov, "Theory of relativistic radiation reflection from plasmas," Physics of Plasmas **25**, 013108 (2018), https://doi.org/10.1063/1.5000785 .

[70] D. an der Brügge, *Ultrashort and ultraintense electromagnetic pulses*, Ph.D. thesis, Ph. D. thesis. Heinrich-Heine-Universität Düsseldorf (2010).

[71] C. Thaury, F. Quéré, H. George, J. Geindre, G. Bonnaud, and P. Martin, "Intrinsic phase of high order harmonics generated on plasma mirrors," AIP Conference Proceedings **1228**, 393 (2010), https://aip.scitation.org/doi/pdf/10.1063/1.3426078 .

[72] S. G. R. F. K. G. D. T. Rainer Hörlein, Yutaka Nomura, "Factors influencing the temporal characteristics of coherent wake field harmonic emission from solid surfaces," Proc.SPIE **7359**, 7359 (2009).

[73] A. Malvache, A. Borot, F. Quéré, and R. Lopez-Martens, "Coherent wake emission spectroscopy as a probe of steep plasma density profiles," Phys. Rev. E **87**, 035101 (2013).

[74] D. von der Linde, T. Engers, G. Jenke, P. Agostini, G. Grillon, E. Nibbering, A. Mysyrowicz, and A. Antonetti, "Generation of high-order harmonics from solid surfaces by intense femtosecond laser pulses," Phys. Rev. A **52**, R25 (1995).

[75] P. A. Norreys, M. Zepf, S. Moustaizis, A. P. Fews, J. Zhang, P. Lee, M. Bakarezos, C. N. Danson, A. Dyson, P. Gibbon, P. Loukakos, D. Neely, F. N. Walsh, J. S. Wark, and A. E. Dangor, "Efficient Extreme UV Harmonics Generated from Picosecond Laser Pulse Interactions with Solid Targets," Phys. Rev. Lett. **76**, 1832 (1996).

[76] L. D. Landau and E. M. Lifshitz, *The Classical Theory of Fields*, fourth revised english ed., Course of Theoretical Physics, Vol. 2 (Butterworth-Heinemann, 2005).

[77] R. Capdessus, E. d'Humières, and V. T. Tikhonchuk, "Modeling of radiation losses in ultrahigh power laser-matter interaction," Phys. Rev. E **86**, 036401 (2012).

[78] M. C. Levy, S. C. Wilks, M. Tabak, and M. G. Baring, "Conservation laws and conversion efficiency in ultraintense laser-overdense plasma interactions," Physics of Plasmas **20**, 103101 (2013).

[79] A. Bourdier, "Oblique incidence of a strong electromagnetic wave on a cold inhomogeneous electron plasma. Relativistic effects," The Physics of Fluids **26**, 1804 (1983).

[80] J. Sanz, A. Debayle, and K. Mima, "Model for ultraintense laser-plasma interaction at normal incidence," Phys. Rev. E **85**, 046411 (2012).

[81] A. Debayle, J. Sanz, L. Gremillet, and K. Mima, "Toward a self-consistent model of the interaction between an ultra-intense, normally incident laser pulse with an overdense plasma," Physics of Plasmas **20**, 053107 (2013).

[82] A. Debayle, J. Sanz, and L. Gremillet, "Self-consistent theory of high-order harmonic generation by relativistic plasma mirror," Phys. Rev. E **92**, 053108 (2015).

[83] T. D. Arber, K. Bennett, C. S. Brady, A. Lawrence-Douglas, M. G. Ramsay, N. J. Sircombe, P. Gillies, R. G. Evans, H. Schmitz, A. R. Bell, and C. P. Ridgers, "Contemporary particle-in-cell approach to laser-plasma modelling," Plasma Physics and Controlled Fusion **57**, 113001 (2015).

[84] A. Gonoskov, S. Bastrakov, E. Efimenko, A. Ilderton, M. Marklund, I. Meyerov, A. Muraviev, A. Sergeev, I. Surmin, and E. Wallin, "Extended particle-in-cell schemes for physics in ultrastrong laser fields: Review and developments," Phys. Rev. E **92**, 023305 (2015).

[85] E. Fijalkow, "A numerical solution to the Vlasov equation," Computer Physics Communications **116**, 319 (1999).

[86] E. Sonnendrücker, J. Roche, P. Bertrand, and A. Ghizzo, "The Semi-Lagrangian Method for the Numerical Resolution of the Vlasov Equation," Journal of Computational Physics **149**, 201 (1999).

[87] L. O. Silva, M. Marti, J. R. Davies, R. A. Fonseca, C. Ren, F. S. Tsung, and W. B. Mori, "Proton Shock Acceleration in Laser-Plasma Interactions," Phys. Rev. Lett. **92**, 015002 (2004).

[88] Y. Ping, R. Shepherd, B. F. Lasinski, M. Tabak, H. Chen, H. K. Chung, K. B. Fournier, S. B. Hansen, A. Kemp, D. A. Liedahl, K. Widmann, S. C. Wilks, W. Rozmus, and M. Sherlock, "Absorption of Short Laser Pulses on Solid Targets in the Ultrarelativistic Regime," Phys. Rev. Lett. **100**, 085004 (2008).

[89] A. J. Kemp, Y. Sentoku, and M. Tabak, "Hot-Electron Energy Coupling in Ultraintense Laser-Matter Interaction," Phys. Rev. Lett. **101**, 075004 (2008).

[90] A. J. Kemp, Y. Sentoku, and M. Tabak, "Hot-electron energy coupling in ultraintense laser-matter interaction," Phys. Rev. E **79**, 066406 (2009).

[91] S. C. Wilks, "Absorption of ultra intense light pulses," Phys. Rev. Lett. **69,**, 1383 (1992).

[92] S. C. Wilks and W. L. Kruer, "Absorption of ultrashort, ultra-intense laser light by solids and overdense plasmas," IEEE Journal of Quantum Electronics **33**, 1954 (1997).

[93] M. G. Haines, M. S. Wei, F. N. Beg, and R. B. Stephens, "Hot-Electron Temperature and Laser-Light Absorption in Fast Ignition," Phys. Rev. Lett. **102**, 045008 (2009).

[94] M. C. Levy, S. C. Wilks, M. Tabak, S. B. Libby, and M. G. Baring, "Petawatt laser absorption bounded," Nature communications **5** (2014).

[95] I. Watts, M. Zepf, E. L. Clark, M. Tatarakis, K. Krushelnick, A. E. Dangor, R. Allott, R. J. Clarke, D. Neely, and P. A. Norreys, "Measurements of relativistic self-phase-modulation in plasma," Phys. Rev. E **66**, 036409 (2002).

[96] Y. Ping, A. J. Kemp, L. Divol, M. H. Key, P. K. Patel, K. U. Akli, F. N. Beg, S. Chawla, C. D. Chen, R. R. Freeman, D. Hey, D. P. Higginson, L. C. Jarrott, G. E. Kemp, A. Link, H. S. McLean, H. Sawada, R. B. Stephens, D. Turnbull, B. Westover, and S. C. Wilks, "Dynamics of Relativistic Laser-Plasma Interaction on Solid Targets," Phys. Rev. Lett. **109**, 145006 (2012).

[97] L. Cialfi, L. Fedeli, and M. Passoni, "Electron heating in subpicosecond laser interaction with overdense and near-critical plasmas," Phys. Rev. E **94**, 053201 (2016).

[98] J. M. Mikhailova, M. V. Fedorov, N. Karpowicz, P. Gibbon, V. T. Platonenko, A. M. Zheltikov, and F. Krausz, "Isolated Attosecond Pulses from Laser-Driven Synchrotron Radiation," Phys. Rev. Lett. **109**, 245005 (2012).

[99] M. Chini, K. Zhao, and Z. Chang, "The generation, characterization and applications of broadband isolated attosecond pulses," Nature Photonics **8**, 178 EP (2014), review Article.

[100] A. Präkelt, M. Wollenhaupt, C. Sarpe-Tudoran, and T. Baumert, "Phase control of a two-photon transition with shaped femtosecond laser-pulse sequences," Phys. Rev. A **70**, 063407 (2004).

[101] R. Hajima and R. Nagai, "Generating Carrier-Envelope-Phase Stabilized Few-Cycle Pulses from a Free-Electron Laser Oscillator," Phys. Rev. Lett. **119**, 204802 (2017).

[102] M. Ossiander, F. Siegrist, V. Shirvanyan, R. Pazourek, A. Sommer, T. Latka, A. Guggenmos, S. Nagele, J. Feist, J. Burgdörfer, *et al.*, "Attosecond correlation dynamics," Nature Physics **13**, 280 (2017).

[103] Y. Nomura, R. Horlein, P. Tzallas, B. Dromey, S. Rykovanov, Z. Major, J. Osterhoff, S. Karsch, L. Veisz, M. Zepf, D. Charalambidis, F. Krausz, and G. D. Tsakiris, "Attosecond phase locking of harmonics emitted from laser-produced plasmas," Nat Phys **5**, 124 (2009).

[104] R. Wong, *Asymptotic approximations of integrals*, Vol. 34 (SIAM, 2001).

[105] S. Gordienko and A. Pukhov, "Scalings for ultrarelativistic laser plasmas and quasimonoenergetic electrons," Physics of Plasmas **12**, 043109 (2005), https://doi.org/10.1063/1.1884126 .

[106] B. Dromey, S. Rykovanov, M. Yeung, R. Horlein, D. Jung, D. C. Gautier, T. Dzelzainis, D. Kiefer, S. Palaniyppan, R. Shah, J. Schreiber, H. Ruhl, J. C. Fernandez, C. L. S. Lewis, M. Zepf, and B. M. Hegelich, "Coherent synchrotron emission from electron nanobunches formed in relativistic laser-plasma interactions," Nat Phys **8**, 804 (2012).

[107] T. Pfeifer, C. Spielmann, and G. Gerber, "Femtosecond x-ray science," Reports on Progress in Physics **69**, 443 (2006).

[108] G. Materlick and T. Tschentscher, *TESLA Technical Design Report Part V-The X-ray Free Electron Laser*, Tech. Rep. (DESY, Hamburg, 2001).

[109] G. D. Tsakiris, K. Eidmann, J. M. ter Vehn, and F. Krausz, "Route to intense single attosecond pulses," New Journal of Physics **8**, 19 (2006).

[110] P. Heissler, R. Hörlein, J. M. Mikhailova, L. Waldecker, P. Tzallas, A. Buck, K. Schmid, C. M. S. Sears, F. Krausz, L. Veisz, M. Zepf, and G. D. Tsakiris, "Few-Cycle Driven Relativistically Oscillating Plasma Mirrors: A Source of Intense Isolated Attosecond Pulses," Phys. Rev. Lett. **108**, 235003 (2012).

[111] M. Behmke, D. an der Brügge, C. Rödel, M. Cerchez, D. Hemmers, M. Heyer, O. Jäckel, M. Kübel, G. G. Paulus, G. Pretzler, A. Pukhov, M. Toncian, T. Toncian, and O. Willi, "Controlling the Spacing of Attosecond Pulse Trains from Relativistic Surface Plasmas," Phys. Rev. Lett. **106**, 185002 (2011).

[112] J. Braenzel, A. Andreev, M. Schnürer, S. Steinke, K. Platonov, G. Priebe, and W. Sandner, "Sub-structure of laser generated harmonics reveals plasma dynamics of a relativistically oscillating mirror," Physics of Plasmas **20**, 083109 (2013).

[113] P. Gibbon, "Harmonic generation by femtosecond laser-solid interaction: A coherent water-window light source?" Phys. Rev. Lett. **76,**, 50 (1996).

[114] V. Yanovsky, V. Chvykov, G. Kalinchenko, P. Rousseau, T. Planchon, T. Matsuoka, A. Maksimchuk, J. Nees, G. Cheriaux, G. Mourou, and K. Krushelnick, "Ultra-high intensity- 300-TW laser at 0.1 Hz repetition rate." Opt. Express **16**, 2109 (2008).

[115] A. P. L. Robinson, P. Gibbon, M. Zepf, S. Kar, R. G. Evans, and C. Bellei, "Relativistically correct hole-boring and ion acceleration by circularly polarized laser pulses," Plasma Physics and Controlled Fusion **51**, 024004 (2009).

[116] E. C. Welch, P. Zhang, F. Dollar, Z.-H. He, K. Krushelnick, and A. G. R. Thomas, "Time dependent Doppler shifts in high-order harmonic generation in intense laser

interactions with solid density plasma and frequency chirped pulses," Physics of Plasmas **22**, 053104 (2015), https://aip.scitation.org/doi/pdf/10.1063/1.4919857 .

[117] I. V. Sokolov, N. M. Naumova, J. A. Nees, G. A. Mourou, and V. P. Yanovsky, "Dynamics of emitting electrons in strong laser fields," Physics of Plasmas **16**, 093115 (2009).

[118] M. Tamburini, F. Pegoraro, A. D. Piazza, C. H. Keitel, and A. Macchi, "Radiation reaction effects on radiation pressure acceleration," New Journal of Physics **12**, 123005 (2010).

[119] M. Chen, A. Pukhov, T.-P. Yu, and Z.-M. Sheng, "Radiation reaction effects on ion acceleration in laser foil interaction," Plasma Physics and Controlled Fusion **53**, 014004 (2011).

[120] M. Tamburini, F. Pegoraro, A. D. Piazza, C. Keitel, T. Liseykina, and A. Macchi, "Radiation reaction effects on electron nonlinear dynamics and ion acceleration in laser−solid interaction," Nuclear Instruments and Methods in Physics Research Section A: Accelerators, Spectrometers, Detectors and Associated Equipment **653**, 181 (2011), superstrong 2010.

[121] M. Vranic, J. L. Martins, J. Vieira, R. A. Fonseca, and L. O. Silva, "All-Optical Radiation Reaction at 10^{21} W/cm^2," Phys. Rev. Lett. **113**, 134801 (2014).

[122] E. Wallin, A. Gonoskov, and M. Marklund, "Effects of high energy photon emissions in laser generated ultra-relativistic plasmas: Real-time synchrotron simulations," Physics of Plasmas **22**, 033117 (2015).

[123] M. Tabak, J. Hammer, M. E. Glinsky, W. L. Kruer, S. C. Wilks, J. Woodworth, E. M. Campbell, M. D. Perry, and R. J. Mason, "Ignition and high gain with ultrapowerful lasers," Physics of Plasmas **1**, 1626 (1994).

[124] J. Huba, "NRL (Naval Research Laboratory) Plasma Formulary, revised," Naval Research Lab. Report NRL/PU/6790-16-614 (2016).

[125] A. Macchi, F. Cattani, T. V. Liseykina, and F. Cornolti, "Laser Acceleration of Ion Bunches at the Front Surface of Overdense Plasmas," Phys. Rev. Lett. **94**, 165003 (2005).

[126] T. Baeva, *High harmonic generation from relativistic plasma*, Ph.D. thesis, Ph. D. thesis (2008).

[127] W. Kruer and K. Estabrook, "J× B heating by very intense laser light," The Physics of fluids **28**, 430 (1985).

[128] M. Tamburini, F. Pegoraro, A. D. Piazza, C. H. Keitel, and A. Macchi, "Radiation reaction effects on radiation pressure acceleration," New Journal of Physics **12**, 123005 (2010).

[129] G. Lehmann, "Efficient Semi-Lagrangian Vlasov-Maxwell Simulations of High Order Harmonic Generation from Relativistic Laser-Plasma Interactions," Communications in Computational Physics **20**, 583 (2016).

[130] M. TAMBURINI, "Radiation reaction effects in superintense laser-plasma interaction," (2011).

[131] T. D. Arber, K. Bennett, C. S. Brady, A. Lawrence-Douglas, M. G. Ramsay, N. J. Sircombe, P. Gillies, R. G. Evans, H. Schmitz, A. R. Bell, and C. P. Ridgers, "Contemporary particle-in-cell approach to laser-plasma modelling," Plasma Physics and Controlled Fusion **57**, 113001 (2015).

[132] C. Thaury and F. Quéré, "High-order harmonic and attosecond pulse generation on plasma mirrors: basic mechanisms," Journal of Physics B: Atomic, Molecular and Optical Physics **43**, 213001 (2010).

[133] J. Bell, M. Kearslev, L. Pitaevskii, L. Landau, E. Lifshitz, and J. Sykes, "Electrodynamics of continuous media," (1984).

[134] F. Krausz and M. I. Stockman, "Attosecond metrology: from electron capture to future signal processing," Nature Photonics **8**, 205 (2014).

[135] R. Kienberger, M. Hentschel, *et al.*, "Steering Attosecond Electron Wave Packets with Light," Science **297**, 1144 (2002).

[136] G. Sansone, L. Poletto, and M. Nisoli, "High-energy attosecond light sources," Nature Photonics **5**, 655 (2011).

[137] Z. Chang, P. B. Corkum, and S. R. Leone, "Attosecond optics and technology: progress to date and future prospects," J. Opt. Soc. Am. B **33**, 1081 (2016).

[138] N. M. Naumova, J. A. Nees, I. V. Sokolov, B. Hou, and G. A. Mourou, "Relativistic Generation of Isolated Attosecond Pulses in a λ^3 Focal Volume," Phys. Rev. Lett. **92**, 063902 (2004).

[139] H. Vincenti and F. Quéré, "Attosecond Lighthouses: How To Use Spatiotemporally Coupled Light Fields To Generate Isolated Attosecond Pulses," Phys. Rev. Lett. **108**, 113904 (2012).

[140] A. Tarasevitch, "Generation of high-order spatially coherent harmonics from solid targets by femtosecond laser pulses," Phys. Rev. A **62,**, 023816 (2000).

[141] D. an der Brügge and A. Pukhov, "Enhanced relativistic harmonics by electron nanobunching," Physics of Plasmas **17**, 033110 (2010).

[142] B. Dromey, S. Rykovanov, M. Yeung, R. Horlein, D. Jung, D. C. Gautier, T. Dzelzainis, D. Kiefer, S. Palaniyppan, R. Shah, J. Schreiber, H. Ruhl, J. C. Fernandez, C. L. S. Lewis, M. Zepf, and B. M. Hegelich, "Coherent synchrotron emission from electron nanobunches formed in relativistic laser-plasma interactions," Nat Phys **8**, 804 (2012).

[143] S. V. Bulanov, T. Z. Esirkepov, M. Kando, A. S. Pirozhkov, and N. N. Rosanov, "Relativistic mirrors in plasmas. Novel results and perspectives," Physics-Uspekhi **56**, 429 (2013).

[144] M. Yeung, B. Dromey, S. Cousens, T. Dzelzainis, D. Kiefer, J. Schreiber, J. H. Bin, W. Ma, C. Kreuzer, J. Meyer-ter Vehn, M. J. V. Streeter, P. S. Foster, S. Rykovanov, and M. Zepf, "Dependence of Laser-Driven Coherent Synchrotron Emission Efficiency on Pulse Ellipticity and Implications for Polarization Gating," Phys. Rev. Lett. **112**, 123902 (2014).

[145] M. Yeung, J. Bierbach, E. Eckner, S. Rykovanov, S. Kuschel, A. Sävert, M. Förster, C. Rödel, G. G. Paulus, S. Cousens, M. Coughlan, B. Dromey, and M. Zepf, "Noncollinear Polarization Gating of Attosecond Pulse Trains in the Relativistic Regime," Phys. Rev. Lett. **115**, 193903 (2015).

[146] P. Heissler, R. Hörlein, M. Stafe, J. M. Mikhailova, Y. Nomura, D. Herrmann, R. Tautz, S. G. Rykovanov, I. Földes, K. Varjú, *et al.*, "Toward single attosecond pulses using harmonic emission from solid-density plasmas," Applied Physics B **101**, 511 (2010).

[147] D. Hoff, M. Krüger, L. Maisenbacher, A. M. Sayler, G. G. Paulus, and P. Hommelhoff, "Tracing the phase of focused broadband laser?pulses," Nature Physics **13**, 947 EP (2017).

[148] S. Cousens, B. Reville, B. Dromey, and M. Zepf, "Temporal Structure of Attosecond Pulses from Laser-Driven Coherent Synchrotron Emission," Phys. Rev. Lett. **116**, 083901 (2016).

[149] S. X. Hu and L. A. Collins, "Attosecond Pump Probe: Exploring Ultrafast Electron Motion inside an Atom," Phys. Rev. Lett. **96**, 073004 (2006).

[150] N. Rohringer, D. Ryan, R. A. London, M. Purvis, F. Albert, J. Dunn, J. D. Bozek, C. Bostedt, A. Graf, R. Hill, *et al.*, "Atomic inner-shell X-ray laser at 1.46 nanometres pumped by an X-ray free-electron laser," Nature **481**, 488 (2012).

[151] C. K. Birdsall and A. B. Langdon, *Plasma physics via computer simulation* (CRC press, 2004).

[152] M. N. Rosenbluth, W. M. MacDonald, and D. L. Judd, "Fokker-Planck Equation for an Inverse-Square Force," Phys. Rev. **107**, 1 (1957).

[153] E. Epperlein, G. Rickard, and A. Bell, "A code for the solution of the Vlasov-Fokker-Planck equation in 1-D or 2-D," Computer Physics Communications **52**, 7 (1988).

[154] G. J. Rickard, A. R. Bell, and E. M. Epperlein, "2D Fokker-Planck simulations of short-pulse laser-plasma interactions," Phys. Rev. Lett. **62**, 2687 (1989).

[155] R. Kingham and A. Bell, "An implicit Vlasov-Fokker-Planck code to model non-local electron transport in 2-D with magnetic fields," Journal of Computational Physics **194**, 1 (2004).

[156] A. Weiner, *Ultrafast optics*, Vol. 72 (John Wiley & Sons, 2011).

[157] K. Varjú, Y. Mairesse, P. Agostini, P. Breger, B. Carré, L. J. Frasinski, E. Gustafsson, P. Johnsson, J. Mauritsson, H. Merdji, P. Monchicourt, A. L'Huillier, and P. Salières, "Reconstruction of Attosecond Pulse Trains Using an Adiabatic Phase Expansion," Phys. Rev. Lett. **95**, 243901 (2005).

Acknowledgements

At this point, I would like to sincerely thank all the people who have helped me during my doctoral studies and in my life.

First of all, I would like to express my deepest and strongest gratitude to my supervisor Honorarprof. Christoph H. Keitel not only for offering me the opportunity to work in his outstanding group, but also for giving me the strong and selfless supports when I was in trouble. I am also grateful for his great guidance and enlightenment for all the work in this thesis. I am always inspired and motivated after every discussions of physics with him. Even though sometime the discussion is short, it is very fruitful. His deep insight and powerful skills for doing science impressed me and always improved my work in the most effective and efficient way.

I would like to sincerely thank my second supervisor Dr. Naveen Kumar for giving my chance to work with him and for the very long time discussions during my doctoral studis. I am also grateful to him for being patient to my poor English and for polishing my publications, specially the first one.

I would also like to extend my gratitude to Prof. Dr. Jörg Jäckel for refereeing this thesis and writing the reference report, and to Prof. Dr. Rüdiger Klingeler and Prof. Dr. Thomas Leisner for being my examination committee and their interest in my research topic.

I express my great gratitude to my proof readers: Dr. Shikha Bhadoria, Archana Sampath, Dr. Bastian Sikora, especially to Jiri Danek, and Maitreyi Sangal who have contributed super-careful proofreading to polish my thesis. I am also deeply grateful to Dr. Bastian Sikora for translating the abstract of this thesis into German. I will remember all of your helps in my heart forever and these would be the solid proof for our friendship.

I would like to take this chance to thank Dr. Frank Köck for all the computer-related supports. It is impossible to finish so many high-resolution simulations in this thesis without his support and selfless help. I would also like to thank Ms Sibel Babacan for her kind and considerate help in administrating all the affairs.

I have best thanks to Dr. Meng Wen, Dr. Yuanbin Wu and Dr. Qingzheng Lyu for the fruitful discussions about physics and the great shills for writing papers.

I am very lucky to have so many great friends in Heidelberg: Chunhai Lyu, Jiri Danek, Shikha Bhadoria, Bastian Sikora, Archana Sampath, Maitreyi Sangal, Alessandro Angioi, Pavlo Bilous, Sergey Bragin, Pei-Lun He, Sergei Kobzak, Niklas Michel....

At the end, I would like to express my endless love to my parents Weifu Tang, Fanhua Meng and my fiancee Yuanhong Zhao. With their unlimited supports, I can always recharge and refresh myself to overcome all the difficulties in my life. I would like to express my deepest and greatest love to them.